HAL
open science

Simulation numérique de verres dopés par des points quantiques CdSe

Wenke Li

To cite this version:

Wenke Li. Simulation numérique de verres dopés par des points quantiques CdSe. Chimie analytique. Université Paris sciences et lettres; Wuhan University of Technology, 2021. Français. NNT : 2021UPSLC022 . tel-03956374

HAL Id: tel-03956374

https://pastel.hal.science/tel-03956374v1

Submitted on 25 Jan 2023

HAL is a multi-disciplinary open access archive for the deposit and dissemination of scientific research documents, whether they are published or not. The documents may come from teaching and research institutions in France or abroad, or from public or private research centers.

L'archive ouverte pluridisciplinaire **HAL**, est destinée au dépôt et à la diffusion de documents scientifiques de niveau recherche, publiés ou non, émanant des établissements d'enseignement et de recherche français ou étrangers, des laboratoires publics ou privés.

PSL UNIVERSITÉ PARIS

THÈSE DE DOCTORAT DE L'UNIVERSITÉ PSL

Préparée à l'École Nationale Supérieure de Chimie de Paris
Dans le cadre d'une cotutelle avec Wuhan University of Technology

Simulation numérique de verres dopés par des points quantiques CdSe

Computational simulation of CdSe quantum dots doped glasses

Soutenue par
Wenke LI
Le 21 juin 2021

Ecole doctorale n° 388
CHIMIE PHYSIQUE ET CHIMIE ANALYTIQUE DE PARIS CENTRE

Spécialité
CHIMIE PHYSIQUE

Composition du jury :

Mme Dominique COSTA Directeur de Recherche, Chimie ParisTech/ENSCP	*Présidente*
M. Majdi HOCHLAF Professeur des Universités, Université Gustave Eiffel	*Rapporteur*
M. Kai XU Full Professor, Wuhan University of Technology	*Rapporteur*
Mme Hong LI Full Professor, Wuhan University of Technology	*Examinateur*
Mme Hazar GUESMI Chargé de recherche, ENSCM	*Examinateur*
M. Chao LIU Full Professor, Wuhan University of Technology	*Examinateur*
M. Xiujian ZHAO Full Professor,Wuhan University of Technology	*CoDirecteur de thèse*
M. François-Xavier COUDERT Directeur de Recherche, Chimie ParisTech/ENSCP	*Directeur de thèse*

Chimie Paris ParisTech | PSL

Acknowledgement

I would like to acknowledge my PhD supervisor Xiujian Zhao for receiving me as a PhD student in his lab and for providing an excellent research platform. He is profound and professional, often providing insightful suggestions to my study.

I am grateful to my co-supervisor, Chao Liu, who has been giving scientific guidance to me since I was a bachelor. His enthusiasms about quantum dots inspired me to choose it as my research direction. He taught me how to experimentally fabricate quantum dots doped glasses and how to characterize them. He helped me to find the science problem behind my research and to explore the solutions to it. He cultivated my attitude towards research-integrity and skeptical spirit. He trained my skills about organizing scientific papers. His availability made discussion with him always fruitful. Moreover, he is not only the supervisor of my research but also my life career. He has witnessed every failure and progress I made since I was a beginner.

I want to express my warm appreciations for my co-supervisor, François-Xavier Coudert, who gave me a chance to study abroad and helped me to adjust to life in France. His wealth knowledge in theoretical modelling and frequent discussion with him allowed me to develop the methodology of my research projects. He often provides efficient suggestions when I am stuck in simulations. I am always moved by his consideration which helped me to integrate into our lab. He is humorous, considerate, kind-hearted, and cool, making my three years in France enjoyable.

I also would like to thank to all of my colleagues in China: Zhiyong Zhao, Mengling Xia, Bing Ai, Qiaoyun Yin, Yunnan Guo, Yundong Li, Yuda Xiong, and Wenchao Zhang et al., for showing me their passion for science, for giving guidance to me from their experience and for cheering my up when I failed.

I wish to thank all of my colleagues in France: Guillaume Fraux, Siwar Chibani, Maxime Ducamp, Emmanuel Ren, Nicolas Castel, and Thibaud Dreher. They recommended useful codes and scripts for my simulation. They introduced French culture to me and I am especially grateful to their consideration for speaking English in our daily life even I am the only one who cannot speak French.

Many thanks to my friends in China and France, for happy life they bring to me and for hands they give to me when I am in trouble. They share my happiness and listen to my complains.

Finally, I acknowledge to my parents, for their unconditional love and support for me. They never give up me and never lose faith in me even in my most rebellious adulthood. The same appreciation to my boyfriend who has been standing with me since high school, sharing happiness and sorrows with me. Without his understanding and supports, I would not hold on to the last and he is always there whenever I need.

Remerciements

Je tiens à remercier mon directeur de thèse, Xiujian Zhao, de m'avoir accueilli en tant que doctorant dans son laboratoire et de m'avoir fourni une excellente plate-forme de recherche. Il est profond et professionnel, et apporte souvent des suggestions judicieuses à mon étude.

Je suis reconnaissante à ma co-directeur de recherche, Chao Liu, qui me donne des conseils scientifiques depuis que je suis en licence. Son enthousiasme pour les points quantiques m'a incité à le choisir comme orientation de recherche. Il m'a appris à fabriquer expérimentalement des verres dopés aux points quantiques et à les caractériser. Il m'a aidé à trouver le problème scientifique qui se cache derrière mes recherches et à en explorer les solutions. Il a cultivé mon attitude envers l'intégrité de la recherche et mon esprit sceptique. Il a formé mes compétences en matière d'organisation des articles scientifiques. Sa disponibilité a rendu les discussions avec lui toujours fructueuses. De plus, il n'est pas seulement le superviseur de mes recherches, mais aussi de mon parcours de vie. Il a été témoin de tous mes échecs et de tous mes progrès depuis que je suis débutant.

Je tiens à exprimer toute ma reconnaissance à mon co-directeur de recherche, François-Xavier Coudert, qui m'a donné la chance d'étudier à l'étranger et m'a aidé à m'adapter à la vie en France. Sa grande connaissance de la modélisation théorique et ses fréquentes discussions avec lui m'ont permis de développer la méthodologie de mes projets de recherche. Il m'apporte souvent des suggestions efficaces lorsque je suis bloqué dans des simulations. Je suis toujours ému par sa considération qui m'a aidé à m'intégrer dans notre laboratoire. Il est humoristique, attentionné, gentil et cool, ce qui rend mes trois années en France agréables.

J'aimerais également remercier tous mes collègues en Chine : Zhiyong Zhao, Mengling Xia, Bing Ai, Qiaoyun Yin, Yunnan Guo, Yundong Li, Yuda Xiong, Wenchao Zhang et autres, pour m'avoir montré leur passion pour la science, pour m'avoir guidé grâce à

leur expérience et pour m'avoir remonté le moral quand j'ai échoué.

Je tiens à remercier tous mes collègues en France : Guillaume Fraux, Siwar Chibani, Maxime Ducamp, Emmanuel Ren, Nicolas Castel, et Thibaud Dreher. Ils m'ont recommandé des codes et des scripts utiles pour ma simulation. Ils m'ont fait découvrir la culture française et je leur suis particulièrement reconnaissant de m'avoir permis de parler anglais dans notre vie quotidienne, même si je suis le seul à ne pas parler français.

Un grand merci à mes amis en Chine et en France, pour la vie heureuse qu'ils m'apportent et pour les mains qu'ils me donnent quand je suis en difficulté. Ils partagent mon bonheur et écoutent mes plaintes.

Enfin, je remercie mes parents, pour leur amour et leur soutien inconditionnels à mon égard. Ils ne m'abandonnent jamais et ne perdent jamais confiance en moi, même dans ma vie d'adulte la plus rebelle. La même reconnaissance à mon petit ami qui m'accompagne depuis le lycée et qui partage avec moi les joies et les peines. Sans sa compréhension et son soutien, je ne m'accrocherais pas à la dernière et il est toujours là quand j'ai besoin.

Abstract

CdSe Quantum dots (QDs) doped glasses attracted enormous attention due to tunable optical and electronic properties, enabling their potential application in optoelectronic devices. However, the main roadblock of quantum dots doped glasses is the poor quantum efficiency compared with colloidal quantum dots.

My Ph.D work was focused on investigating the structure and electronic structure origins of defect states of CdSe quantum dots doped glasses using computational simulations.

Initially, simplified models of Cd_nSe_n clusters capped by non-bridging oxygen, glass modifiers were built to probe the impact of adatoms on the structure and electronic structure of QDs under the framework of density functional theory. The adatoms led to structural reconstruction and formed defect states near the edge of frontier orbitals.

In depth, the local atomic structure of CdSe quantum dot-doped glass was obtained by a combination of classical molecular dynamics and *ab initio* molecular dynamics. Based on the analysis of radial distribution function, coordination, and ring structures, my results showed good agreement with experimental data, demonstrating the formation of Cd-O and Se-Na bonds at interface between glass matrix and CdSe QD with breakages of some Na-O bonds and Cd-Se bonds.

Furthermore, the electronic structure of the CdSe quantum dot-doped glasses has been calculated to shed light on the influence of structural reconstruction on its optical properties. According to the calculation of density of states, the glass composition played a predominant role in determining the luminescence mechanisms of CdSe quantum dot-doped glasses. The disappearance of intrinsic emission of CdSe QD and wide bandgap distribution was observed, explaining why the quantum efficiency was so low and the broad emission linewidth.

My studies enhanced the understanding of interfacial structure and optical properties of CdSe QD-doped glasses, serving as a new paradigm in compositional design of highly luminescent glasses.

Key words: Quantum dots, Glass, Molecular simulation, Interfacial structure, Electronic structure

Contents

Acknowledgement **1**
Remerciements ..... **III**
Abstract ..... **V**
Contents ..... **VI**
List of Figures ..... **X**
Chapter 1 ..... **1**
1 Introduction **1**
1.1 Quantum dot 1
1.1.1 Quantum confinement and size effect 2
1.1.2 Luminescence Mechanism 4
1.2 Colloidal quantum dots 6
1.2.1 Aqueous synthesis of QDs 6
1.2.2 Hot-injection organometallic synthesis 7
1.2.3 Noninjection organometallic synthesis 7
1.2.4 Obstacles 8
1.3 Quantum dots doped glasses 8
1.3.1 Fabrication Method 9
1.3.2 Nucleation mechanism 10
1.3.3 Research background 11
1.4 Computational simulation 19
1.4.1 Computational simulation of glasses 20
1.4.2 Computational simulation of quantum dots 25
1.5 Scope of this thesis 28
Chapter 2 ..... **31**
2 Methods **31**
2.1 Computational simulations 31
2.2 Statistical physics 31
2.2.1 Phase space and trajectories 32
2.2.2 Properties as ensemble averages 33

2.2.3 Properties as time averages of trajectories.....33
2.3 Classical molecular dynamics.....34
2.3.1 Equation of motion 35
2.3.2 Thermostat 37
2.3.3 Force field.....39
2.3.4 Pairwise potential in this thesis.....40
2.3.5 Periodic boundary conditions 42
2.4 Quantum Mechanics 44
2.4.1 Schrödinger equation.....44
2.4.2 Born-Oppenheimer approximations 45
2.4.3 Density functional theory 47
2.4.4 Hohenberg-Kohn theorems.....47
2.4.5 The Kohn-sham scheme 48
2.4.6 Ab initio molecular dynamics.....50
2.5 Modelling properties.....53
2.5.1 Short-range order structure.....54
2.5.2 Medium-range order structure 56
2.5.3 Mean squared displacement.....57
2.5.4 Electronic Structures.....57
2.6 Experimental method.....58
Chapter 3 59
3 Atomic and Electronic Structure of Capped Cd_nSe_n-X Clusters and Experimental Validation 59
3.1 Introduction 59
3.2 Methods 60
3.2.1 Computational details 60
3.2.2 Experimental methods 63
3.3 Results & Discussion.....63
3.3.1 CdSe clusters capped by Se atoms.....63
3.3.2 CdSe clusters capped by Cd atoms.....66
3.3.3 CdSe clusters capped by O atoms.....70
3.3.4 CdSe clusters capped by Na atoms.....71

3.3.5 CdSe clusters capped by Ca atoms 74
3.3.6 CdSe clusters capped by multiple types of atoms 76
3.3.7 Experimental validation.....78
3.4 Summary & Conclusions.....83
Chapter 4 86
4 Local atomic structure of a Na_2O-2SiO_2 glass 86
4.1 Introduction 86
4.2 Classical molecular dynamics.....87
4.2.1 Initial methodology to generate glass matrix.....87
4.2.2 Results and discussion 89
4.2.3 Adjustment of the parameters 92
4.2.4 New methodology to generate glass matrix.....97
4.2.5 Results and discussion 97
4.3 Summary & Conclusions.....101
Chapter 5 103
5 Local atomic structures of CdSe quantum dot-doped glasses 103
5.1 Introduction 103
5.2 Development of the methodology 104
5.2.1 Quenching method.....104
5.2.2 System size 112
5.2.3 Computational details 116
5.3 Results & discussion.....117
5.3.1 Geometry 117
5.3.2 Radial distribution function 119
5.3.3 Coordination &ring structures 122
5.4 Summary & conclusions.....126
Chapter 6 129
6 Atomic and electronic structures of CdSe quantum dot-doped $x$$Na_2O$-(1-$x$)$SiO_2$ glasses.....129
6.1 Introduction 129
6.2 Computational details 130
6.2.1 Generation of x Na_2O-$(1-x)$ SiO_2 glasses matrix 131

6.2.2 Generation of CdSe quantum dot-doped glasses structure 132
6.2.3 *AIMD* of CdSe quantum dot in glass matrix 132
6.2.4 Electronic structures calculation 132
6.3 Results of calculations & Discussions 134
6.3.1 Atomic structure 134
6.3.2 HOMO-LUMO gap distribution 136
6.3.3 Luminescence Mechanisms 138
6.3.4 Impact of glass matrices on the electronic structure of CdSe QD 142
6.3.5 Impact of CdSe QD on the electronic structures of glass matrices ..143
6.4 Summary & conclusions 147
Chapter 7 149
7 Conclusions and perspectives 149
7.1 Conclusions 149
7.2 Perspectives 151
Bibliography 153
Résumé en Français 162
Contexte de mon travail 163
Questions scientifiques ouvertes 170
Apports de mes travaux 171
Conclusions et perspectives 178

List of Figures

Figure 1.1 Idealized model of electronic states in a bulk semiconductor (left) and a spherical QD made of the same material (right). Taken from ref.1. 1

Figure 1.2 Representative QDs materials scaled as a function of their emission wavelength superimposed over the spectrum. Taken from ref.3. 3

Figure 1.3 Surface states in a spherical CdSe colloidal quantum dot with unpassivated (111) facets. (a) Model, (b)Projected density of states, (c) Se-related surface state on the valence band side, (d) Cd-related state on the conduction band side. Taken from ref.11.....4

Figure 1.4 Luminescence mechanism of quantum dots.....5

Figure 1.5 The electronic structure of ligated QD illustrating the appearance of trap states due to imperfect passivation (a) and the elimination of these defect states by perfect passivation (b). Adapted from ref.14. 6

Figure 1.6 Schematic diagram of the preparation process of QDs-embedded glasses. Taken from ref.39. 9

Figure 1.7 Schematic diagram of dissolution, nucleation, and growth process of QDs in glasses relevant to the doping concentration and temperature. Taken from ref.39. 10

Figure 1.8 Raman frequency shifts of the quantum dots in borosilicate (circle), silicate (triangle), and germanate (square) glasses with fitting curves. Taken from ref. 63. 16

Figure 1.9 (a) Normalized absorption coefficient (dashed) and PL spectra under 455-nm excitation (solid) of modified CdSe quantum dots-doped glasses. Images of the samples are also displayed within the figure. (b) Commission international de l'eclairage (CIE) color coordinates of LEDs mounted with modified CdSe QDs doped glasses of various thickness heat-treated for 5, 10, 15, and 20 h at 500 ^{o}C. Lines are drawn as guides for the eye. The inset presents the EL and PL spectra of wLED. Actual photos of the LEDs with CdSe QDs doped glasses of the same thickness (1.2 mm) with varying heat-treatment duration are presented at the right of the figure. (c) Thermal

quenching (TQ) property of the wLED with modified CdSe QDs doped glasses compared with other wLEDs with phosphor-in-glass or phosphor with silicone resin employed, and colloidal QD with multi-shells as the color converter. Taken from ref. 30.....19

Figure 1.10 Different types of ligands capped with CdSe quantum dots. Taken from ref. 109. 27

Figure 2.1 Illustration of the use of periodic boundary conditions 8 (2x2x2) unit cells are presented while only 1 is really considered in the simulation. Cd, magenta, Se, blue. 43

Figure 2.2 Flow chart of the Kohn-Sham self-consistent field method.....50

Figure 2.3 Space discretization for the evaluation of the radial distribution function. 54

Figure 2.4 A radial distribution function for Si-O pairs in silicate glasses. The interatomic distance of Si-O pairs is 1.64 Å. 55

Figure 3.1 The optimized structure of Cd_nSe_n clusters (n = 3, 10, 13, 33) constructed based on a wurtzite phase with the bulk Cd-Se bond length. White balls represent the Cd atoms while the yellow balls represent Se atoms. 61

Figure 3.2 Initial structure of Cd_nSe_n-X (X=Se, Cd, O, Na, and Ca). White, yellow, and blue balls represent the Cd atoms, Se atoms and X atoms, respectively. 61

Figure 3.3 Initial structure for $Cd_{33}Se_{33}$ clusters capped by (a) O (red ball)-Na (purple ball); (b) O-Ca (green ball), (c) Na, Ca; (d) Na, O, Ca. 62

Figure 3.4 Optimized structures, DOS, and HOMO/LUMO levels of the pristine clusters (black line), the Se atom (yellow balls)-capped Cd_nSe_n clusters (red line). The value in the insets represents the E_{gap} of capped Cd_nSe_n QDs. The black arrows and red arrows represent the energy level of frontier orbitals of pristine and capped clusters, respectively. Structure of pristine QDs are on **Figure 3.1.** 64

Figure 3.5 Optimized structures, DOS, and HOMO/LUMO levels of the pristine clusters (black line), the Cd atom (white balls)-capped Cd_nSe_n clusters (red line). The value in the insets represents the E_{gap} of capped Cd_nSe_n QDs. The

black arrows and red arrows represent the energy level of frontier orbitals of pristine and capped clusters, respectively. 67

Figure 3.6 (a) The initial structure of Cd_nSe_n-Cd QDs where Cd is bonded with surface Se atom of CdSe clusters. (b) The optimized structure of Cd_nSe_n-Cd QDs. The Zn atom has the same structural reconstruction as Cd atom so I just put the results of Cd atom. 69

Figure 3.7 Optimized structures, DOS, and HOMO/LUMO levels of the pristine clusters (black line), the O atom (red balls)-capped Cd_nSe_n clusters (red line). The value in the insets represents the E_{gap} of capped Cd_nSe_n QDs. The black arrows and red arrows represent the energy level of frontier orbitals of pristine and capped clusters, respectively. 70

Figure 3.8 Optimized structures, DOS, and HOMO/LUMO levels of the pristine clusters (black line), the Na atom (purple balls)-capped Cd_nSe_n clusters (red line). The value in the insets represents the E_{gap} of capped Cd_nSe_n QDs. The black arrows and red arrows represent the energy level of frontier orbitals of pristine and capped clusters, respectively. 72

Figure 3.9 Optimized structures of $Cd_{33}Se_{33}$ clusters capped with different number of Na atoms. (n = 1, 2, 3, and 22) 74

Figure 3.10 (a) Density of states of pristine $Cd_{33}Se_{33}$ clusters and $Cd_{33}Se_{33}$ clusters capped by 1, 2, 3 and 22 sodium atoms. (b) Energy diagrams originated from DOS include HOMO and LUMO levels of pristine clusters, capped clusters and E_{gap} values formed by Se-Na bonds. 74

Figure 3.11 The optimized structure of Cd_nSe_n-Ca QDs. 75

Figure 3.12 Energy diagrams originated from DOS include HOMO and LUMO levels of pristine clusters (black line), capped clusters (red dashed line) and E_{gap} values formed by Cd-Ca bonds. 75

Figure 3.13 Optimized structure for $Cd_{33}Se_{33}$ clusters capped by (a) O (red ball)-Na (purple ball); (b) O-Ca (green ball), (c) Na, Ca; (d) Na, O, Ca. 76

Figure 3.14 (a) Density of states of pristine $Cd_{33}Se_{33}$ clusters and clusters capped by Na, O, Ca, Na and Ca, Na, Ca and O, O and Ca, O and Na atoms. (b) Energy diagrams from DOS include HOMO and LUMO levels of pristine clusters, capped clusters and E_{gap} values. 77

Figure 3.15 (a) TEM micrograph of glass heat treated at 530 ºC for 10 h under an accelerating voltage of 150 kV. Upper inset: TEM image of one nanocrystal in the glass. Bottom inset: Size distribution histogram of nanocrystals shown in (a). (b) Raman spectra of the as-prepared glasses and glasses heat treated at 490 ºC, 510 ºC and 530 ºC for 10 h. 79

Figure 3.16 (a) Absorption spectra and (b) normalized photoluminescence spectra (recorded under 365 nm laser excitation) of as-prepared and heat-treated glass specimens. (c) Energy level diagram of pristine and capped Cd_nSe_n QDs with different adatoms. The black, blue, pink, green lines and red lines correspond to the HOMO and LUMO of pristine CdSe QDs, and Cd-Cd, Se-O, Se-Se, and Se-Na bonds, respectively. (d) Near-infrared photoluminescence spectra of as-prepared and heat-treated glass specimens recorded under 404 nm laser excitation. 80

Figure 3.17 (a), (b) and (c) The experimental data of each sample are shown in hollow circles. The blue and green lines are the individual components by Gaussian fitting, and the red lines are the sum of individual fitting lines. (d) E_{gap} is the energy of the first absorption peak and the solid line demonstrates that the energy of the PL peak is equal to the energy of the first absorption peak. 82

Figure 3.18 E_{gap} of pristine Cd_nSe_n QDs and capped Cd_nSe_n QDs of different size. (n=3, 10, 13 and 33).....83

Figure 4.1 Initial structure of the classical molecular dynamics simulation. The red, yellow, and purple balls represent O atoms, Si atoms and Na atoms respectively. 88

Figure 4.2 Temperature profile during the stepwise melt-quenching approach followed to generate a Na_2O-$2SiO_2$ glass structure of 300 atoms, with molecular dynamics simulations.....89

Figure 4.3 (a) The initial configuration of Na_2O-$2SiO_2$ glasses, (b) 300 K at melting stage, (c) 4000 K at melting stage, (d) 4000K at the end of NPT equilibration stage, (e) 4000K at the end of NVE equilibration stage, (f) 300K at quenching stage, (g) 300K at the end of NPT equilibration stage, and (h) 300K at the end of NVE equilibration stage. The yellow parts represent the

$[SiO_4]^{4-}$ tetrahedra. The yellow, red and purple atoms represent Si, O, and Na atoms respectively.....90

Figure 4.4 Radial distribution functions of Si-O pairs (Black line), Na-O pairs (Red line), and the whole system (Blue line), averaged over the 200ps equilibration run at 300K in NVE ensemble. 91

Figure 4.5 The average mean squared displacement (MSD) for Na, O, and Si ions, simulated in (a) 300K at melting stages, (b) 4000K at equilibration NVE stages, and (c) 300K at equilibration NVE stages. 92

Figure 4.6 Final configuration of previous classical MD simulations at 3900 K within NPT ensemble during the melting stage. The yellow, red and purple atoms represent Si, O, and Na atoms respectively.....93

Figure 4.7 Radial distribution functions for Si-O (a) and Na-O (b) pairs averaged over the 60 ps run at 4000K within NPT ensemble. C6, C7.5, and C7.9 represents the cutoff radius of 6 Å, 7.5 Å, and 7.9 Å respectively. 94

Figure 4.8 Radial distribution functions for Si-O pairs and Na-O pairs averaged over the 60 ps run at 4000K within NPT ensemble (Black lines) or NVT ensemble (Red lines). C6, C7.5, and C7.9 represents the cutoff radius of 6 Å, 7.5 Å, and 7.9 Å respectively.....94

Figure 4.9 Mean squared displacements for the Na^{+}, O^{2-}, and Si^{4+} in Na_2O-$2SiO_2$ system averaged over the 60 ps run at 4000K within NPT ensemble. 95

Figure 4.10 Mean squared displacements for the Na^{+}, O^{2-}, and Si^{4+-} in Na_2O-$2SiO_2$ system averaged over the 60 ps run at 4000K within NVT ensemble. 95

Figure 4.11 (a) is the final configuration of previous classical MD run at 4000K within NPT ensemble for 60 ps. (a) is the initial configuration of the subsequent classical MD run at 4000K and at 1000K within NPT ensemble for 200 ps, which final configuration was (b) and (c) respectively. 96

Figure 4.12 (a) Radial distribution functions for Si-O (black lines) and Na-O (red lines) pairs for MD runs at 1000 K (solid lines) and 4000 K (dashed lines), (b) and (c) MSDs for temperature at 4000 K and 1000 K respectively.....96

Figure 4.13 Final structure of the classical MD simulations. The left graph is in the ball-stick view while the right graph is in the polyhedron view, where the

yellow parts represent the $[SiO_4]^{4-}$ tetrahedra.....98
Figure 4.14 Radial distribution functions of Si-O pairs in melting process (a) and quenching process (c), and Na-O pairs in melting process (b) and quenching process (d).....99
Figure 4.15 (a) Silico-oxygen-silicon bond angle distributions for the final structure of the MD runs, (b) Oxygen-silicon-oxygen bond angle distributions for the final structure of the MD runs.....100
Figure 4.16 Mean squared displacements for the Na^+, O^{2-}, and Si^{4+} in Na_2O-2SiO_2 system averaged over the 60 ps run at 4000 K within NVT ensemble using potential developed by (a) Pedone et al. and (b)12-6 potential respectively. 101
Figure 5.1 The initial configuration for the classical MD calculations. CdSe QD-doped glass compositions: (a) 16 Na_2O-32 SiO_2-33 CdSe; (b) 39 Na_2O-78 SiO_2-33 CdSe; (c) 180 Na_2O-360 SiO_2-33 CdSe. Si: yellow, O: red, Na: purple, Se: magenta, Cd: blue.....105
Figure 5.2 (a) The initial configuration of $Cd_{33}Se_{33}$ QD in a simulation box which size is 2.5 nm; (b) The final configuration of the 200 ps MD run at 1300 K of NVT dynamics.....105
Figure 5.3 The final configuration for the classical MD calculations. The CdSe QD was allowed to move in (a) and (b) while kept frozen from 1000 K to 500K in (c) and (d). 107
Figure 5.4 Total radial distribution functions for glass with different quenching method and glass compositions. (a) 16 Na_2O-32 SiO_2-33 CdSe; (b) 39 Na_2O-78 SiO_2-33 CdSe. The first method was referred as "Not Frozen" (Black Lines) and the second method was referred as "Frozen" (Red Lines). 108
Figure 5.5 The final configuration for the classical MD calculations for (a) 16 Na_2O-32 SiO_2-33 CdSe; (b) 39 Na_2O-78 SiO_2-33 CdSe; (c) 180 Na_2O-360 SiO_2-33 CdSe. The CdSe QD was frozen from 1000 K to 500 K and allowed to move from 500K to 300K.....113
Figure 5.6 Total radial distribution functions for glass with different size of glass matrix. Black lines: 16 Na_2O-32 SiO_2-33CdSe; Red lines: 39 Na_2O-78 SiO_2-33 CdSe, Blue lines: 180 Na_2O-360 SiO_2-33 CdSe.....114

Figure 5.7 (a) The initial configuration for the classical MD calculations. (b) The final configuration for classical MD simulations, used as initial configuration for the geometry optimization by DFT method. (c) The geometry-optimized structure at the DFT level, used as the initial configuration for the *ab initio* molecular dynamics. (d) The final configuration from the AIMD simulations. Se atoms and Cd atoms dissociated from the quantum dot are highlighted in pink and green, respectively. 118

Figure 5.8 Radial distribution functions for (a) Si–O, (b) Na–O and (c) Cd–Se pairs in the initial structure (black lines) and averaged over the *ab initio* molecular dynamics (red lines), for a quantum dot embedded in the 39 Na_2O-78 SiO_2 glass matrix. 120

Figure 5.9 (a) The final configuration from the *ab initio* molecular dynamics. Radial distribution functions for (b) Cd-O, (c) Se-Na, (d) Se-O, (e) Se-Se, and (f) Cd-Cd pairs, averaged over the *ab initio* molecular dynamics (red), for a quantum dot embedded in the 39 Na_2O-78 SiO_2 glass matrix. 121

Figure 5.10 Histograms of coordination numbers for different pairs of atoms, comparing the initial structure (in black) and the average over the *ab initio* MD simulation (in red). (a) O coordination around Si atoms. (b) O coordination around Na atoms. (c) Se coordination around Cd atoms. (d) Cd coordination around Se atoms. 124

Figure 6.1 Illustration of structural composition of CdSe quantum dot-doped glasses. 131

Figure 6.2 Density of states of $Cd_{33}Se_{33}$ quantum dot calculated based on B3LYP (black line), PBE (red line), PBE0 (blue line), and HSE06 (magenta line) exchange-correlation functionals. The top of the valence band and the Fermi level was set at 0 eV. 133

Figure 6.3 Final configuration from the AIMD simulations of the CdSe quantum dot-doped glasses. Glass composition: (a)112 SiO_2-33 CdSe, (b) 30 Na_2O-90 SiO_2-33 CdSe, (c) 39 Na_2O-78 SiO_2-33 CdSe, (d) 62 Na_2O-62 SiO_2-33 CdSe. 135

Figure 6.4 Histograms of HOMO-LUMO gap for 50 configurations of CdSe quantum dot-doped silicate glasses. The composition of the x Na_2O- (1-x)

SiO_2 glass matrices: (a) x = 0; (b) x= 0.25; (c) x = 0.33; (d) x =0.5. A simple Gaussian function was used to fit the data and SD represent the standard deviation. This is not a physical model but a guide for the eye and a way of comparing distributions. 137

Figure 6.5 Density of states and projected density of states of final structure of the AIMD calculation of CdSe quantum dot-doped glasses. The hybrid glass included O atoms, Na atoms and Si atoms, while hybrid QD was composed of Cd atoms and Se atoms. Cd-O (Se- Na) represent the projected density of states of the Cd(Se) atoms bonded with O(Na) atoms and O(Na) atoms bonded with Cd(Se) atoms. The HOMO and the Fermi level are set at 0 eV. Panel (a) to (d) correspond to compositions of x = 0, 0.25, 0.33, and 0.5, respectively. 139

Figure 6.6 Energy diagrams of CdSe quantum dot-doped glasses. 140

Figure 6.7 HOMO-LUMO gap of the 50 configurations of the AIMD production run of CdSe quantum dot-doped glass. The solid black line represent the HOMO-LUMO gap of the pristine QD which is for reference here. The black symbols represent the luminescence mechanism of this configuration belonging to type I and red symbols represent type II (see **Figure 6.6**). ..141

Figure 6.8 The density of states of the hybrid QD of AIMD simulation of CdSe quantum dot-doped glasses and pristine QD. Cd(O) represents the Cd atoms bonded with O atoms and Se(Na) represents the Se atoms bonded with Na atoms. Cd represents the Cd atoms not bonded with O atoms. Se represent the Se atoms not bonded with Na atoms.....143

Figure 6.9 The density of states of the hybrid of the AIMD simulation of CdSe quantum dot-doped glasses and pristine glasses. O(Cd) represents the O atom bonded with Cd atom and Na(Se) represent the Na atom bonded with Se atom. 145

Figure 6.10 This configuration was obtained from the AIMD production run with x = 0.33 at 7 ps. (a) The density of states of hybrid glass, hybrid QD, pristine QD, pristine glass (x= 0.33), Cd-O bonds and Se-Na bonds. (b) The density of states of the hybrid glasses and pristine glasses (x =0.33). (c) The density of states of the hybrid QD and the pristine QD. 147

Chapter 1

1 Introduction

1.1 Quantum dot

An exciton (a bound state consisting of a hole and an electron) in a bulk semiconductor has a characteristic delocalization length, which is its "Bohr radius". The exciton becomes quantum-confined when one or more spatial dimensions of the semiconductor crystal are on the order of, or smaller than, the Bohr radius. A quantum dot (QD) is a semiconductor whose electronic wavefunction is quantum-confined in all dimensions. A distinct feature of QD regime is the discrete structure of electronic states, much different from the continuous energy bands of the bulk material (**Figure 1.1**). The quantized states are ordered in energy and are denoted by a pair of principal quantum number (n) and azimuthal quantum number (L), in which n is usually shown by the number and L by the letter (S, P, D, … for L = 0, 1, 2, …, respectively) and the corresponding states are 1S, 1P, 1D, 2S, etc.

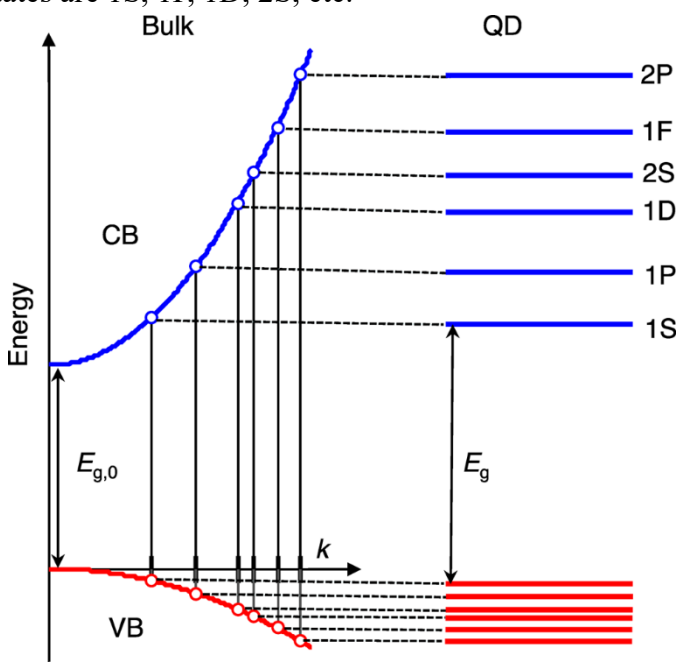

Figure 1.1 Idealized model of electronic states in a bulk semiconductor (left) and a spherical QD made of the same material (right). Taken from ref.1.

1.1.1 Quantum confinement and size effect

The quantum-confined excitons can be approximately illustrated by a simple three-dimensional particle-in-a box potential. The envelope function of the ground states has the following radial:

$$\Phi_{1,0,0}(\mathbf{r},\boldsymbol{\theta},\boldsymbol{\varphi}) = \frac{1}{\sqrt{2\pi R}}\frac{\sin(\pi r/R)}{r} \qquad \textbf{Eq. 1-1}$$

The corresponding energy is:

$$\boldsymbol{E}_{1,0} = \frac{\hbar^2\pi^2}{2mR^2} \qquad \textbf{Eq. 1-2}$$

where $\hbar$ is the Planck's reduced constant and m is the particle mass, which is replaced by the effective electron mass (m_e) or hole mass (m_h) in the case of conduction or the valence band, respectively. R is the radius of quantum dots. The bandgap energy (E_g) is defined by the spacing between the band-edge electron ($1S_e$) and hole ($1S_h$) levels, and it can be calculated as the sum of the bulk bandgap ($E_{g,0}$) and the $E_{1,0}$ energies of the electron and the hole:[2]

$$\boldsymbol{E_g} = \boldsymbol{E}_{g,0} + \frac{\hbar^2\pi^2}{2m_eR^2} + \frac{\hbar^2\pi^2}{2m_hR^2} = \boldsymbol{E}_{g,0} + \frac{\hbar^2\pi^2}{2m_{eh}R^2} \qquad \textbf{Eq. 1-3}$$

where $m_{eh} = m_e m_h/(m_e+m_h)$ is the reduced electron-hole mass. And the Coulombic effects should be taken into consideration:

$$\boldsymbol{E_g} = \boldsymbol{E}_{g,0} + \frac{\hbar^2\pi^2}{2m_{eh}R^2} - \frac{1.765e^2}{\varepsilon_\infty R} \qquad \textbf{Eq. 1-4}$$

where ε_∞ is the high-frequency dielectric constant. By calculating the energy of Coulomb e-h interaction within the first-order perturbation theory, the third term at the right side was obtained.

Therefore, the bandgap of the quantum dots (QDs) can be tuned by its size. A blue shift of the first absorption peak can be observed compared with their bulk counterparts. This unique feature at nanoscale has prompted development of research and commercialization of QDs. By choosing suitable materials with desirable bandgap and

changing the size of QDs, their emission spectra can cover the ultraviolet (UV), visible, and near-infrared regions (NIR) (**Figure 1.2**).[3]

Quantum dots can be divided into several categories depending on their composition.

(1) II-VI (CdS, CdSe, CdTe, ZnSe) quantum dots are the most commonly studied materials because their emission spectra can cover the visible region.

(2) IV-VI (PbS, PbSe, PbTe) quantum dots also receive great attention due to their advantages for near-infrared emission.

(3) III-V (GaAs, InAs) quantum dots find their application in laser amplifier for the mid-infrared emission.

(4) Recently, there has been growing interest in the perovskite ($CsPbBr_3$, $CH_3NH_3PbCl_3$) quantum dots owing to their high quantum efficiency in visible regions. Besides, the carbon, silicon, and silver quantum dots also attract researchers' attention. Their high quantum efficiency, narrow emission linewidth and size-tunable optical properties make QDs fascinating in applications for solar cells[4-5], LEDs,[6-8] bio-labelling[9-10] and so on.

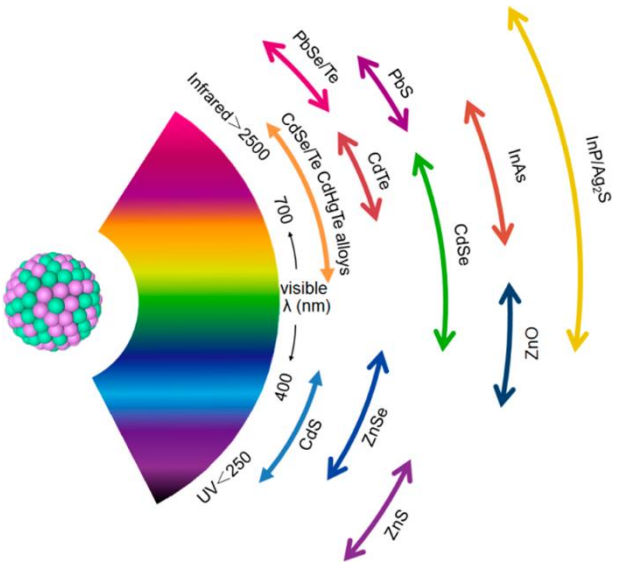

Figure 1.2 Representative QDs materials scaled as a function of their emission wavelength superimposed over the spectrum. Taken from ref.3.

1.1.2 Luminescence Mechanism

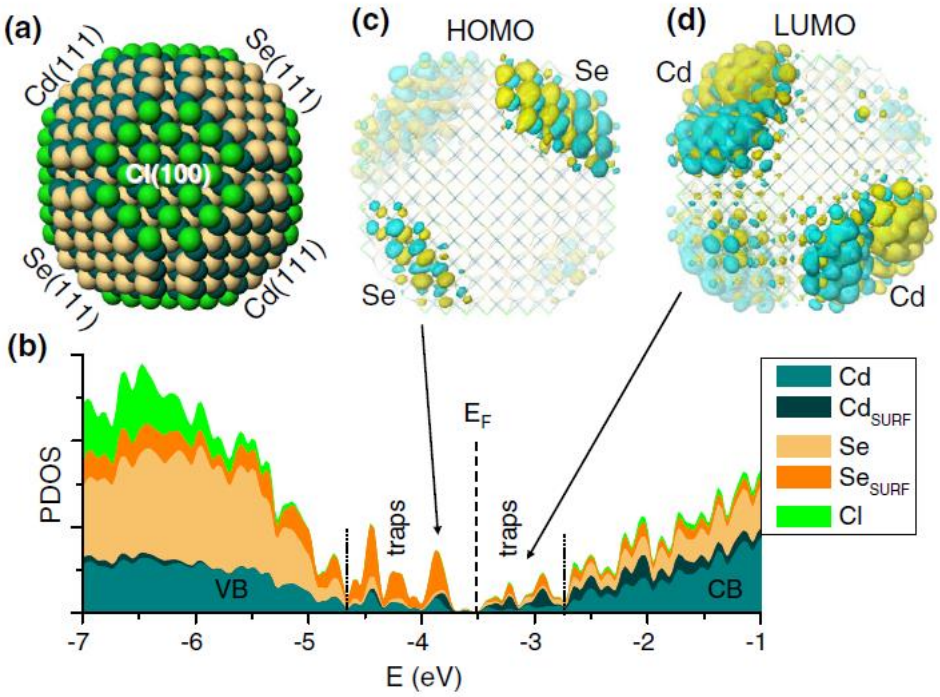

Figure 1.3 Surface states in a spherical CdSe colloidal quantum dot with unpassivated (111) facets. (a) Model, (b)Projected density of states, (c) Se-related surface state on the valence band side, (d) Cd-related state on the conduction band side. Taken from ref.11.

Due to the high surface-to-volume ratio, there can be a lot of surface defects such as dangling bonds and vacancies, forming shallow or deep trap states in the bandgap (**Figure 1.3**).[11] For example, the trap states were observed to be localized on the valence band side according to partial density of states (PDOS) (**Figure 1.3 (b)**), and the electron density of the highest occupied molecular orbitals (HOMO) was found to be distributed in the unpassivated Se-terminated (111) facets (**Figure 1.3 (c)**). Meanwhile, the Cd-terminated (111) facets also introduced trap states near the edge of conduction band, with the electron density of lowest unoccupied molecular orbitals (LUMO) localized on these facets (**Figure 1.3 (d)**).

The luminescence mechanism of quantum dots is illustrated in **Figure 1.4**.[12] Upon excitation, the electron can be excited to the high energy level in the conduction band

(process i), and a hole is created in the valence band, which cools rapidly to the highest valence level ($1S_h$). The electron in the high energy levels relax to the lowest conduction level ($1S_e$) within hundreds of femtoseconds by dissipating the excess energy into thermal energy (process ii). Subsequently, the electron in the lowest conduction level can directly recombine with the hole in the highest valence level radiatively, leading to the intrinsic emission of QDs (process iii). However, the electrons can be trapped by the trap states (process iv), and then relax to the valence band (process v), contributing to the so-called defect emission, which is red-shifted compared with the intrinsic emission. Auger recombination is also observed in quantum dots upon intense excitation (process vi). Finally, the energy can be dissipated by non-radiative process (process vii) without emission.

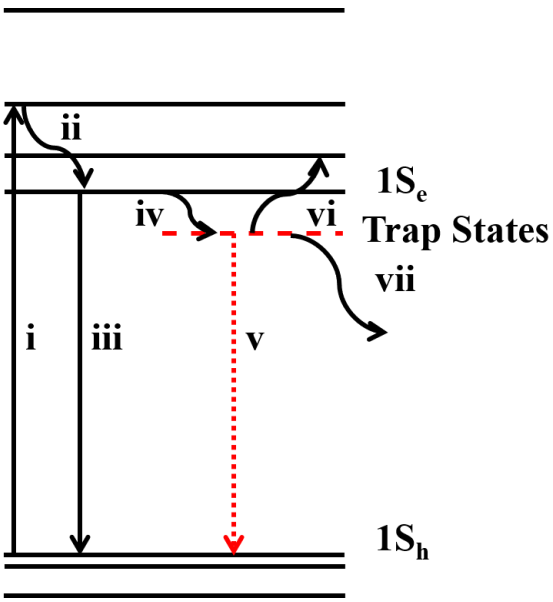

Figure 1.4 Luminescence mechanism of quantum dots

Defect emission is competitive to intrinsic emission, resulting in broad emission linewidth and low quantum efficiency. Usually, defects can be passivated by organic ligands but in realistic the insufficient coverage of organic layers may fail to remove defect states (**Figure 1.5 (a)**). However, the surface defects can be eliminated by forming organic ligands layer to terminate dangling bonds (**Figure 1.5 (b)**).[13-14] As Core/Shell structure is also a common and effective method to remove surface defects

and improve the quantum efficiency.[15-16]

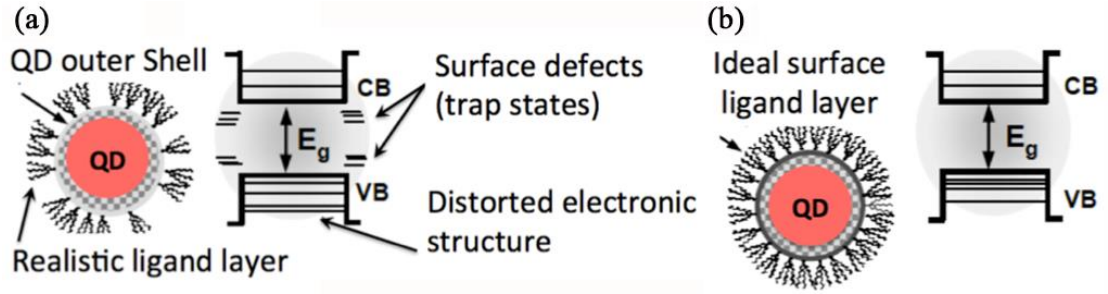

Figure 1.5 The electronic structure of ligated QD illustrating the appearance of trap states due to imperfect passivation (a) and the elimination of these defect states by perfect passivation (b). Adapted from ref.14.

1.2 Colloidal quantum dots

Although quantum dots were first fabricated in glasses,[17] most of the research efforts in the nanocrystal field have shifted in the direction of colloidal samples that allowed for a more facile size control, narrower size distributions, the ease of surface passivation and higher quantum efficiency. There are several methods to fabricate QDs: (1) aqueous methods, (2) hot-injection organometallic methods, (3) noninjection organometallic methods. Apart from those methods, QDs can be synthesized by biosynthesis,[18] microwaves[19], sol-gel[20] and so on. However, I chose in this thesis to put emphasis on the introduction of these three methods, which are the most widely used.

1.2.1 Aqueous synthesis of QDs

The concept of "colloidal quantum dots" was first proposed by L.E. Brus et al. in 1983.[21] The aqueous colloid was prepared by slowly injecting $CdSO_4$ solution into a stirring $(NH_4)_2S$ solution (pH = 9). The $(NH_4)_2S$ contained 0.1% by weight of styrene/maleic anhydride copolymer, acting as a stabilizing agent to prevent coagulation and flocculation. They also synthesized the acetonitrile colloid by injecting the $Cd(NO_3)_2 \cdot 4H_2O$ acetonitrile solution into $(NH_4)_2S$. Electron diffraction showed the CdS QDs had a structure similar to the zinc blend CdS bulk structure. The average size of the CdS QDs was 3 nm, and a large shift of 0.8 eV to higher energy in the lowest

electronic excited state was observed compared to bulk CdS.

An important landmark in the development of wet chemical routes for CdX (X = S, Se, Te) nanocrystals was the use of different thiols as stabilizing agents in aqueous solution. Rogach et al[22] fabricated the CdSe nanoparticles through the addition of freshly prepared oxygen-free NaHSe solutions to N_2-saturated $Cd(ClO_4)\cdot 6H_2O$ solutions at pH 11.2 in the presence of different thiols as stabilizing agents. It was found that the size of the CdSe QDs can be controlled by stabilizing agents, with thioalcohols tending to form smaller CdSe QDs (1.4 - 2.2 nm diameter) while larger CdSe QDs (2.1-3.2 nm diameter) could be obtained using thioacids.

1.2.2 Hot-injection organometallic synthesis

The pioneering work by Murray et al.[23] in 1993 proposed a simple route to the production of high-quality CdSe QDs, which size ranging from 1.2 nm to 11.5 nm with narrow size distributions (< 5% rms in diameter). $(CH_3)_2Cd$ and TOPSe (Appropriate masses of selenium were dissolved directly in sufficient Tri-*n*-octylphosphine (TOP)) was added to TOPO (Tri-*n*-octylphosphine oxide) in a drybox separately, before mixing together in a syringe. Then the mixture was injected into a stirring reaction flask in a single injection through a rubber septum and the temperature kept around 230-260 ºC. By obtaining the product from the reaction solution at regular intervals, the size of the QDs increase with time. However, $(CH_3)_2Cd$ is extremely toxic. Researchers have worked for decades to develop green and low-cost synthesis methods by adjusting the source of precursor and stabilizing agent. One breakthrough was by Peng et al.,[24-25] who used inexpensive and less toxic CdO instead of $(CH_3)_2Cd$. More recently, Deng et al.[26] used liquid paraffin and oleic acid as the stabilizing agents replacing TOP/TOPO.

1.2.3 Noninjection organometallic synthesis

The hot-injection method requires rapid injection of the mixture of organometallic precursor into a hot mixture of organic solvents, indicating the difficulty to control the

temperature upon injection, resulting in low batch-batch reproducibility. Therefore, a number of nonjection organometallic synthesis methods have been developed to prepare the QDs at large scale. One-pot noninjection organometallic synthesis developed by Ouyang et al.[27] used cadmium acetate dihydrate ($Cd(OAc)_2)\cdot 2H_2O$ and elemental selenium as Cd and Se source compounds, respectively. The growth of the nanocrystals was carried out in a reaction flask consisting of source compounds, one fatty acid, and 1-octadecene (ODE) at temperature ranging from 120 - 240 ºC. The reactants were staying at several intermediate temperature for some time like 15 mins. This approach fabricated three families of magic-size QDs, with sharp bandgap absorption at 395 nm, 463 nm, and 513 nm. Most importantly, this synthesis method exhibited highly synthetic reproducibility and large-scale production without decreasing the quality of CdSe QDs.

1.2.4 Obstacles

As I mentioned above, the high surface-to-volume ratio of quantum dots contributes to their dual nature (poor stability and high reactivity), thus they are extremely unstable and easily change themselves or react with active substance s to reach a relatively stable states in some cases. On the one hand, their high reactivity enable them can be easily processed into desired functional nanomaterials by suitable chemical transformations. On the other hand, the high reactivity also make them unstable, however, as the foundation of application of QDs, it is supposed to maintain a stable state during storage, processing, and utilization. Even passivated by ligand layers, the use of organic solutions cannot protect QDs from oxygen, water and thermal effects in the environments, so colloidal QDs can be easily oxidized or degraded during use.[15]

1.3 Quantum dots doped glasses

The research of quantum dots was initiated in 1980 by Ekimov et al.,[17] who fabricated CuCl nanocrystals. Due to their size-dependent properties and narrow emission linewidth, QDs have attracted enormous attention in thirty years. Compared to QDs in glass matrix, it is easy to passivate the surface of colloidal QDs by organic ligands or forming core/shell structure, improving the quantum efficiency. Meanwhile, the size

distribution of colloidal quantum dots is also controllable. However, the main obstacle of colloidal QDs is the agglomeration. The organic ligands are sensitive to oxygen, water, and temperature of the environment, restricting the practical application of colloidal QDs.[15] QDs embedded in glass matrix can take advantage of the mechanical, thermal and chemical stability of glasses. Thus, the quantum dots-doped glass can have potential application in lasers,[28] LEDs,[29-30] and so on.

1.3.1 Fabrication Method

Quantum dots-doped glasses can be fabricated by sol-gel method,[4, 31-34] ion-implantation method,[35-37] ion-exchange method.[38] The shortcoming of the sol-gel prepared glasses are the residual stress and the difficulty in the elimination of organic ligands while the depth of ions that can be implanted or exchanged is limited in the latter two methods.

Apart from the above methods, the most common route of preparation of QDs in a glass matrix is by the melt-quenching method (**Figure 1.6**).[39] First, the raw materials including glass components and QDs components are mixed thoroughly. Then the mixed powders are melted at high temperature in crucibles. The melts are poured onto a brass mold and quenched by pressing with other plates. The obtained glasses are subsequently annealed at a lower temperature to remove the thermal stress. After annealing, further heat-treatments at different temperature (depending on the transition and crystallization temperature of glasses) for various duration (from several minutes to couples of hours) are conducted on the as-prepared glasses in order to fabricate the quantum dots-doped glasses.

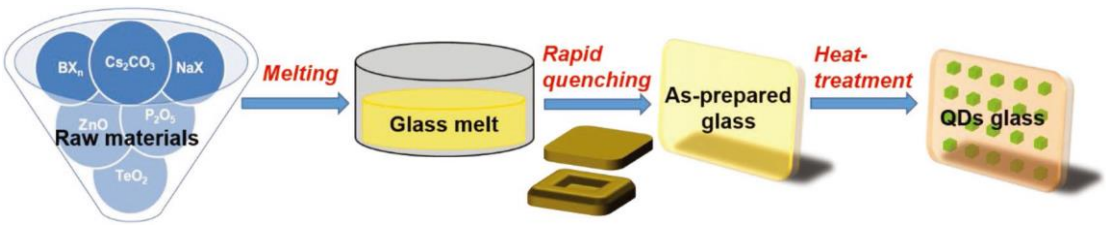

Figure 1.6 Schematic diagram of the preparation process of QDs-embedded glasses. Taken from ref.39.

1.3.2 Nucleation mechanism

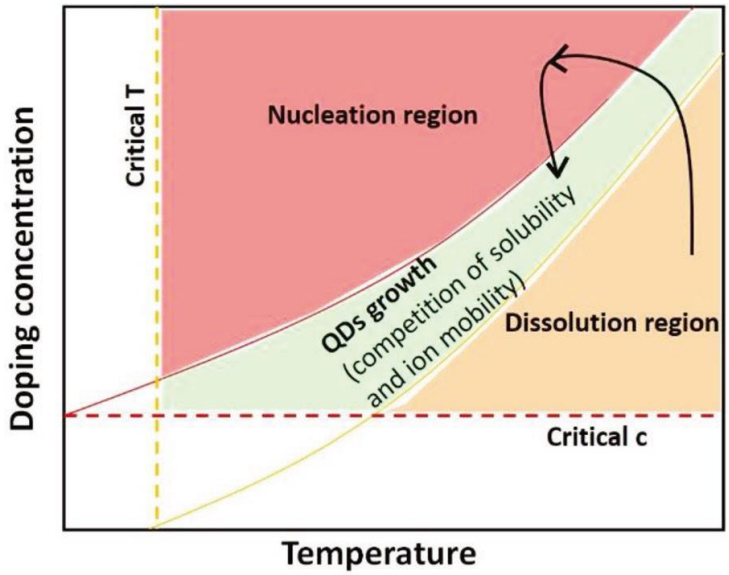

Figure 1.7 Schematic diagram of dissolution, nucleation, and growth process of QDs in glasses relevant to the doping concentration and temperature. Taken from ref.39.

The nucleation mechanism has been enormous studied in CdS,[40-42] CdS_xSe_{1-x},[42-44] $Cd_{1-x}Zn_xSe$,[44] CdSe[45-49] quantum dots doped glass. It is generally classified that the formation of quantum dots in glass matrices occurs in three stages (**Figure 1.7**): (1) nucleation (either homogenous or heterogeneous),[40] (2) diffusion-limited growth,[43] and (3) coarsening (Oswald ripening).[44]

Taking CdSe QDs as an example, Cd^{2+} and Se^{2-} exist homogenously in the as-prepared glass after melting. The basic principle of the formation of CdSe QDs in glass is the diffusion-controlled phase decomposition of the over-saturated solid solutions. The nucleation sites get created during glass quenching due to the persistent thermal fluctuations. Homogenous nucleation, on the other hand, occurs when the local concentration exceeds the over-saturated solubility of the reactants in glasses. The number of the nuclei increases with the time. Heterogenous nucleation happens when nucleation sites such as defects sites in the glass network, preexist. The number of the nuclei depends on the number of these nucleation site. Formation of nuclei keeps on taking place, which are unstable if their size is smaller than the critical radius (R_c), and are stable if bigger than R_c.

The nucleation stage ends when the supply of Cd or Se in the glass matrix begins to deplete. The diffusion of dopants occurs by raising the temperature (T) of the glass to between glass transition temperature (T_g) and crystallization temperature (T_c). T is determined by three parameters : (1) composition of the glass matrix, (2) solubility of the dopants in the matrix, and (3) diffusion of particles in the glass.[41] In the diffusion stage, the dopant ions diffuse from glass matrix to the position of the nucleation site, the driving force is the concentration difference between small-sized particles and large-sized ones. The size of the semiconductor gradually increases with the square root of the duration of heat-treatment. However, the time-dependency of the QDs size can be different, depending on the growth and coarsening stages.[43, 47]

If the size distribution of the QDs formed by controlled diffusion stages is broad, the coarsening process starts to occur, with large-sized particles growing at the expense of the smaller-sized particles keeping overall concentration of precipitated material constant. The size distribution can be extremely large (56% in ref. 47) if these three stages happens simultaneously, which is not desirable. Nucleation is more dominant compared to crystallization at a lower temperature and crystallization plays a vital role in high temperature region. By employing a two-step heat-treatment method, this high size dispersion can be reduced.[50]

1.3.3 Research background

QDs made of II-VI group and IV-VI group[51-53] have been extensively studied in glass matrices due to their remarkable luminescent properties in visible and near-infrared region, respectively. Most recently, these years have witnessed the bloom of the research on the halide perovskite quantum dots doped glass,[54-55] which exhibit outstanding performance with high quantum efficiency compared with II-VI and IV-VI quantum dots.

The CdS quantum dots-doped glasses were first reported in 1984 by Ekimov and Onuschchenko.[56] The microscopic CdS cyrstals were grown in the interior of a silicate glass matrix, with radius ranging from 1.4 nm to 40 nm. The size quantization of their energy spectrum have been observed. As the crystal size decreases, the shift of the absorption edge to short wavelength direction has been found. For the smallest crystals

(r = 1.4 nm), the effective increase of the bandgap reached 0.8 eV with the first absorption peak located around 375 nm.

My Ph.D study is focused on the optical properties of CdSe quantum dots-doped glass. Here, I will give some introduction to the development of II-VI quantum dots-doped glasses in four parts. The first two parts were focused on their fabrication while latter two parts on their characterization.

Firstly, growth regimes of quantum dots in glass control the average particle size and size distribution. As a result, researches in earlier stages were concentrated on the exploration of how the type of nucleation and growth mechanisms change depending on the parameters such as heat-treatment temperature and duration, composition of semiconductor and glass matrix. Secondly, the effect of glass components and semiconductor dopants on the formation of nucleation sites were investigated.

Thirdly, in later stages, the size-dependent Raman spectra were extensively studied to probe electron-phonon interaction. Most importantly, in recent ages, considerable efforts were made to enhance optical properties of quantum dots doped glasses by measuring photoluminescence spectra and quantum efficiency, which played an significant role in their practical application.

Type of nucleation mechanism

The optical properties of the quantum dots are size-tunable, thus, nucleation and growth mechanism are of significant importance to achieve size control of QDs, enabling their emission in desirable region.

Liu and Risbud developed the best heat-treatment processing temperature maps for CdS QDs doped glasses to achieve their excellent quantum confinement effect. The QDs were prepared in 56 SiO_2 - 8 B_2O_3 - 24 K_2O - 3 CaO - 9BaO (in wt. % of each oxide) glass matrix.[47] The average radius of CdSe QDs was estimated to be 2.5 nm, with a standard deviation of 1.4 nm. It was found the best heat-treatment range for QD in CdS doped glasses was between 577 ^{o}C (transition temperature for glass matrix) and 735 ^{o}C (crystallization temperature for CdS doped glasses).

Fuyu and Parker obtained CdS_xSe_{1-x} quantum dots-doped glasses using the commercial filter glasses (SiO_2 - Na_2O - ZnO - B_2O_3) as a matrix.[43] They measured the temperature dependence of the growth and coarsening process. By varying the duration (*t*) of the

heat-treatment at different temperatures, the energy of the first absorption peak was found to be proportional to 1/t in diffusion-controlled growth and $1/t^{2/3}$ in coarsening growth, consistent with the theoretical predictions. The coarsening stages occurred after initial growth. Therefore, one can precisely control the size of QDs by controlling the heat-treatment duration.

Despite the effect of heat-treatment, the type of doped semiconductors also determined their nucleation and growth mechanisms. Yükselici used commercial Schott glasses to fabricate the $Cd_{1-x}Zn_xS$ and CdS_xSe_{1-x} quantum dots doped glasses.[44] Based on the Resonant Raman spectra analysis, it was found that the growth pattern of $Cd_{1-x}Zn_xS$ QDs involved a stage of homogeneous nucleation and then a rapid transition to ripening. However, for CdS_xSe_{1-x} QDs, the heterogeneous nucleation and growth was simultaneously observed, with a gradual transition into the ripening stage.

Similar phenomena were found in CdS- and CdTe- doped borosilicate glasses.[40] According to high-resolution electron microscopy and microanalysis of the glasses. It was demonstrated that the homogenous nucleation led to single crystal CdTe QDs with a zinc-blende cubic structure while heterogeneous nucleation in CdS QDs contributed to relatively large polycrystals with wurtzite type hexagonal structure.

The above work achieved size control of QDs but failed to cover the management of size distribution, which is predominant if we want to achieve emission with narrow linewidth. Müller and Woggon[49] explored the phase formation of CdSe QDs in 20 K_2O - 20 ZnO - 5 B_2O_3 - 54 SiO_2 (in wt. % of each oxide) glasses by heating them in a microscope heating stages to the temperature of phase formation, followed by holding at this temperature to grow the microcrystals and cooling to room temperature again. At the same time, the absorption spectra were recorded, based on which the size distribution of QDs can be calculated. It was assumed that an increased CdSe content in glass, the addition of nucleation agents and the lower temperature of heat-treatment for a longer duration (for example, heated at 580 ºC for more than 100 h), contributed to a narrow size distribution (the best result was a sample with CdSe microcrystals with $R = 2.5 \pm 0.25$ nm).

Nucleation sites

Besides, there were plenty works focused on the initial stage of nucleation, especially

the nucleation sites, and the impact of dopants (such as CdO and ZnSe) or glass components (for example, Na_2O and Al_2O_3) on their formation.

Demourgues et al.[45, 57] employed X-ray absorption fine structure spectroscopy (XAFS) to investigate the local environment of Cd and Se atoms as a function of heat-treatment in CdSe quantum dots-doped borosilicate glasses. The dramatic decrease in Se-Se contacts with increase heat-treatment duration suggested that these were the nucleation sites for the CdSe QDs. Meanwhile, the Cd atoms were found to be dissolved in glass to form Cd-O contacts in as-prepared glasses. In particular, the proportion of Cd-O contacts decreased with progressive heat-treatment whilst the Cd-Se contacts increased. The same conclusion has been drawn by Lee et al. by varying the content in CdO or ZnSe in silicate glasses (65 SiO_2 - 25 Na_2O - 5BaO - 5ZnO) to probe the role of CdO and ZnSe in CdSe QD formation.[46] When CdO was added up to 3 mol% with the amount of ZnSe kept unchanged at 1 mol%, the absorption due to Se_2^- color centers decreased without any evidence of CdSe QDs formation. Importantly, the formation of CdSe QDs was observed when the ZnSe content exceeded 1.5 mol% without additional heat-treatment while the CdO content was fixed at 1 mol%. Therefore, CdO preferentially formed non-bridging oxygens, suppressing the formation of Se_2^- color centers while ZnSe promoted the formation of Se-Se links within silicate glasses network which seem to act as nucleation sites for CdSe QDs at the early stage of nucleation.

Thus, the Se_2^- color centers play an important role in the formation of CdSe QDs. Choi et al. changed the Na_2O content in silicate glasses to investigate the Se_2^- color centers formation mechanism.[58] When increasing Na_2O concentration with a fixed ZnSe content, the characteristic absorption peak at 365 nm and photoluminescence peak at 550 nm due to Se_2^- color centers were found to be reduced and finally disappeared. The presence of ZnSe disrupted the silica network to provide non-bridging Se-ions, and these additional Se-ions can bond to them to form Se-Se links. When Na_2O replaced SiO_2, Na_2O tended to break the silica network to form $\equiv$Si-O^- rather than $\equiv$Si-Se^-, resulting in the decrease of Se-Se links.

Xia et al.[48] studied the impact of Al_2O_3 on the formation of Se_2^- color centers. The absorption attributed to Se_2^- color centers increased when the amount of Al_2O_3 increased from 0 to 2 mol%. However, an opposite trend has been observed when the

concentration of Al_2O_3 further increased up to 5 mol%. The addition of Al_2O_3 contributed to an increase in glass optical basicity. The higher the optical basicity, the larger tendency to form QDs in glasses. When the amount of Al_2O_3 exceeded 3 mol%, the as-prepared glasses were partially crystallized due to the dual effect of Al_2O_3, influencing the saturation solubility of free Se^{2-}.

Raman spectra

After the extensive exploration of the nucleation and growth mechanisms in quantum dots-doped glasses, much emphasis have been put on the characterization of structure,[59-62] electron-phonon interaction,[63] photoluminescence and ultrafast charge carrier dynamics[12, 64-68] of quantum dots, promoting the mutual understanding on the luminescence mechanisms of QDs in glass matrices.

Among these characterization methods, Raman scattering is commonly used to determine the composition and size of QDs, instead of X-ray diffraction due to the amorphous nature of glass and lower concentration of QDs.

Tanaka et al.[69] reported the size- and temperature-dependency of the LO (longitudinal) -phonon peak and bandwidth of CdSe QDs in a 98 GeO_2 - 2 Na_2O (in mol%) glass matrix. The frequency of the peak shifted towards lower-frequency and the bandwidth broadened with decreasing QDs size. These dependencies can be explained by the phonon confinement model, demonstrating the origin of which from the relaxation of the q-vector selection rule.[70] Meanwhile, the temperature dependency of the Raman-scattering spectra was observed. The LO -phonon peak shifted to lower frequency and broadened as the temperature increased, reflecting the decay rate of the zone-center optical phonon and the phonon dispersion increase with the decreasing QDs size.

In contrast, Scamarcio et al.[71] found a blue shift of the phonon bands in the Raman spectra of $CdS_{1-x}Se_x$ quantum dots-doped borosilicate glasses. It demonstrated the existence of lattice contraction which overcame phonon quantum confinement in determining phonon energies. This can be explained by considering the dependence of the surface free energy of clusters on the surface-to-volume ratio, and on the thermal expansion mismatch between the QDs and the host medium to some extent.

Hwang et al.[63] noticed the different size-dependencies of the Raman spectra in different glass matrices. By comparing the phonon energies of CdSe QDs in silicate, borosilicate,

and germanate glasses (**Figure 1.8**), they were observed to be dependent on the host matrix as well as the quantum dot size. Although the size-dependency of decreasing Raman shift with decreasing quantum dot size was the same in these three hosting medium, the phonon energies were observed to be quite different. Since the quantum dots in these three kinds of glasses had the same composition, thus the observed difference was not expected to be connected with the intrinsic properties of quantum dots. In order to understand the host-material dependence, the lattice contraction effect, depended on the thermodynamic conditions decided by the interactions between quantum dots and host medium, were proposed. On the one hand, the lattice contraction contributed to the blueshift of the phonon energy. On the other hand, it also had impact on the redshift since the thermal expansion mismatch and size-dependent surface tension were inherent properties of the QDs in glass matrices.

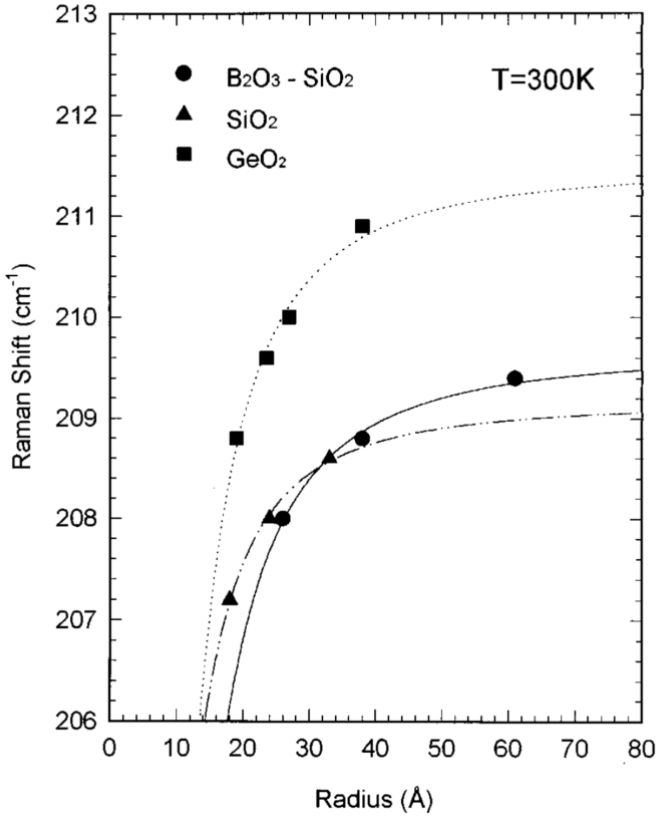

Figure 1.8 Raman frequency shifts of the quantum dots in borosilicate (circle), silicate (triangle), and germanate (square) glasses with fitting curves. Taken from ref. 63.

In all, according to investigation of Raman spectra, the size-dependency and broadening of Raman spectra were not only determined by phonon quantum confinement due to intrinsic properties of QDs , but also the interactions between QDs and glass matrix. Meanwhile, the nucleation mechanisms and formation of nucleation sites were also found to be determined by the glass matrix. These experimental findings in other researchers' work give guidance to my research that the impact of glass matrix is vital and the interaction between QDs and glass matrix should be taken into consideration.

Photoluminescence

The practical application of quantum dots lies in their photoluminescence (PL) properties. Kai Xu and Jong Heo[60] fabricated CdSe QDs doped glasses (50 SiO_2 - 35 Na_2O - 10 ZnO - 5 Al_2O_3), with photoluminescence peak changed from 540 nm to 560 nm when the heat-treatment duration ranged from 10 h to 20 h at 490 ºC. A large Stokes shift around 66 nm compared to the absorption peak was observed due to the broad size distribution (20.6%) and defects on the surface of QDs. For the same composition,[61] they also used different excitation wavelength to excite the QDs in samples of 480 ºC for 30 h. The PL spectra became broader when excited by higher energy source from 532 nm to 325 nm with the wavelength of emission peaks remained unchanged.

The PL spectra and quantum yield of CdSe quantum dots in fluorophosphate glasses with different semiconductor concentration has also been studied.[50] The composition of the glass matrices was 0.5 P_2O_5 - 0.25 Na_2O - 0.1 Ga_2O_3 - 0.05 AlF_3 - 0.05 ZnF_2 - 0.05 NaF. It was found that a low concentration of CdSe made it possible to synthesize CdSe QDs doped glasses at lower temperature and short heat-treatment duration, promoting the narrow size distribution and enhancing quantum yield. The absolute quantum yield was found to be dependent on the excitation energy. When the excitation energy changed from 4.96 eV to 3.1 eV, the quantum yield of as-prepared glasses with higher concentration decreased from 15 % to 4 %. When the glass was heat-treated at 410 ºC for 10 min, the absolute quantum yield could reach 48.6 % upon 405 nm excitation.

Karam Han, Sukeun Yoon and Woon Jing Chung synthesized the CdS and CdSe QDs doped glasses for application as an inorganic color converter for a 450-nm blue light-

emitting diode (LED).[29] However, their work demonstrated that the color tunability and conversion efficiency were still to be developed. The conversion efficiency was only 2.91%, attributed to the lack of proper passivation layers for the CdSe QDs, without which surface related traps acted as fast nonradiative recombination routes for exciton pairs. Meanwhile, the re-absorption of the radiative emission as well as Förster resonant energy transfer along the beam path can also reduce the conversion efficiency.

An enhanced color-converted photoluminescence performance was reported in their recent work by carful adjustment of the composition and heat-treatment condition.[30] The CdSe QDs were modified by forming a CdS inorganic shell via the introduction ZnS as raw materials along with ZnSe, contributing to increase the conversion efficiency to 20 %, which was a significant improvement compared with their former work.

As demonstrated in **Figure 1.9** (b), the color coordinates of the LEDs were easily controlled by adjusting the heat-treatment duration and the thickness of quantum dots doped glasses. In this study, the CdSe QDs color converter was a complete inorganic material based on stable silicate glass, no apparent degradation of the material or spectral properties was observed even after 584 days under ambient atmosphere, unlike for colloidal counterpart. Apart from this, the quantum dots doped glasses can withstand temperature up to 200 ºC (**Figure 1.9** (c)), with its emission intensity up to 65% of the initial intensity. The high color rendering index (CRI, a quantitative measure of the ability of a light source to reveal the colors of various objects faithfully in comparison with a natural light source), up to 90, along with the improved thermal quenching property suggested the practical feasibility of quantum dots doped glasses as alternative color converters for high-power white LEDs (wLED).

Similarly, Xia et al. prepared the CdSe/ $Cd_{1-x}Zn_xSe$ core/shell QDs in silicate glass by varying ZnSe/CdO ratios.[72] When ZnSe/CdO = 20, the intensity ratio between the intrinsic emission and defect emission was further enhanced with the increase in heat-treatment temperature, and pure intrinsic emission was observed in specimen heat-treated at 570 ºC for 10 h.

Although considerable work has been done in terms of improving optical properties of quantum dots doped glasses by compositional design and enhanced heat-treatment methods, the exact origin of their lower quantum efficiency was less studied from

experimental part. Therefore, it is worthy of probing these origins in order to fabricate highly luminescent glasses.

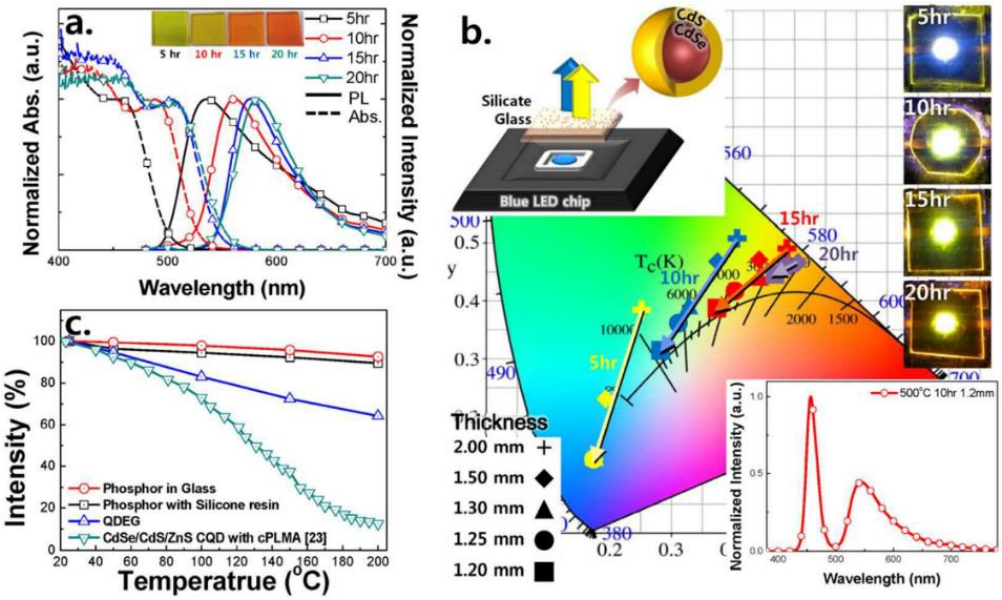

Figure 1.9 (a) Normalized absorption coefficient (dashed) and PL spectra under 455-nm excitation (solid) of modified CdSe quantum dots-doped glasses. Images of the samples are also displayed within the figure. (b) Commission international de l'eclairage (CIE) color coordinates of LEDs mounted with modified CdSe QDs doped glasses of various thickness heat-treated for 5, 10, 15, and 20 h at 500 ºC. Lines are drawn as guides for the eye. The inset presents the EL and PL spectra of wLED. Actual photos of the LEDs with CdSe QDs doped glasses of the same thickness (1.2 mm) with varying heat-treatment duration are presented at the right of the figure. (c) Thermal quenching (TQ) property of the wLED with modified CdSe QDs doped glasses compared with other wLEDs with phosphor-in-glass or phosphor with silicone resin employed, and colloidal QD with multi-shells as the color converter. Taken from ref. 30.

1.4 Computational simulation

Although quantum dots were first synthesized in glass matrices, researchers put much emphasis on the development of colloidal QDs. The surface of colloidal QDs can be

easily modified by capping ligands and the size-distribution is much narrower than quantum dots in glass matrices, typically resulting in much higher quantum efficiency of colloidal QDs. However, the colloidal QDs suffer from the agglomeration and degradation of optical properties, hindering its practical application. As an alternative, QDs doped glasses exhibited the higher chemical and thermal stability but restricted to low quantum efficiency compared to their colloidal counterparts. It has been assumed that the presence of defects at the interface between QDs and glass matrix can quench the excitonic emission and produce unfavorable defect emission.[72] Thus, the suppression of defect emission will extensively promote its practical application.

In order to eliminate the defect emission, it is important to investigate the structural origins of the defect, which is challenging experimentally due to the amorphous nature of glass matrix, instability of glass matrix under electron beam, and the low concentration of QDs in glass. Conventional characterization methods fail to describe the atomic and electronic structures of quantum dots doped glasses in detail. The development of computational approaches provide straightforward insight into these issues. Both classical molecular dynamics (MD) and *ab initio* molecular dynamics (AIMD) have been successfully applied to the modelling of glasses and QDs.

1.4.1 Computational simulation of glasses

In this section, I will briefly review the progresses researchers made in developing computational methodologies to reproduce the structural properties of glasses comparable to experimental data, and further exploring the structure-property relationships. The development of these methods were initiated from classical approaches, and I will focus on progresses in the improvement of force field to give an excellent description of glass structure with high accuracy. Then it moves to the *ab initio* method with the enhancement of computational power, which is parameter-free, not relying on the empirical potential but restricted by small system size and short time scale. Thus, a combination of classical MD and AIMD method has been developed to consider the dynamical and structural properties of glasses with high accuracy at a lower computational cost. Finally, the electronic structures of glasses obtained by these methods have been studied within the DFT framework.

My work is the first exploration of quantum dots doped glasses using computational simulations, lacking of force fields with high accuracy to describe the interactions between quantum dots and glasses matrices. Those methodologies developed by other researchers give guidance to my design of computational methods and help me to investigate their electronic structures.

Classical molecular dynamic methods

Molecular dynamic is a useful tool to deeply understand structural and transport properties of glasses,[73-87] as it provides a description of the system with a level of details hardly accessible via experiments. For example, the pioneering work to apply molecular dynamics calculations to probe the structure of a series of sodium silicate glasses, a common soda-lime glass, a sodium borosilicate glass and a sodium-potassium silicate glass, was reported by T.F. Soles[88] in 1979. The pairwise effective interatomic potential used in his work was the modified Born - Mayer - Huggin potential. The calculated radial distribution functions are consistent with experimental data based on X-ray diffraction study. It was found that the alkali and alkaline earth cations cluster around nonbridging oxygen atoms. The same MD method has been used in their another work to calculate the diffusion coefficients of sodium ions in sodium silicate glasses, showing consistency with experimental values at high temperature.[89] These results provided classical MD methods to generate glasses and proved their capability of giving a reasonable description of the structure and transport properties of glasses.

In such classical molecular dynamics calculations, the forces are obtained from an appropriate interatomic potential model. Thus, the simulated properties rely on the accuracy of the pair potential. The main direction of the computer simulation of glass was therefore focused on improving the accuracy of the pair potential.

In the framework of Born - Mayer - Huggin potential, atoms are treated as point charges, and only include repulsive and attractive terms. But it is necessary to have higher order terms in order to model correctly bonder angle distributions. For materials in which the bonding has more covalent character, reduced, partial charges may be supposed to be used. A. N. Cormack and Jincheng Du used the partial charges based on the Beest - Kramer - Santen (BKS) interactions to avoid the use of three-term in modeling the (25-

x) Na_2O -*x* CaO - 75SiO_2 glasses.[79] The interaction energy of atoms consist of a Coulomb term and a covalent (short-range) contribution, cast into the usual Buckingham form. The Coulomb forces are described by a single free parameter, the effective silicon charge. Only two short-range interactions are considered: Si-O to describe the silica bond and the O-O nonbonded interaction, which modifies the Coulomb repulsion and ensures the tetrahedral arrangement of oxygen atoms around the silicon atoms.[90]

Pedone et al.[91] developed a new empirical pairwise potential for ionic and semi-ionic oxides in order to model multicomponent glasses. A potential with 3 items has been developed in their work: (1) long-range potential, (2) short-range Morse function, and (3) repulsive contribution, which is necessary to model the interaction at high temperature and pressure. This potential has been shown to be able to reproduce structural parameters and mechanical properties of a wide range of crystal silicate glasses. However, the Si-O average distance have been found to be shorter than the experimental value because the Si-O interaction has been derived from α-quartz without non-bridging oxygen atoms. Thus, the potential model can be improved by taking into account different charges for bridging (shared by two glass former cations such as Si atoms) and nonbridging oxygens (with weak and non-directional bonds to glass modifier cations such as Na atoms), which can be determined from radial distribution functions and coordination number calculations.

The large polarizability of oxygen ions should also be taken into consideration. A. Tilocca et al.[92] developed a potential that includes polarization effects through a shell model, showing that the inclusion of polarization effects provides better performance for describing the intertetrahedral structure and the local environment surrounding modifier Na^+ and Ca^{2+} cations.

Ab initio molecular dynamic methods

However, it is hard to combine most of the effects of these complex interactions in a computationally practical force field. An alternative computational approach is the *ab initio* molecular dynamics (AIMD), which is a parameter-free approach, explicitly taking into account the electronic structure of the system. It enables the accurate modeling of many-body and polarization effects, but at the expense of much larger

computational costs compared to classical MD simulations.

X. L. Lei, Y. J, and K. Huang[93] employed AIMD methodology to simulate the ionic transport in solid - state amorphous $Na_2Si_2O_5$ in a temperature ranging from 573 K to 973 K. Their results demonstrated that AIMD was capable of reproducing the local atomic structure of sodium silicate glasses by comparing their radial distribution functions with experimental data obtained from neutron diffraction on the glasses with the same composition. Based on the analysis of mean squared displacement (MSD) of Na^+, O^{2-} and Si^{4+}, the amorphous $Na_2Si_2O_5$ glasses were found to be a fast Na^+ conductor as the MSDs of Na^+ exhibited a monotonic increase with time.

A. Tilocca and N. H. de Leeuw[94] applied Car-Parrinello molecular dynamics (CPMD) simulations to study the structure of soda-lime silicate glasses, especially focusing on the characterization of the effect of the inclusion of Na and Ca on the local environment of the modifier ions and on the electronic structure of glasses.

K. Baral, A. Li and W.-Y. Ching[95] performed the AIMD simulation within the DFT framework as implemented in the Vienna *ab initio* simulation package (VASP), to shed light on the detailed mechanism of mixed alkali effect (MAE) which was not fully resolved. A large deviation in glass properties (for example, electrical conductivities, ionic diffusion and chemical durability) as a function of composition as one alkali ion (such as Na ions) is replaced by another (such as K and Li ions) has been observed experimentally, which phenomena are defined as MAE. The structural environments and spatial distributions of alkali ions in the 10 simulated models with 20% and 30% of Li, Na, K, and equal proportions of Li - Na and Na -K are studied in detail for subtle variations among the models. The structural properties, electronic structure, mechanical properties, and optical properties have been studied, which were generally in excellent agreement with experimental characterizations, and Li -doped glasses showed more difference in the calculated mechanical and optical properties than Na and K doped glasses. Their work can exemplify that AIMD in conjunction with the rigorous quantum mechanical evaluation of the physical properties have advantages in investigating properties related to ionic motion compared with classical approaches.

A combination method of classical MD and AIMD

However, due to the high computing cost of AIMD, it was most employed to determine

structural as well as vibrational properties of glasses in small system. In order to obtain a precise knowledge of both structural and dynamical properties at short time scales, it is thus essential to develop accurate interaction potentials in classical MD with the DFT level of accuracy. Many-body effects such as the polarization of the ions should be taken into account to fit the parameters to DFT calculations as reference data. The combination of classical MD and AIMD enable a much lower computation cost while keeping a high accuracy.[96]

Y. Ishii et al.[97] applied aspherical ion model (AIM) to Na-including aluminosilicates, whose parameters were fitted on DFT data. The AIM successfully reproduced the two roles of Na^+ (network modifiers and charge compensator). Classical MD was applied to generate the structure and dynamic properties of glasses, followed by the application of AIMD to reproduce the final structure and electronic structure with high accuracy. This algorithm has been successfully employed in recent work in silicate glasses.[98]

Electronic structure calculations

Optical properties play an important role in the application of commercial glasses, and electronic structure calculation can provide an different point of view into these issues. R. A. Murray and W. Y. Ching[99] developed an orbital-charge self-consist orthogonalized linear combination of the atomic orbitals method (OLCAO) to calculate the electronic structure of the $(Na_2O)_x(SiO_2)_{1-x}$ glasses with x = 0, 0.018, 0.111. 0.222 and 0.333. Based on the analysis of the density of states (DOS) and partial density of states, the bandgap was found to decrease with increasing Na concentration. Meanwhile, the splitting of the bridging oxygen and non-bridging oxygen peaks in DOS has been observed, similar to experimental findings.

However, the main problem of these method was the systematic construction of large models while simultaneously satisfying the periodic boundary conditions. With the development of computer power, Ching et al. enlarged the modeling system around thousands of atoms in amorphous $Si_{1-x}Ge_xO_2$ glass,[100] $(Na2O)_x(SiO2)_{1-x}$ glasses,[101] and single and mixed alkali silicate glasses,[95] using the DFT framework as implemented in VASP and OLCAO. These algorithm gave excellent description of the bond angle, coordination environment, DOS, charge density, bond order and elastic properties of those systems.

1.4.2 Computational simulation of quantum dots

Even the most thorough experimental characterization is unable to probe the electronic and structural properties of quantum dots in microscopic details. Computational methods can provide interpretation of the data and extract relevant information on photoexcitation, emission, transport and decay mechanism of QDs, promoting the design of new functional materials. It has been successfully applied to the modeling of ground-states geometries,[102-107] electronic structures,[11, 108-118] spectroscopic data,[119-122] and excited-state dynamics.[105, 119, 123-131]

In this part, I will introduce researcher's work in modelling the structure of pristine CdSe quantum dots at DFT level with emphasis on structural and electronic structure reconstructions due to interactions between organic ligands and quantum dots. Their researches teach me how to build structure of pristine QD and how to choose appropriate exchange-correlation functional according to the properties I want to model.

Modelling of pristine CdSe QDs

A. Puzder et al.[118] used a plane wave implementation of DFT to probe the structure and electronic structure of Cd_nSe_n clusters (n = 6, 15, 33, and 45) in 2004. Each cluster was initially constructed on a wurtzite lattice with bulk Cd-Se bond length and relaxed to its lowest energy configuration. Significant geometrical rearrangements of QDs surface were observed with the wurtzite core was maintained. Moreover, the reconstructions contributed to the opening of an optical gap without the aid of passivated ligands, resulting in the self-healing of the surface electronic structure.

M. Yu et al.[102] also demonstrated the importance of surface atoms by performing the calculations using the local density approximation (LDA) within the DFT framework as implemented in the localized orbital SIESTA code. In the geometry optimization, surface Cd atoms were found to move inwards compared with surface Se atoms. The 3-coordinated surface atoms were more stable and resulted in higher optical gap compared with other coordination numbers. Apart from the surface reconstruction of CdSe QDs, surface vacancies were observed to provide an energetically favorable mechanism for surface passivation and stoichiometry adjustment in colloidal QDs, enhancing the quantum yield.[11]

Simulations of ligated CdSe QDs

Due to high surface-to-volume ratio, the functionalities of QDs can be modified by surface ligands, which is a hot topic of research. DFT calculations can shed light on the impact of ligands on the morphology and electronic structure of CdSe QDs.

A. Puzder et al. simulated the interaction between the organic ligands and the surface of Cd_nSe_n clusters (n = 15 and 33). [103] Oxygen atoms in the ligands were found to play a dominant role in the interaction with bonding to cadmium atoms. The binding strength of ligands to different facets was different, predicting that these binding energies control the relative growth rates of different facets, resulting in variable geometry of QDs.

S. Kilina, S. Ivanov, and S. Tretiak[132] used the generalized gradient approximation (GGA) functional within the DFT framework as implemented in VASP to probe the effect of surface ligands on $Cd_{33}Se_{33}$ QDs. Significant surface reorganization and substantial charge redistribution as well as polarization effects were observed on the surface. By comparing QDs passivated by different ligands, the hybridized states were denser at the edge of conduction band of the cluster capped by phosphine oxide than that by primary amines.

P. Yang, S. Tretiak, and S. Ivanov[111] employed the Becke, three-parameter, Lee-Yang-Parr (B3LYP) functional incorporated in Gaussian 03 package to investigate the structural mechanism of ligands binding. The relative binding strength between ligands were found to decrease in order Cd-O > Cd-N > Cd-P with average binding energy per ligand being -25 kcal/mol for OPH_2Me, -20 kcal/mol for NH_3 and -10 kcal/mol for PMe_3.

A. Houtepen et al.[109] carried out atomistic simulations at DFT level using the Perdew-Burke-Ernzerhof (PBE) exchange-correlation functional and a double-zeta basis set as implemented in the CP2K package to study the effect of L, X and Z-type ligands on the electronic structure of CdSe QDs. As **Figure 1.10** illustrated, L-type ligands are two electron donors that interact with Lewis acidic surface sites, while X-type ligands are one-electron donors to compensate the excess of metal charge on surface, and Z-type ligands are two-electron acceptors. The midgap states can be formed when chemical modification at the surface leads to the presence of di-coordinated Cd atoms. L-type and X-type ligands only slightly shift the energy level of frontier orbitals while Z-type

ligands had a profound impact on the electronic structure of colloidal QDs when displaced from the surface.

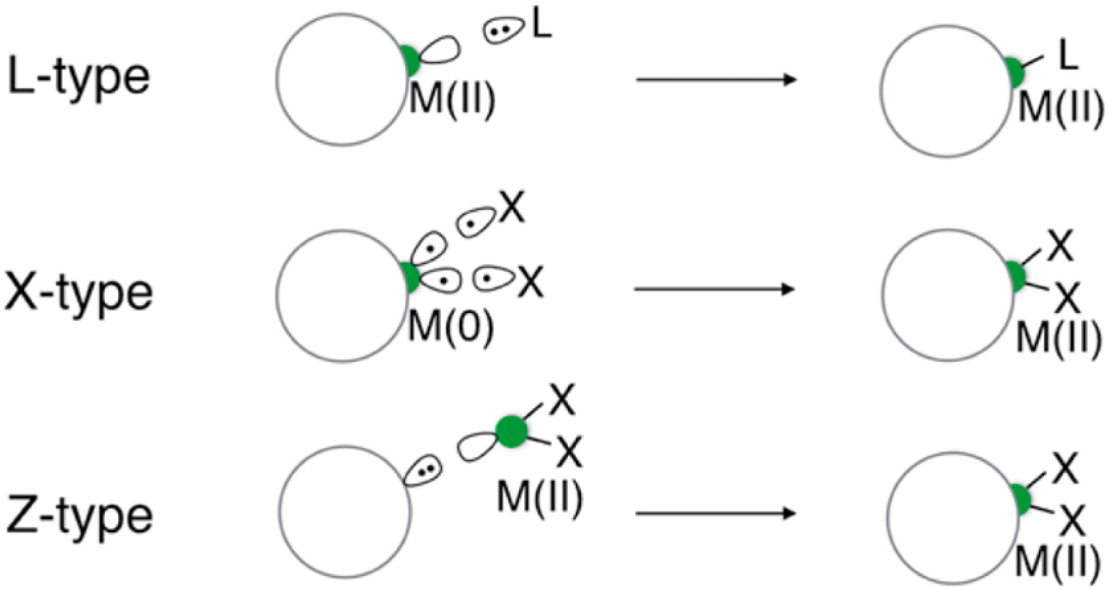

Figure 1.10 Different types of ligands capped with CdSe quantum dots. Taken from ref. 109.

Choice of exchange-correlation functional

However, it is should be noted that the accuracy of the modeling properties depend on the choice of exchange-correlation functional. Each functional has its advantages and disadvantages in terms of describing specific properties. Therefore, intent to only reproduce the experimental results of some properties (for example, geometry structure) will lead to incorrect interpretations of other properties (such as HOMO-LUMO gap). Thus, for the specific physical properties of the ligated QDs, a specific functional and basis set is supposed to be applied.

For the geometry optimization and QD-ligand binding energies computed for capped CdSe QDs strongly depended on the basis set size, which decreased with the increasing basis set size.[133] Besides, the exchange-correlation functional is important in describing appropriate atomic structure of CdSe QDs. X. W et al. found that the B3LYP strongly overestimated the interatomic distances while the PBE results complied better with the experiments.[107]

Despite the modeling of geometry structure of pristine and ligated QDs, the absorption spectra and HOMO-LUMO gap is also extensively simulated by various functionals. It was commonly acknowledged that GGA functional severely underestimated the HOMO-LUMO gap of QDs while the hybrid functional such as B3LYP and PBE0 provided satisfactory results. Especially, the PBE0 functional was found to be the best performing model both for the geometry and for the electronic structure properties.[105] Besides, the time-dependent DFT (TDDFT) gave a better description of the absorption spectra than the time-independent DFT. Although the geometry and electronic structure are dependent on the type of functional, it should be noted that the ground and excited states are well reproduced even when the electronic structure calculation comes from a functional different from the one used to optimized the QDs geometry.

1.5 Scope of this thesis

Quantum dots received enormous attention since their first fabrication in glass in 1981, due to the size-tunable bandgap and narrow emission linewidth, enabling their potential application in optoelectronic devices and bio-labelling fields. The main roadblock of the application of quantum dots-doped glasses is the broad size distribution and low quantum efficiency compared to their colloidal counterparts. Those differences naturally lead to the following question: why is the quantum efficiency in the glass matrix so low? How can this situation be improved to promote the practical application? Experimentalists found the presence of defects at the interface between QD and glass matrix can quench excitonic emission and produce the unfavorable defect emission, which is detrimental to applications. However, it is experimental challenging to probe the interfacial defects and to characterize the atomic as well as electronic structure of quantum dots doped glasses. Theoretical modelling has been applied as an alternative to shed light on these issues, providing straightforward insight into the atomic structure and electronic structure of the quantum dots-doped glasses, which is not accessible from the experimental part.

During my PhD, I conducted studies on computer simulation of CdSe quantum dots-doped glasses to investigate the interfacial atomic structure and electronic structure using classical and *ab initio* simulations. This thesis is organized as follows:

In chapter 1, I introduce the concept of quantum dots based on quantum confinement effect. The advantages and disadvantages of colloidal QDs and QDs doped glass are presented from experimental part. Then, I briefly introduce the development of computational methods in modelling glasses and quantum dots.

In chapter 2, first, I introduce the method I used in this thesis to model the quantum dots-doped glasses. The principles of classical molecular dynamics, density functional theory and *ab initio* molecular dynamics are presented. In the following part, the fabrication and characterization method of the sample I prepared to validate the theoretical results is provided.

In chapter 3, I describe the simplified model I built to probe the atomic and electronic structure of Cd_nSe_n clusters (n = 3, 10, 13, and 33) capped by Cd, Se, non-bridging oxygen, glass modifier such as Na, Ca and Zn atoms. The structural reconstruction and redistribution of HOMO and LUMO orbitals was observed when the CdSe clusters were capped by adatoms, based on the analysis of the geometry structure and density of states as well as the localization of frontier orbitals. Besides, the deep trap states formed by Na ions within the bandgap predicted the near-infrared photoluminescence of CdSe QDs doped glass. Therefore, I fabricated glasses with composition of $65SiO_2$-$35Na_2O$-1CdSe to verify the impact of Na ions on CdSe QDs. Both the TEM micrographs and Raman spectra confirmed the formation of CdSe QDs, exhibiting near-infrared emission, consistent with the theoretical simulation.

In chapter 4, I detail the work I carried out to model the sodium silicate glass matrix with the composition of Na_2O-$2SiO_2$. The model I built in chapter 3 was rather simplified, far from the realistic chemical environment of CdSe QDs in glass matrix. So CdSe quantum dot was supposed to be directly introduced into glass matrices. Therefore, at the first step, structure of glass matrix should be generated. At the initial stage, based on the analysis of radial distribution function and the formation of SiO_4 tetrahedra, I failed to reproduce the experiment data using classical MD. Thus, I probed the impact of cutoff radius, ensemble, temperature and force field on the final structure. After adjusting the force filed, I built a method to generate the glass structure with high accuracy and good quality, in excellent agreement with experiment data by analyzing radial distribution functions, formation of SiO_4 tetrahedra, and bond angle distribution. So in chapter 5, I present the work I conducted to generate the structure of CdSe

quantum dot-doped glasses by introducing the $Cd_{33}Se_{33}$ QD into the glass structure. Several algorithm was employed to generate the hybrid structure by a combination of classical molecular dynamics and *ab initio* molecular dynamics. The effect of quenching method and system size are discussed in this chapter to find an appropriate methodology to generate the structure of CdSe quantum dot-doped glasses. The interfacial structure was analyzed according to the radial distribution function, coordination numbers, and ring structures. It was found that Se-Na bonds and Cd-O bonds formed at the interface, and disrupted the Cd-Se bonds at the same time, contributing to significant structural reconstruction of CdSe QD.

In chapter 6, I analyze the atomic and electronic structure of CdSe quantum dot-doped $(Na_2O)_x(SiO_2)_{1-x}$ glasses. The sodium oxygen contents were varied in glass matrix to probe the impact of Na ions on the interfacial structure and electronic structure of CdSe QD. By comparing the density of states of pristine glass, pristine QD, hybrid glass and hybrid QD, the influence of the glass matrix on the electronic structure of QD and the effect of QD on glass was discussed. Meanwhile, a new luminescence mechanism is proposed in this chapter to give a better understanding of the photoluminescence of CdSe QDs doped glasses.

Finally, in chapter 7, I conclude the calculated results presented in this thesis and further potential calculations related to the CdSe quantum dots-doped glasses.

Chapter 2

2 Methods

2.1 Computational simulations

With the increase of computational power and the development of efficient numerical algorithms, computational simulations, also called *in silic*o experiments, act as a bridge between the real experiments and analytical theories. They interpret the macroscopic properties with the microscopic structures, investigating the system on a level of detail which is not possible or only indirectly to reach in real experiments or characterization methods. There are two common methods to conduct computational simulations of chemical systems: classical approaches and *ab initio* methods. One can choose different methods depending on the system size, time scale and desired properties to be modeled. In this chapter, I will present the methods I used during my Ph.D study. In general, I used the combination of classical molecular dynamics (MD) and *ab initio* molecular dynamics (AIMD) to study the structure and properties of sodium silicate glasses and CdSe quantum dot-doped glasses. The classical MD simulations were conducted by the DL_POLY code[134] and the AIMD runs were conducted by CP2K code.[135] The electronic structures of the quantum dot, glasses and quantum dots doped glasses were calculated at the density functional theory (DFT) level using the Dmol^3 code[136-137] (implemented in Material Studio package) and the CP2K code.

2.2 Statistical physics

Prior to discussing the details of computational algorithms, we need to briefly review some basic concepts from statistical mechanics, acting as a bridge between the atomic scale and macroscopic properties, and the central idea is the concept of thermodynamical ensemble. A thermodynamical ensemble represents all the different ways in which the positions and momenta of atoms in a system can arrange themselves. Particularly, the electronic details of the ensemble are not considered in this condition

and we focus on the movement of nucleus while electrons are localized in the atom nucleus. The nucleus are heavy enough that the behave as classical particles to a good approximation.

2.2.1 Phase space and trajectories

The phase space of a classical system can be completely described by specifying the positions and momenta of all particles. For a system of *N* particles with space being three-dimensional, each particle is associated with six coordinates, resulting in *6N* coordinates. The *6N*-dimensional space defined by these coordinates is called 'phase space' of the system. At any instant time, the system occupies one point in phase space:

$$\boldsymbol{X} = (\boldsymbol{x_1}, \boldsymbol{y_1}, \boldsymbol{z_1}, \boldsymbol{p_{x,1}}, \boldsymbol{p_{y,1}}, \boldsymbol{p_{z,1}}, \boldsymbol{x_2}, \boldsymbol{y_2}, \boldsymbol{z_2}, \boldsymbol{p_{x,2}}, \boldsymbol{p_{y,2}}, \boldsymbol{p_{z,2}}, \dots) \qquad \textbf{Eq. 2-1}$$

where the position and momentum coordinates are defined as:

$$\boldsymbol{q} = (\boldsymbol{x_1}, \boldsymbol{y_1}, \boldsymbol{z_1}, \boldsymbol{x_2}, \boldsymbol{y_2}, \boldsymbol{z_2}, \dots) \qquad \textbf{Eq. 2-2}$$

$$\boldsymbol{p} = (\boldsymbol{p_{x,1}}, \boldsymbol{p_{y,1}}, \boldsymbol{p_{z,1}}, \boldsymbol{p_{x,2}}, \boldsymbol{p_{y,2}}, \boldsymbol{p_{z,2}}, \dots) \qquad \textbf{Eq. 2-3}$$

Therefore, the phase space point can be written as:

$$\boldsymbol{X} = (\boldsymbol{q}, \boldsymbol{p}) \qquad \textbf{Eq. 2-4}$$

The dynamical system maps out a 'trajectory' over time, which is a curve formed by the phase space points the system passes through.

Accessing macroscopic quantities from microscopic ones is done by the means of statistical physics, thus, the basic idea of computer simulation is to probe the phase space in order to extract the system properties. Due to the high number of microscopic degrees of freedom of the system, it is almost impossible to directly compute its time evolution. Therefore, the statistical *ensemble* is proposed to act as a link between microstates of a system and the related macroscopic observables. The ensemble of microstates has to obey certain external constraints manifested as fixed thermodynamic variables, such as temperature, pressure, chemical potential, volume, total energy,

enthalpy, and so on. The choice of each ensemble depends on the experimental conditions that are being considered.

Molecular simulation is all about generating a physically meaningful phase space sampling, which can be achieved by two main methods: molecular dynamics (MD) and Monte-Carlo (MC) simulations. The former one samples the phase space by following the system evolution over the course of time and generates time averages, while the latter one corresponds to generating ensemble averages by statistical sampling.

2.2.2 Properties as ensemble averages

Macroscopic properties can be extracted from an ensemble by taking an ensemble average. Because phase space is composed of every possible state of a system, the average value of a property A can be obtained by taking average of the observable value over all the states in the ensemble:

$$< A > = \int A(\Omega) f(\Omega) d\Omega \qquad \textbf{Eq. 2-5}$$

where $f(\Omega)$ is the probability density of a micro-state Ω. The probability density of every ensemble is unique, i.e. $f(\Omega) = f_{ensemble}(\Omega)$. Therefore:

$$< A > = \int A(\Omega) f(\Omega) d\Omega = < A >_{ensemble} = \int A(\Omega) f_{ensemble}(\Omega) d\Omega \qquad \textbf{Eq. 2-6}$$

where $<A>_{ensemble}$ is the ensemble average taken over large number of replicas of the modelled system. In fact, during the equilibration stage of a molecular dynamics simulation, each timestep represents a member of the ensemble. According to the ergodic hypothesis, the time and ensemble averages are equivalent. Therefore，MC and MD simulation both sample the phase space in different ways but result in the same macroscopic properties. It has been only proved that the time average over the states of a single structure was equal to the ensemble average over many structures for a hard-sphere gas in 1973.[138]

2.2.3 Properties as time averages of trajectories

A way to compute a property average is to compute the value of the property periodically at time t_i and assuming:

$$< A > = \frac{1}{M}\sum_{i}^{M} A(t_i) \qquad \textbf{Eq. 2-7}$$

where M is the number of times the property is sampled. In the limit of sampling continuously and following the trajectory indefinitely, this equation becomes:

$$< A > = \lim_{t\to\infty}\frac{1}{t}\int_{t_0}^{t_0+t} A(\tau)d\tau \qquad \textbf{Eq. 2-8}$$

where t is the simulation length and t_0 is the initial step of the simulation. Therefore, a sufficient amount of the trajectory in the phase space is required and sampled over long time scale to generate enough information. In order to use the molecular dynamics correctly, the modelling system is supposed to be ergodic, corresponding to a system that evolves for an infinite time and samples the full energy landscape. Besides, it should be noted here **Eq.2-8** only applies for stationary properties at equilibrium.

2.3 Classical molecular dynamics

When a number of atoms, with a suitable composition, are cooled quickly from the molten state, a glass can be formed. In this thesis, the glass structures were produced employing the melt-quenching method conducted by molecular dynamics, to mimic the thermal process experienced during the melt-quenching method in experimental part, resulting in the amorphous state. The procedures are as follows:

STEP 1 Melt: An atomic system is heated to a high temperature to form a liquid-like state.

STEP 2 Quench: The molten system is rapidly cooled to create an amorphous system.

STEP 3 Equilibration and Data collection: The system is allowed to equilibrate and data are collected from the production stage.

The initial atomic configuration of glass was obtained by classical molecular dynamic simulations in my thesis. Therefore, I will give a brief introduction about molecular dynamics in this part.

Molecular dynamics (MD) is involved in generating a series of time-correlated points in phase space (a trajectory) by propagating a starting set of coordinates and velocities according to Newton's second equation by a series of finite timesteps. As a result, MD

is suitable for explore the influence of temperature on the time dependent properties of a system, ideal for reproducing the thermal process involved in glass formation. The application of MD can give insights into the atomic structure and composition-structure relationships of glasses. I will give some details of the simulation principles in the following sections.

2.3.1 Equation of motion

The positions and velocities of atoms in the system are determined by the Newton's second law:

$$m_i \frac{d^2 r_i}{dt^2} = F_i \qquad \textbf{Eq. 2-9}$$

where m_i, r_i, and F_i is the mass, position and force acting on this atom, respectively. The force can be linked to the gradient of the potential energy (V) and the equation of motion can be written as:

$$m_i \frac{d^2 r_i}{dt^2} = -\frac{dV(r_1, r_2, \ldots, r_N)}{dr_i} \qquad \textbf{Eq. 2-10}$$

in which $(r_1, r_2, \ldots, r_N)$ contains the coordinates of all the particles, i.e. in Cartesian coordinates, it is a vector of length $3N_{atom}$. It is difficult to solve this equation analytically, and Newton's law of motion can be numerically integrated with time being treated as a discrete quantity. The initial positions r can be determined from available crystallographic and structure data while the initial velocities can be assigned randomly to each particle subject to a thermal distribution. The relationship between instantaneous temperature and momentum is:

$$T(t) = \frac{1}{(3N-n)k_B} \sum_{i=1}^{N} \frac{|p_i(t)|^2}{m_i} \qquad \textbf{Eq. 2-11}$$

where N is the total number of atoms, n is the number of constrained degrees of freedom. Therefore, knowing the positions and momenta at initial ($t = 0$), it is possible to determine the positions and velocities at some later time Δt based on the equation of motion. Following this approach, a discrete trajectory in the phase space is generated

over consecutive time intervals Δt, i.e. timestep.

A simple numerical integration scheme is the Verlet algorithm,[139-140] considering the Taylor expansion of the position vector at time t for forward and reverse timesteps Δt:

$$r_i(t+\Delta t) = r_i(t) + \frac{dr_i(t)}{dt}\Delta t + \frac{1}{2}\frac{d^2r_i(t)}{dt^2}\Delta t^2 + \frac{1}{6}\frac{d^3r_i(t)}{dt^3}\Delta t^3 + O(\Delta t^4) \qquad \textbf{Eq. 2-12}$$

$$r_i(t-\Delta t) = r_i(t) - \frac{dr_i(t)}{dt}\Delta t + \frac{1}{2}\frac{d^2r_i(t)}{dt^2}\Delta t^2 - \frac{1}{6}\frac{d^3r_i(t)}{dt^3}\Delta t^3 + O(\Delta t^4) \qquad \textbf{Eq. 2-13}$$

The sum of the two expansions above results in the disappearance of all the odd-order derivatives:

$$r_i(t+\Delta t) = 2r_i(t) - r_i(t-\Delta t) + a_i(t)\Delta t^2 + O(\Delta t^4) \qquad \textbf{Eq. 2-14}$$

Thus, for any particle, each subsequent position is determined by the current position, the previous position, and the acceleration (determined from the force on the particle). The advantage of this scheme is that the error is of 4th order.

However, the new position is determined by the positions difference ($2r_i(t)-r_i(t-\Delta t)$), in which the velocities do not appear explicitly, which is a problem we will see, making it harder to perform at constant temperature simulations with a thermostat. Moreover, the estimation of the velocities of the particles are not a straightforward task with 2nd order error, making the calculation of velocities much less accurate than those of the positions.

The velocity Verlet integration scheme is an extension of the Verlet algorithm,[141] which improves the efficiency of the scheme by introducing the velocities directly to calculate the position:

$$\boldsymbol{r_i(t+\Delta t) = r_i(t) + u_i(t)\Delta t + \frac{1}{2}a_i(t)\Delta t^2 + O(\Delta t^4)} \qquad \textbf{Eq. 2-15}$$

$$\boldsymbol{u_i(t+\Delta t) = u_i(t) + \frac{1}{2}(a_i(t) + a_i(t+\Delta t)\Delta t + O(\Delta t^3)} \qquad \textbf{Eq. 2-16}$$

where u_i and a_i is the velocity and acceleration of atom i, respectively.

The choice of the value of timestep is of vital importance to the success of the numerical

integration scheme. Each timestep requires a computation of all of the molecular forces, which is computationally intensively. A small value of timestep allows to maintain the integration numerically stable but may fail to explore the system at sufficiently long time scale to correctly sample the space phase with low computational cost. However, a large value of timestep may fail to sample the trajectory and get a better approximation. The error increases with the increase of Δt. The largest value of Δt that can be chosen in practice is determined by the fastest process occurring in the system, Δt typically being chosen an order of magnitude smaller than the fastest process. For example, in a typical molecular system, the fastest motion is bond vibration which frequencies are in the range of 10^{11}-10^{14} s^{-1}. Therefore, Δt is supposed to be in the order of 1 fs or less to model such motions with sufficient accuracy. This means that a total simulation of 1 nanosecond requires ~ 10^6 timesteps, which is a significant computational effort. As a result, typical simulation times are in the nanosecond or picosecond range. In my thesis, the timestep was 1 fs in classical MD simulations.
In this scheme the velocities are calculated directly from the second equation. With knowledge of velocities and positions of atoms at specific time, it is possible to calculate their positions and velocities at later time. The trajectory can be calculated by repeating this procedure until the desired time is reached, with numerical accuracy. In my thesis, this scheme was employed as implemented in the DL_POLY and CP2K codes.

2.3.2 Thermostat

In this thesis, the canonical ensemble (*NVT*), where the number of the atoms (*N*), the volume of the simulation cell (*V*) and the temperature (*T*) is constant, was used in MD simulation for equilibration runs during the melting and quenching procedure, until an average temperature of the system is reached. For production runs to collect part of the trajectory in order to calculate the desired properties, the microcanonical ensemble was used with number of the atoms (*N*), the volume of the simulation cell (*V*) and the total energy (*E*) kept constant in each MD simulation at 300K.
There are several existing methods to perform MD simulation with the NVT ensemble. One common approach is the scaling of velocities to achieve the desired temperature.

As we know, the temperature of the system is given by the average of the kinetic energy:

$$< E_{kin} > = \frac{1}{2}(3N - n)kT \qquad \textbf{Eq. 2-17}$$

where N is the number of atoms and n is the number of constraints. By scaling the velocity at each time step with a factor of $(T_{desired}/T_{actual})^{1/2}$, we can obtain the desired temperature. However, such an "instant" correction procedure changes the real dynamics and introduces some undesired periodicity into the simulation, making the fluctuations unphysically small.

Alternatively, a thermostat is introduced by gradually adding or removing energy to/from the system with a suitable time constant. It introduces a "soft" coupling between system and thermostat. The kinetic energy of the system is still modified by scaling of velocities but the rate of heat transfer is controlled by a coupling parameter τ:

$$\frac{dT}{dt} = \frac{1}{\tau}(T_{desired} - T_{actual}) \qquad \textbf{Eq. 2-18}$$

$$velocity\ scale\ factor = \sqrt{1 + \frac{\Delta t}{\tau}\left(\frac{T_{desired}}{T_{actual}} - 1\right)} \qquad \textbf{Eq. 2-19}$$

Although this method, called the Berendsen thermostat is widely used, it produces correct temperature averages but incorrect fluctuations of properties.

The Nosé-Hoover thermostat[142] uses the friction coefficient ξ to describe the modified equation of motion and control the fluctuation of temperature. Then, the time evolution of the positions and the velocities are determined as follows:

$$\frac{dp_i}{dt} = F_i - \xi p_i \qquad \textbf{Eq. 2-20}$$

$$\frac{d\xi(t)}{dt} = \left(\sum_{i=1}^{N} \frac{{p_i}^2}{2m_i} - \frac{3}{2}Nk_BT\right) \cdot \frac{2}{Q} \qquad \textbf{Eq. 2-21}$$

where Q is the effective "mass" of the thermostat associated with the additional variable which is introduced to the modelled system. This parameter is important for regulating

the rate of exchange of the system energy with the fictitious heat bath, having an impact on the relaxation time of the thermostat. When the kinetic energy of the system is higher than $3/2Nk_BT$, the friction coefficient ξ increases, contributing to the decrease of velocities. On the contrary, the friction coefficient ξ decreases when the kinetic energy of the system is less than $3/2Nk_BT$, resulting in the increase of velocities. This method can accurately approximate the canonical ensemble and it is applied to all the classical MD simulations in this thesis.

2.3.3 Force field

As I mentioned above, the molecular dynamics allows the time evolution of atom positions by giving a set of atoms and a description of the forces acting between them. Therefore, the accuracy and the quality of the results are heavily dependent on the accurate description of the interatomic forces, and thus rely on the accuracy of the representation of the potential energy. This is calculated in practice from an interatomic potential energy function that is described by parameters, from what is called the force field. It is a mathematical expression describing the dependence of the energy of a system on the coordinates of its particles, consisting of an analytical form of the interatomic potential energy. These parameters are typically obtained either from *ab initio* or semi-empirical quantum mechanical calculations, or by fitting to experimental data such as neutron, X-ray and electron diffraction, etc.
The force field may have a wide variety of analytical forms and in DL_POLY code, the total configuration energy of a molecular system maybe written as:

$$\boldsymbol{V(r_1, r_2, \dots, r_N) = V_{bond} + V_{angle} + V_{dihed} + V_{inv}}$$

$$\boldsymbol{+V_{pair} + V_{3-body} + V_{Tersoff} + V_{4-\mathrm{body}}}$$

$$\boldsymbol{+V_{metal} + V_{extn}} \qquad \textbf{Eq. 2-22}$$

where V_{bond}, V_{angle}, V_{dihed}, V_{inv}, V_{pair}, $V_{3\text{-}body}$, $V_{Tersoff}$ and $V_{4\text{-}body}$ are empirical interaction functions representing chemical bonds, valence angles, dihedral angles, inversion angels, pair-body, three-body, Tersoff (many-body covalent) and four-body forces

respectively. The first four terms are regarded by DL_POLY as intra-molecular interactions and the next four as inter-molecular interactions. The terms V_{metal} is a density dependent (and therefore many-body) metal potential and the V_{extn} represents an external field potential.

Usually for the modelling of oxide glasses, only the two-body interactions are considered and higher order terms are neglected. Furthermore, as all ionic species considered here are atomic (points in space), there are no intramolecular terms. Thus, in this thesis, the pair-body terms (V_{pair}) arise from the sum of van der Waals (short-ranged) and electrostatic (long-ranged) interactions:

$$\boldsymbol{V(r_1, r_2, \dots, r_N) = V_{short} + V_{long}} \qquad \textbf{Eq. 2-23}$$

Van der Waals interactions between two neutral atoms originate from the balance between repulsive and attractive forces. The former one is due to the overlap of the electron clouds of both atoms while the interactions between induced dipoles result in an attractive component. In DL_POLY code, many short ranged pair forces are available such as 12-6 potential, Buckingham potential, Born-Huggins-Meyer potential, Morse potential and so on. Depending on the desired properties and the availability of the parameters for the modelled system, one can choose different pair potentials.

2.3.4 Pairwise potential in this thesis

As I mentioned in chapter 1 (1.4.1), researchers have worked for decades to improve the accuracy of pairwise potential to give a better description of the structure and properties of glasses. Pedone et al.[91] developed a force field with high accuracy in handling the partial covalence of the silicate glasses, received considerable success in many previous modelling studies of silicate glasses of various molar composition. Thus, for the interaction of Na-O, Si-O and O-O pairs, I used this potential, including a repulsive term apart from the non-bonded energies. The full expression for the potential as follows:

$$\boldsymbol{U_{ij} = \frac{z_i z_j e^2}{4\pi\varepsilon_0 r_{ij}} + D_{ij}\left[\left\{1 - \exp\left[-a_{ij}(r_{ij} - r_0)\right]\right\}^2 - 1\right] + \frac{C_{ij}}{r_{ij}^{12}}} \qquad \textbf{Eq. 2-24}$$

The first term is the long-range Coulombic potential, where z_i and z_j are the charges of the atomic species i and j respectively, ε_0 is the vacuum permittivity, and r_{ij} is the interatomic distance between two atoms . The second term is a Morse potential for short range interactions with input parameters D_{ij}, a_{ij}, and r_0. C_{ij} is the parameter for repulsion term. Besides, this model is based on a rigid ionic model with partial charges to handle the partial covalency of silicate systems.

It should be noted here that a partial charge is created due to the asymmetric distribution of electrons in chemical bonds, which is a non-integer charge. These are "effective charges" and they must be treated as parameters in the potential model, and together with the short-range terms they form an "effective potential". So the charge on oxygen atoms has been fixed at $q_0 = -1.2e$. The partial charges on the cations are related to the value of oxygen charge for self-consistency of the force field. Thus, the silicon atom has a charge of $2q_0$ and the sodium ions of $0.5q_0$. The potential parameters are in **Table 2.1**:

Table 2.1 Potential parameters describing interactions in glass matrices.

	D_{ij} (eV)	a_{ij} (Å^{-2})	r_0 (Å)	C_{ij} (eV Å^{12})
$Na^{0.6}$-$O^{-1.2}$	0.023363	1.763867	3.006315	5.0
$Si^{2.4}$-$O^{-1.2}$	0.340554	2.006700	2.100000	1.0
$O^{-1.2}$- $O^{-1.2}$	0.042395	1.379316	3.618701	22.0

For Cd-Se pairs, there were few choices available in the scientific literatures and I only found the 12-6 potential to represent interactions in CdSe composites.[143-144] The full expression is as follows:

$$U_{ij} = \frac{z_i z_j e^2}{4\pi\varepsilon_0 r_{ij}} + [\frac{A}{r_{ij}^{12}} + \frac{B}{r_{ij}^{6}}] \qquad \text{Eq. 2-25}$$

A and B are the input parameters for the 12-6 potential, which can be found in **Table 2.2**. It is possible to define a set of parameters for each different pair of atoms, but for convenience most force fields give individual atomic parameters, together with some rules to combine them. Moreover, as far as I am concerned, it is hard to find a system simultaneously contain Cd, Se, O, Si, and Na atoms. Therefore, the combination rule

is applied to describe the interactions between glass matrices and CdSe quantum dot (Cd-O, Se-Si, and Se-Na pairs), where $A = (A_1A_2)^{1/2}$ and $B = (B_1B_2)^{1/2}$.

Table 2.2 Parameters for the short-range potential in Eq.2-25, representing interactions within CdSe QD and interactions between CdSe QD and glass matrices.

Atom	A (eV Å^{12})	B (eV Å^{6})
$Na^{0.6}$	9735.806	103.097
$Si^{2.4}$	368.510	0.000
$O^{-1.2}$	42895.736	29.351
$Cd^{2.4}$	21.0245	0.348926
$Se^{-1.2}$	2761307.14	119.0878

2.3.5 Periodic boundary conditions

In macroscopic systems, only a small percentage of the atoms are surface atoms while things are quite different for the small number of atoms constituting a MD simulation box. In simulations, due to high surface-to-volume ratio, the surface effect is enormous and would affect the properties of the modelled system, resulting in the inaccurate description of bulk properties. Therefore, periodic boundary conditions (PBC) are introduced to avoid the contribution of surface effect and to overcome the obstacle of system size, which is considerably small compared with the real system.

A simulation cell is built, where a sample of the macroscopic system with specific geometry is placed in a finite box. It is supposed to have the same symmetry, size, and total number of atoms as decided by the molar composition and density of the target system. The PBC is achieved by surrounding the primary simulation cell by images of itself in three dimensions, as illustrated in **Figure 2.1**. Atoms moved in the primary cell are also moved in the image cells. An atom leaves the central simulation cell at one side, and it re-enters the cell through the opposite side with the same velocity.

Therefore, the walls and surface atoms disappear with the introduction of PBC, making a bridge between the very small simulation cell and macroscopic systems. A cubic simulation box with periodic boundary conditions, which cell size was calculated from the bulk glass density, was built in all the classical MD and AIMD simulations in my

thesis.

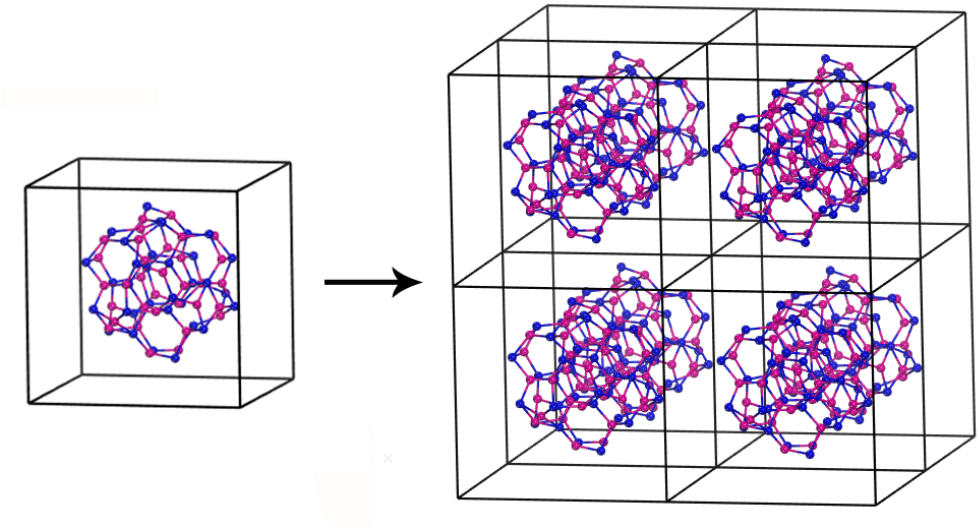

Figure 2.1 Illustration of the use of periodic boundary conditions 8 (2x2x2) unit cells are presented while only 1 is really considered in the simulation. Cd, magenta, Se, blue.

The introduction of PBC influences the short-range and long-range interactions between atoms in the modelled system. For short-range interactions, it is calculated by assuming the potential energy between them is determined by its interaction with the nearest atoms or nearest periodic images of its neighbors.

The time needed to calculate the forces will scale as N^2, and the interatomic potential will decay to a negligible value for distances much smaller than half of the lattice size if the system size is large enough. Therefore, there is no need to compute all the forces. So a cutoff distance is employed to truncate the potential, meaning the interaction only happens when the distance is smaller than the cutoff, which should be smaller than the half of simulation box. Meanwhile, it is supposed to be large enough so that the potential can be safely neglected beyond cutoff radius. In all classical MD run, the cutoff radius for short-range interaction was set at 7.6 Å in my thesis.

It must also be noted here that this truncation should be applied only to short-ranged interactions. Long-range forces (typically electrostatic interactions) should not be truncated because they do not decay with distance rapidly enough. There are several methods to solve this problem, and the Ewald sum method[145] was employed in my thesis.

2.4 Quantum Mechanics

The mathematical form for the dynamical equation is determined by the velocity and mass of particles. The classic mechanics apply for heavy and slow-moving particles while light particles such as electrons display both wave and particle characteristics, which must be described by quantum mechanics. A major difference between classical mechanics and quantum mechanics is that the former one is deterministic while the latter one is probabilistic. Quantum mechanics only allow the calculation of the probability of a particle being at a certain place at a certain time. The probability function is given as a square of the wavefunction:

$$\boldsymbol{P(r,t) = |\Psi(r,t)|^2} \qquad \textbf{Eq. 2-26}$$

The wavefunction can be obtained by solving either the Schrödinger equation for non-relativistic systems or Dirac equation for relativistic systems depending on the velocity of the particles. For the movement of electrons, which is the major focus of my research, is determined by the Schrödinger equation because I do not study heavy elements (5f electrons).

2.4.1 Schrödinger equation

The time-dependent Schrödinger equation can be written as follows:

$$\boldsymbol{H\Psi(r,t) = i\hbar \frac{\partial \Psi(r,t)}{\partial t}} \qquad \textbf{Eq. 2-27}$$

where H is the Hamiltonian operator, which is given as a sum of kinetic and potential energy operators:

$$\boldsymbol{H(r,t) = T(r) + V(r,t)} \qquad \textbf{Eq. 2-28}$$

In the absence of an external, time-dependent field acting on the system, for a bound system, the potential energy operator is time-independent, thus the Hamiltonian operator becomes time-independent and yields the total energy when acting on the wavefunction. The energy (E) is a constant, independent on time but dependent on

space variables:

$$\boldsymbol{H(r,t) = H(r) = T(r) + V(r)} \qquad \textbf{Eq. 2-29}$$

$$\boldsymbol{H(r)\Psi(r,t) = E(r)\Psi(r,t)} \qquad \textbf{Eq. 2-30}$$

This equation shows that the time and space variables of the wavefunction can be separated:

$$\boldsymbol{\Psi(r,t) = \Psi(r)e^{-iEt}} \qquad \textbf{Eq. 2-31}$$

For a time-independent part of the wavefunction, this equation can be written as the time-independent Schrödinger equation:

$$\boldsymbol{H(r)\Psi(r) = E(r)\Psi(r)} \qquad \textbf{Eq. 2-32}$$

2.4.2 Born-Oppenheimer approximations

In order to solve the time-independent Schrödinger equation for polyelectronic systems, several approximations are made. As we know, electrons are very light particles compared with the nuclei, and this large mass difference contributes to a huge difference in velocities. Therefore, it can be assumed that the nuclei are clamped at fixed positions while electrons are moving in the field of fixed nuclei. Hence, the kinetic energy of the nuclei is zero and the potential energy is merely a constant. Under the Born-Oppenheimer approximations, the motion of nuclei and electrons can be separated and the total wavefunction of the system can be written as:

$$\boldsymbol{\Psi_{tot}(R,r) = \Psi_e(r,R)\Psi_N(R)} \qquad \textbf{Eq. 2-33}$$

where r and R is the coordinates of electrons and nuclei respectively.
The Hamiltonian operator can be written as follows:

$$\boldsymbol{H = H_e + T_N} \qquad \textbf{Eq. 2-34}$$

where H_e and T_N is the Hamiltonian operator for electrons and the kinetic energy of

nuclei respectively, and the **Eq.2-32** can be written as:

$$(\boldsymbol{H_e} + \boldsymbol{T_N})\boldsymbol{\Psi_e}(\boldsymbol{r},\boldsymbol{R})\boldsymbol{\Psi_N}(\boldsymbol{R}) = \boldsymbol{E_{tot}}\boldsymbol{\Psi_e}(\boldsymbol{r},\boldsymbol{R})\boldsymbol{\Psi_N}(\boldsymbol{R}) \qquad \textbf{Eq. 2-35}$$

among which the full expression of H_e is:

$$\boldsymbol{H_e}(\boldsymbol{r},\boldsymbol{R}) = \boldsymbol{T_e}(\boldsymbol{r}) + \boldsymbol{V_{e-e}}(\boldsymbol{r}) + \boldsymbol{V_{e-N}}(\boldsymbol{r},\boldsymbol{R}) + \boldsymbol{V_{N-N}}(\boldsymbol{R}) \qquad \textbf{Eq. 2-36}$$

$$\boldsymbol{H_e}(\boldsymbol{r},\boldsymbol{R})\boldsymbol{\Psi_e}(\boldsymbol{r},\boldsymbol{R}) = \boldsymbol{E_e}(\boldsymbol{R})\,\boldsymbol{\Psi_e}(\boldsymbol{r},\boldsymbol{R}) \qquad \textbf{Eq. 2-37}$$

where **Eq. 2-37** is the Schrödinger equation for electrons and E_e is the energy of the electrons. Use the orthonormality of the $\Psi_e(r,R)$ by multiplying from the left by a specific electronic function $\Psi_e^*(r, R)$ and integrate over the electron coordinates, then the **Eq. 2-35** can be written as:

$$\int \boldsymbol{\Psi_e^*}(\boldsymbol{H_e} + \boldsymbol{T_N})\,\boldsymbol{\Psi_e}(\boldsymbol{r},\boldsymbol{R})\boldsymbol{\Psi_N}(\boldsymbol{R})\boldsymbol{dr} = \int \boldsymbol{\Psi_e^*}\ \boldsymbol{E_{tot}}\boldsymbol{\Psi_e}(\boldsymbol{r},\boldsymbol{R})\boldsymbol{\Psi_N}(\boldsymbol{R})\boldsymbol{dr} \qquad \textbf{Eq. 2-38}$$

Considering the E_{tot} is constant and $\Psi_N(R)$ is independent on the coordinates of electrons, by inserting **Eq. 2-37** into **Eq. 2-38**, and the Hamiltonian operator is an Hermitian operator, thus $< \Psi_e^* \mid H\Psi_{tot}> = <\Psi_e^* H \mid \Psi_{tot}>$, the following equation can be obtained:

$$\int \boldsymbol{\Psi_e^*}\boldsymbol{\Psi_e}(\boldsymbol{r},\boldsymbol{R})\boldsymbol{dr}(\boldsymbol{E_e}(\boldsymbol{R}) + \boldsymbol{T_N})\,\boldsymbol{\Psi_N}(\boldsymbol{R}) = \int \boldsymbol{\Psi_e^*}\,\boldsymbol{\Psi_e}(\boldsymbol{r},\boldsymbol{R})\boldsymbol{dr}\boldsymbol{E_{tot}}\boldsymbol{\Psi_N}(\boldsymbol{R}) \qquad \textbf{Eq. 2-39}$$

Thus, the Schrödinger equation of the nuclei can be obtained:

$$(\boldsymbol{E_e}(\boldsymbol{R}) + \boldsymbol{T_N})\boldsymbol{\Psi_N}(\boldsymbol{R}) = \boldsymbol{E_{tot}}\boldsymbol{\Psi_N}(\boldsymbol{R}) \qquad \textbf{Eq. 2-40}$$

Therefore, in Born-Oppenheimer picture, the nuclei move on a potential energy surface (PES) which is a solution to the electronic Schrödinger equation. Solving **Eq. 2-40** for the nuclei wavefunction leads to the energy levels for molecular vibrations and rotations, which in turn are the fundamentals for many forms of spectroscopy, such as infrared spectra, Raman and so on. It can be solved numerically in nuclear quantum simulations.

2.4.3 Density functional theory

To solve the electronic Schrödinger equation, many approaches have been employed such as the Hatree-Fock self - consistent field method, post-Hatree Fock methods, quantum Monte-Carlo methods, and the density functional theory (DFT). In my work, I used DFT approach which I will describe here. The wavefunction approach for an *N* electrons system contains *4N* variables, three spatial and one spin coordinates. Therefore, the complexity of a wavefunction increases exponentially. The obvious advantage of DFT is that it depends on the electron density, which is the square of wavefunction (**Eq. 2-26**), integrated on *N-1* electron coordinates, and each spin density is only decided by three spatial coordinates, independent of the number of electrons.
In the following part, I will present two main ways in which we have used DFT: it can be used for "static" calculations where only the energy is calculated for a given configuration of the nuclei. The other one is *ab initio* molecular dynamics where the forces and velocities are computed from the electron density to propagate the equations of motion.

2.4.4 Hohenberg-Kohn theorems

The DFT methods rely on two Hohenberg-Kohn theorems[146] to decrease the dimensionality of the problem. In the language of DFT, electrons interact with one another and with an external potential, which is the attraction of the nuclei in a molecule. As the total integration of the density gives the number of electrons in the system, so all that remains to define the Hamiltonian operator is the determination of the external potential (i.e., the charges and positions of the nuclei). Therefore, the first theorem is an existence theorem, which demonstrates that there is a unique electron density that is linked unambiguously to the external potential. The second theorem states that the ground-state electron density minimizes the overall energy functional and subsequently is the solution of the electronic Schrödinger equation. This, in turn, implies that the ground state density can be determined by variational methods.

2.4.5 The Kohn-sham scheme

The discussion above emphasized that the density uniquely determines the Hamiltonian, which determines the wavefunction. However, it is still challenging to solve the Schrödinger equation, which difficulty derives from the electron-electron interaction term. In a key breakthrough, Kohn and Sham developed a scheme which considerably simplified the problem by assuming the electron density of a fictitious system of N non-interacting electrons is the same as the interacting, real system, which can be described by a Slater determinant of $N\{\Phi_i(r_i)\}$ single-particle orbitals. These fictitious non-interacting electrons move in local effective potential, which is different from that of the real system. Thus, the wavefunction of the system under Hatree-Fock approximation can be written as:

$$\boldsymbol{\Psi_e(r) = \Phi(r_1)\Phi_2(r_2) \ldots \Phi_i(r_i) \ldots \Phi_N(r_N)} \qquad \textbf{Eq. 2-41}$$

Hence, the energy of the system is the sum of one-electron energy (E_i):

$$\boldsymbol{E(r) = \sum_{i=1}^{N} E_i} \qquad \textbf{Eq. 2-42}$$

In Kohn-Sham approach,[147] the electron density can be constructed from wavefunction of N single-electron:

$$\boldsymbol{\rho[r] = \sum_{i=1}^{N} |\Phi_i(r)|^2} \qquad \textbf{Eq. 2-43}$$

Therefore the kinetic energy is:

$$\boldsymbol{T[\rho] = \sum_{i=1}^{N} \int dr \Phi_i^*(r) \left(-\frac{1}{2}\nabla^2\right) \Phi_i(r)} \qquad \textbf{Eq. 2-44}$$

According to **Eq. 2-36**, for a single-electron system, the full expression of Koh-Sham equation is:

$$\boldsymbol{\left\{-\frac{1}{2}\nabla^2 + V_{KS}[\rho(r)]\right\} \Phi_i(r) = E_i \Phi_i(r)} \qquad \textbf{Eq. 2-45}$$

among which:

$$\boldsymbol{V_{KS}[\rho(r)] = V_{e-N}(r) + V_{e-e}[\rho(r)] + V_{xc}[\rho(r)]}$$

$$= \boldsymbol{V_{e-N}(r)} + \int \boldsymbol{dr'} \frac{\boldsymbol{\rho(r')}}{\boldsymbol{|r-r'|}} + \frac{\boldsymbol{\delta E_{xc}[\rho(r)]}}{\boldsymbol{\delta\rho[r]}} \qquad \textbf{Eq. 2-46}$$

where V_{KS} is the effective Kohn-Sham potential, which includes the potential between the nuclei and electron, the repulsion between electron and the total electron density and the exchange-correlation potential, respectively.

As we can see from **Eq. 2-46**, the V_{e-e} potential includes a self-interaction contribution as the electron described by the Kohn-Sham equation also contribute to the electron density. Therefore, to solve this equation, the definition of V_{KS} requires the electron density ($\rho(r)$), which is determined by the single-electron wavefunction $(\Phi_i(r_i))$, which in turn requires the solution of the Kohn-Shame equation. As a result, an iterative approach is employed to solve the problem. This scheme is illustrated in **Figure 2.2**.

The starting point is a generated guess of the initial electron density which is inserted into the V_{KS} in order to solve the Kohn-Sham equation and obtain a single-electron KS orbital. Then the new electron density is calculated from the orbitals. By comparing the difference between this density and the density from previous step with a predetermined cut off, one can determine whether the KS equation is converged and the ground state density is obtained. Otherwise, the updated density needs to be inserted back to the V_{KS} and the single-particle orbitals recalculated.

The accuracy of the computational simulation depends on the approximation of exchange-correlation functional. One can choose appropriate functional concerning the properties they want to model.

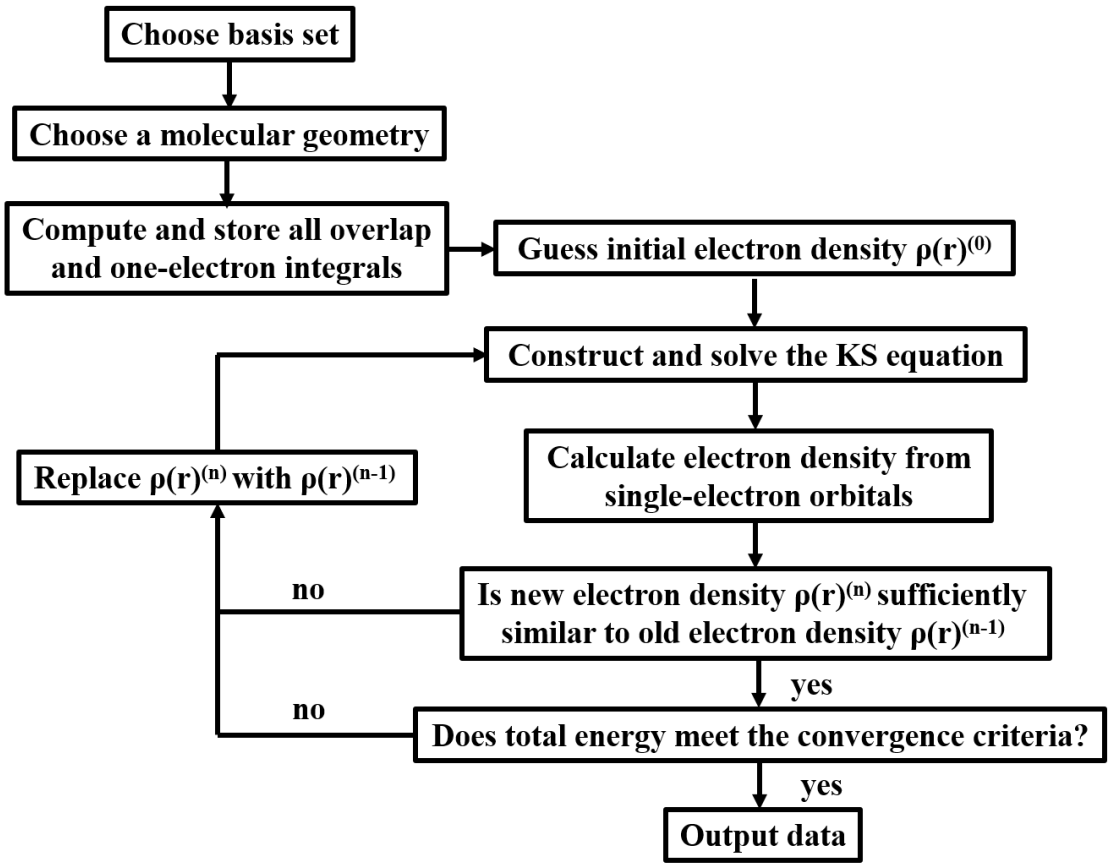

Figure 2.2 Flow chart of the Kohn-Sham self-consistent field method

In my thesis, both the geometry optimization and electronic structures calculation are conducted at DFT level. In chapter 3, due to the small system size and the excellent performance of B3LYP functional, both the geometry optimization and electronic structures calculation was conducted using B3LYP functional as exchange-correlation functionals. However, in chapter 4, 5, and 6, the system size is enormously increased and the hybrid functional is not suitable for the generation of the geometry structure in terms of computational cost, thus, the GGA functional was applied in AIMD run. But GGA functional has a well-known problem in describing the electronic structures, so the PBE0 hybrid functional was employed to do the electronic structures calculation in chapter 4 and 6.

2.4.6 Ab initio molecular dynamics

The classical molecular dynamics methods have enjoyed tremendous success in the

treatment of glasses systems as I mentioned in chapter 1, however, there are a number of serious limitations. Firstly, charges appear as static parameters in the force field, so electronic polarization effects are not included. Although several attempts to rectify this problems have been made by allowing the charges and/or induced dipoles to fluctuate in response to a changing environment, those polarized classical models lacks transferability and generality. Secondly, force fields generally assume a pre-specified connectivity between the atoms, therefore, suffering from an inability to describe chemical bond breaking and forming events. It can solved by using techniques such as the empirical valence bond method, but such methods are also not fully transferable. Furthermore, once a specific system is understood after elaborate development of satisfactory potentials, changing a single species provokes typically enormous efforts to parameterize the new potentials needed.[148-150]

Due to the limitations of force field based approaches, the so-called *ab initio* molecular dynamics (or first-principles MD) was developed to address these problems. It differs from classical MD in two ways. For one thing, AIMD is based on the quantum Schrödinger equation for the electronic degree of freedom while its counterparts relies on Newton's equation. For another thing, classical MD relies on semiempirical effective potentials which approximate quantum effects while AIMD is based on the real physical potential. The basic idea of the AIMD method is to compute the forces acting on the nuclei from electronic structure calculations that are performed "on-the-fly" as the molecular dynamics trajectory is generated. There are several types of AIMD, the Ehrenfest dynamics, the Car-Parinello dynamics (CPMD), and the Born-Oppenheimer dynamics (BOMD). During my Ph.D study, I used the CP2K code to conduct AIMD simulations. In CP2K, AIMD comes in two distinct flavors, second-generation CPMD and BOMD.[151] Here, I will give a brief introduction to BOMD, which was employed in my thesis.

Within the Born-Oppenheimer approximation, the nuclei are considered classical particles whose potential is determined by the Ehrenfest theorem. It states that the potential is equal to the average, in the quantum sense, of the electronic Hamiltonian with respect to the electronic wavefunction. In the BOMD approach, it is further assumed that the electronic wavefunction is in its ground states. Under the holonomic orthonormality constraint ($<\Psi_i(r) \ / \ \Psi_j(r)> \ = \ \delta_{ij}$), the Schrödinger equation must be

solved while enforcing a Lagrange multiplier, leading to the following Lagrangian, which is defined as the difference between the kinetic and the potential energy:

$$\boldsymbol{L_{BO} = \frac{1}{2}\sum_I M_I \dot{R}_I^2 - < \Psi_0 \mid H_e \mid \Psi_0 > + \sum_{i,j} \Lambda_{ij}(< \Psi_i \mid \Psi_j > - \delta_{ij})} \qquad \textbf{Eq. 2-47}$$

The first term of the Lagrangian is the kinetic energy of the nuclei, the second term corresponds to the nuclear potential as obtained from the Ehrenfes theorem, and the last term represents a Lagrange function which ensures that the orbitals remain orthonormal all the time, where Λ is a Hermitian Lagrangian multiplier matrix since the electrons obey the Pauli Exclusion Principle (two electrons cannot be in the same quantum state). One can obtain the associated equation of motion by solving the corresponding Euler-Lagrange equations:

$$\boldsymbol{\frac{d}{dt}\frac{\partial L}{\partial \dot{R}_I} = \frac{\partial L}{\partial R_I}} \qquad \textbf{Eq. 2-48}$$

$$\boldsymbol{\frac{d}{dt}\frac{\partial L}{\partial <\dot{\Psi}_i|} = \frac{\partial L}{\partial <\Psi_i}} \qquad \textbf{Eq. 2-49}$$

For the nuclear equations of motion:

$$\boldsymbol{M_I \ddot{R}_I = -\nabla_I min < \Psi_0 \mid H_e \mid \Psi_0 >} \qquad \textbf{Eq. 2-50}$$

For the electronic equations of motion:

$$\boldsymbol{H_e \Psi_i(r) = \sum_j \Lambda_{ij} \Psi_i(r)} \qquad \textbf{Eq. 2-51}$$

Thus, according to **Eq. 2-50**, $<\Psi_0 \ / \ H_e \ / \ \Psi_0>$ correspond to the Kohn-Sham total energy in **Eq. 2-45** and can be calculated from the single-particle orbitals, It should be noted that this energy changes as the results of motions of the ions, therefore, in the BOMD approach, the self-consistent one-particle Kohn-Sham equations are calculated and solved at each timestep. Thus, the drawback of this approach is that the electronic structure needs to be solved at each timestep, making the BOMD simulation computationally expensive. The classical MD can be applied to systems consisting of 10^4-10^6 atoms with timescales on the order of tens of nanoseconds. However, the

BOMD approach can be employed in systems composed of just a few hundreds of atoms and access timescales on the order of tens of picoseconds. For example, for simulations in the NVT ensemble of systems with composition of $39Na_2O$-$78SiO_2$-33CdSe (417 atoms in total), it costs 48 hours using 384 cores on high performance computing systems for 20 ps simulations.

The definition of force field in AIMD is a parameter-free simulation compared with the classical MD especially considering the fact that there is little availability of pairwise potential in describing my research items (containing Cd, Se, O, Si, and Na elements). AIMD exhibits excellent performance on describing the atomic structure of the system but smaller system size and shorter timescale compared with the classical MD. Therefore, in this thesis, classical MD was employed to explore the size effect of the modelled system and generated initial configurations for the AIMD run. The AIMD calculation was applied to obtain the atomic structure with high accuracy and then used to conduct the electronic structure calculations.

2.5 Modelling properties

By analyzing the trajectories of the production run in MD, the radial distribution function (RDF), the coordination environment, and the ring structure was calculated by using the R.I.N.G.S. code.[152] These results played an predominant role in determining the interfacial bond formation between the QD and glass matrix. Meanwhile, it is also useful for probing the impact of the glass matrix on the QD structure, giving a straightforward description of the local atomic structure of the CdSe quantum-dot doped glasses, which is not possible experimentally.

The optical properties are closely related to the energy diagram of the CdSe quantum dot-doped glasses. Thus, the density of states and the HOMO-LUMO gap were calculated. By comparing the density of states and HOMO-LUMO gap of the pristine QD, pristine glass, and CdSe quantum dot-doped glasses, I was able to investigate the impact of glass matrix on the electronic structure and further luminescence mechanism of CdSe quantum dot-doped glasses.

2.5.1 Short-range order structure

The radial distribution function is important in testing the reliability of my simulations by comparing it with experimental data (such as X-ray and neutron diffraction data) and in investigating the local atomic structure of the CdSe quantum dot-doped glasses. Considering an homogeneous repartition of the particles in space, it represents the probability to find a particle (yellow circles) in the shell *dr* at the distance *r* of another atom (the red circle), as illustrated in **Figure 2.3**:

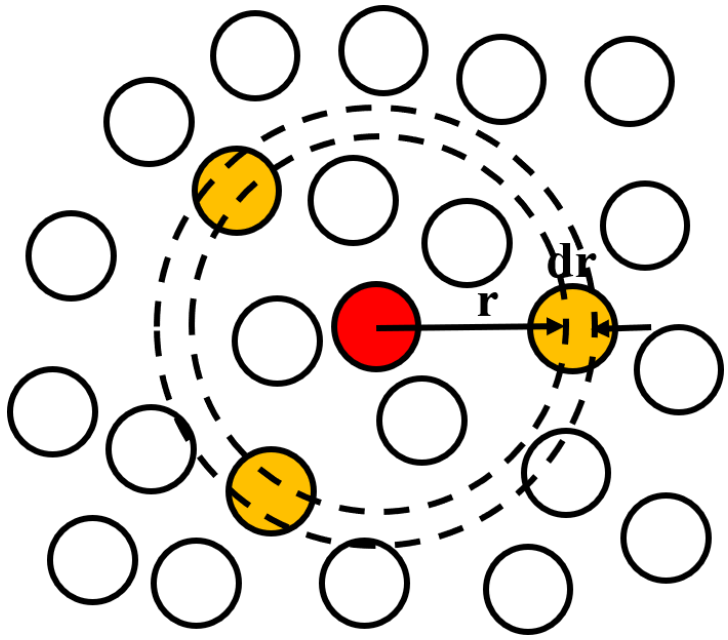

Figure 2.3 Space discretization for the evaluation of the radial distribution function.

By discretizing the space in intervals *dr*, it is possible to compute for a given atom of ith species (the red circle), the number of atoms of jth species (yellow circles) at a distance between *r* and *r* + *dr* of this atom:

$$dn_{ij}(r) = \frac{N}{V} g_{ij}(r) 4\pi r^2 dr \qquad \textbf{Eq. 2-52}$$

where *N* is the total number of particles, *V* is the volume, and $g_{ij}(r)$ is the radial distribution function. Therefore:

$$g_{ij}(r) = \frac{dn_{ij}(r)}{4\pi r^2 dr \rho_i} \qquad \textbf{Eq. 2-53}$$

$$\rho_i = \frac{V}{N_i} \qquad \textbf{Eq. 2-54}$$

Determining $g_{ij}(r)$ from a MD simulation involves computing all *i-j* distances, and each occurrence is added to the appropriate bin of a histogram running from $r=0$ to the maximum radius for the system. The distinct peaks in $g_{ij}(r)$ give information of the nearest neighbors, second-nearest neighbors, etc., of specific species of atoms in a solid. In R.I.N.G.S. code (http://rings-code.sourceforge.net/), the existence or the absence of a bond between two atoms is determined by the analysis of the partial $g_{ij}(r)$ and total $g(r)$ radial distribution function. Precisely the program will consider that a bond exists if the interatomic distance D_{ij} is smaller than both the cutoff given to describe the maximum distance for first neighbor atoms between species *i* and *j*, the first minimum of the $g_{ij}(r)$, and the first minimum of the total radial distribution ($g(r)$). For example, **Figure 2.4** illustrates the radial distribution of Si-O pairs. It goes to zero very rapidly when *r* become less than the sum of van der Waals radii of Si and O atoms. The first-peak indicates preferred locations for O atoms and the average interatomic distance can be obtained.

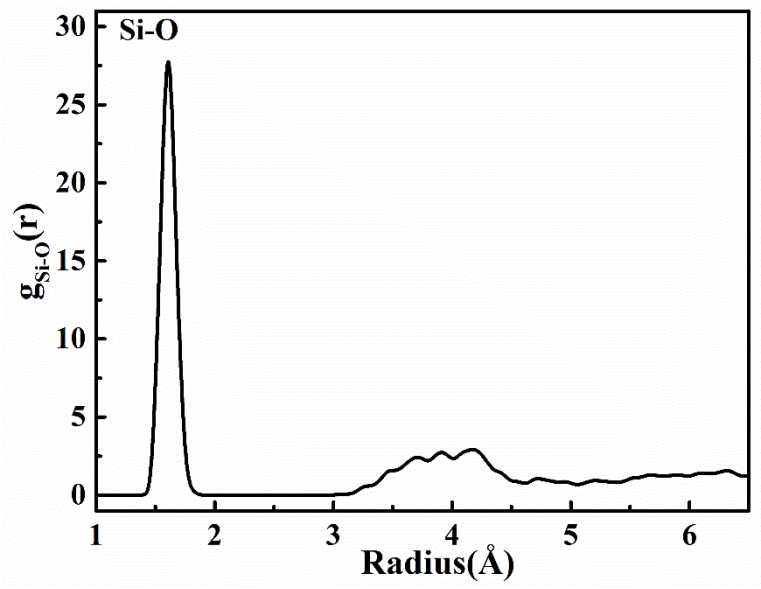

Figure 2.4 A radial distribution function for Si-O pairs in silicate glasses. The interatomic distance of Si-O pairs is 1.64 Å.

The integration of the $g_{ij}(r)$ between two positions, r_1 and r_2, provides information about the coordination number (CN) of the respective coordination shell, which can be obtained based on the radial distribution function:

$$\boldsymbol{CN_i(r_1, r_2) = \sum_j \int_{r_1}^{r_2} 4\pi\rho_i r^2\, g_{ij}(r)dr} \qquad \textbf{Eq. 2-55}$$

The stability of the glass network and CdSe units depend on the coordination between Si and O atom, and Cd and Se atoms respectively. In the description of the local atomic structure of glasses, most of the emphasis is put on the geometry of the first coordination shell of the atoms. Therefore, the radial distribution function and coordination number was calculated in my simulations in order to describe the short-range order structure.

2.5.2 Medium-range order structure

In glass science, the exploration of the origin of the disorder and understanding the origin of the intermediate range order is a key for the interpretation of the optical and conduction phenomena. Thus, ring statistics is mainly used to gain knowledge inaccessible using standard tools such as the radial distribution functions and the neutron or X-ray structure factor when studying amorphous systems. Particularly, it allows to scan the network at a larger scale than the first or second coordination shell. The analysis of topological networks is often based on the part of the structural information which can be presented in the graph theory, which uses nodes for the atoms and links for the bonds. The absence or existence of a link between two nodes is determined by the analysis of the total and partial radial distribution function of the system.

In such a network, a series of nodes and links connected sequentially without overlap, which is defined as a path, and a ring therefore is simply a closed path. In my Ph.D thesis, I focused on the ring size to give description of the glass network and CdSe units, using R.I.N.G.S. code, which has been successfully applied to the description of amorphous SiO_2 glass.[152] The ring size in my thesis was determined by the total number of nodes of the ring, therefore a N-membered ring is a ring containing N nodes. Besides, the bond angle distribution was also calculated to test the reliability of my simulations.

2.5.3 Mean squared displacement

As molecular dynamics allows one to follow the time evolution of the system, therefore we can obtain the dynamic properties of the system. The mean squared displacement (MSD) contains information about the atomic diffusivity of the individual species in the glass structure. It measures the average distance that an atom of the jth species travels in the time t:

$$\boldsymbol{MSD}\ (\boldsymbol{t}) = \frac{\mathbf{1}}{\boldsymbol{N_j}}\sum_{\boldsymbol{i=1}}^{\boldsymbol{N_j}} < |\vec{\boldsymbol{r}}_{\boldsymbol{i}}(\boldsymbol{t}) - \vec{\boldsymbol{r}}_{\boldsymbol{i}}(\boldsymbol{t} = \mathbf{0})|^{\mathbf{2}} > \qquad \textbf{Eq. 2-56}$$

where $\vec{\boldsymbol{r}}_{\boldsymbol{i}}(\boldsymbol{t}) - \vec{\boldsymbol{r}}_{\boldsymbol{i}}(\boldsymbol{t} = \mathbf{0})$ is the vector distance travelled by an atom i during the time interval of length t. The squared magnitude of this vector is averaged over many such time intervals and over all the atoms of the jth species in the simulated glasses. Based on the analysis of MSD, one can calculate the self-diffusion coefficient, which can be experimentally measured. In chapter 4, I calculated the MSDs of sodium silicate glasses to test the accuracy of force fields using the code developed by Guillaume Fraux in my lab.

2.5.4 Electronic Structures

The investigation of electronic structures is of predominant importance in understanding the optical properties of CdSe QDs in glass matrix. Particularly, based on the analysis of the total density of states and partial density of states (DOS), I can find the structural origin of the defect emission. The density of states for a given band n, $N_n(E)$, is defined as:

$$\boldsymbol{N_n}(\boldsymbol{E}) = \int \frac{\boldsymbol{dk}}{\boldsymbol{4\pi^3}}\boldsymbol{\delta}(\boldsymbol{E} - \boldsymbol{E_n}(\boldsymbol{k})) \qquad \textbf{Eq. 2-57}$$

where $E_n(K)$ describes the dispersion of the given band and the integral is determined over the Brillouin zone. The total density of states is obtained by summation over all bands, which is often used for quickly visual analysis of the electronic structure. Characteristics such as the energy gap between the highest occupied molecular orbital (HOMO) and lowest unoccupied molecular orbital (LUMO), and the number and

intensity of the main features are helpful in qualitatively interpreting experimental spectroscopic data. DOS can also help to understand the changes in electronic structure caused by, for example, adatoms. Local density of states shows which atoms in the system contribute electronic states to various parts of the energy spectrum. Partial density of states further qualifies results by resolving the contributions according to the angular momentum of the states.

In chapter 3, the electronic structures calculation of CdSe clusters were conducted with the $Dmol^3$ code as implemented in Materials Studio package.[136] The B3LYP functional was selected as exchange-correlation functionals as it can give better description to the HOMO-LUMO gap. In chapter 6, the density of states was calculated by CP2K codes and the PBE0 hybrid functional was applied. Different exchange-correlation functionals were chose because the system size of CdSe quantum dot-doped glass (several hundreds of atoms) was much bigger than CdSe clusters (66 atoms). Besides, it should be noted that in $Dmol^3$, the energy level of HOMO and LUMO was directly given but in CP2K, the energy level of HOMO was set at 0 eV as a reference. Since we are only interested in energy differences, this is not a problem in my studies.

2.6 Experimental method

In chapter 3, CdSe quantum dots doped glasses were prepared in order to validate the near-infrared photoluminescence of Cd_nSe_n-Na (n= 3, 10, 13, and 33) clusters, which was predicted by the DFT calculation. I fabricated the glass samples and characterize the optical properties of the quantum dots doped glass by measuring its absorption and emission spectra. The details of the fabrication method will be presented in chapter 3. Besides, the formation of the CdSe QDs was proved by using the high-resolution field transmission electron microscope and micro-confocal laser Raman spectrophotometer, conducted by the colleagues in our lab.

Chapter 3

3 Atomic and Electronic Structure of Capped Cd_nSe_n-X Clusters and Experimental Validation

3.1 Introduction

Due to the high surface-to-volume ratio, there are many defects (dangling bonds, vacancies and so on) on the surface of quantum dots, encompassing radiative or nonradiative recombination channels, which can easily compete with the intrinsic recombination. Therefore, it is of predominant importance to explore the atomic and structural origin of defect luminescence of the CdSe quantum dots in glass matrices. However, it is experimentally challenging to characterize the defect states and chemical environment of QDs in glasses, due to the lower number densities of QDs and the instability of glass matrices under electron beam as well as the amorphous nature of glass matrices. Computational methods, such as density functional theory (DFT), have been applied to search for new ways of surmounting these issues.

Surface states of QDs in glass matrices are complex, such as color centers (e.g. S_2^-, Se_2^- without forming semiconductor QDs when they are incorporated successfully in the inorganic host materials, leading to the visible emission and giving color to the glasses),[153-154] and intrinsic defects[155] of QDs including dangling bonds. Additionally, interfacial defects between the glass and the QD surface (e.g. non-bridging oxygens and network modifiers, such as sodium and other alkaline-earth metal ions) have a significant impact on the electronic structure of QDs.[57] In terms of CdSe QD embedded in glass matrices, Cd and Se can be present in the as-prepared glasses environments such as Cd-O, Cd-Se, Cd-Cd, and Se-Se. Upon thermal annealing, Se-Se contacts were considered as the nucleation sites, and thermal diffusion of Cd to the Se-rich zones promote the growth of CdSe QDs. During these processes, Cd-O gradually changed into Cd-Se, as evidenced by the extended X-ray absorption fine structure spectroscopy analysis.[57] At the interface between CdSe QDs and the glass matrices, presence of Cd-O, Cd-Cd, and Se-Se linkages is still possible due to the random distribution of these

elements in glassy matrices, leading to a large number of combination of surface states. For the charge balance, the dangling bonds of CdSe QDs in glasses can be compensated by non-bridging oxygen, structure intermediates (such as Ca, Zn, etc., which does not form glasses by themselves but acts like glass formers when combined with others), and structural modifiers (such as Na, etc.) in glasses. However, effects of these interface states on the optoelectronic properties of CdSe QDs still remain largely unknown. Therefore, I wanted to investigate structures containing the above mentioned surface and interface states such as Cd-Cd_nSe_n, Cd_nSe_n-Se, Cd_nSe_n-Cd, Cd_nSe_n-O, Cd_nSe_n-Na, Cd_nSe_n-Ca, Cd_nSe_n-O-Na, Cd_nSe_n-O-Ca and so on.

In this chapter, the dangling bonds of the CdSe QDs and their interactions with the glass matrices were systematically explored over combining DFT calculations and experimental approaches. Because of size constraints of the DFT method for tackling a comprehensive collection of many different cluster configurations, I have confined my study to atomistic simulations of the morphology and electronic structure of Cd_3Se_3, $Cd_{10}Se_{10}$, $Cd_{13}Se_{13}$ and $Cd_{33}Se_{33}$ nanoclusters as the most representative models. Effects of adatoms such as Cd, Se, O, Na, and Ca on the HOMO/LUMO energies and density of states of CdSe QDs in glasses were investigated, and experimentally examined using large-sized CdSe QDs precipitated in glasses. Especially, the near-infrared emission from Na-CdSe QDs in glasses was forecasted through the simulation and experimentally confirmed in this work. This work was published as "Understanding the atomic and electronic structures origin of defect luminescence of CdSe quantum dots in glass matrix" in J Amer Ceram Soc.[156]

3.2 Methods

3.2.1 Computational details

As CdSe QDs in the glass matrices mainly consist of the wurtzite phase, validated according to the TEM image, each cluster was initially constructed from this phase with the bulk Cd-Se geometry, and then relaxed to the lowest energy configuration.[131] This method has been successfully applied to the modelling of CdSe clusters to give an accurate description of CdSe QDs.[105, 129] In addition to the pristine Cd_nSe_n (n= 3, 10,

13 and 33) nanoclusters (**Figure 3.1**), much emphasis was placed on the defect engineering of Cd_nSe_n nanoclusters with different types of atoms attached to the surface of the dot, denoted as Cd_nSe_n-X (X=Se, Cd, O, Na, Ca) (**Figure 3.2**). The capped atoms were neutral when added to Cd_nSe_n clusters and charge transfer between capped atoms and clusters happened after geometry optimization. Therefore, in the optimized structure, the capped atoms were not neutral but with charges.

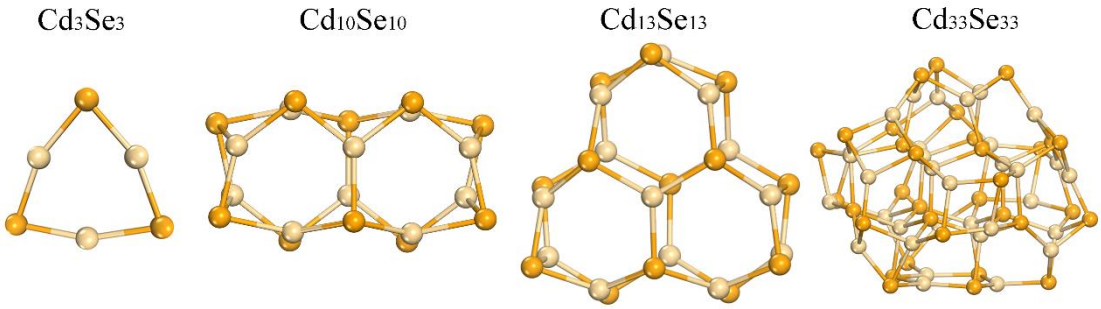

Figure 3.1 The optimized structure of Cd_nSe_n clusters (n = 3, 10, 13, 33) constructed based on a wurtzite phase with the bulk Cd-Se bond length. White balls represent the Cd atoms while the yellow balls represent Se atoms.

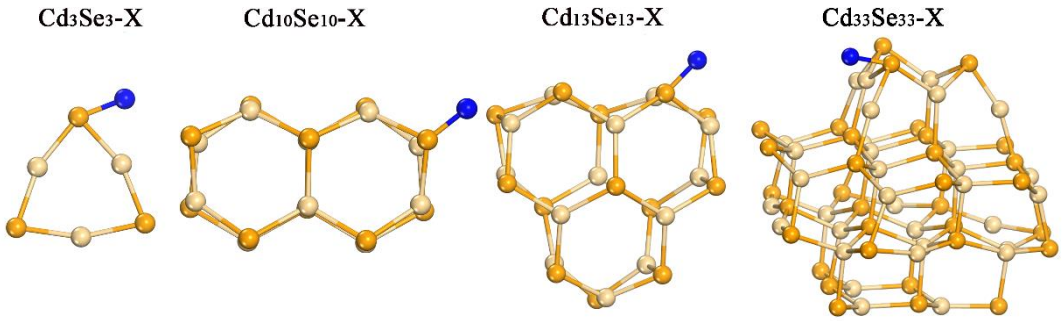

Figure 3.2 Initial structure of Cd_nSe_n-X (X=Se, Cd, O, Na, and Ca). White, yellow, and blue balls represent the Cd atoms, Se atoms and X atoms, respectively.

Furthermore, from the experimental point of view, the glass matrix is often a multi-component glass. Thus, the model I built above is the simplest model to mimic the chemical environment of CdSe clusters in glass matrix. The realistic chemical environment of the interface between CdSe clusters and glass matrices was supposed to be more complicated and rich in multiple types of interfacial bonds. Here, I also built some more complex models to probe the effect of the glass matrices (**Figure 3.3**) by

capping the CdSe clusters with multiple types of atoms.

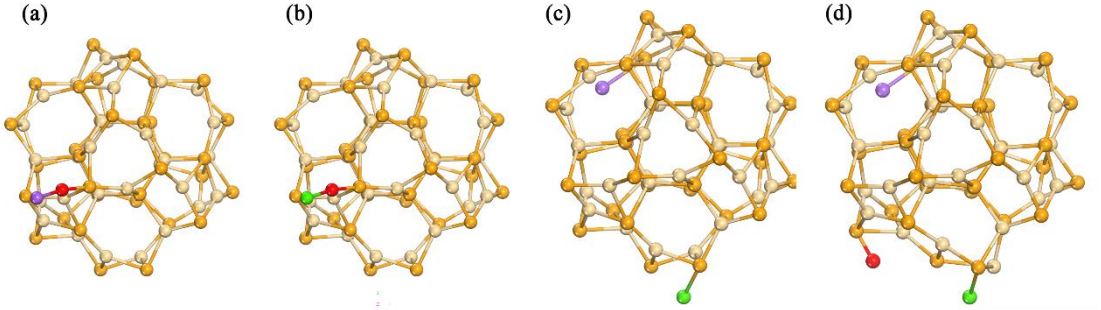

Figure 3.3 Initial structure for $Cd_{33}Se_{33}$ clusters capped by (a) O (red ball)-Na (purple ball); (b) O-Ca (green ball), (c) Na, Ca; (d) Na, O, Ca.

In Dmol^3 code, an iterative procedure is conducted in which the coordinates of the atoms are adjusted that the energy of the structure is brought to a stationary point, one in which the forces on the atoms are zero. The geometry optimization is an energy minimization procedure, searching a relative minimum on the energy hypersurface, but it does not guarantee a global minimum. Therefore, multiple optimizations from different starting configurations should be run to confirm that a global minimum has indeed been found. However, in my simulation, I only chose one initial configuration for each composition other than multiple conformations. On the one hand, in the wurtzite structure, Se (Cd) atoms at different coordinates are equivalent, there is little difference for X atoms bonding with another Se (Cd) surface atoms. On the other hand, I employed a similar routine to other researchers work, which successfully capped the organic ligands with the CdSe clusters as I reviewed in chapter 1.

According to previous studies,[113] the electronic structure calculations based on the generalized gradient approximations (GGA)[157] or local density approximations (LDA)[158] functional severely underestimated E_{gap} and long-range Coulombic interactions. Hence, I chose in this study, a more accurate approach, the hybrid functional, Becke, three-parameter, Lee-Yang-Parr (B3LYP)[159] incorporated in the Dmol^3 module[136-137] in Materials Studio. It was employed in this work to obtain values of the bandgaps, which were found to be very close to the experimental data. The d-polarization functions (DNP) basis set was applied to all calculations, while the core treatment was based on DFT Semi-core Pseudopotentials (DSPP). The geometry

optimizations were performed with a convergence threshold of 0.002 au/Å on the gradient, 0.005 Å on displacements, and 10^{-5} au on the energy. The self-consistent field (SCF) procedure was used with a convergence threshold of 10^{-6} au on the energy and electron density.

3.2.2 Experimental methods

Glasses with nominal compositions (mol%) of $65SiO_2$-$35Na_2O$-1CdSe were prepared using the conventional melt-quenching method (**1.3.1**). Raw chemical powders with purity of >99.9% were mixed thoroughly and melted in alumina crucibles at 1350 °C for 40 minutes under the ambient atmosphere. The melts were poured onto a brass mould and quenched by pressing with another plate. The as-obtained glasses were annealed at 300 °C for 3 h to reduce the thermal stress. After annealing, the glasses were cut into small samples for further treatment. CdSe QDs were precipitated in the glasses through one-step heat-treatment at various temperatures, i.e., 490 °C (10 h), 510 °C (10 h), 530 °C (10 h).

The absorption spectra were recorded using an UV/Vis/NIR spectrophotometer (UV3600, Shimadzu, Japan). Photoluminescence spectra were recorded using QM/TM/NIR time-resolved spectrofluorometer (QM/TM/NIR, PTI, USA). Raman spectra of the as-prepared and heat-treated glasses were recorded using a micro-confocal laser Raman spectrophotometer (INVIA, Renishaw, UK) with a 20 mW at 488 nm laser as the excitation. TEM micrographs were measured by high-resolution field emission transmission electron microscope (FEI Tecnai G2 F3, USA). The Raman spectra and TEM micrograph were obtained by the characterization center of materials in our lab.

3.3 Results & Discussion

3.3.1 CdSe clusters capped by Se atoms

The final optimized structures of the Cd_nSe_n clusters capped with Se atoms are shown in **Figure 3.4**. It is found that the added Se atom breaks the Se-Cd bonds nearby, and forms Se-Se-Cd bonds, consistent with the experimentally observed Se-Se bonds.[57-58,

[160] Meanwhile, compared with the DOS of pristine Cd_nSe_n clusters (**Figure 3.4**), the added Se introduces occupied Se 4*p* lone pair orbitals localized on the QD beyond the valence band within the electronic gap, pairing with unoccupied Cd 5s orbitals situated above the conduction band edge for each size of Cd_nSe_n QDs. This leads to a reduction in the effective E_{gap} of capped clusters, compared to the pristine clusters. By comparison, for pristine Cd_nSe_n clusters, the HOMO states principally comprise occupied lone pair Se 4*p* orbitals, while LUMO states are formed from unoccupied Cd 5*s* states. Here, the gap between HOMO and LUMO states was defined as E_{gap}. The capped cluster sizes are small ranging from 0.8 to 1.6 nm compared with the size of experimentally fabricated CdSe QDs in glass matrices, with E_{gap} decreasing from 3.48 to 2.63 eV.

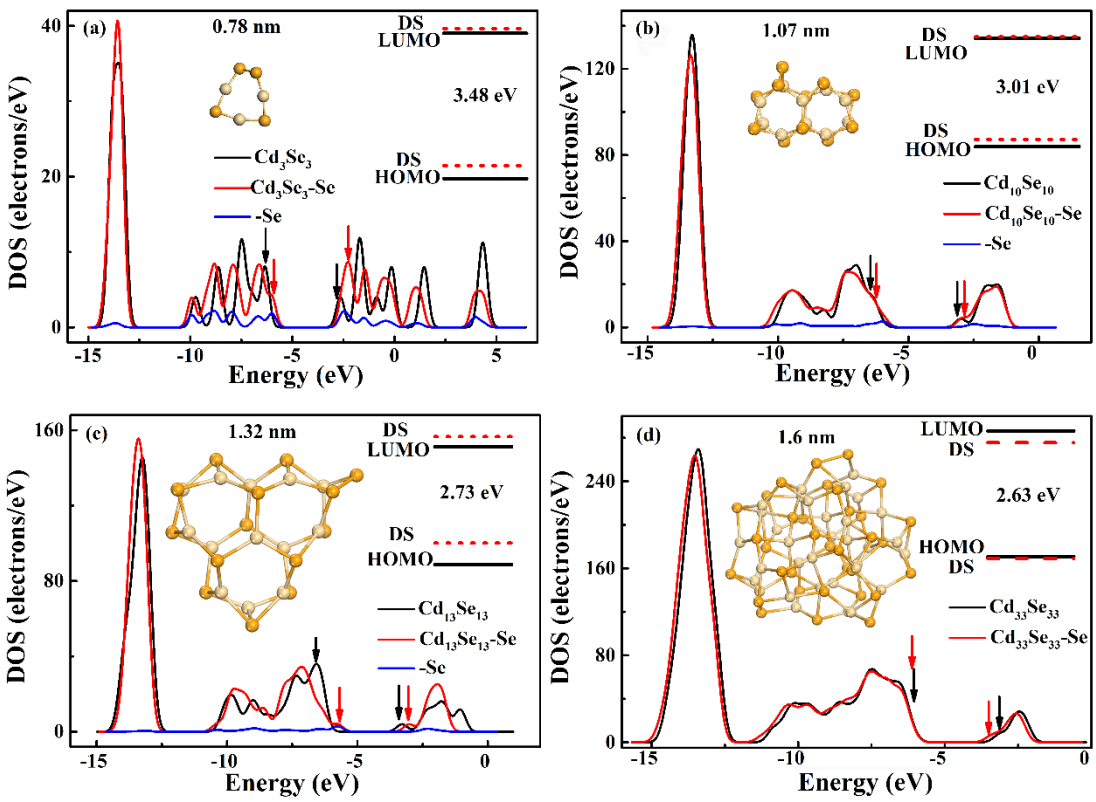

Figure 3.4 Optimized structures, DOS, and HOMO/LUMO levels of the pristine clusters (black line), the Se atom (yellow balls)-capped Cd_nSe_n clusters (red line). The value in the insets represents the E_{gap} of capped Cd_nSe_n QDs. The black arrows and red arrows represent the energy level of frontier orbitals of pristine and capped clusters, respectively. Structure of pristine QDs are on **Figure 3.1.**

Table 3.1 Visualization of HOMO and LUMO of Cd_nSe_n and Cd_nSe_n-Se clusters.

	$(CdSe)_3$	$(CdSe)_{10}$	$(CdSe)_{13}$	$(CdSe)_{33}$
HOMO	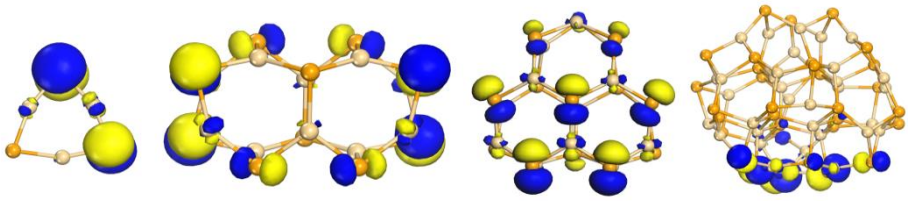			
	$(CdSe)_3$-Se	**$(CdSe)_{10}$-Se**	**$(CdSe)_{13}$-Se**	**$(CdSe)_{33}$-Se**
HOMO	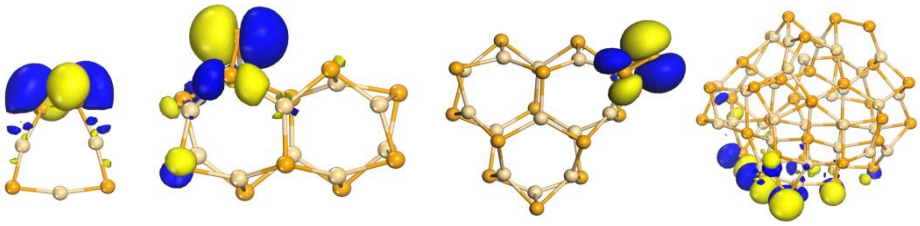			
	$(CdSe)_3$	**$(CdSe)_{10}$**	**$(CdSe)_{13}$**	**$(CdSe)_{33}$**
LUMO	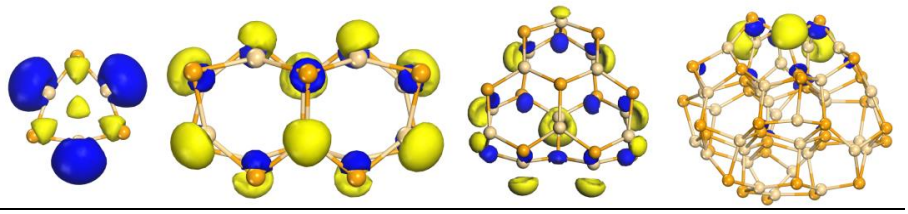			
	$(CdSe)_3$-Se	**$(CdSe)_{10}$-Se**	**$(CdSe)_{13}$-Se**	**$(CdSe)_{33}$-Se**
LUMO	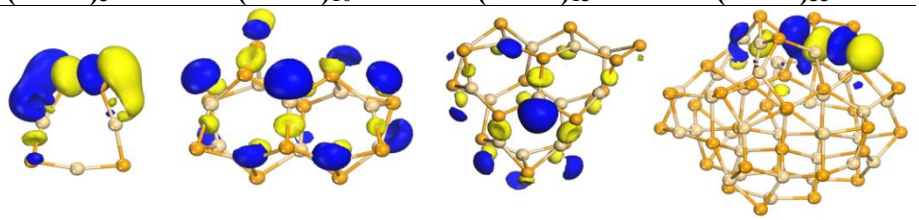			

For Cd_nSe_n-Se, the energy diagrams originate from the individual DOS, inferring the shift of the frontier orbitals as the size of the QDs changes, providing one explanation of unusual Stokes shifts of QDs. The Stokes shift was commonly observed in semiconductor QDs and several underlying mechanisms have been proposed, which were far from clear. For CdSe QDs, this shift decreases with the increase in radius of QDs, and disappears beyond a certain radius.[161-162] As the position of the defect states is size-dependent, this verifies the theoretical models that the energy level of defect

states changes as the size of QDs increases inducing a size-dependent Stokes shift.[163-164] However, such size-dependent Stokes shift was not observed in my work, probably due to the small size in molecules or clusters, where the Stokes shift originates from the energy difference of the ground state vibrational levels.[161]

In addition, redistribution of the HOMO and LUMO orbitals is observed for the Se-capped Cd_nSe_n clusters (**Table 3.1**). For pristine clusters, the majority of the HOMO density is distributed over Se atoms, while the LUMO density is spread over the Cd atoms. For Se capped clusters, the majority of HOMO density in the total DOS is distributed over the Se-Se bonds for the small clusters, but the HOMO density changes little in $Cd_{33}Se_{33}$-Se clusters owing to the concentration of the defects is lower than that in the Cd_nSe_n (n=3, 10 and 13), whereas the LUMO density rarely changes.

In all, the introduction of Se atoms to the CdSe clusters contributed to the structural reconstruction with the formation of Se-Se-Cd bonds. Besides, it also led to the formation of defect states and smaller bandgap compared with pristine QDs. Particularly, the redistribution of HOMO orbitals were observed.

3.3.2 CdSe clusters capped by Cd atoms

A similar phenomenon was observed when one of the surface Cd atoms of the pristine cluster was bonded with another Cd atom. The geometry was retained when the initial structure was fully relaxed. Similar to Cd_nSe_n-Se clusters, **Figure 3.5** shows how the edge of the valence band originates from the orbitals localized on the Cd-Cd_nSe_n QDs, while unoccupied states are introduced near the edge of the conduction band, belonging to the electron density localized over the added Cd atom. Likewise, the defects states formed by the Cd-Cd bonds decrease the bandgap of pristine clusters, which match well to the experimental findings.[165] In comparison, for Cd-Cd_nSe_n clusters, the majority of LUMO density, and HOMO density is redistributed towards the Cd-Cd bonds (**Table 3.2**). The increase in the size of the pristine and Cd_nSe_n-Se QDs leads to the separation of HOMO and LUMO orbitals, thus contributing to the spatial separation of holes and electrons that mitigates the possibility of defects-related recombination. However, the introduction of the Cd-Cd bonds narrows the spatial separation of HOMO and LUMO orbitals, indicating high possibility of defect related recombination.[166-168]

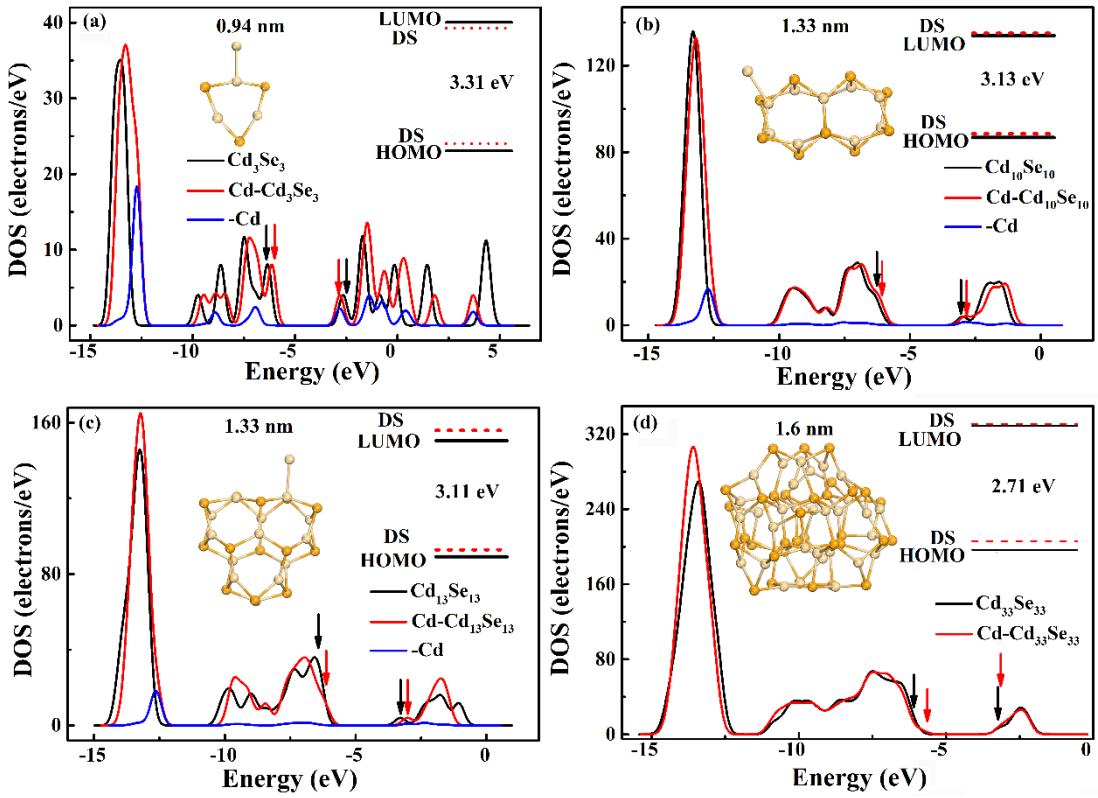

Figure 3.5 Optimized structures, DOS, and HOMO/LUMO levels of the pristine clusters (black line), the Cd atom (white balls)-capped Cd_nSe_n clusters (red line). The value in the insets represents the E_{gap} of capped Cd_nSe_n QDs. The black arrows and red arrows represent the energy level of frontier orbitals of pristine and capped clusters, respectively.

In addition, models of Cd or Zn atoms bonded to Se atoms of the QDs were also explored, as experimentally Zn is employed to fix Se which tends to evaporate when the temperature is high. However, computational results were inconclusive, signifying little possibility of interactions between Cd or Zn atoms and Se, with Cd or Zn is dissociating from the optimized Cd_nSe_n QDs when the size was small (**Figure 3.6**). In the contrary, there exists a bonding between the added Cd or Zn atom and surface Cd atom when the size was large, which is concordant with Cd-Cd_nSe_n clusters as discussed earlier (**Figure 3.5**).

Table 3.2 Visualization of HOMO and LUMO of Cd_nSe_n and Cd-Cd_nSe_n clusters.

	$(CdSe)_3$	$(CdSe)_{10}$	$(CdSe)_{13}$	$(CdSe)_{33}$
HOMO	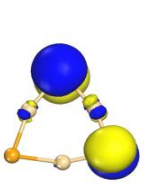	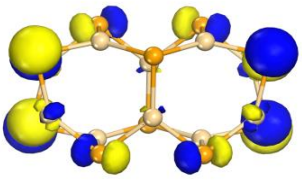	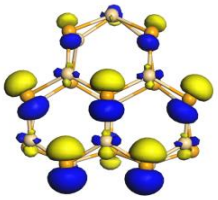	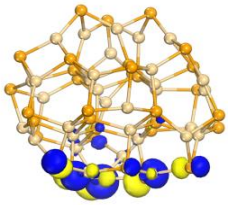
	Cd-$(CdSe)_3$	**Cd-$(CdSe)_{10}$**	**Cd-$(CdSe)_{13}$**	**Cd-$(CdSe)_{33}$**
HOMO	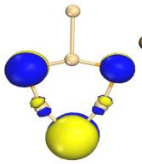	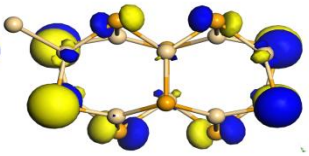	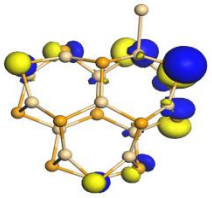	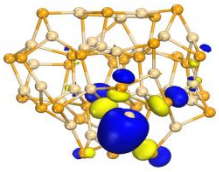
	$(CdSe)_3$	**$(CdSe)_{10}$**	**$(CdSe)_{13}$**	**$(CdSe)_{33}$**
LUMO	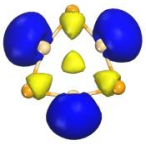	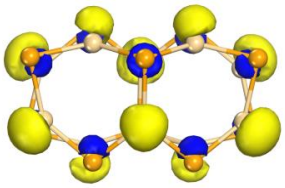	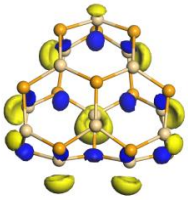	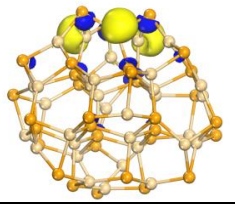
	Cd-$(CdSe)_3$	**Cd-$(CdSe)_{10}$**	**Cd-$(CdSe)_{13}$**	**Cd-$(CdSe)_{33}$**
LUMO	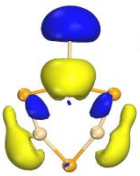	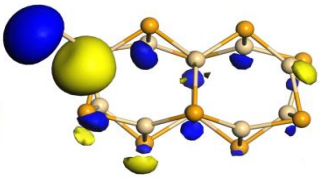	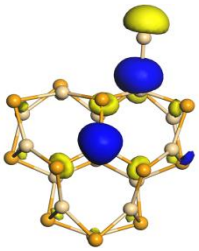	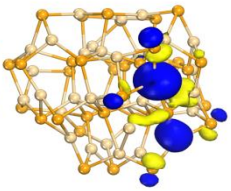

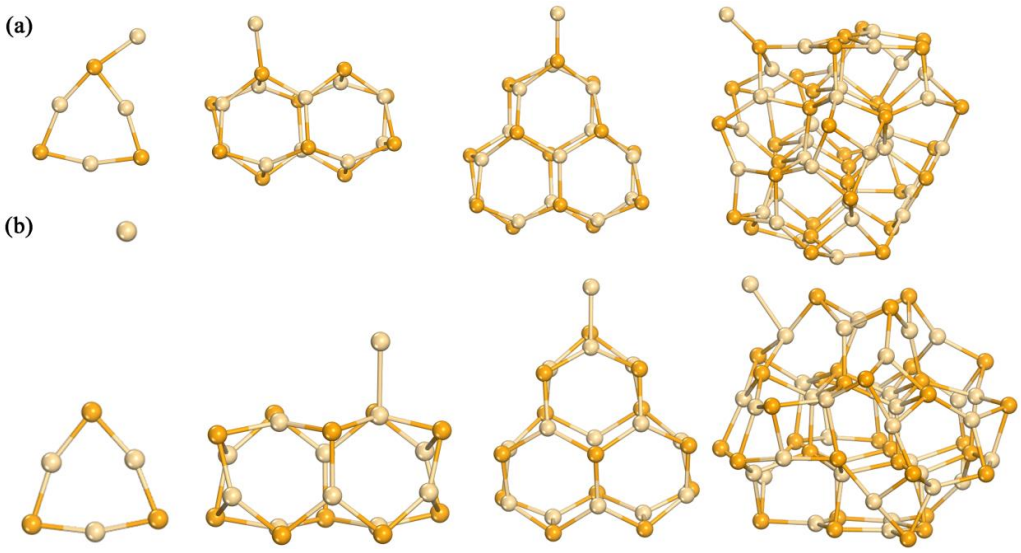

Figure 3.6 (a) The initial structure of Cd_nSe_n-Cd QDs where Cd is bonded with surface Se atom of CdSe clusters. (b) The optimized structure of Cd_nSe_n-Cd QDs. The Zn atom has the same structural reconstruction as Cd atom so I just put the results of Cd atom.

We concluded that preferential bonds between Cd or Zn atoms and CdSe clusters were Cd-Cd or Cd-Zn bonds other than Cd-Se or Zn-Se bonds. These results were interesting because Cd atoms were supposed to be bonded with surface Se atoms from electrostatic point of view. Computational simulation demonstrated a different tendency but it was consistent with the experimental finding that Cd-Cd linkages were observed in XAFS results.[57] The simplest Group 12 species were reported to display a metal-metal interaction, which was the diatomic M_2 dimer (M = Zn, Cd, Hg) and has been studied experimentally and theoretically.[169-170] For transition-metal elements, two σ bonds, one pair of π bonds, and one pair of δ bonds are possible owing to the availability of *s* and *d* orbitals. Thus, a maximum possible bond order of six has been proposed.[169] Furthermore, the binding energy of Cd-Se[122] and Cd-Cd bonds[169] is around 60 Kcal/mol, so the tendency to form Cd-Se and Cd-Cd bonds is supposed to be similar. Moreover, the Cd defects named as Cd-Cd energy levels were observed during CdS QDs sensitization, as a result of covalent dangling bonds between the sp^2 hybrid orbitals of cadmium cations according to XPS analysis.[170]

3.3.3 CdSe clusters capped by O atoms

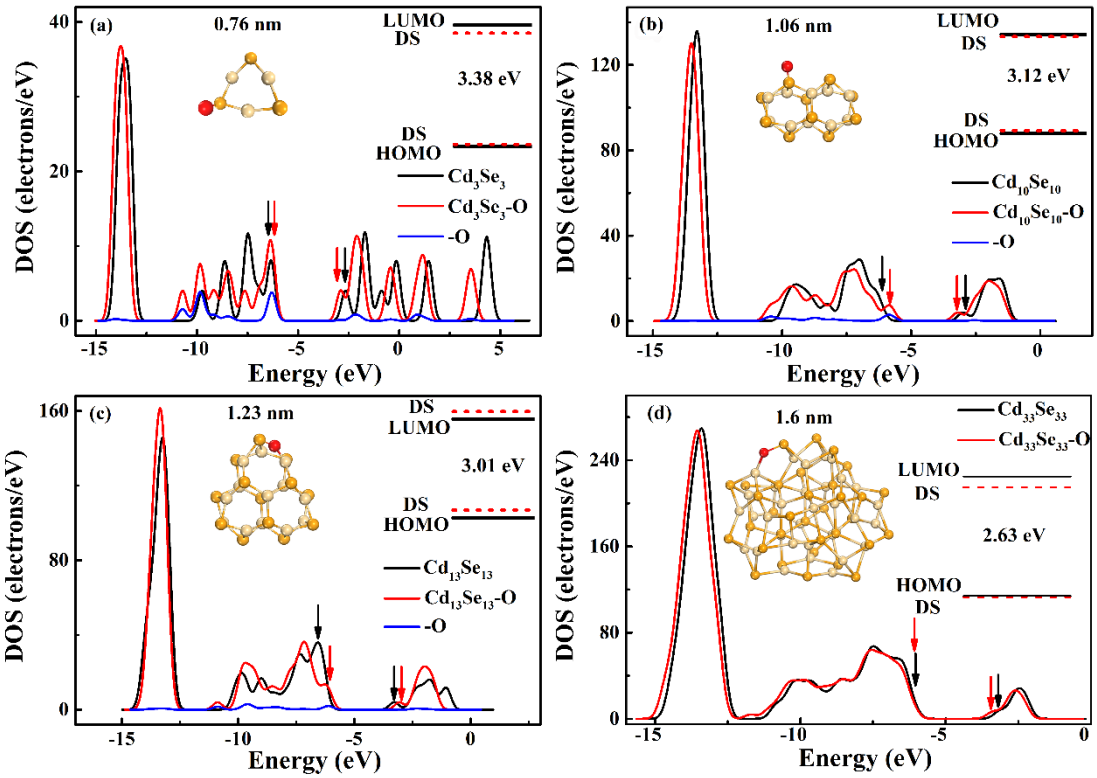

Figure 3.7 Optimized structures, DOS, and HOMO/LUMO levels of the pristine clusters (black line), the O atom (red balls)-capped Cd_nSe_n clusters (red line). The value in the insets represents the E_{gap} of capped Cd_nSe_n QDs. The black arrows and red arrows represent the energy level of frontier orbitals of pristine and capped clusters, respectively.

For QDs embedded oxide glasses, the interface between CdSe clusters and the glass matrices will also likely to include non-bridging oxygens, similar to the interface between the glass network and the micro-segregation of modifiers, like Na and Ca.[171-172] Capping Cd_nSe_n clusters with O atoms leads to surface reconstruction (**Figure 3.7**), where they enter the six-membered Cd_nSe_n rings, breaking Cd-Se bonds to form Se-O bonds. **Figure 3.7** illustrates how extrinsic O atoms result in the electron density of the QD being localized at the edges of the valence and conduction bands. Defect states involving Se-O bonds also decrease the band gap of pristine QDs. Moreover, HOMO states are mainly spread over the Se atoms (**Table 3.3**), spatially separated from LUMO

orbitals, thus offering little possibilities for defect emission. However, the electron density of frontier orbitals are not mainly localized on the Se-O bonds in $Cd_{33}Se_{33}$-O clusters, similar to that of Se capped CdSe clusters. One possible explain may be that O atoms are in the same group as Se atoms, so that the slight structural reconstruction and redistribution of electron density are observed.

Table 3.3 Visualization of HOMO and LUMO of Cd_nSe_n-O QDs.

	$(CdSe)_3$-O	**$(CdSe)_{10}$-O**	**$(CdSe)_{13}$-O**	**$(CdSe)_{33}$-O**
HOMO	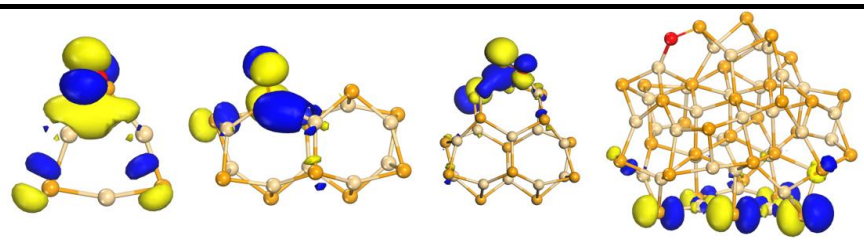			
LUMO	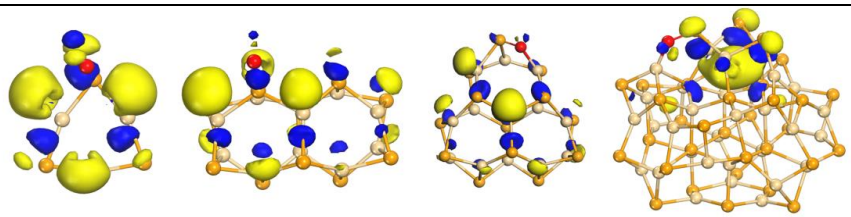			

3.3.4 CdSe clusters capped by Na atoms

Within the silicate glass network, cationic modifiers, such as alkalis and alkaline-earth metal ions, form micro-segregation area, i.e. clustering of these ions.[171-172] To explore the interaction between these ions and the surface of CdSe QDs, several models, which CdSe clusters were capped by different type and number of alkalis and alkaline-earth atoms, were established to examine bonding between specific modifier ions and QD surface atoms. The theoretical results demonstrated that sodium ions, acting as structure modifier in glass, had an enormous effect on the electronic structure of the pristine clusters, by introducing defect states in the middle of the E_{gap} (**Figure 3.8**), leading to a sharp decrease in band gap energy, compared to pristine clusters. In particular, the E_{gap} of Na atoms capped clusters is ~1.2 eV, indicating that the wavelength of defect

emission is expected to be in the visible-near infrared region. Moreover, the HOMO and LUMO states are spread over the same region (**Table 3.4**), indicating that holes and electrons are generated in the same place. This will typically result in localized excitons and associated recombination of holes and electrons excited from these defect states, indicating high possibility of defect emission, which is not desirable in practical applications.

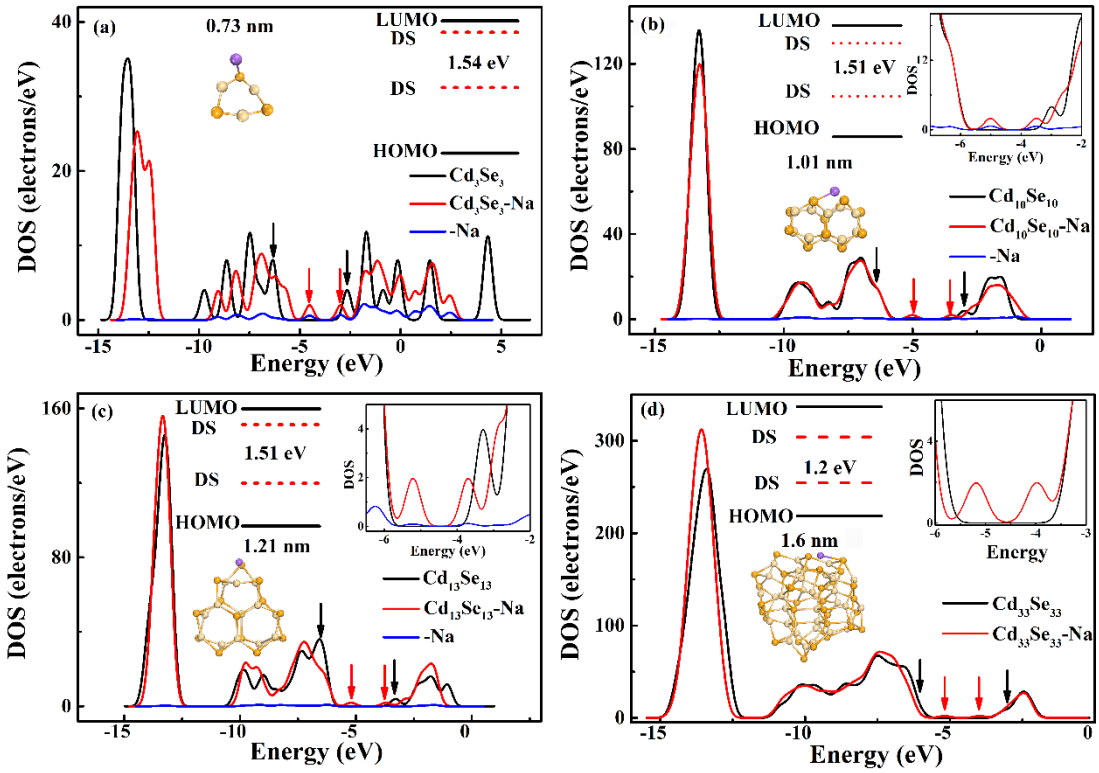

Figure 3.8 Optimized structures, DOS, and HOMO/LUMO levels of the pristine clusters (black line), the Na atom (purple balls)-capped Cd_nSe_n clusters (red line). The value in the insets represents the E_{gap} of capped Cd_nSe_n QDs. The black arrows and red arrows represent the energy level of frontier orbitals of pristine and capped clusters, respectively.

However, it was a simplified model that the CdSe clusters were only capped by one Na atoms. As glass modifiers, the sodium ions were in the space around Si-O skeleton, and the dangling bonds in the surface of CdSe cluster may attract two or more Na ions rather than one Na ion in a realistic environment. Based on our calculations, sodium

could play an important role in the electronic structure of the CdSe cluster. Therefore, I studied models with different number of sodium ions (n = 1, 2, 3, 22) bonded to $Cd_{33}Se_{33}$ clusters, to probe the impact of different number of sodium ions on the electronic structures of it. The optimized structure is shown in **Figure 3.9**, i.e. it is a local minimum in energy with displacement, force and energy gradient converged. All the surface Se atoms were bonded with Na atoms when n =22 in optimized structure. However, the Mayer bond order of 19 Na ions bonded with Se atoms were negative, indicating antibonding between Na atoms and Se atoms and instability of this structure. Thus, it indicated that bonding between Na atoms and Se atoms should be further investigated.

Table 3.4 Visualization of HOMO and LUMO of QDs capped by Na ions.

	$(CdSe)_3$-Na	**$(CdSe)_{10}$-Na**	**$(CdSe)_{13}$-Na**	**$(CdSe)_{33}$-Na**
HOMO	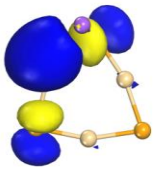	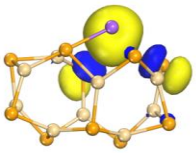	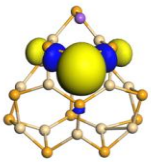	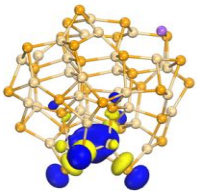
LUMO	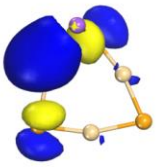	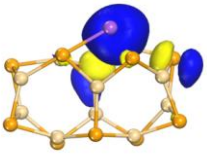	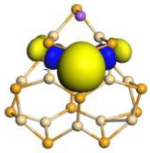	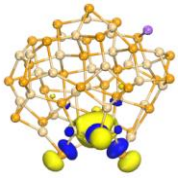

Different number of Na atoms contributed to variable electronic structures of capped $Cd_{33}Se_{33}$ clusters (**Figure 3.10(a)**), resulting in different E_{gap} (**Figure 3.10(b)**). But due to the instability of the optimized $Cd_{33}Se_{33}$-22Na cluster structure, it was not appropriate to use this structure to conduct further DFT calculations. Another interesting result was the bandgap of n =2 (E_{gap} = 2.3 eV) much higher than n =1 (E_{gap} =1.2 eV) and n =3 (E_{gap} = 0.59 eV). It seems like that when the CdSe clusters capped by odd number of sodium atoms, the bandgap was sharply decreased compared with even number. The underlying mechanism should be studied in depth by building more models with clusters capped by different number of Na atoms. Overall, the number of

sodium bonded to Se atoms significantly changed the electronic structure of pristine QD by forming midgap states deep inside the HOMO-LUMO gap, and most importantly, the electron density of HOMO and LUMO orbitals were found to be localized on the same spatial region, which may greatly lead to unfavorable defect emission.

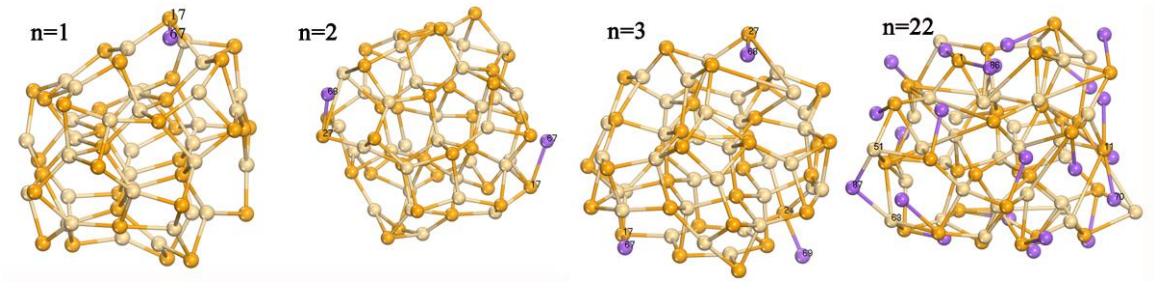

Figure 3.9 Optimized structures of $Cd_{33}Se_{33}$ clusters capped with different number of Na atoms. (n = 1, 2, 3, and 22)

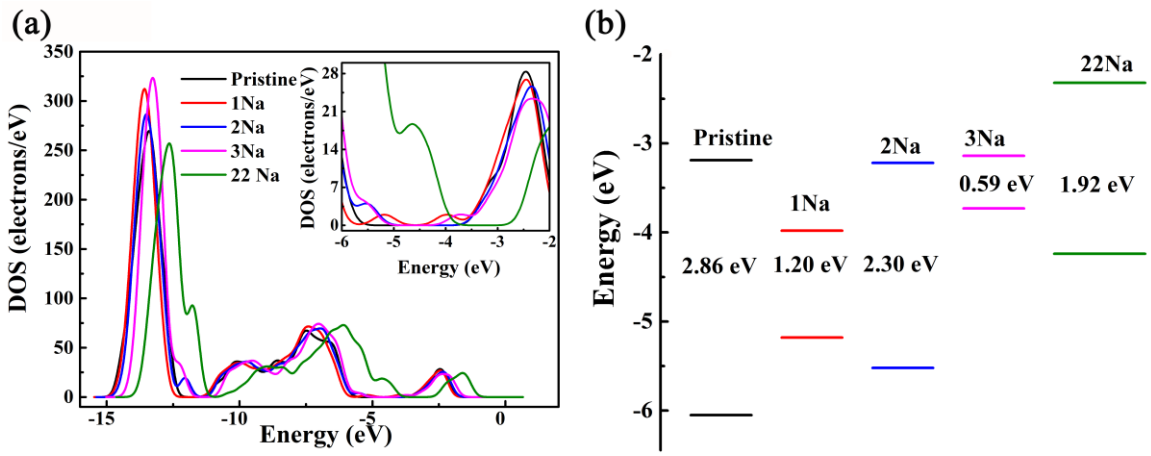

Figure 3.10 (a) Density of states of pristine $Cd_{33}Se_{33}$ clusters and $Cd_{33}Se_{33}$ clusters capped by 1, 2, 3 and 22 sodium atoms. (b) Energy diagrams originated from DOS include HOMO and LUMO levels of pristine clusters, capped clusters and E_{gap} values formed by Se-Na bonds.

3.3.5 CdSe clusters capped by Ca atoms

For alkaline-earth modifying ions like Ca capping Cd_nSe_n QDs, the surface reconstruction is relatively larger compared to Na ions. I observe that Ca ions break the

bonds between the neighbor Se-Cd pairs, forming Cd-Ca-Se bonds (**Figure 3.11**). The structure reconstruction of Cd_3Se_3-Ca, $Cd_{10}Se_{10}$-Ca and $Cd_{13}Se_{13}$-Ca clusters was bigger than that of $Cd_{33}Se_{33}$-Ca, which may be attributed to the higher defect concentration in the former three models. Unlike CdSe clusters capped by sodium atoms, the Ca-Se bonds introduce defect states beyond the HOMO level inside the pristine cluster E_{gap} (**Figure 3.12**), leading to the majority of HOMO density being spread over the Se atom, while the majority of the LUMO density is unchanged (**Table 3.5**).

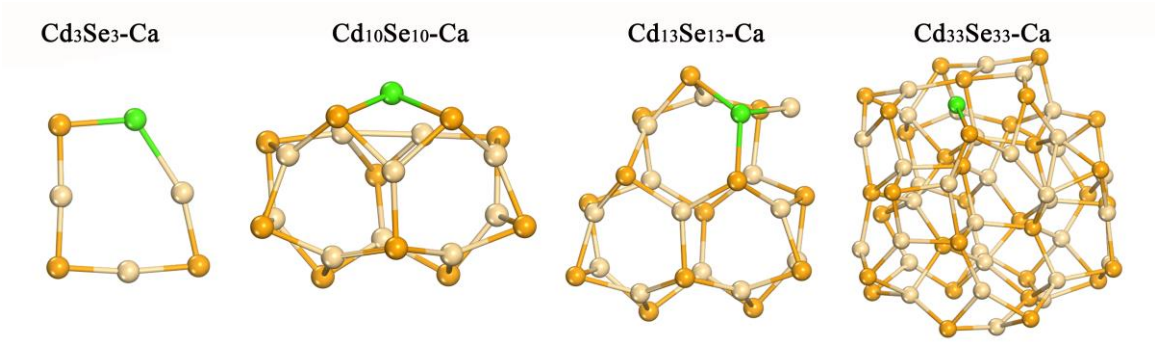

Figure 3.11 The optimized structure of Cd_nSe_n-Ca QDs.

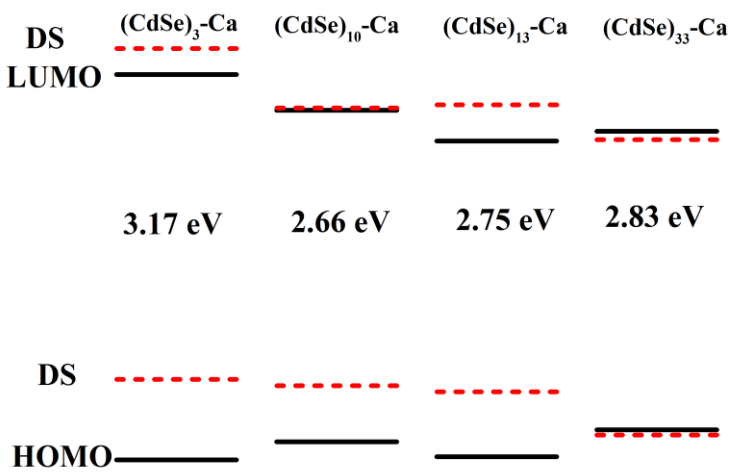

Figure 3.12 Energy diagrams originated from DOS include HOMO and LUMO levels of pristine clusters (black line), capped clusters (red dashed line) and E_{gap} values formed by Cd-Ca bonds.

Table 3.5 Visualization of HOMO and LUMO of Cd_nSe_n-Ca.

	$(CdSe)_3$-Ca	$(CdSe)_{10}$-Ca	$(CdSe)_{13}$-Ca	$(CdSe)_{33}$-Ca
HOMO	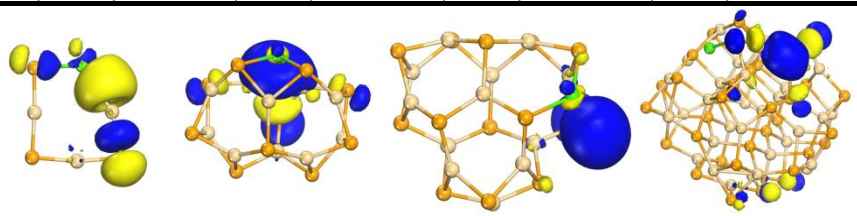			
LUMO	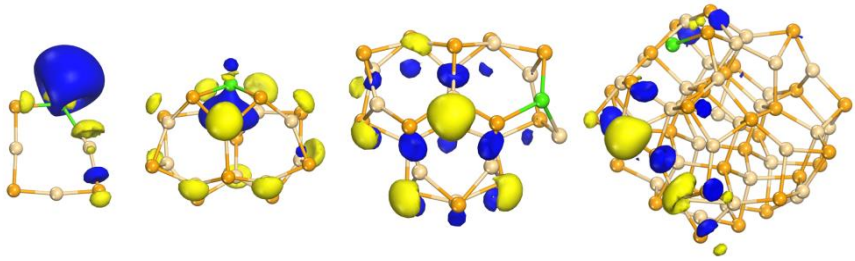			

3.3.6 CdSe clusters capped by multiple types of atoms

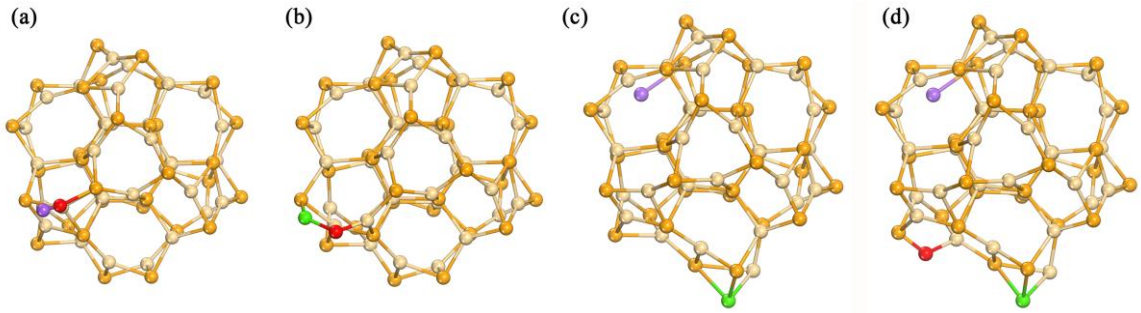

Figure 3.13 Optimized structure for $Cd_{33}Se_{33}$ clusters capped by (a) O (red ball)-Na (purple ball); (b) O-Ca (green ball), (c) Na, Ca; (d) Na, O, Ca.

The final optimized structure of $Cd_{33}Se_{33}$ clusters capped by O-Na pairs, O-Ca pairs, Na and Ca atoms, and Na, O, Ca atoms is shown in **Figure 3.13**. Compared with the initial structure (**Figure 3.3**), little structural reconstruction was observed. Besides, the structural reconstruction was smaller of CdSe clusters capped by multiple types of atoms than it capped by single type of atoms. These results may be due to the simultaneous introduction of cations and anions. Moreover, although the structure at the local minimum in energy of those clusters can be obtained after geometry optimization, the Mayer bond order calculation showed the bond order between Na and

Se atoms was negative when the CdSe clusters were capped by Ca atom at the same time. It demonstrated that there is little possibility of structures of the clusters capped with Na, Ca (**Figure 3.13 (c)**) or Na, O, Ca (**Figure 3.13 (d)**), simultaneously. The repulsion between Na cation and Ca cation may contribute to the little possibility of those structures. It also indicated the preferential structure of CdSe clusters in glass matrix, that the CdSe clusters were more likely to be capped by Ca atoms than Na atoms. However, more criteria should be employed to discuss the possibility of bonding between Na and Se atoms in those structures as the geometry optimization and Mayer bond order calculation give different results.

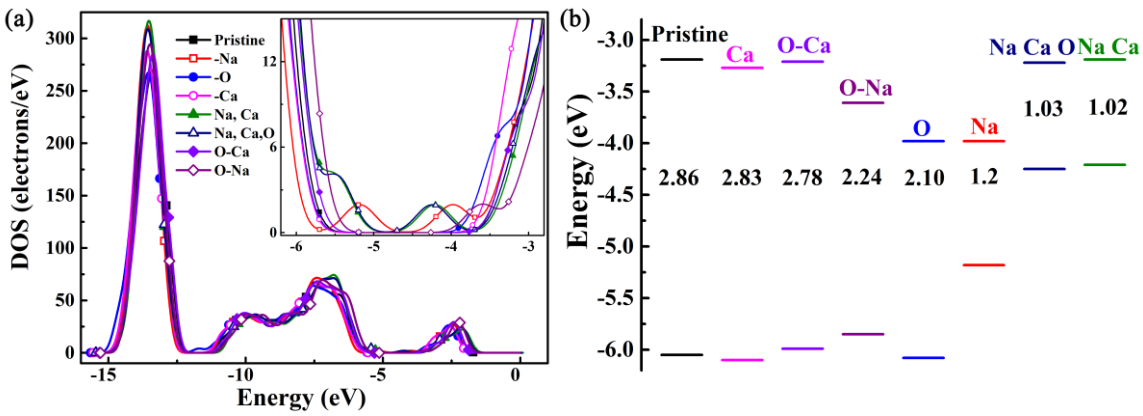

Figure 3.14 (a) Density of states of pristine $Cd_{33}Se_{33}$ clusters and clusters capped by Na, O, Ca, Na and Ca, Na, Ca and O, O and Ca, O and Na atoms. (b) Energy diagrams from DOS include HOMO and LUMO levels of pristine clusters, capped clusters and E_{gap} values.

The density of states and the E_{gap} were calculated for each clusters (**Figure 3.14**). When the CdSe clusters capped by Na atoms only, we can clearly see the two trap states formed deep inside the bandgap of pristine QD (two peaks in redline), resulting in a sharply decreased bandgap (1.2 eV). However, when the CdSe clusters were capped by O-Na bonds, the peak near the valence band appeared in $Cd_{33}Se_{33}$-Na clusters disappeared, leading to a higher bandgap (2.24 eV) compared with $Cd_{33}Se_{33}$-Na clusters (1.2 eV). The existence of O atoms may passivate the defect states formed by Na atoms.

Meanwhile, the defect states near the conduction band were observed when CdSe

clusters were only capped by O atoms. However, the introduction of Na atom and Ca atoms to the O capped CdSe clusters, making the disappearance of those defect states, contributing to a higher value of E_{gap} (2.24 eV for $Cd_{33}Se_{33}$-O-Na clusters and 2.78 eV for $Cd_{33}Se_{33}$-O-Ca clusters) than that of $Cd_{33}Se_{33}$-O clusters (2.10 eV). So Na atoms and Ca atoms can also eliminate the defect states formed by O atoms.

Although the Mayer bond order calculation indicated little possibility of Na-Se bonding when the CdSe clusters capped by Na, O, Ca atoms and Na, Ca atoms simultaneously, the density of states indicated a different electronic structure of those structure from the $Cd_{33}Se_{33}$-O-Ca and $Cd_{33}Se_{33}$-Ca clusters, respectively. Interestingly, the curve of the density of states of CdSe clusters capped by Na, O, Ca atoms and Na, Ca atoms simultaneously was the same, resulting in a similar HOMO-LUMO gap, 1.03 eV and 1.02 eV respectively. And we can clearly see the characteristic peaks in the bandgap formed by Na atoms in those structures. Overall, the geometry optimization results, the Mayer bond order calculation, and the density of states gave controversial conclusions about the bonding between Se and Na atoms at the presence of Ca atoms. More criteria should be taken into consideration. However, it was apparent that the doping of adatoms decreased the HOMO-LUMO gap of CdSe clusters and the structural reconstruction were smaller than that of CdSe clusters capped by single atoms.

3.3.7 Experimental validation

The presence of capping atoms induces changes in the electronic structure of Cd_nSe_n clusters, which I illustrated experimentally using CdSe QDs embedded in sodium silicate glass. During melting, sublimation of CdSe could occur, however, due to the well-controlled melting condition and high viscosity of the glass melt, most of the CdSe was kept in the quenched glasses, where most of the Cd was bonded with O and Se were transformed into Se-Se clusters, chains, etc.[57] As a result, precipitation of CdSe QDs was largely unaffected.

Precipitation of CdSe QDs in glass was confirmed by TEM images (**Figure 3.15(a)**) and the Raman spectra (**Figure 3.15(b)**) analysis. The structure of the nanocrystals was analyzed according to TEM micrograph of samples heat treated at 530 ºC for 10 h. The inter-planar distance of the QDs was found to be 0.214 nm (upper inset in **Figure**

3.15(a)), corresponding to the {110} facet, which is comparable to that of the bulk CdSe crystal (JCPDS No.: 77-2307, d=0.215 nm). The mean size of the nanocrystals was ~3.6 nm with a size dispersion of 15.9% (bottom inset in **Figure 3.15(a)**). These results were obtained by measuring the size of quantum dots according to the TEM micrograph. It was difficult to characterize the CdSe QDs doped glass by TEM since these small-sized CdSe QDs were buried by the amorphous matrices and the insulating properties of glass matrices made it prone to be damaged by the high energy electron beam irradiation. Consequently, the computational modelling is of vital importance to investigate the QDs doped glasses. Besides, a strong Raman peak at 205 cm^{-1} and its overtone at 410 cm^{-1} were observed for heat-treated glasses, consistent with the longitudinal optical phonon of CdSe (**Figure 3.15(b)**).[63]

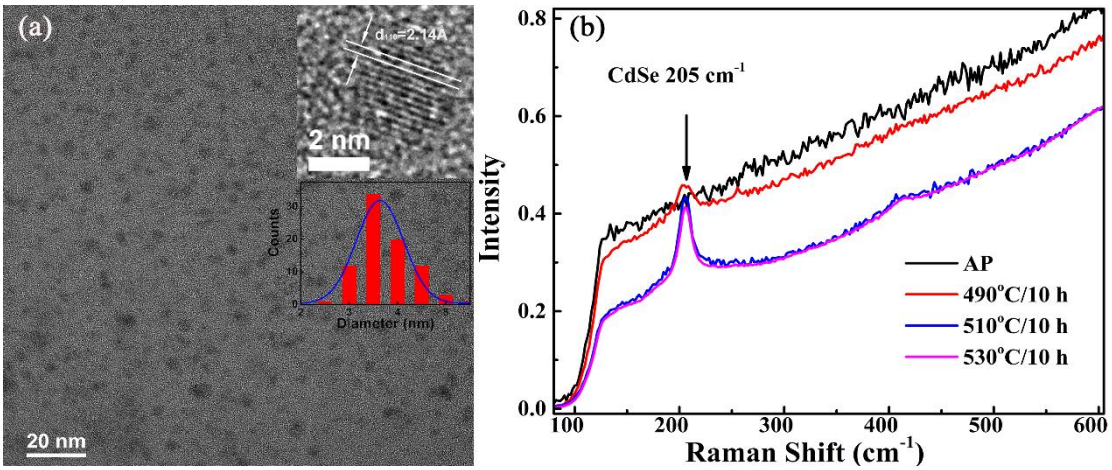

Figure 3.15 (a) TEM micrograph of glass heat treated at 530 ºC for 10 h under an accelerating voltage of 150 kV. Upper inset: TEM image of one nanocrystal in the glass. Bottom inset: Size distribution histogram of nanocrystals shown in (a). (b) Raman spectra of the as-prepared glasses and glasses heat treated at 490 ºC, 510 ºC and 530 ºC for 10 h.

$$\boldsymbol{D = (1.6122 \times 10^{-9})\lambda^4 - (2.6575 \times 10^{-6})\lambda^3 + (1.6242 \times 10^{-3})\lambda^2 - (0.4277)\lambda + (41.57)} \qquad \textbf{Eq. 3-1}$$

where D is the size and λ is the wavelength of the first excitonic absorption peak.

The optical absorption peak (**Figure 3.16(a)**) shifted from 374 nm (3. 31 eV) to 451 nm (2.75 eV), 498 nm (2.49 eV), and 565 nm (2.19 eV) as the heat treatment

temperature varied from as-prepared to 490 ºC, 510 ºC, and 530 ºC for 10 h, respectively. The shift of these absorption peaks indicated the growth of CdSe QDs during heat-treatment. Using the empirical equation (**Eq. 3-1**),[173] the calculated diameters of these CdSe QDs increased from 1.3 nm to 2.0 nm, 2.3 nm, and 3.4 nm, through the magic-sized range.[174] The calculated diameter based on first excitonic absorption peak of CdSe QDs formed in specimen heat-treated at 530 ºC for 10 h was almost the same as that observed from the TEM image (**Figure 3.15(a)**). Meanwhile, the calculated diameter of QDs in the as-prepared glass is the same as the pristine $Cd_{33}Se_{33}$ clusters (1.3 nm). However, band gap energy of 1.3 nm-sized CdSe QDs in glass is found to be ~3.31 eV (**Figure 3.16(a)**), slightly larger than the calculated value (2.86 eV).

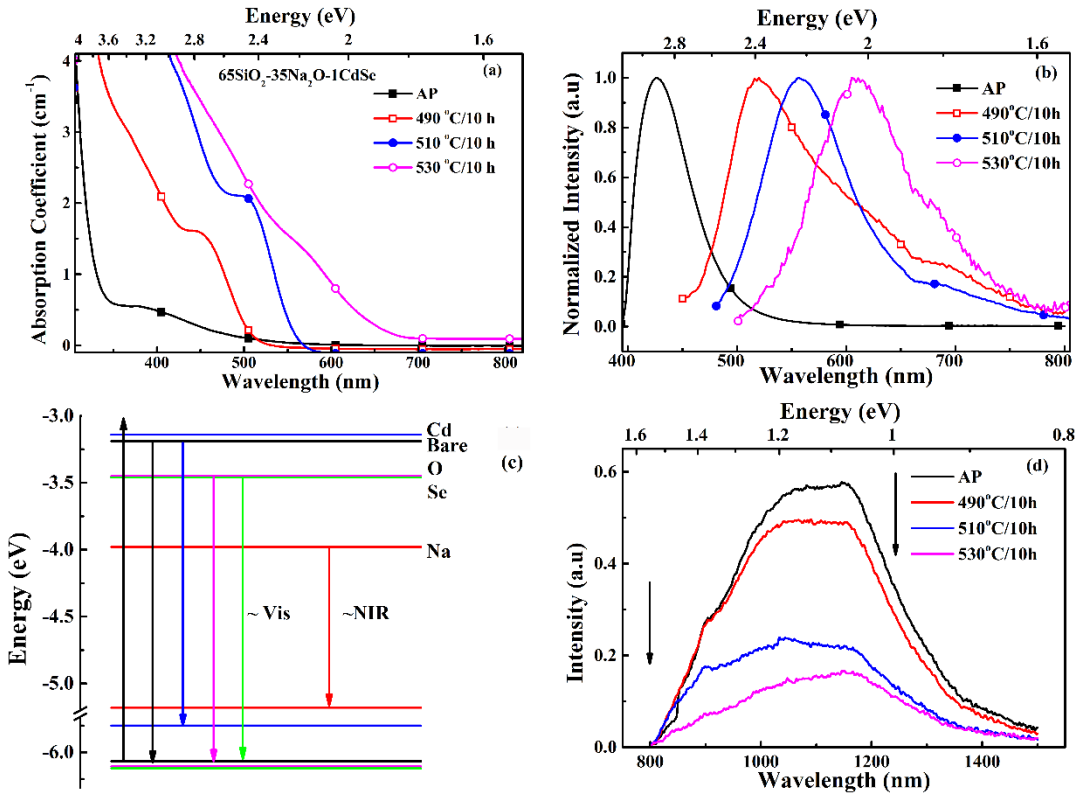

Figure 3.16 (a) Absorption spectra and (b) normalized photoluminescence spectra (recorded under 365 nm laser excitation) of as-prepared and heat-treated glass specimens. (c) Energy level diagram of pristine and capped Cd_nSe_n QDs with different adatoms. The black, blue, pink, green lines and red lines correspond to the HOMO and

LUMO of pristine CdSe QDs, and Cd-Cd, Se-O, Se-Se, and Se-Na bonds, respectively. (d) Near-infrared photoluminescence spectra of as-prepared and heat-treated glass specimens recorded under 404 nm laser excitation.

Several factors can be responsible for this. Firstly, the experimental gap is usually obtained from optical experiments, and therefore, HOMO-LUMO and optical gaps can be different, because some transitions can have vanishing oscillator strength. Secondly, DFT calculations do not include hole-electron interactions.[175] Consequently, the B3LYP functionals tend to slightly underestimate the band gap. Thirdly, the dielectric constant of the local environment may also exert a strong effect on the band gap energy of CdSe QDs. For example, the experimental band gap energy of $Cd_{33}Se_{33}$ colloidal quantum dots dispersed in solution was found to be 2.99 eV,[176-177] similarly different from the optical gap we obtained from our specimens. The different dielectric constants of glass matrices and solutions may lead to the different sizing curves of first absorption peaks.

Upon 365 nm light excitation, both visible and near-infrared emission were observed from these glass specimens (**Figure 3.16**). Central wavelength of the visible emission band shifted from 425 nm (2.92 eV, as-prepare specimen) to 519 nm (2.39 eV, specimen annealed at 490 ºC), 557 nm (2.23 eV, specimen annealed at 510 ºC) and to 610 nm (2.03 eV, specimen annealed at 530 ºC), exhibiting small Stokes shifts compared with the absorption spectra (**Figure 3.16(b)**). However, all the visible emission spectra were found to be non-symmetric, rising sharply at short wavelength side and extending to long wavelength side.

All these visible emission spectra can be fitted with at least three Gaussian functions (**Figure 3.17**), where the left (high energy) peak can be assigned to the band edge emission from CdSe QDs in glasses, and the other two to the emission from the surface states. For CdSe QDs formed in as-prepared glasses, the emissions from surface states peaked at 2.86 eV and 2.68 eV, comparable to the values obtained from Cd-$Cd_{33}Se_{33}$ and $Cd_{33}Se_{33}$-O (or Se). As the heat-treatment temperature increased, both the band edge emission and defect emissions shifted towards long wavelength side (**Figure 3.16(b)** and **Figure 3.17**), consistent with the absorption spectra (**Figure 3.16 (a)**) and the calculated band gap energy of the pristine and capped Cd_nSe_n QDs (**Figure 3.18**

and **Figure 3.16(c)**). However, due to the complex local environment of CdSe QDs in glasses, emission spectra from the surface states were broader than those of band edge emissions (**Figure 3.17**), indicating the presence of multiple surface states for CdSe QDs in glasses. These broad surface states emission showed the surface states were more complex than the single-atom capped Cd_nSe_n QDs, probably with two or more capping atoms.

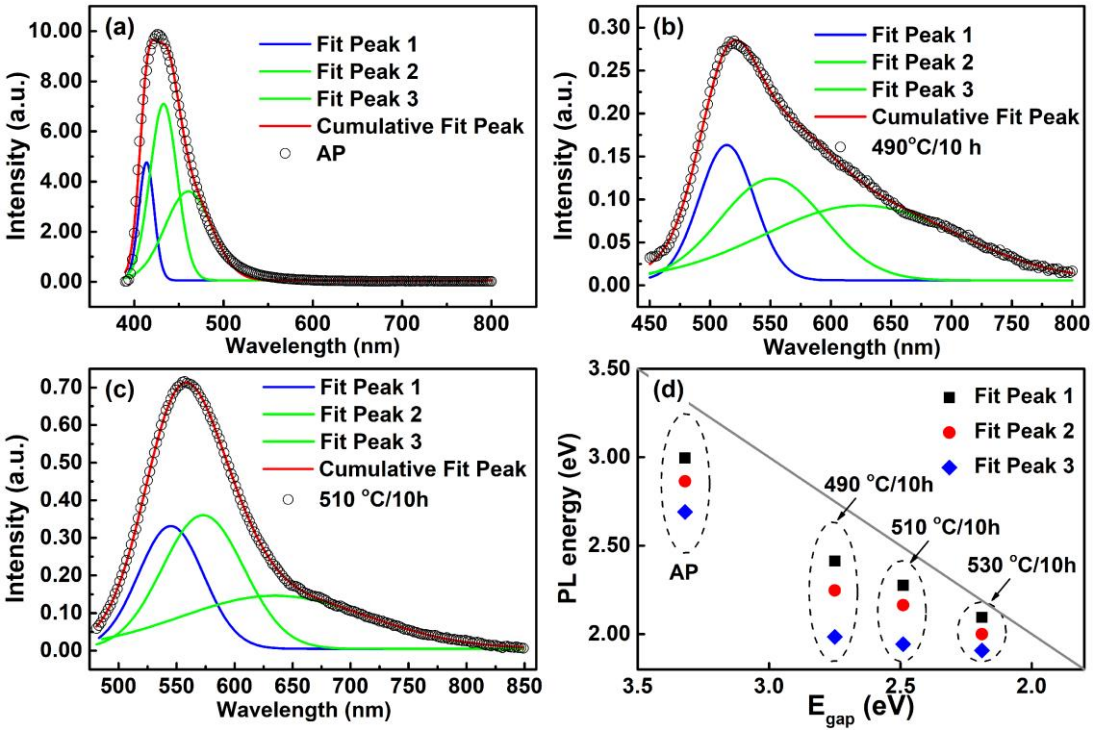

Figure 3.17 (a), (b) and (c) The experimental data of each sample are shown in hollow circles. The blue and green lines are the individual components by Gaussian fitting, and the red lines are the sum of individual fitting lines. (d) E_{gap} is the energy of the first absorption peak and the solid line demonstrates that the energy of the PL peak is equal to the energy of the first absorption peak.

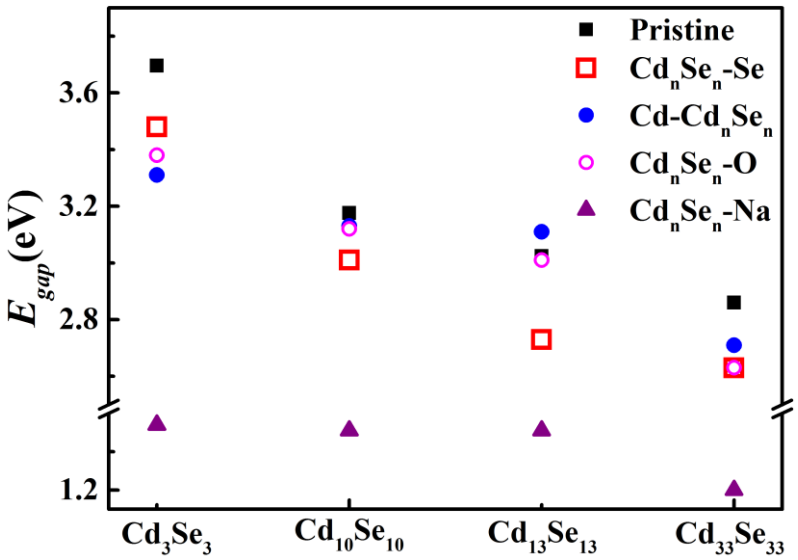

Figure 3.18 E_{gap} of pristine Cd_nSe_n QDs and capped Cd_nSe_n QDs of different size. (n=3, 10, 13 and 33)

Most importantly, the reduction in E_{gap} of Cd_nSe_n QDs capped with Na was confirmed by the near-infrared emission spectra (**Figure 3.16(d)**). As shown in **Figure 3.18**, E_{gap} of Na-capped Cd_nSe_n QDs gradually decreased from 1.54 eV (Cd_3Se_3-Na QDs) to 1.2 eV ($Cd_{33}Se_{33}$-Na QDs), and larger Na-capped Cd_nSe_n QDs should have even smaller E_{gap}, resulting in the appearance of broad band emission in near-infrared range (**Figure 3.16 (d)**). Due to the large surface to volume ratio, the CdSe QDs formed in the glass can be further capped with additional Na atoms, other than the single Na atom, which further lead to the wider variation in E_{gap} of Na-capped Cd_nSe_n QDs and broader emission band (**Figure 3.16 (d)**). The variation in E_{gap} for different number of Na atoms capped by $Cd_{33}Se_{33}$ clusters has been proved in our previous calculations (**Figure 3.10**).

3.4 Summary & Conclusions

In summary, I have modeled Cd_nSe_n QDs capped by non-bridging oxygens and glass modifiers to computationally model the interactions between glass matrices and small QDs. The DFT calculations demonstrate that the introduction of ions contributes to significant surface reconstruction and redistribution of HOMO and LUMO orbitals, thus substantially altering the electronic structure of pristine Cd_nSe_n clusters.

Importantly, once Cd_nSe_n QDs are capped by Na ions, defect states are created deep inside the band gap, from which near infrared emission (NIR) is predicted and actually observed in experimental measurements. However, the number of Na ions that can be introduced to the surface of CdSe clusters is limited. As for alkaline-earth metal ions ligated to Cd_nSe_n QDs, Ca ions result in considerable electronic structure distortion, replacing Cd, providing insights into the core-shell structure formed by these elements. Meanwhile, Se and O atoms exhibited a similar impact on the surface reconstruction and electronic structure of Cd_nSe_n clusters by entering six-membered rings and decreasing the E_{gap}. It should be highlighted here, these results reveal that defects states shift with the size of the QDs, providing new understanding of the mechanism of the size-dependent Stokes shift. However, the clusters are small, therefore minimizing the relationship between QD size and Stokes shift.

The experimental studies for defect and size effects on Cd_nSe_n QDs in glass matrices are also presented here. Red shifts in the first optical absorption peak with heat treatment indicate how QDs grow into the magic-sized region, with optical emission in the UV-Vis region matching the predictions of defects influencing E_{gap}. From simulations, emission at longer wavelengths approaching the near infrared (i.e. narrower E_{gap}) can be associated with Na ion defects.

However, the calculation of Mayer bond order and the geometry optimization often give controversial results of the bonding between sodium and selenium atoms, while the former one indicated antibonding between those atoms. It reflects that the bonding of CdSe clusters capped by multiple type of atoms is complicated and one is supposed to be cautious to decide the bonding, with more criteria should be taken into account. It is apparent that the structural reconstruction is smaller when the cations and anions are introduced to the surface of CdSe clusters simultaneously compared to CdSe clusters capped only by one atoms.

Meanwhile, at the initial configuration, the CdSe clusters were capped by neutral atoms rather than cations or anions. Although the charge transfer is observed between adatoms and CdSe clusters at the final configuration, the cation or anion is supposed to be introduced to the surface of CdSe clusters directly for the initial configuration to see the impact of charges. Moreover, these models in this chapter is rather simplified and idealistic in terms of realistic chemical environment, more complicated interfacial

environment should be developed to model the real interfacial structure of CdSe quantum dots-doped glasses.

Chapter 4

4 Local atomic structure of a Na_2O-$2SiO_2$ glass

4.1 Introduction

In the last chapter, I used a rather simplified model to simulate the CdSe clusters in a glass matrix, far from the realistic description of their chemical environment. For one thing, there is little possibility of CdSe clusters being capped by only several atoms in glass matrix considering the sufficient supply of glass network modifiers, non-bridging oxygen atoms in glass matrix and the high ratio of active 2-coordinated surface Cd or Se atoms. For another thing, the electrical neutrality of CdSe clusters can be destroyed when they are capped by one glass network modifier atom or non-bridging oxygen atom, thus it tends to interact with other atoms in the glass matrix in order to maintain the electrical neutrality. Therefore, the real local atomic structure of the CdSe quantum dots doped glass is supposed to be more complex than the model I built and studied in last chapter.

The best approach to mimic the interfacial environment of CdSe QD in glass matrix is to introduce the QD in a glass matrix model, describing the QD/glass interface explicitly. Although there are various studies of the computer simulation of glass and QD separately, to the best of my knowledge, no literature has been reported to probe this hybrid system modelled explicitly. It is technically challenging to generate these hybrid structures through classical MD simulations especially considering the scare availability of adequate pair potentials for a system simultaneously containing all the elements (O, Si, Na, Cd, and Se). Moreover, the methodology to incorporate the CdSe QD into glass matrix is hard to develop. The great difference between the geometry of the CdSe cluster and the glass matrix makes it hard to relax the interface between them. As I presented in chapter 1, the CdSe QDs are prepared in the glass matrix by a nucleation and subsequent crystal growth stage, the time scale of which is far beyond the current capabilities of computational simulation. Therefore, I did not intend to simulate the thermal process in the melt-quenching and heat-treatment procedure of

preparing the CdSe quantum dots doped glasses.

In this thesis, I made the approximation that it would be a good starting configuration for the classical MD and *ab initio* MD simulations by directly introducing CdSe QD into the preformed glass matrix. As a result, the glass matrix configurations are supposed to be generated before the CdSe QD being incorporated. According to the continuous random network model proposed by Zachariasen,[178] silicon atoms in silicate glasses are mostly coordinated with 4 oxygen atoms, forming the $[SiO_4]^{4-}$ tetrahedra, which are connected by an oxygen atom (bridging oxygen) at the corner. This connection method forms a polymerized network, and the random distribution of inter-tetrahedral angles in the glass network leads to the disorder at the long-range. Thus, the silicate glasses are amorphous solids that exhibit short-range order and long-range disorder, making the simulation of glasses not easy due to the large time scale needed compared with modelling crystalline.

From the experimental part, glasses can be prepared by melting the glass components at high temperature and quenching it quickly. Therefore, molecular dynamics can mimic the thermal process happened on glass, to generate the local atomic structure of glasses.

In this chapter, I investigated various methods of generating the sodium silicate glass matrix in order to find an appropriate methodology with high quality and accuracy. By comparing the radial distribution functions (RDF), the mean squared displacements (MSDs) of the simulation results with the experimental data, an appropriate method was chose to generate the initial glass matrix structures for the introduction of CdSe QD in the following chapters.

4.2 Classical molecular dynamics

4.2.1 Initial methodology to generate glass matrix

The starting configuration for the glass matrix was generated by placing atoms randomly in a cubic simulation box using Packmol code (**Figure 4.1**).[179-180] The total number of atoms for the glass was 300 (66 Na, 67 Si, and 167 O), with the simulation cell sizes ($a = b = c = 15.93$ Å, $\alpha = \beta = \gamma = 90°$), giving the density consistent with

experimental values ($\rho = 2.492$ g/cm^3).[97] From the experimental part, this Na_2O/SiO_2 ratio is commonly adapted in fabricating the CdSe QDs doped glasses. Besides, it is also an enormous studied system in computer simulation of glasses, providing sufficient data to validate the accuracy of my modelling. Hard constraints were imposed to avoid unphysically small interatomic distances. In this initial stage, an initial classical molecular dynamics simulation was performed using 12-6 Lennard Jones potential in DL_POLY code.[134] The expression and parameters of the potential are in chapter 2 (2.3.3). The Coulomb interactions were calculated using the Ewald summation method with a precision of 10^{-5} eV.[145] The velocity Verlet algorithm was applied for the integration of the equations of motion with a timestep of 1 fs.[141]

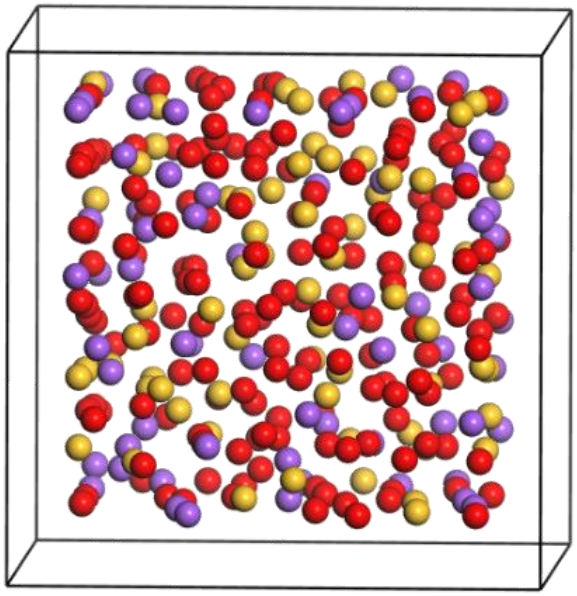

Figure 4.1 Initial structure of the classical molecular dynamics simulation. The red, yellow, and purple balls represent O atoms, Si atoms and Na atoms respectively.

The glass structures were generated using an *in silico* melt-quenching approach, in *NPT* ensemble using a Nosé–Hoover thermostat and barostat with relaxation times of 0.1 ps and 0.5 ps respectively.[142, 181] The initial structure was heated up gradually in steps of 100 K with a 60 ps MD run at each temperature from 300 K to 4000K with a timestep of 1 fs. After equilibration of the liquid at 4000 K during 600 ps, the system was cooled gradually in steps of 50 K with a 60 ps MD run at each temperature from 4000 K to

300 K. A further 200 ps NPT simulation was carried out at 300 K, together with a 200 ps NVE simulation in order to equilibrate the structure. The data was collected from the final 40 ps during the equilibration. It is should be noted here that a 2 ps equilibration stage was set in the initial stage of 60 ps run at each temperature in the quenching procedure. The whole procedure was illustrated in **Figure 4.2**.

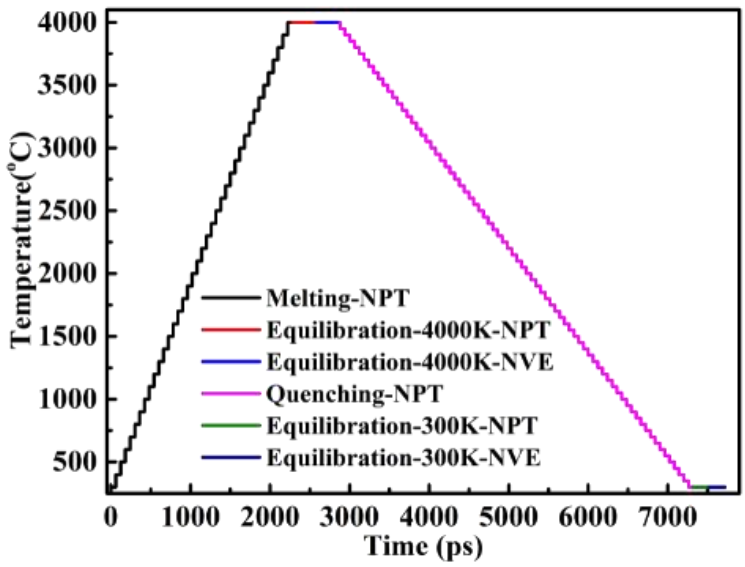

Figure 4.2 Temperature profile during the stepwise melt-quenching approach followed to generate a Na_2O-$2SiO_2$ glass structure of 300 atoms, with molecular dynamics simulations.

4.2.2 Results and discussion

The final cell size was 14.495 Å with the density of 2.708 g/cm^3, much higher than the experimental value of Na_2O-$2SiO_2$ glasses (2.492 g/cm^3). The final configurations have been extracted from the trajectories of different temperature, as illustrated in **Figure 4.3**. In the initial configuration (**Figure 4.3 (a)**) before conducting MD simulations, almost all Si atoms did not interact with O atoms due to the random distribution. However, in the highest temperature at 4000K after equilibration in NVE ensemble (**Figure 4.3 (e)**), the percentages of the $[SiO_4]^{4-}$ tetrahedra was very high, which was not in a liquid-like states that atoms were randomly distributed. The tendency of the formation of $[SiO_4]^{4-}$ tetrahedra was not similar to the experimental finding, which was

supposed to increase at low temperature during quenching process (**Figure 4.3 (f)-(h)**). Besides, the radial distribution functions for the Si-O pairs, Na-O pairs, and the whole system were calculated based on the configurations from the final production run at 300K within the NVE ensemble (**Figure 4.4**).

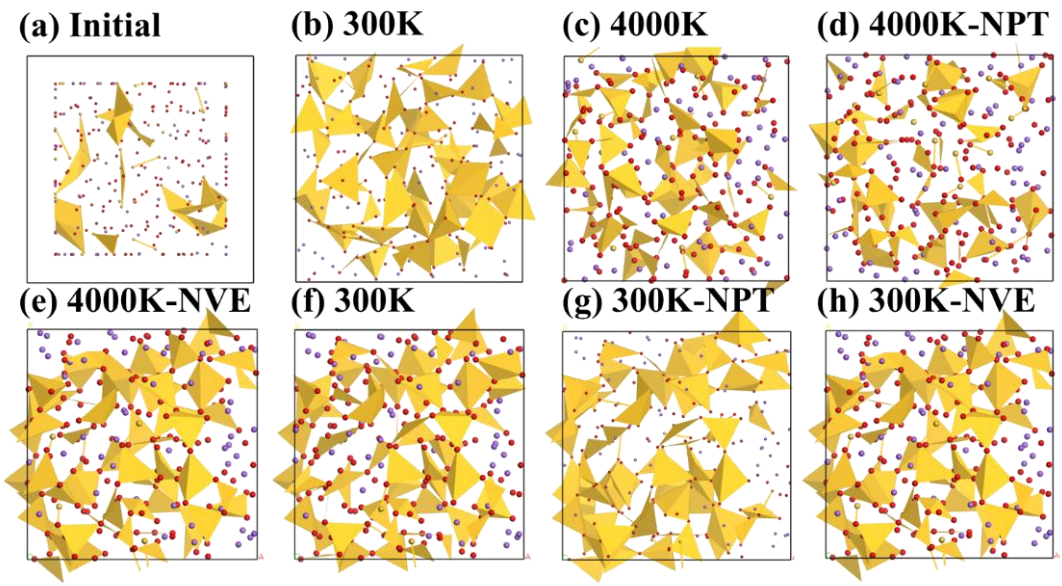

Figure 4.3 (a) The initial configuration of Na_2O-$2SiO_2$ glasses, (b) 300 K at melting stage, (c) 4000 K at melting stage, (d) 4000K at the end of NPT equilibration stage, (e) 4000K at the end of NVE equilibration stage, (f) 300K at quenching stage, (g) 300K at the end of NPT equilibration stage, and (h) 300K at the end of NVE equilibration stage. The yellow parts represent the $[SiO_4]^{4-}$ tetrahedra. The yellow, red and purple atoms represent Si, O, and Na atoms respectively.

Si atoms are the main glass formers in the continuous random network of the silicate glasses. The calculated value of the first-neighbor peak was 1.875 Å and 2.475 Å for Si-O and Na-O pairs respectively, however, the experimental values are 1.64 Å and 2.36 Å respectively.[96, 98] These results demonstrated that the interactions in computational simulation between these pairs were much weaker than the real interactions. The parameters of the 12-6 potential were derived from the alkali borosilicate glasses. [182-183] In their work,[183] the height and position of the Si-O pairs was in very good agreement with the neutron diffraction results. However, the poor

reproducibility of results in this thesis may be attributed to the different system studied, which does not contain boron atoms.

Therefore, the inconsistency in the tendency of the formation of $[SiO_4]^{4-}$ tetrahedra and the first-neighbor peak value of the RDF both indicated that the classical molecular dynamics run failed to mimic the experimental fabricated glasses.

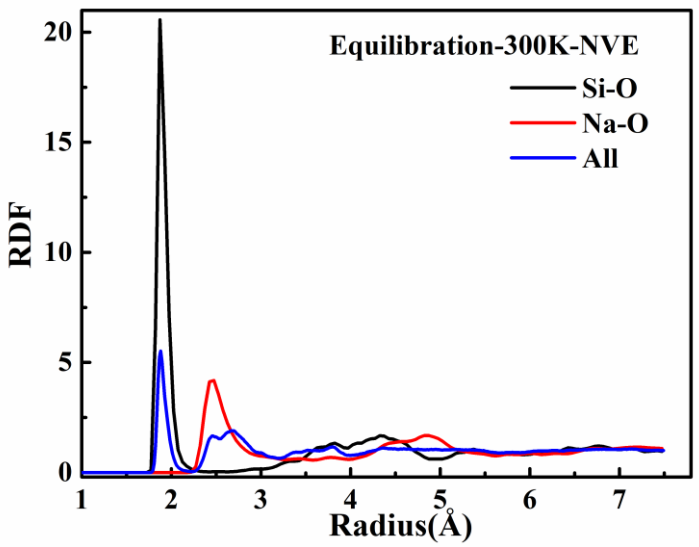

Figure 4.4 Radial distribution functions of Si-O pairs (Black line), Na-O pairs (Red line), and the whole system (Blue line), averaged over the 200ps equilibration run at 300K in NVE ensemble.

However, the analysis of the mean squared displacement over time showed a similar tendency with the experimental findings. **Figure 4.5** shows the average MSDs calculated for the whole system, Si^{4+}, O^{2-}, and Na^{+} at different temperatures. The plots of mean squared displacement can clearly show diffusive behavior of the ions. It is well known that the plots of MSDs for all ions feature plateaus independent of time for a poor conductor while they exhibit a monotonic increase with time for a good conductor. It was obvious that the MSDs increased linearly with time during the melting process, indicating a fast Na transport (**Figure 4.5 (a) and (b)**). The non-linear portion of the MSDs plot, corresponding to the initial ballistic regime. Meanwhile, with the decrease of temperature and the formation of glass matrix during the quenching process (**Figure 4.5 (c)**), the MSDs of Na ions dropped sharply (~ 0.55 $Å^2$) compared with that of 4000 K (maximum at 350 $Å^2$). The diffusion of Na ions in general increases with temperature.

Lei, Jee, and Huang demonstrated[93] that the favorable pathway for Na^+ transport in amorphous $Na_2Si_2O_5$ was along the two-dimensional channels formed by the SiO_4 tetrahedra layers, which was attributed to the disruption of Na-O coulombic attraction by the long-range disorder, resulting in the enhanced Na^+ conduction compared with crystalline $Na_2Si_2O_5$. In contrast, the MSDs of O^{2-} and Si^{4+} were almost parallel to the time axis, demonstrating immobile O^{2-} and Si^{4+}.

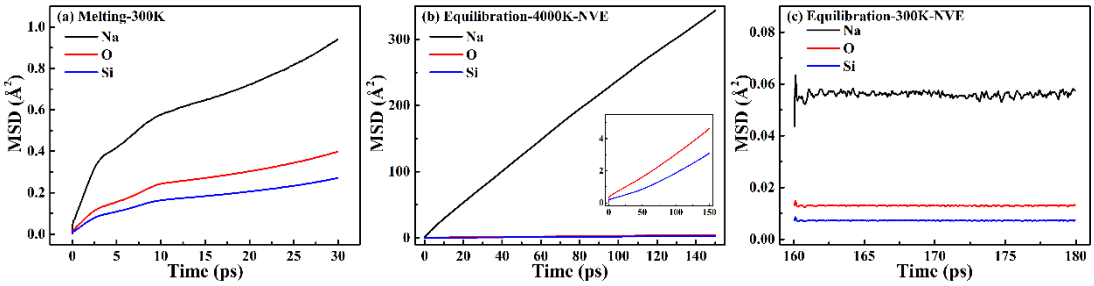

Figure 4.5 The average mean squared displacement (MSD) for Na, O, and Si ions, simulated in (a) 300K at melting stages, (b) 4000K at equilibration NVE stages, and (c) 300K at equilibration NVE stages.

Although the MSDs calculations showed consistency with previous research, the great difference between the RDF calculations in my thesis and experimental findings indicates the poor performance of the classical MD methodology I applied to generate the glass matrix. Thus, the methodology was necessary to be adjusted to increase its accuracy and quality. Several factors has been considered: (a) cutoff radius, (b) ensemble, (c) temperature, (d) force field. Several classical MD runs have been conducted to probe the reasons for the inaccuracy of our computational simulations. I will present those studies in the following.

4.2.3 Adjustment of the parameters

Firstly, as I mentioned in chapter 2 (2.3.5), the cutoff radius for the short-range interaction is predominant in the quality and accuracy of computational simulations as well as their computational cost. The cutoff radius is supposed to be smaller than the half of the simulation cell. Hence, in my tests, three cutoff radiuses have been set

ranging from 6 Å, 7.5 Å, to 7.9 Å. The initial configuration was illustrated in **Figure 4.6**, which was the final configuration of the previous classical MD run at 3900 K within NPT ensemble for 60 ps. The initial configurations were melted at 4000K with NVT or NPT ensemble for 60 ps to investigate the impact of the cutoff radius and simulation ensemble.

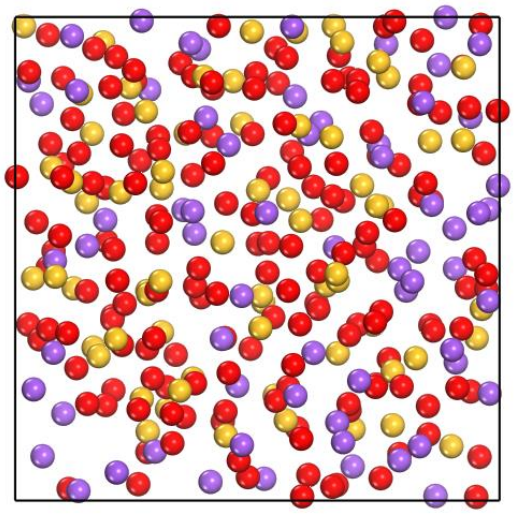

Figure 4.6 Final configuration of previous classical MD simulations at 3900 K within NPT ensemble during the melting stage. The yellow, red and purple atoms represent Si, O, and Na atoms respectively.

Based on the analysis of RDF of various cutoff radiuses (**Figure 4.7**), it was apparently that the cutoff radius had little impact on the final results. Although with different cutoff radius, the first-neighbor peaks were still at 1.875 Å and 2.475 Å for Si-O (**Figure 4.7 (a)**) and Na-O contacts (**Figure 4.7 (b)**).

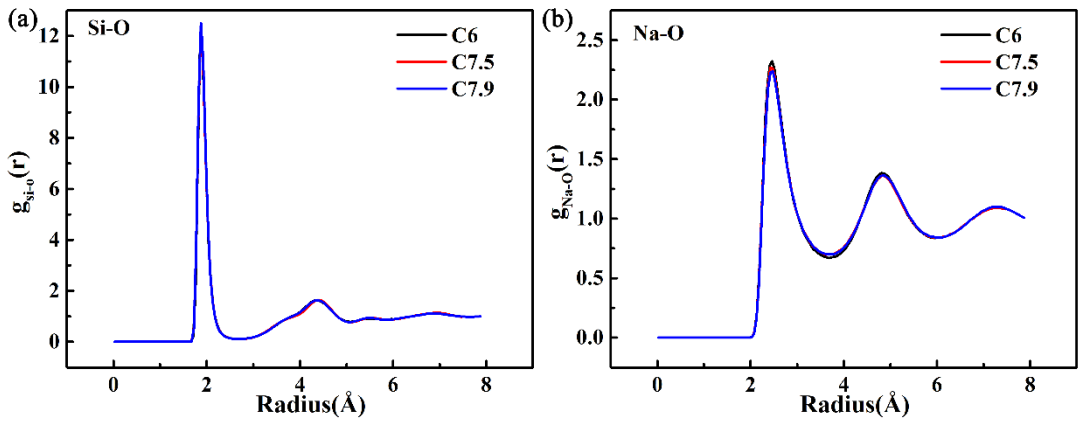

Figure 4.7 Radial distribution functions for Si-O (a) and Na-O (b) pairs averaged over the 60 ps run at 4000K within NPT ensemble. C6, C7.5, and C7.9 represents the cutoff radius of 6 Å, 7.5 Å, and 7.9 Å respectively.

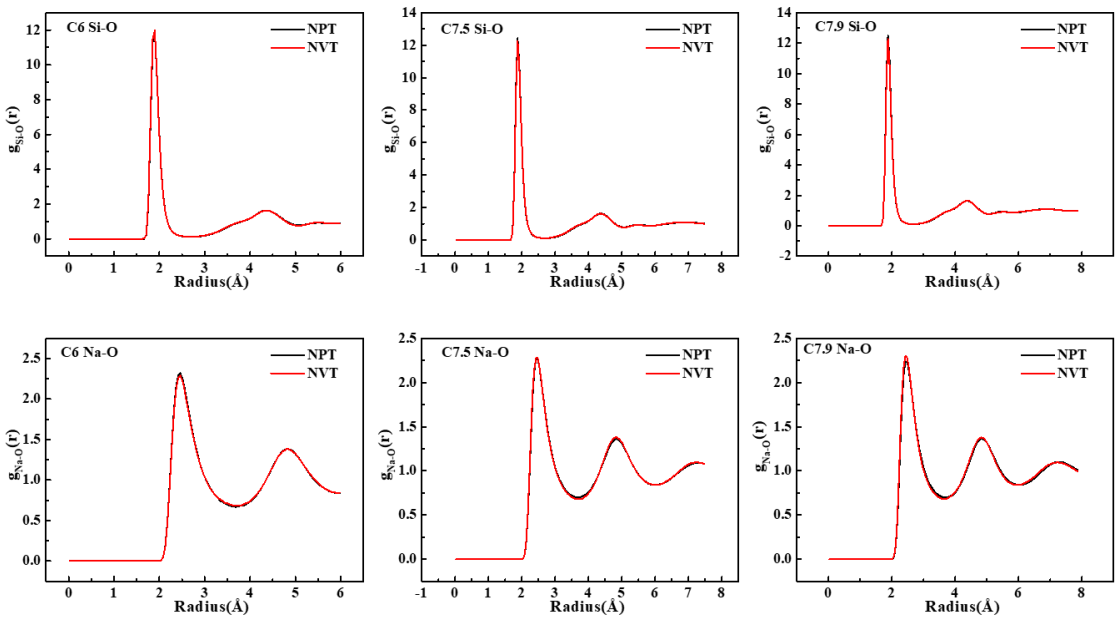

Figure 4.8 Radial distribution functions for Si-O pairs and Na-O pairs averaged over the 60 ps run at 4000K within NPT ensemble (Black lines) or NVT ensemble (Red lines). C6, C7.5, and C7.9 represents the cutoff radius of 6 Å, 7.5 Å, and 7.9 Å respectively.

Besides, the ensembles were also proved to have little impact on the RDF of these structures, with similar curves in NVT and NPT ensemble (**Figure 4.8**). Similarly,

although there were some fluctuations, little differences can be observed in the MSDs curves for different cutoff radiuses both within the NPT (**Figure 4.9**) and NVT ensemble (**Figure 4.10**). Moreover, ensembles were also less likely to influence the transportation behavior of those ions. For instance, the highest value for Na ions within NPT ensemble was ~ 70 $Å^2$while the counterpart within NVT ensemble was ~80 $Å^2$.

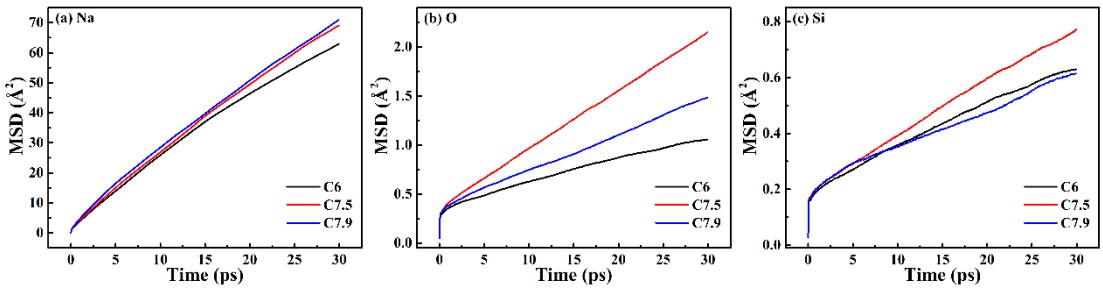

Figure 4.9 Mean squared displacements for the Na^+, O^{2-}, and Si^{4+} in Na_2O-$2SiO_2$ system averaged over the 60 ps run at 4000K within NPT ensemble.

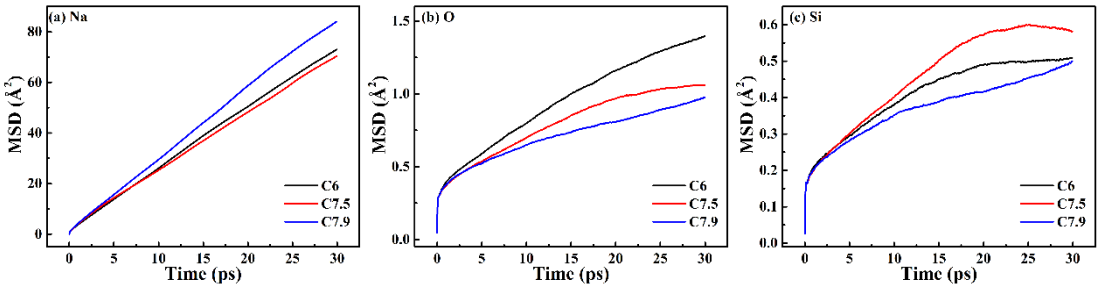

Figure 4.10 Mean squared displacements for the Na^+, O^{2-}, and Si^{4+-} in Na_2O-$2SiO_2$ system averaged over the 60 ps run at 4000K within NVT ensemble.

Another factor- temperature was also taken into consideration, the final configuration of the previous classical MD run at 4000 K within NPT ensemble for 60 ps (**Figure 4.3 (c)**) was taken as the initial configuration (**Figure 4.11 (a)**) for the further MD run at 4000 K or at 1000K within NPT ensemble for 200 ps. The final structure was shown in **Figure 4.11 (b)** and **Figure 4.11 (c)**. By comparing the initial configuration and the final configuration of temperature at 4000K, the structure was the same, indicating that the 60 ps was enough for the system to achieve the equilibration. Although, the final structure with temperature at 1000K was a little different from the initial structure, only a slight difference was observed in terms of the RDF (**Figure 4.12 (a)**). The first-

neighbor peak at 4000 K was broader than 1000 K, due to thermal agitation of the liquid-like states. As it was expected, the lower the temperature, the slower the transport for ions in systems based on the MSDs analysis for structure at 4000 K (**Figure 4.12 (b)**) and 1000 K (**Figure 4.12 (c)**).

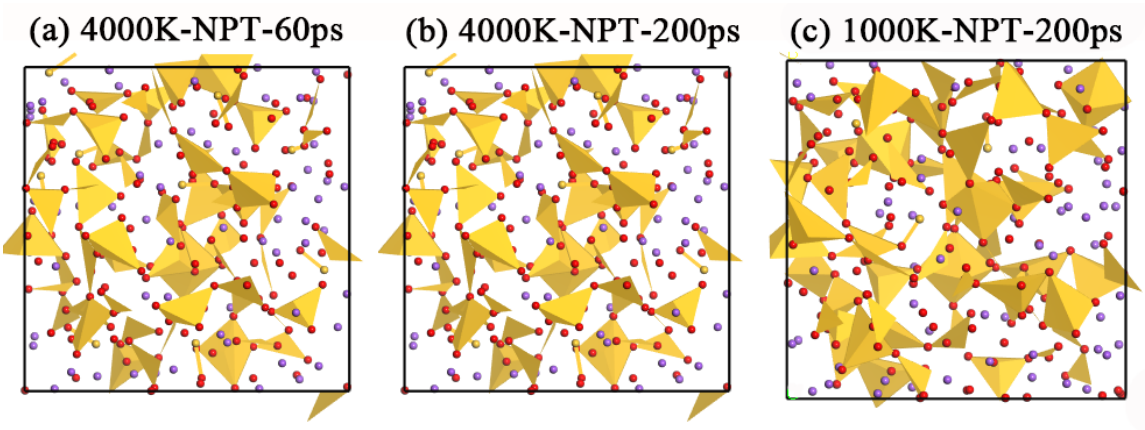

Figure 4.11 (a) is the final configuration of previous classical MD run at 4000K within NPT ensemble for 60 ps. (a) is the initial configuration of the subsequent classical MD run at 4000K and at 1000K within NPT ensemble for 200 ps, which final configuration was (b) and (c) respectively.

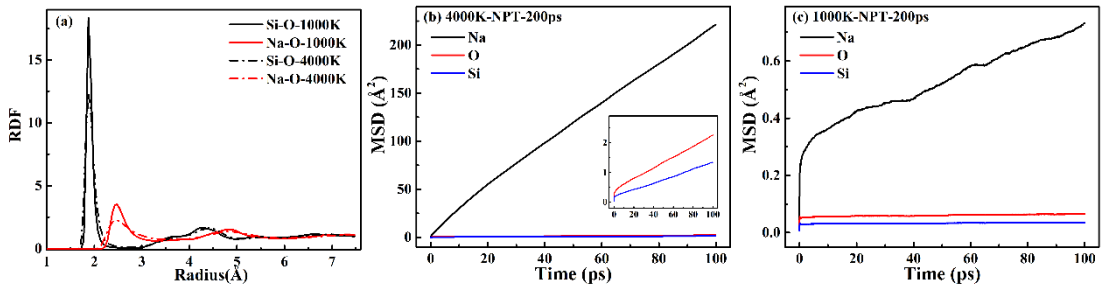

Figure 4.12 (a) Radial distribution functions for Si-O (black lines) and Na-O (red lines) pairs for MD runs at 1000 K (solid lines) and 4000 K (dashed lines), (b) and (c) MSDs for temperature at 4000 K and 1000 K respectively.

Overall, I have taken the cutoff radius, ensemble, and temperature into account in order to find the factors contributed to the failure of describing the interatomic distance of Si-O and Na-O pairs. However, the results indicated little connection between them. Hence, the pair potential was taken into consideration to enhance the quality and

accuracy of the computational simulation and a new method has been developed.

4.2.4 New methodology to generate glass matrix

Pedone et al[91] developed a pair potential based on a rigid ionic potential using partial charges to handle the partial covalency of silicate systems, which transferability and reliability have been proven by comparing the structural and mechanical properties of a wide range of silicate glasses with experimental data. Moreover, it includes a repulsive term compared to 12-6 potential. I used this potential instead of 12-6 potential to describe the force acting on the atoms. Besides, in my previous study, the final density changed a lot in classical MD runs with NPT ensemble compared with initial structure, resulting in big differences between the densities of calculated structure and experimental values. Thus, the NVT ensemble was applied to the MD simulation with a higher melting temperature at 6000 K.

The initial structure (**Figure 4.1**) was heated up gradually in steps of 1000 K with a 60 ps MD run at each temperature from 300 K to 6000 K. After equilibration of the liquid at 6000 K during 400 ps, the system was cooled gradually in steps of 500 K with a 60 ps MD run at each temperature from 6000 K to 300 K. A further 200 ps NVT simulation was carried out at 300 K, together with a 200 ps NVE simulation in order to equilibrate the structure.

4.2.5 Results and discussion

Figure 4.13 illustrates the atomic structure of the final configuration obtained from the molecular dynamics run. All the silicon atoms were found to form $[SiO_4]^{4-}$ tetrahedra by calculating their coordination using the R.I.N.G.S. code. A nearly perfect Si-O network was formed in our calculation.

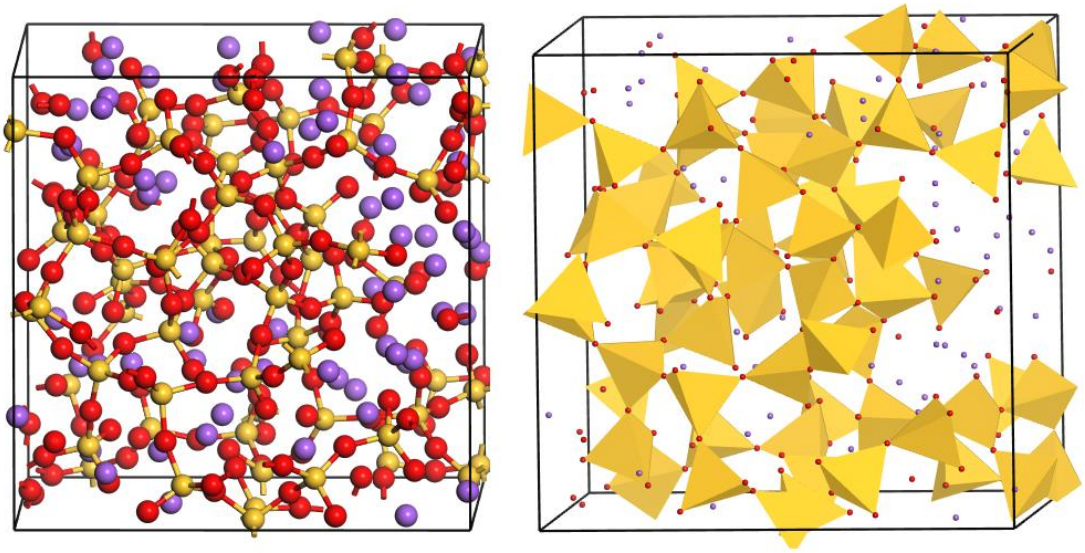

Figure 4.13 Final structure of the classical MD simulations. The left graph is in the ball-stick view while the right graph is in the polyhedron view, where the yellow parts represent the $[SiO_4]^{4-}$ tetrahedra.

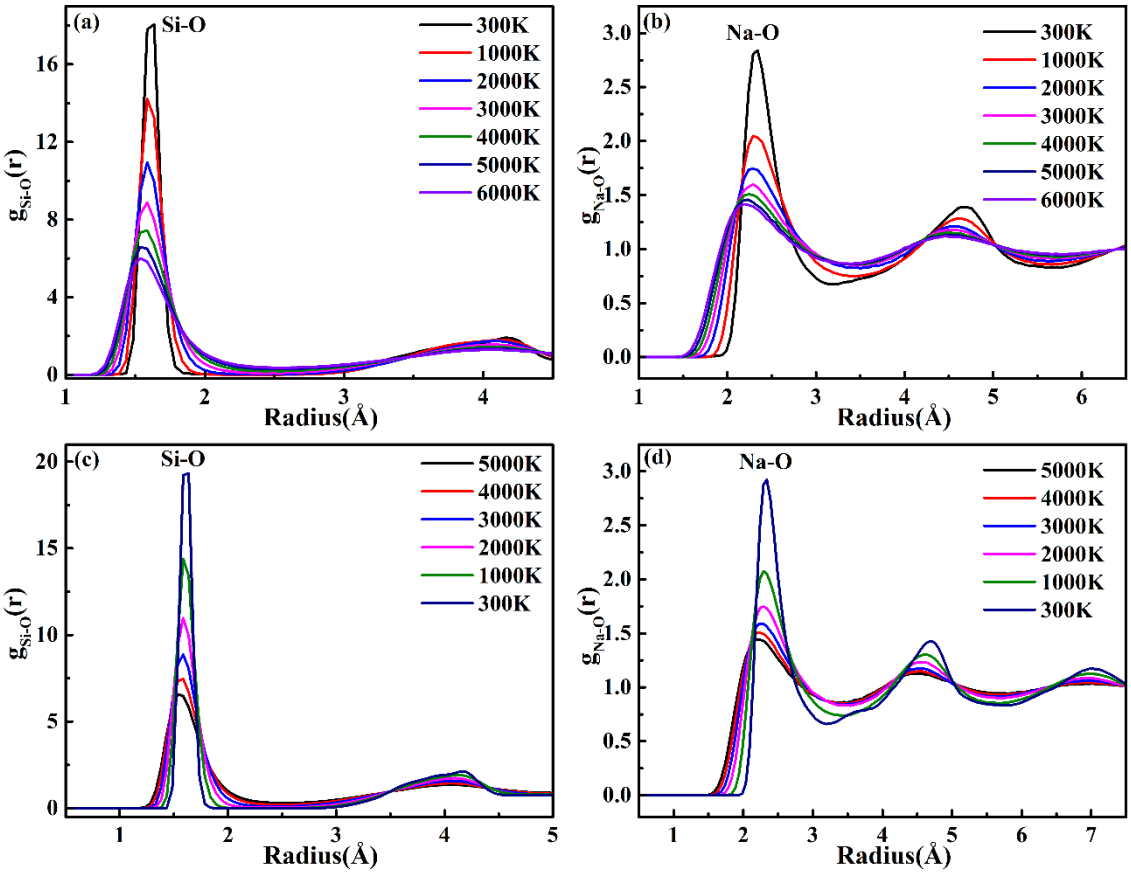

Figure 4.14 Radial distribution functions of Si-O pairs in melting process (a) and quenching process (c), and Na-O pairs in melting process (b) and quenching process (d).

Furthermore, the radial distribution functions were analyzed based on the final structure at each temperature. **Figure 4.14 (a)** and **(c)** show the RDF of Si-O contacts during the melting process and quenching process, respectively. When the glass was quenched to 300 K, the interatomic distance was found to be 1.64 Å (**Figure 4.14 (a)**), the same as the previous research.[96] The accuracy of this potential was also confirmed by the first-neighbor peak value for Na-O pairs at 2.34 Å (**Figure 4.14 (d)**), which was close to the previous research.[96]

Interestingly, as the temperature increased, the interatomic distance of Si-O contacts and Na-O contacts both exhibited broader distribution and lower peak height. Similar temperature-dependencies of the interatomic distances have been found both in the melting process and quenching process. When the structure was heated at high temperature, the system was more likely to be at a liquid-like state, resulting in the disorder of the structure, thus contributing to the broader first-neighbor peak in the RDFs.

Moreover, the bond angle distribution was also employed to test the accuracy of my results, providing further information about the local atomic structure of the first coordination shell of each atomic species in the glass matrix. The Si-O-Si bond angle distribution is shown in **Figure 4.15 (a)**. Although the peak fluctuated because only the final structure was calculated, the center of the peak was located at 148°. In pure amorphous SiO_2 glasses, this angle is supposed to be 150°,[184] and it is found that the addition of sodium ions into pure SiO_2 glasses deceases this value, consistent with our calculations. The value of Si-O-Si bond angle indicated the connection method between the $[SiO_4]^{4-}$ tetrahedra within the glass network. In this work, all the $[SiO_4]^{4-}$ tetrahedra were observed to share corners.

Figure 4.12 (b) presented the bond angle distribution of the O-Si-O for the final structure, with the center of the peak being at 106°. In a perfect tetrahedron, the value of this angle is supposed to the 109.5°, which is in good agreement with my results.

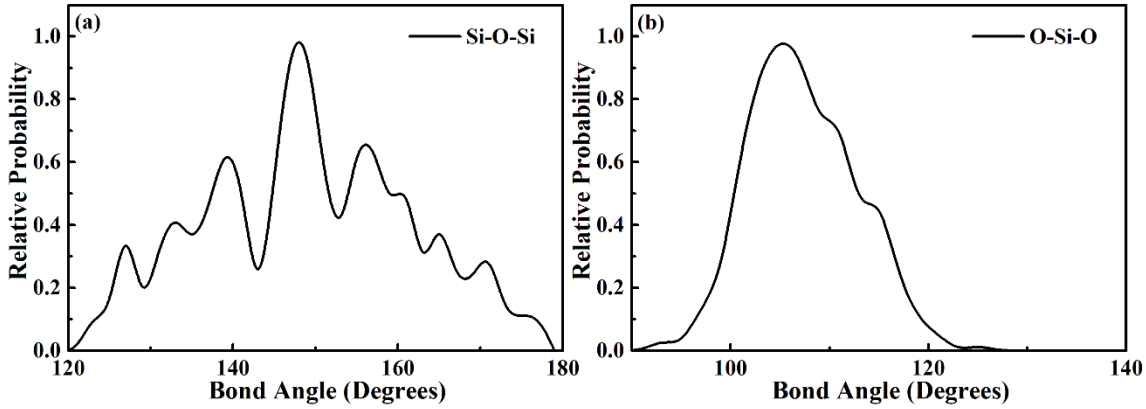

Figure 4.15 (a) Silico-oxygen-silicon bond angle distributions for the final structure of the MD runs, (b) Oxygen-silicon-oxygen bond angle distributions for the final structure of the MD runs.

Furthermore, I compared the MSDs of structure obtained from this simulation using the potential developed by Pedone et al. (**Figure 4.16 (a)**) and previous simulations using the 12-6 potential (**Figure 4.16 (b)**). Both configurations were heated at 4000 K for 60 ps within NVT ensemble. These potentials demonstrated the same tendency of diffusions of Na, O, and Si ions. However, the highest values of the MSDs described by the new methodology were an order of magnitude higher than previous simulations. For example, for Na ions, the highest MSD of this method was ~ 600 $Å^2$ while that of the former method was ~ 70 $Å^2$. Unlike the limited effect of cutoff radius, ensemble and temperature in my tests, we can conclude that force field indeed impact the calculations of MSDs.

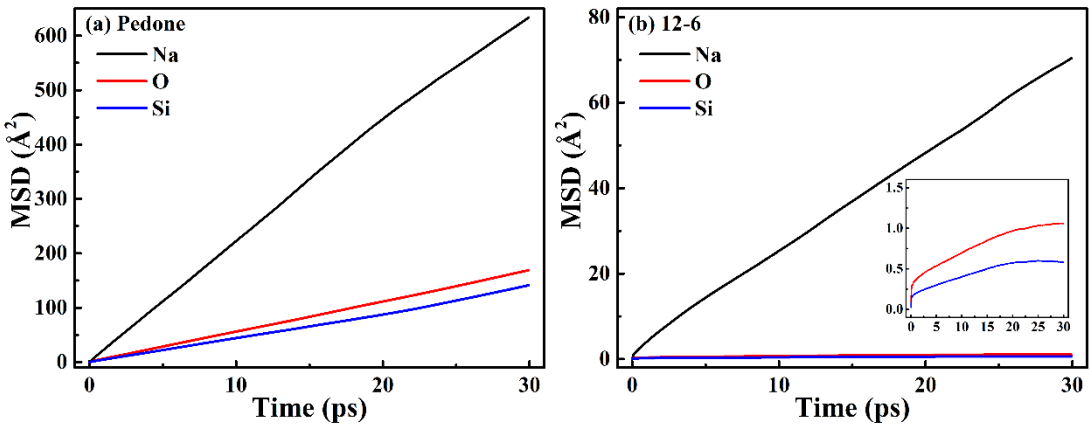

Figure 4.16 Mean squared displacements for the Na^{+}, O^{2-}, and Si^{4+} in Na_2O-$2SiO_2$ system averaged over the 60 ps run at 4000 K within NVT ensemble using potential developed by (a) Pedone et al. and (b)12-6 potential respectively.

In all, both the value of the first-neighbor peak of the Si-O and Na-O contacts, the Si-O-Si and O-Si-O bond angle distribution showed excellent similarity to the experimental findings, demonstrating the formation of amorphous glass structure through my computational simulations. The force field used in the new methodology was capable of reproducing the glass structure with high accuracy.

4.3 Summary & Conclusions

In this chapter, I have developed and tested the methodology of running classical molecular dynamics simulation to generate the local atomic structure of a glass matrix with composition of Na_2O-$2SiO_2$.

In the initial methodology, a 12-6 Lennard - Jones potential with formal charges was employed, exhibiting poor performance in describing the interatomic distance between Si-O and Na-O pairs and calculating the density. In order to enhance the accuracy and quality of computational simulations, the impact of cutoff radius, ensemble, temperature and pairwise potential was investigated by changing corresponding parameters in several classical MD runs.

However, the cutoff radius and ensemble were found to have little impact on the first-neighbor peak of the Si-O and Na-O contacts as well as the mean squared displacements of those ions in glass matrix. The higher the temperature, the broader the peak, which was attributed to the liquid-like states at high temperature, indicating the disorder of structure.

By replacing the 12 - 6 potential with a rigid ionic potential using partial charges developed by Pedone et al. to describe the interactions between Na-O, Si-O, and O-O pairs, nearly-perfect glass networks were formed with all the Si atoms were 4-coordinated with O atoms. This potential showed excellent consistency with the experimental finding in terms of describing the first-neighbor peak of Si-O and Na-O contacts and bond angle distribution of Si-O-Si and O-Si-O. Thus, I validated a scheme

of classical MD simulations to generate the glass matrix with high accuracy and quality. This will be used in the rest of my work to generate the glass matrix for the CdSe quantum dots doped glasses.

Chapter 5

5 Local atomic structures of CdSe quantum dot-doped glasses

5.1 Introduction

In the last chapter, I explored the methodology developed for generating the structure of a glass matrix with high quality and accuracy using classical MD calculations. In this chapter, I started from these classical MD calculations of the glass matrix, and the quantum chemical models of the quantum dots validated in chapter 3. Because the interaction between the CdSe QD and glass matrix cannot be described accurately in classical MD due to the lack of the appropriate interatomic potentials in the existing literature, I decided to use *ab initio* methods. The *ab initio* MD methodology is based on quantum mechanics at density functional theory (DFT) level, which means it does not rely on a fixed functional form for interatomic interactions, but the electronic degrees of freedom of each atom are fully modelled. To keep the computational cost reasonable, before running AIMD calculations, several classical MD simulations were conducted in order to find the appropriate quenching method and representative system size.

In this chapter, firstly, the appropriate quenching methods to relax the interface between the CdSe QD and glass matrix have been explored. Two methods have been employed to generate the CdSe quantum dot-doped glasses using classical MD, whose difference lay on the treatment of forces on CdSe quantum dot.

Secondly, taking the computational cost and the limitation of system size in AIMD into account, it is impossible to simulate a large-scale system which size is comparable to experiments. On the other hand, size-effect is an important character of quantum dots so we do not want to simulate that is not too small to be realistic. From the experimental part, the QD's size usually is bigger than the $Cd_{33}Se_{33}$ quantum dot (~ 1.3 nm). However, if I increase the size of the QD, the total number of atoms of the glass matrix will be

increased enormously considering the compositional ratio between CdSe QD and glass matrix, resulting in a system size beyond the computational power currently accessible. Thus, in order to explore this effect, the size of the glass matrix instead of the size of the QD has been changed. The maximum total number of atoms that it is possible to have in a simulation cell in classical MD is much higher than AIMD. Therefore, three simulation cells have been built to investigate whether the interfacial structure changed with the cell size, from which I knew whether the simulation cell I used to further conduct the AIMD simulation was representative of all sizes.

Based on the investigation of the impact of quenching method and system size on the final interfacial structure through classical MD simulation, I developed a combination of classical MD and AIMD methods to generate CdSe quantum dot-doped glasses. Due to limitations of computational power cost, I chose a model of the composite system with the composition of 60 Na_2O-120 SiO_2-33 CdSe (mol%) to conduct the AIMD simulations. The radial distribution functions for Si-O, Na-O, Cd-Se, Cd-O, Se-Na, Se-Se and Cd-Cd were calculated to compare with experimental data available. The coordination environment and the ring structures were analyzed. The results demonstrate that enormous structural reconstruction happens simultaneously in the QD and surrounding glass matrix, with creation of Cd-O bonds and Se-Na bonds at the interface. The incorporation of the CdSe QD disrupts Na-O bonds, while stronger SiO_4 tetrahedra are reformed. The glass matrix contributes to great structural reconstruction at the external surface of the quantum dot, making it hard to maintain the bulk structure even at its core. We will see in the next chapter that this has an impact on the electronic properties of CdSe QDs.

5.2 Development of the methodology

5.2.1 Quenching method

My goal in this thesis is to analyze the nature of the QD/glass matrix interface, and to quantify the reconstruction that takes place. As such, the initial structure is a “naïve” view of the hybrid system, and somewhat representative of the simplistic models that are sometimes used in the existing literature. In order to find an appropriate quenching

method for the generation of these models, several ways have been employed for different glass matrix sizes. The $Cd_{33}Se_{33}$ quantum dot obtained in chapter 3 was incorporated into the glass matrix. Glass matrices with composition of 33 Na_2O-67 SiO_2 (mol%) and 60 Na_2O-120 SiO_2 were generated through the methodology I developed in chapter 4, and some glass atoms were removed so interatomic distances between the QD and the glass matrix were longer than 2.5 Å, making a "hole" in the glass to incorporate the QD. The final composition was 16 Na_2O-32 SiO_2-33 CdSe (**Figure 5.1(a)**) and 39 Na_2O-78 SiO_2-33 CdSe (**Figure 5.1(b)**). The interatomic interactions in CdSe QD used a Lenard-Jones pairwise potential validated in the literature[144] and the Lorentz-Berthelot combining rules were used for interactions between CdSe QD and the glass matrix for the classical simulations.

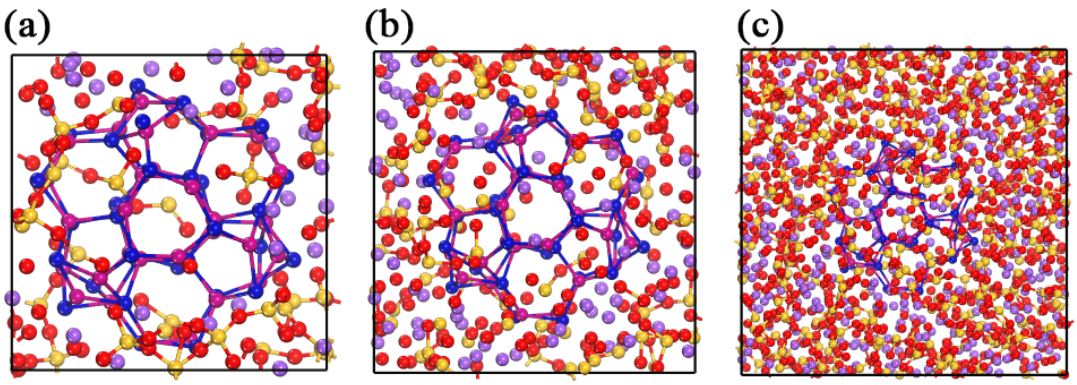

Figure 5.1 The initial configuration for the classical MD calculations. CdSe QD-doped glass compositions: (a) 16 Na_2O-32 SiO_2-33 CdSe; (b) 39 Na_2O-78 SiO_2-33 CdSe; (c) 180 Na_2O-360 SiO_2-33 CdSe. Si: yellow, O: red, Na: purple, Se: magenta, Cd: blue

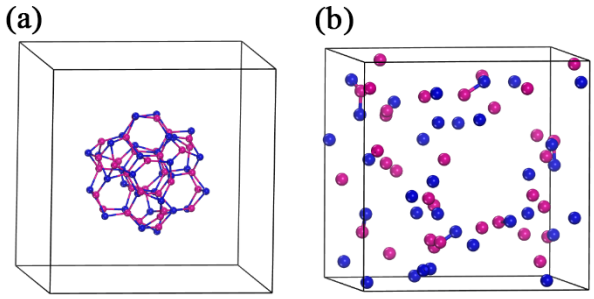

Figure 5.2 (a) The initial configuration of $Cd_{33}Se_{33}$ QD in a simulation box which size

is 2.5 nm; (b) The final configuration of the 200 ps MD run at 1300 K of NVT dynamics.

In order to find the starting quenching temperature, a classical MD simulation has been employed to find the melting point of CdSe QD. The $Cd_{33}Se_{33}$ QD was put into a simulation cell (lattice size = 2.5 nm), and then it was heated from 300 K in steps of 100 K with a 200 ps MD run at each temperature of NVT dynamics. The initial configuration is illustrated on **Figure 5.2 (a)**. The initial structure of $Cd_{33}Se_{33}$ as a well-defined QD was maintained until the temperature reaching 1300 K, at which temperature the $Cd_{33}Se_{33}$ was melted and evaporated (**Figure 5.2 (b)**).

Therefore, regarding the choice of starting quenching temperatures, the initial temperature should be chosen to be high enough to allow good reorganization of the whole system and melting the glass matrix, especially over the relatively short time scales accessible to simulation. On the other hands, it needs to be not too hot for the QD to retain its integrity. I chose 1000 K as starting temperature, which allows good mobility of the atoms in the glass. However, some preliminary classical MD simulations showed that 1000K was still a little hot for QD. Yet, simulations starting only at lower temperature would not adequately let the glass relax. Therefore, I decided to take a two-stage simulation approach, in which I first equilibrate the glass at high temperature (keeping the CdSe QD frozen not letting its atoms move), then equilibrate the whole system (glass and QD free dynamics) at intermediate temperatures. Besides, in order to make sure this treatment will not lead to unphysical properties, the quenching method without frozen QD atoms were also investigated, to be compared with the frozen method.

In the first quenching method, the whole structures were equilibrated at 1000 K, first using 200 ps of NVT dynamics and then 200 ps of NVE dynamics. The structures were then cooled gradually in steps of 50 K with a 60 ps MD run at each temperature from 1000 K to 300 K. Finally, the structures were further equilibrated at 300 K with a 200 ps NVT dynamics, and a final 200 ps NVE dynamics (**Figure 5.3 (a)** and **Figure 5.3 (b)**). In the second quenching method, the CdSe QD was frozen from 1000 K to 500 K while allowed to move from 500 K to 300 K (**Figure 5.3 (c)** and **Figure 5.3 (d)**).

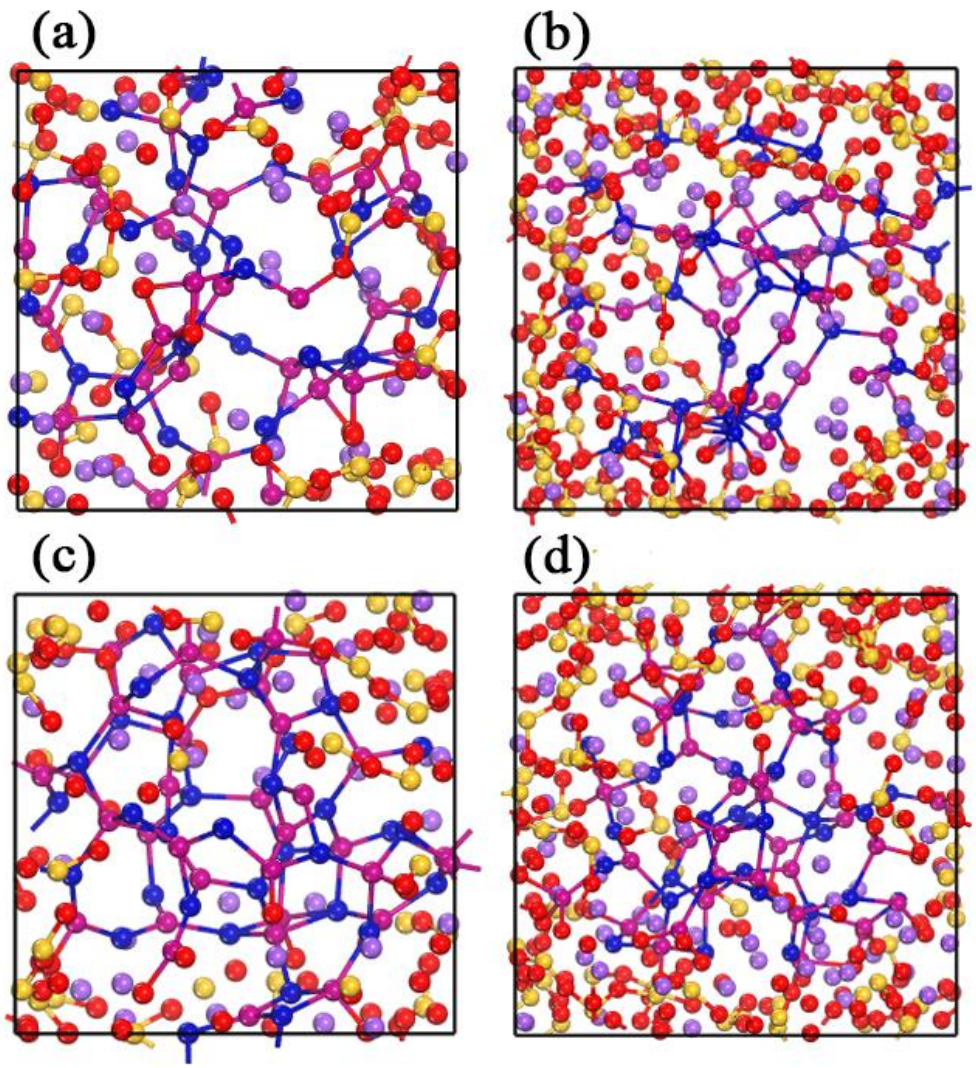

Figure 5.3 The final configuration for the classical MD calculations. The CdSe QD was allowed to move in (a) and (b) while kept frozen from 1000 K to 500K in (c) and (d).

I analyzed the radial distribution functions for the final structure with these two different quenching methods (**Figure 5.4**). Though there were slight shifts for the position of the peaks, the interatomic distances were almost keep the same in each method. The interatomic distance of Si-O, Cd-O, O-Na, Cd-Se, and Se-Na pairs was around 1.64 Å, 1.92 Å, 2.34 Å, 2.62 Å and 3.20 Å, respectively. It should be mentioned that the interatomic pair potential used to describe the interactions between the QD and glass matrix was not accurate enough in molecular dynamics. It was not explicitly

developed or validated for this hybrid system, so the interatomic distance for the Cd-O and Se-Na pairs was a little different from the experimental value.

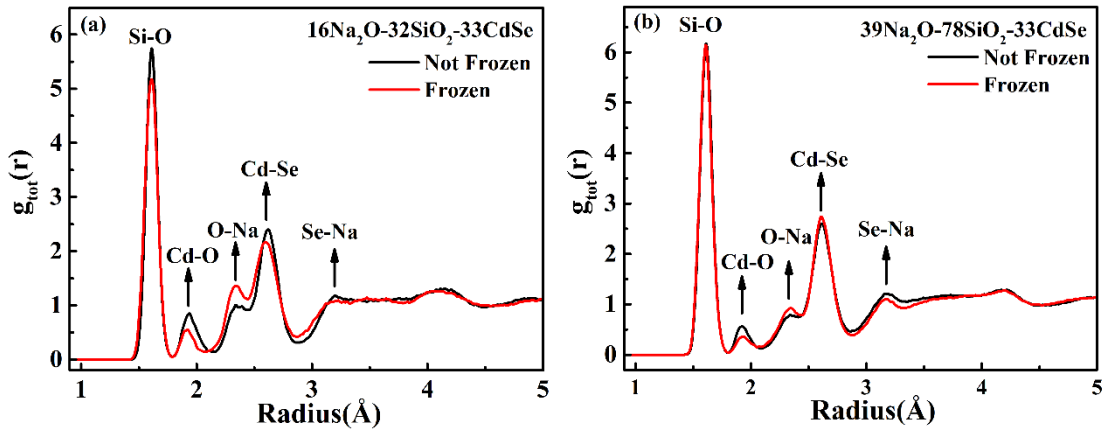

Figure 5.4 Total radial distribution functions for glass with different quenching method and glass compositions. (a) 16 Na_2O-32 SiO_2-33 CdSe; (b) 39 Na_2O-78 SiO_2-33 CdSe. The first method was referred as "Not Frozen" (Black Lines) and the second method was referred as "Frozen" (Red Lines).

Besides, the coordination environment summarized in **Table 5.1** and **Table 5.2** as well as the ring structures (**Table 5.3** and **Table 5.4**) of these systems were explored to give a deeper insight into the quantum dot/glass interface. Although there were some fluctuations, the conclusions were the same for these two methods for these two hybrid system sizes. For instance, 52.94% of O atoms were bonded to Na atoms in the initial structure, while in the MD that number was 28.14% for the "not frozen" method and 40.24% for the "frozen method" when the composition of glass was 16 Na_2O-32 SiO_2-33 CdSe (**Table 5.1**). Similarly, for the composition of 39 Na_2O-78 SiO_2-33 CdSe, 52.4% of O atoms were found to be bonded with Na atoms in the initial configuration, and this ratio decreased to 40.52% for the "not frozen" method and 43.46% for the "frozen" method (**Table 5.2**).

In contrast, there were opposite tendencies for the coordination between O atoms and Si atoms, with percentages increased from 46.61% in the initial structure to 55.41% for the "not frozen" method and 50.60% for the "frozen" method (**Table 5.1**). Thus, we can conclude that the introduction of CdSe QD breaks Na-O bonds but promote Si-O

bonding for both methods and compositions. Additionally, it was found that 16.45% O atoms for the "not frozen" method were bonded with Cd atoms and 9.16% for the "frozen" method, proving the formation of Cd-O bonds in the interface.

Furthermore, the coordination number between those pairs were also changed in final configurations compared with initial configurations. For example, Si atoms were coordinated with ~ 3 O atoms in initial structures. However, after MD runs, Si atoms were found to be almost 4-coordinated with O atoms in both methods (**Table 5.1**). Hence, it contributed to the formation of $[SiO_4]^{4-}$ tetrahedra.

Table 5.1 Average coordination number (CN) and percentages of Na, O, Si, Se and Cd with different atoms in initial configuration (16 Na_2O-32 SiO_2-33 CdSe), and averaged over the MD simulation

System		Initial Structure		Not Frozen		Frozen	
Atom	**Bond**	**CN**	**Percentage**	**CN**	**Percentage**	**CN**	**Percentage**
Na	**Na–O**	**3.66**	**86.03%**	**2.03**	**91.55%**	**3.15**	**84.87%**
	Na–Se	**0.19**	**4.41%**	**0.03**	**1.41%**	**0.09**	**2.52%**
O	**O–Na**	**1.46**	**52.94%**	**0.81**	**28.14%**	**1.26**	**40.24%**
	O–Si	**1.29**	**46.61%**	**1.60**	**55.41%**	**1.59**	**50.60%**
	O–Cd	**--**	**--**	**0.48**	**16.45%**	**0.29**	**9.16%**
Si	**Si–O**	**3.22**	**84.43%**	**4.00**	**97.71%**	**3.97**	**93.38%**
Se	**Se–Cd**	**3.30**	**87.90%**	**2.49**	**98.80%**	**2.73**	**96.77%**
	Se–Na	**0.18**	**4.84%**	**0.03**	**1.20%**	**0.09**	**3.23%**
	Se–O	**0.03**	**0.81%**	**--**	**--**	**--**	**--**
Cd	**Cd–O**	**--**	**--**	**0.15**	**31.15%**	**0.70**	**19.33%**
	Cd–Se	**3.30**	**93.16%**	**2.49**	**67.12%**	**2.73**	**75.63%**

Table 5.2 Average coordination number (CN) and percentages of Na, O, Si, Se and Cd with different atoms in initial configuration (39 Na_2O-78 SiO_2-33 CdSe), and averaged over the MD simulation

System		Initial Structure		Not Frozen		Frozen	
Atom	Bond	CN	Percentage	CN	Percentage	CN	Percentage
Na	Na–O	4.06	88.80%	3.18	89.53%	3.45	92.12%
	Na–Se	0.08	1.68%	0.06	0.72%	--	--
O	O–Na	1.63	52.40%	1.27	40.52%	1.38	43.46%
	O–Si	1.42	45.62%	1.60	50.98%	1.60	50.40%
	O–Cd	--	--	0.27	8.50%	0.20	6.14%
Si	Si–O	3.54	87.64%	4.00	92.86%	4.00	94.26%
Se	Se–Cd	3.36	82.84%	2.06	97.14%	2.33	100.00%
	Se–Na	0.18	4.48%	0.06	2.86%	0.09	--
	Se–O	0.36	8.96%	--	--	--	--
Cd	Cd–O	--	--	1.58	40.94%	1.15	30.89%
	Cd–Se	3.36	94.87%	2.06	53.54%	2.33	62.60%

Table 5.3 The number of rings with different ring size for different ring members in initial structure (16 Na_2O-32 SiO_2-33 CdSe) and averaged over molecular dynamics.

Ring Members	Ring Size	Initial Structure	Not Frozen	Frozen
Si-O	6	--	--	1
	8	2	6	8
	10	--	10	5
Na-O	4	22	2	19
	6	8	1	1
	8	1	2	9
Cd-Se	4	12	2	3
	6	67	4	8
	8	6	3	4
	10	--	3	16
	12	--	1	4
	14	--	4	1

Therefore, it can be concluded that the presence of the CdSe QD disturbed the Na-O bonds but promoted the reformation of Si-O bonds, while Cd-O bonds can be observed at the interface. It should be noted that the interatomic pair potential failed to describe the coordination between the Se atoms and Na atoms, so I cannot make a concrete conclusion about the formation of Se-Na bonds at the interface in classical MD simulations. We will study this later with AIMD.

Table 5.4 The number of rings with different ring size for different ring members in initial structure (39 Na_2O-78 SiO_2-33 CdSe) and averaged over molecular dynamics.

Ring Members	Ring Size	Initial Structure	Not Frozen	Frozen
Si-O	8	--	11	15
	10	3	6	8
	12	--	2	2
	14	1	--	--
	16	1	1	--
Na-O	4	88	42	44
	6	26	16	19
	8	16	1	
Cd-Se	4	12	2	1
	6	67	--	2
	8	6	2	6
	10	--	1	6
	12	--	--	1
	14	--	6	--

Meanwhile, the rings statistics further strengthened the conclusions I drew. For example, for the composition of 16 Na_2O- 32 SiO_2- 33 CdSe (**Table 5.3**), the number of 8-membered rings (8MR) for Si-O rings changed from 2 in the initial structure to 6 in the final structure in the "not frozen" method and 8 in the "frozen" method. Besides, 11 8-membered rings (8MR) can be found in the final structure of the "not frozen"

method while there were no 8-membered Si-O ring (8MR) in the initial structure of 39 Na_2O-78 SiO_2-33 CdSe (**Table 5.4**). Furthermore, in the "frozen" method, 15 8-membered Si-O ring (8MR) were observed. In addition, the number of 4MR in the CdSe QD was found to decrease from 12 in the initial structure to 2 in the "not frozen" method and 1 in the "frozen" method (**Table 5.4**). The presence of the glass matrix therefore contributed to a significant structural reconstruction of the CdSe QD.

In all, despite that there were some differences in the final structures derived from these two methods, similar conclusions still can be drawn. Due to the instability of the CdSe QD in the "not frozen method", we chose the "frozen" method to conduct the further MD simulation and the following AIMD simulation, which was more analogous to the experimental condition at the same time. The heat-treatment temperature for the fabrication of CdSe QDs doped glasses is higher than the glass transition temperature but lower than the crystallization temperature. Therefore, the CdSe QDs are formed in relatively low temperature but not undergo high temperature treatment compared to its melting point.

5.2.2 System size

To achieve a balance between the accuracy of the method and the computational power required, I tested these hybrid systems with different matrix size with the same QD size. The QD was introduced into three different glass matrix, and the final compositions were 16 Na_2O-32 SiO_2-33 CdSe (**Figure 5.1 (a)**), 39 Na_2O-78 SiO_2-33 CdSe (**Figure 5.2 (b)**) and 180 Na_2O-360 SiO_2-33 CdSe (**Figure 5.2 (c)**), and the corresponding cell size were 1.6 nm, 1.9 nm and 2.9 nm, respectively. The whole structures were equilibrated at 1000 K, first using 200 ps of NVT dynamics and then 200 ps of NVE dynamics. The structures were then cooled gradually in steps of 50 K with a 60 ps MD run at each temperature from 1000 K to 500 K while the CdSe QD was kept frozen. Subsequent cooling from 500 K to 300 K took place in steps of 10 K, with all atoms allowed to move. Finally, all the structures were further equilibrated at 300 K with a 200 ps NVT dynamics, and a final 200 ps NVE dynamics (**Figure 5.5**).

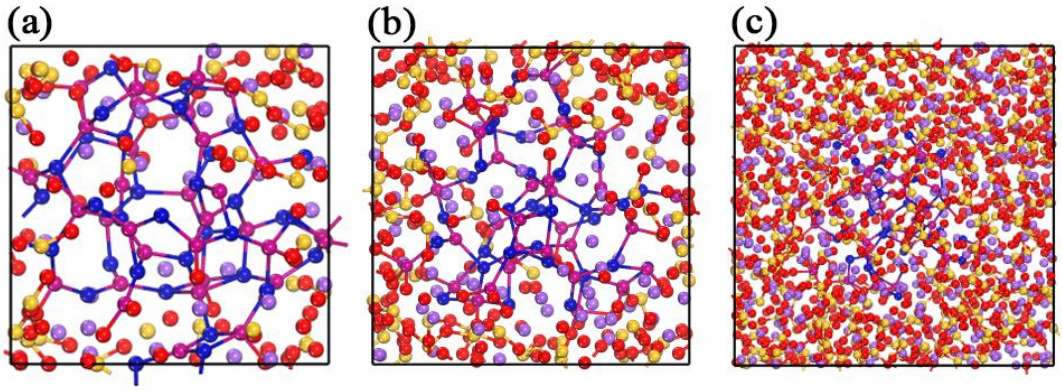

Figure 5.5 The final configuration for the classical MD calculations for (a) 16 Na_2O-32 SiO_2-33 CdSe; (b) 39 Na_2O-78 SiO_2-33 CdSe; (c) 180 Na_2O-360 SiO_2-33 CdSe. The CdSe QD was frozen from 1000 K to 500 K and allowed to move from 500K to 300K.

Table 5.5 Percentages of Na, O, Si, Se and Cd with different atoms in initial configuration, and averaged over the MD simulation.

System		$16Na_2O$-$32SiO_2$-33CdSe		$39Na_2O$-$78SiO_2$-33CdSe		$180Na_2O$-$360SiO_2$-33CdSe	
Atom	**Bond**	**Initial**	**MD**	**Initial**	**MD**	**Initial**	**MD**
Na	**Na–O**	**86.03%**	**84.87%**	**88.80%**	**92.12%**	**92.78%**	**92.78%**
	Na–Se	**4.41%**	**2.52%**	**1.68%**	**--**	**0.27%**	**0.12%**
O	**O–Na**	**52.94%**	**40.24%**	**52.40%**	**43.46%**	**54.52%**	**52.06%**
	O–Si	**46.61%**	**50.60%**	**45.62%**	**50.40%**	**44.90%**	**46.68%**
	O–Cd	**--**	**9.16%**	**--**	**6.14%**	**--**	**1.26%**
Si	**Si–O**	**84.43%**	**93.38%**	**87.64%**	**94.26%**	**91.06%**	**92.73%**
Se	**Se–Cd**	**87.90%**	**96.77%**	**82.84%**	**100.00%**	**79.29%**	**97.44%**
	Se–Na	**4.84%**	**3.23%**	**4.48%**	**--**	**3.57%**	**2.56%**
	Se–O	**0.81%**	**--**	**8.96%**	**--**	**12.86%**	**--**
Cd	**Cd–O**	**--**	**19.33%**	**--**	**30.89%**	**--**	**28.47%**
	Cd–Se	**93.16%**	**75.63%**	**94.87%**	**62.60%**	**94.87%**	**55.47%**

According to the final structures (**Figure 5.5**), most of the basic units of the CdSe QD were broken and it was hard for them to maintain the bulk structure in all system sizes. Meanwhile, the Cd-O bonds were found to be formed at the interface. We analyzed the radial distribution functions for the Si-O, Cd-O, Cd-Se, O-Na and Se-Na pairs in each system (**Figure 5.6**), and the interatomic distances were almost the same for each pair in different sizes of the hybrid system, despite minor shifts of peaks.

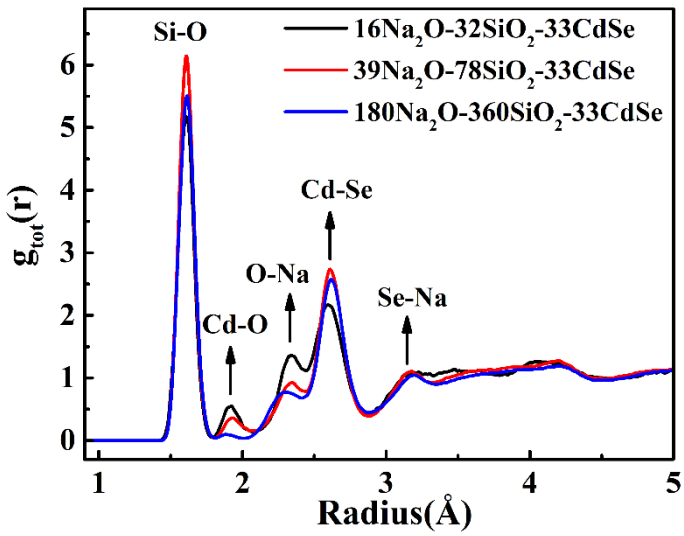

Figure 5.6 Total radial distribution functions for glass with different size of glass matrix. Black lines: 16 Na_2O-32 SiO_2-33CdSe; Red lines: 39 Na_2O-78 SiO_2-33 CdSe, Blue lines: 180 Na_2O-360 SiO_2-33 CdSe.

To give insight into the local atomic structure, the coordination environment was further explored (**Table 5.5**). According to the Table, the same tendencies are observed when compared the final configuration of the MD simulation with the initial configuration in all the glass matrices with different sizes. The percentages of O atoms bonded with Na atoms in the initial structure were 52.94%, 52.40% and 54.52% in three glass matrix sizes, respectively, decreased to 40.24%, 43.46% and 52.06% in the final structures. Meanwhile, an increase of the percentages of O atoms bonded with Si atoms in the final structure compared with the initial structure have been found, from 46.61%, 45.62%, and 44.90% to 50.60%, 50.40% and 46.68% in all the systems.

The formation of Cd-O bonds can be further confirmed by the coordination analysis, where 9.16%, 6.14% and 1.26% of O atoms were found to be bonded with Cd atoms

in the final configuration (**Table 5.5**).

The structure reconstruction of the CdSe QD also be proved by the changes of coordination between Cd atoms and Se atoms. A big decrease of the percentages of Cd atoms bonded with Se atoms can be seen in all the systems, from 93.16%, 94.87%, and 94.87% in the initial structure to 75.63%, 62.6% and 55.47% in the final structure.

Table 5.6 The number of rings with different ring size for different ring members in initial structure and averaged over molecular dynamics.

System		$16Na_2O$-$32SiO_2$-33CdSe		$39Na_2O$-$78SiO_2$-33CdSe		$180Na_2O$-$360SiO_2$-33CdSe	
Ring Members	Ring Size	Initial	MD	Initial	MD	Initial	MD
Si-O	6	--	1	--	15	--	--
	8	2	8	3	8	16	28
	10	--	5	--	2	35	42
	12	--	--	1	--	22	17
	14	--	--	1	--	2	6
Na-O	4	22	19	88	44	567	450
	6	8	1	26	19	298	247
	8	1	9	16	--	82	65
	10	--	--	--	--	25	19
	12	--	--	--	--	5	5
	14	--	--	--	--	12	--
Cd-Se	4	12	3	12	1	12	--
	6	67	8	67	2	67	9
	8	6	4	6	6	6	1
	10	--	16	--	6	--	6
	12	--	4	--	1	--	--
	14	--	1	--	--	--	--

I have also analyzed the ring statistics for each system size(**Table 5.6**). There was no 6-membered Si-O rings in the initial structure, but 1 and 15 6MR Si-O rings were observed in the final structure of the former two system size, respectively. The number of 8MR Si-O rings almost doubled in the final structure compared to the initial structure. 4-Membered and 6-Membered Cd-Se rings are the basic units of CdSe QDs, and it had 12 4MR and 67 6MR in the initial structure. However, after being introduced to the glass matrix, the number of 4MR decreased to 3, 1, and 0, while the number for 6MR was 8, 2, and 9 in these systems, respectively. Both system sizes indicated the formation of small Si-O rings and breaks of the 4-Membered and 6-Membered Cd-Se rings.

In conclusion, I increased the size of the glass matrix in the MD simulations of QD/glass models and the findings based on the results in all the systems are found to be rather uniform. Thus, the configuration with smaller cell size can represent their bigger counterparts in AIMD simulations, without loss of quality in the description.

5.2.3 Computational details

Based the results and discussion above, I have demonstrated that the two-step quenching method proposed enables to relax the glass/QD interface and at the same time keep the integrity of QD without any unphysical phenomenon such as QD melting or dispersion. Moreover, the investigation of various system sizes showed even a small system size can give similar descriptions of the interfacial structure to the bigger systems. Due to the limitation of the AIMD simulations, the maximum total number of the computing system is around 500 atoms, so I used the glass composition with 39 Na_2O-78 SiO_2-33 CdSe, which can represent models of bigger sizes.

Based on those results, a new consistent methodology has been developed to generate the models of CdSe quantum dot-doped glasses, involving in three steps:

(1) **Generation of the glass matrix with composition of 60 Na_2O-120 SiO_2.** The melt-quenching procedure was the same as chapter 4.

(2) **Generation of $Cd_{33}Se_{33}$ quantum dot-doped glasses structure using classical MD.** The $Cd_{33}Se_{33}$ QD was incorporated into the glass matrix, removing glass atoms so interatomic distances between the QD and the glass matrix were longer than 2.5 Å. The final composition was 39 Na_2O-78 SiO_2-33 CdSe (**Figure 5.7(a)**). The whole

structure was equilibrated at 1000 K, first using 200 ps of NVT dynamics and then 200 ps of NVE dynamics, initially with atoms from the CdSe QD frozen. The structure was then cooled gradually in steps of 50 K with a 60 ps MD run at each temperature from 1000 K to 500 K, while keeping CdSe QD frozen. Subsequent cooling from 500 K to 300 K took place in steps of 10 K, with all atoms allowed to move. Finally, the structure were further equilibrated at 300 K with a 200 ps NVT dynamics, and a final 200 ps NVE dynamics (**Figure 5.7 (b)**).

(3) ***Ab initio* molecular dynamics of CdSe quantum dot in glass matrix.** After equilibration of these systems using classical MD simulations as described above, we used the resulting configurations as starting point for *ab initio* modelling at the Density Functional Theory (DFT) level, using Kohn–Sham formulation as implemented in the CP2K code. Simulations were run at the Generalized Gradient Approximation level, employing the PBE exchange–correlation functional. The plane wave cutoff was set to 600 Ry. For Na, Cd, and Se, we used short-range molecularly optimized double-ζ single polarized basis sets (DZVP-MOLOPT-SR-GTH), while for O and Si we used a double-ζ single polarized basis set (DZVP-MOLOPT-GTH). After an initial geometry optimization with DFT, the resulting relaxed structure (**Figure 5.7(c)**) was used as initial structure for the AIMD simulations. The structure was quenched from 500 K to 300 K in steps of 50 K, with a total 10 ps AIMD run at a time step of 2 fs. The production run was conducted in the NVT ensemble at 300 K for 10 ps. This step is the most demanding stage in terms of computational cost compared with the first two steps. For example, for simulations in the NVT ensemble of systems with composition of $39Na_2O$-$78SiO_2$-33CdSe (417 atoms in total), it costs 48 hours using 384 cores on high performance computing systems for 20 ps simulations.

5.3 Results & discussion

5.3.1 Geometry

Compared with the initial configuration (**Figure 5.7 (a)**), by visual inspection, large structural reconstructions are found to occur after equilibration of the system, regardless of whether it is the final configuration of classical MD simulations of the

glass matrix relaxation (**Figure 5.7 (b)**), the DFT geometry optimization (**Figure 5.7(c)**), or the final structure of AIMD simulations (**Figure 5.7 (d)**).

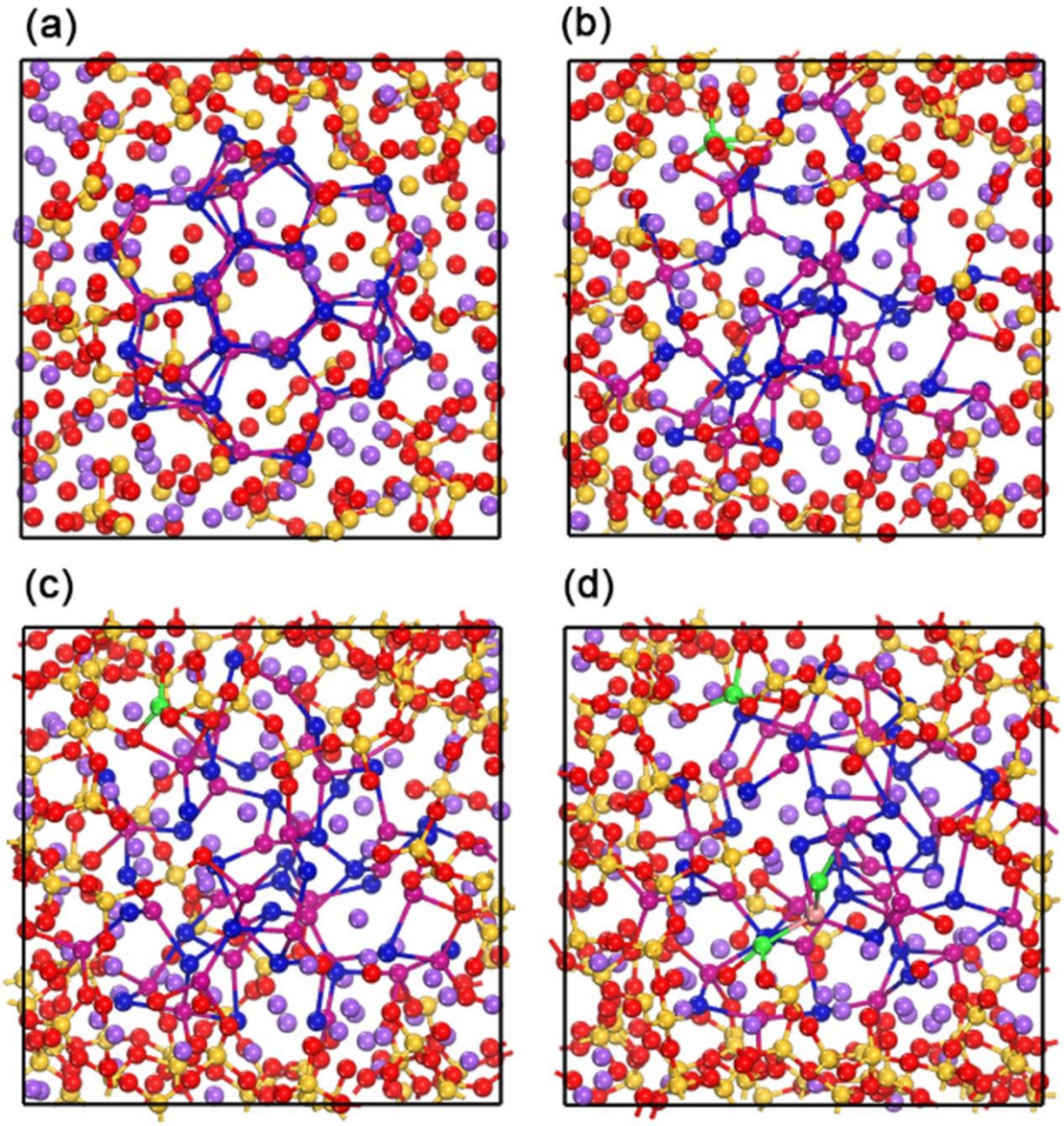

Figure 5.7 (a) The initial configuration for the classical MD calculations. (b) The final configuration for classical MD simulations, used as initial configuration for the geometry optimization by DFT method. (c) The geometry-optimized structure at the DFT level, used as the initial configuration for the *ab initio* molecular dynamics. (d) The final configuration from the AIMD simulations. Se atoms and Cd atoms dissociated from the quantum dot are highlighted in pink and green, respectively.

In particular, I clearly observed the influence of the matrix in the introduction of strong disorder in the quantum dot structure. For the original QD structure, the Cd atoms were either coordinated with 4 Se atoms (in the core of the QD) or 3 Se atoms (at its external surface). A more complex coordination of the Cd and Se atoms in the glass-embedded QD can be found, where some of the Cd–Se linkages were broken, the coordination rings opened up, and coordination between the QD and glass was observed. The fact that the QD, in its glass matrix, cannot maintain its pristine structure, is an important conclusion that is very different from most of the models studied in the existing literature of QD in solution.[126, 185]

In addition to these changes in the environment of the QD atoms, I observed a small number of Cd ions from the QD surface that completely dissociated from the quantum dot structure, and migrated into the glass matrix (highlighted in green in **Figure 5.7**). This was observed for one atom during MD at the classical level, and confirmed in the AIMD with the migration of a second ion. Therefore, it is not an artefact of the classical pair potential. Furthermore, during the *ab initio* MD I observed the dissociation of Cd–Se–Cd clusters (Se atom highlighted in pink). For the system size under study here, the percentages of dissociation were found to be 1.52% (**Figure 5.7 (b)** and **Figure 5.7 (c)**) and 6.06% (**Figure 5.7 (d)**), respectively. These observations at the microscopic scale are novel, but they were in good agreement with experimental evidence of Cd atoms found to be dissolved in the matrix in as-prepared glass, seen by the extended X-ray absorption fine structure spectroscopy analysis (EXAFS).[57] In the CdSe QD-doped glass with the initial composition of 50 SiO_2-20 K_2O-20 ZnO-5 B_2O_3-1.5 CdO-1.5 CdS-1.0 Na_2SeO_3 (wt%), the Cd-O contacts in all specimens with different thermal treatment were observed, attributed to the cadmium dissolved in the glass matrix.

5.3.2 Radial distribution function

I then analyzed the radial distribution functions for Si-O (**Figure 5.8 (a)**), Na-O (**Figure 5.8 (b)**), Cd-Se (**Figure 5.8 (c)**) pairs. In each case, I compared RDFs for the initial structure of classical MD run (**Figure 5.7 (a)**) and distribution functions obtained over the *ab initio* molecular dynamics simulation. Compared with the initial structure, only

minor changes in Si-O and Na-O interatomic distances were observed, with first-neighbor peaks at 1.64 Å and 2.34 Å respectively, consistent with previous research of silicate glasses.[96, 98]

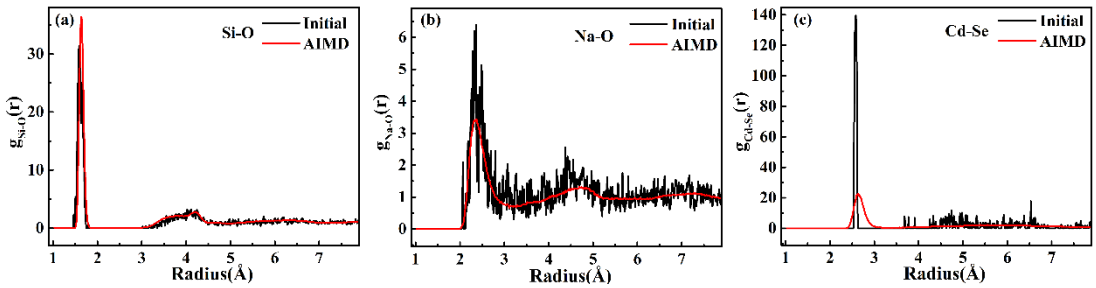

Figure 5.8 Radial distribution functions for (a) Si–O, (b) Na–O and (c) Cd–Se pairs in the initial structure (black lines) and averaged over the *ab initio* molecular dynamics (red lines), for a quantum dot embedded in the 39 Na_2O-78 SiO_2 glass matrix.

Interestingly, an evolution in the Cd-Se distances was observed, from 2.59 Å to a broader distribution with an average of 2.64 Å (2% longer), due to both the finite temperature and the influence of the glass matrix, which weakens some of the Cd-Se bonds. This influence of coordination was previously discussed in the literature.[104, 107, 118, 122, 131, 186] The Cd-Se bond length was measured at 2.68 Å when one Se atom is coordinated with 4 Cd atoms, and 2.62 Å when one Se atom is coordinated with 3 Cd atoms in $Cd_{33}Se_{33}$ clusters.[129] Besides, the Cd-Se bond length was 2.60 Å when one Se atom is coordinated with 2 Cd atoms in Cd_3Se_3 clusters.[104] These geometry structures were obtained from DFT calculations rather than AIMD calculations in the this thesis. Hence, we can conclude that the higher the coordination between Cd-Se pairs, the longer the bond length.

In this thesis, it was also interesting to note the size dependence of the Cd-Se bond length,[104, 131] i.e., the smaller the QD's size, the shorter the average Cd-Se bond length - while a lattice contraction was observed in the CdSe QD-doped glasses.[63] This effect was linked to the surface/volume ratio, where smaller QDs had more surface atoms leading to shorter Cd–Se bonds. I noted however in our *ab initio* MD simulations, that the diameter of the QD in final structure was 16 Å, increased from 13 Å in the initial structure. This demonstrates that the glass-embedded QD does not behave like the QD in vacuum: firstly, because of the chemical environment that the glass matrix

constitutes, with glass/QD coordination. But other explanations have been advanced in the literature,[187] it was suggested that the isotropic nature of the ordering of QDs in solution given rise to the strain effects between QDs and solution, resulting in the size-dependent and ligand dependent reconstruction of the QD surface. Moreover, the thermal and elastic mismatch between the nanocrystals and glass matrix can give rise to residual stresses upon cooling,[188-190] increasing the extent of surface reconstruction.

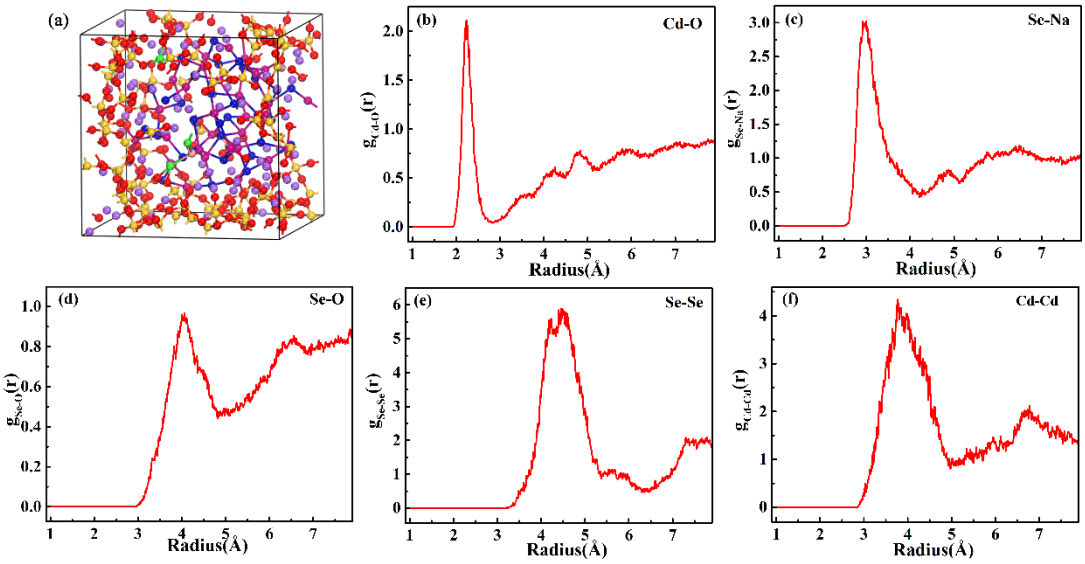

Figure 5.9 (a) The final configuration from the *ab initio* molecular dynamics. Radial distribution functions for (b) Cd-O, (c) Se-Na, (d) Se-O, (e) Se-Se, and (f) Cd-Cd pairs, averaged over the *ab initio* molecular dynamics (red), for a quantum dot embedded in the 39 Na_2O-78 SiO_2 glass matrix.

Now I turn my attention to the QD/glass interface (**Figure 5.9 (a)**). Looking at the respective radial distribution functions, I observed the formation of Cd-O and Se-Na bonds. They were characterized by interatomic distance of 2.25 Å (**Figure 5.9 (b)**) and 2.91 Å (**Figure 5.9 (c)**), respectively. These values, obtained from the *ab initio* molecular dynamics, are in excellent agreement with experimental data available. The interatomic Cd-O distances were found to be 2.25 Å based on the EXAFS characterization of CdSe QD-doped glasses,[57] while the Se-Na distances in the bulk Na_2Se structure are known to be around 2.95 Å (Crystallography Open Database ID: 9009065). From the experimental crystal lattice energies of CdO, CdSe, Na_2O and

Na_2Se,[191] it is expected that the Na-Se bond would be weaker than Na-O, and the Cd-O bond to be stronger than Cd-Se. This can explain that the driving force for this reconstruction find its root in the Cd-O interactions. On the other hand, *ab initio* MD simulations confirm that there were no close contacts with formation of Se-O (**Figure 5.9 (d)**), Se-Se (**Figure 5.9 (e)**) and Cd-Cd pairs (**Figure 5.9 (e)**) at the QD/glass interface. The interatomic distances of first neighbors for these pairs are 3.92 Å, 4.46 Å and 3.70 Å, inconsistent with the previous research, which were 1.83 Å (obtained from DFT calculations),[156] 2.53 Å[57] and 4.20 Å (experimental EXAFS data for wurtzite CdSe QDs)[57]. This shows that they are not actual bonds, because the distances in such a case would be smaller.

5.3.3 Coordination &ring structures

Table 5.7 Average coordination number and percentages of Na, O, Si, Se and Cd with different atoms in initial configuration, and averaged over the *ab initio* MD simulation

System		Initial Structure		*Ab initio* MD	
Atom	**Bond**	**Coordination Number**	**Percentage**	**Coordination Number**	**Percentage**
Na	**Na–O**	**4.06**	**88.80%**	**3.54**	**86.21%**
	Na–Se	**0.08**	**1.68%**	**0.33**	**8.05%**
O	**O–Na**	**1.63**	**52.40%**	**1.42**	**44.54%**
	O–Si	**1.42**	**45.62%**	**1.60**	**50.29%**
	O–Cd	**--**	**--**	**0.16**	**5.17%**
Si	**Si–O**	**3.54**	**87.64%**	**4.00**	**100%**
Se	**Se–Cd**	**3.36**	**82.84%**	**2.52**	**76.26%**
	Se–Na	**0.18**	**4.48%**	**0.78**	**23.72%**
	Se–O	**0.36**	**8.96%**	**--**	**--**
Cd	**Cd–O**	**--**	**--**	**0.97**	**27.70%**
	Cd–Se	**3.36**	**94.87%**	**2.52**	**71.72%**

In order to understand the QD/glass interface in more depth, the coordination

environment (**Table 5.7**) as well as the ring structures inside the CdSe QD/glass systems were explored. I found that 52.40% of O atoms were bonded to Na atoms in the initial structure, while in the *ab initio* MD that number was 44.54%. Meanwhile, there were opposite tendencies for the coordination between O and Si atom, with the percentages increased from 45.62% (initial structure) to 50.29% (*ab initio* MD). Moreover, while there was no Cd-O bond in the initial structure, the AIMD showed 5.17% of O atoms were bonded with Cd atoms, confirming the formation of Cd-O bonds in the interface. These are not well described by the classical potentials and their presence shows the value of conducting AIMD simulations.

Somewhat surprisingly, 100% of Si atoms were 4-coordinated with O atoms in our AIMD trajectory, while the coordination number of the Si atom with O atoms was 3.54 in the initial structure. This points to a dissymmetry in the Si-O and Na-O bonds of the glass, where the presence of the QD leads to disruption of the Na-O bonds, while Si-O coordination (and Cd-O, to a smaller extent) is kept intact, due to its stronger bond. In addition, the glass matrix also has a marked impact on the Cd-Se bonds in the QD. 23.72% of Se atoms were bonded with Na atoms and 27.70% of Cd atoms were bonded with O atoms in the QD/glass interface, with great decrease of the bonds between Cd atoms and Se atoms.

It is should be noted here in chapter 3, I studied a simple model of $Cd_{33}Se_{33}$ clusters capped with one sodium ion, and demonstrated that this results in the introduction of defect states in the HOMO–LUMO gap, giving rise to unusual near-infrared luminescence. In addition, the HOMO and LUMO states were spread in the same region, indicating high probability of recombination of holes and electrons excited from these defect states.

The results obtained in this chapter from *ab initio* MD show that when QD are surrounded by a glass matrix, the number of surrounding sodium ions within short distance (Na-Se linkages) is quite important. The defects at the interface are found to be not as simple as I expected in chapter 3: a large percentage of Se atoms are bonded with Na atoms, in the glass where Na_2O was introduced as glass modifier. Again, this highlights the importance of realistic modelling. The abundant nature of the sodium atoms in the glass matrix will greatly contribute to the defect emission, and a decrease in sodium content may diminish the number of interfacial defects, giving guidance to

the design of glass composition in future work.

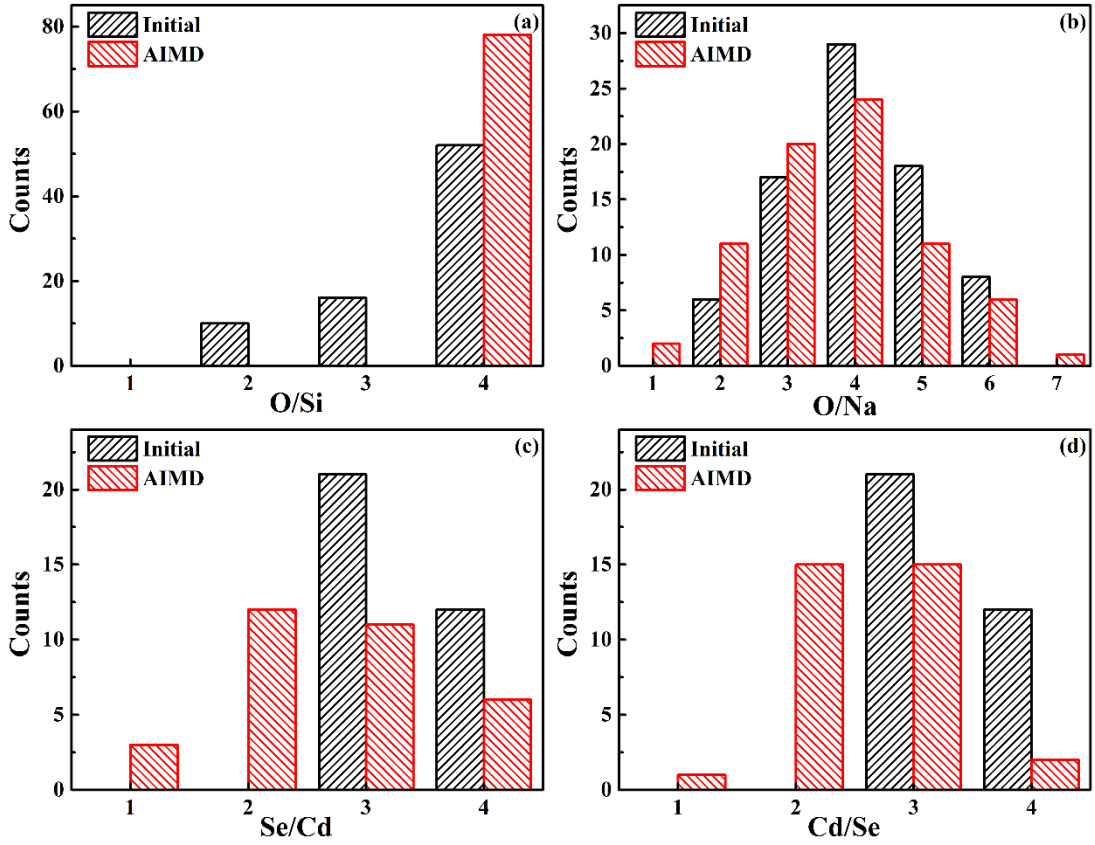

Figure 5.10 Histograms of coordination numbers for different pairs of atoms, comparing the initial structure (in black) and the average over the *ab initio* MD simulation (in red). (a) O coordination around Si atoms. (b) O coordination around Na atoms. (c) Se coordination around Cd atoms. (d) Cd coordination around Se atoms.

I further analyzed the details of the coordination numbers for Si-O pairs (**Figure 5.10 (a)**), Na-O pairs (**Figure 5.10 (b)**), Cd-Se pairs (**Figure 5.10 (c)**) and Se-Cd pairs (**Figure 5.10 (d)**). These confirmed the strong rearrangement of the interface to promote the formation of SiO_4 tetrahedra, which was also seen in the ring statistics (**Table 5.8**) — with the occurrence of small ring sizes for Si-O rings. For example, I observed 16 8-membered rings (8MR) in the final structure, while no such ring was present in the initial configuration. Consistent with the data in **Table 5.7**, the occurrence of higher coordination numbers of Na atoms with O atoms (O/Na = 6, 5, and 4)

decreased while the frequency of lower coordination number for Na atoms with O atoms increased (O/Na = 3, 2, 1) compared with the initial structure (**Figure 5.10 (b)**). Additionally, I observed a clear reduction of Na-O rings, for all ring sizes but especially for the 4-member rings. This strengthens our conclusion that the rearrangement at the interface of the CdSe QD tends to break the weaker Na-O bonds to maintain Si-O coordination.

Table 5.8 The number of rings with different ring size for different ring members in initial structure and averaged over *ab initio* molecular dynamics.

Ring Members	Ring Size	Initial Structure	*Ab initio* MD
Si-O	8	--	16
	10	3	10
	12	--	4
	14	1	1
	16	1	--
Na-O	4	88	45
	6	26	9
	8	16	2
Cd-Se	4	12	1
	6	67	3
	8	6	7
	10	--	4
	12	--	1

The basic coordination environments of the CdSe QD are $CdSe_4$ and $CdSe_3$, whose counts were 12 and 21 in the initial structure, respectively. However, the average number of Se atoms around Cd dropped down compared with initial structure of classical MD simulations, with counts for $CdSe_4$, $CdSe_3$, $CdSe_2$, and $CdSe_1$ of 6, 11, 12, and 3 in the *ab initio* MD (**Figure 5.10 (c)**), respectively. The total number of the Cd atoms bonded with Se atoms was 32, with one Cd atom not bonded with any Se

atom (that atom had migrated in the glass matrix, see **Figure 5.7(d)**). In terms of the coordination environment of Se atoms, all the Se atom were bonded with Cd atoms in the initial and final structure. The number of Se atoms with the Cd/Se ratio = 4 and 3 changed from 12 and 21, to 2 and 15. In the same time, the appearance of Se atoms with a ratio of Cd/Se = 2 and Cd/Se = 1 was observed (**Figure 5.10 (d)**). The obvious changes in the ring size of Cd-Se member rings confirmed the huge reconstruction of the quantum dot. The 4-membered and 6-membered Cd-Se rings opened up, with only one 4-membered and three 6-membered Cd-Se rings left in the final structure.

The significant reconstruction of QD in this work distinguishes it from other work for the reason that the QDs almost keep the bulk structure in the center in other computer simulations. The common method to explore the QDs in solutions was to passivate the surface atom with limited number of organic ligands while the QD was incorporated into the inorganic glass matrix in our work. Only the surface atom were capped with organic ligands, without the simulation of the real chemical environment of the solution, leading to the smaller structural reconstruction compared to our work. Although there were some simulations where the QD was directly introduced into the solid crystalline matrix,[192] my work was aimed at the amorphous inorganic matrix for the first time, which constitutes a big part of research regarding the application of QDs for which the atomic structure and origin of defect emission have been rarely studied. The simulations in my work are closer to the real situation of a QD in a glass matrix, in which the matrix can have a more direct influence on the QD compared with the intended passivation of the QD.[126, 129, 185] Apart from the different initial structure building method, the difference in the bond nature between the inorganic atoms with QDs, such as glass modifiers Na atoms and non-bridging O atoms, and the organic ligand with QDs might have a relation to the different structure of QDs in glass matrix and solutions.

5.4 Summary & conclusions

In the first part of this chapter, I proposed and explored two different classical MD approaches for relaxing the glass/QD interface while keeping the integrity of CdSe QD in a hybrid QD/glass model: (a) Cd and Se atoms were allowed to move feely during

the whole quenching-process (the “not frozen” method), (b) Cd and Se atoms were frozen from 1000 K to 500 K while allowed to move from 500 K to 300 K (the “frozen” method). Both methods demonstrated similar structural reconstructions in the interface while the latter could better maintain the integrity of CdSe QD.

Besides, several classical MD simulations were conducted on systems with different size before further AIMD simulation, in which the system size were limited due to computer power. The results indicated that the formation of interfacial bonds and the breakage of bonds within glass matrix or CdSe QD were qualitatively similar even the system sizes were different. Therefore, for the sake of lowering computational cost, the CdSe quantum dot-doped glass with composition of 39 Na_2O-78 SiO_2-33 CdSe were chose to perform the further AIMD simulations.

To the best of my knowledge, my calculations are the first *ab initio* molecular dynamics study of a CdSe quantum dot embedded in a glass matrix. Particularly, the structure of the CdSe QD-doped glass was obtained by the melt-quenching method, generated by the combination of the molecular dynamics and the *ab initio* molecular dynamics. Distinct structural reconstructions were observed simultaneously in the glass matrix and CdSe QD. The incorporation of CdSe QD greatly disrupts the bonds between Na atoms and O atoms, with a reduction in the number of O atoms bonded with Na atoms, replaced by the Si atoms and Cd atoms.

Unexpectedly, it also gives rise to the formation of the SiO_4 tetrahedra and small ring size of Si–O member rings, with all the Si atoms are 4-coordinated with the O atoms in the final structure. The Si-O bonds are clearly favored during reconstruction.

As for the interfacial structure, both the radial distribution function for the interatomic distance of Cd atoms and O atoms, Se atoms and Na atoms, as well as the analysis of the coordination environment of these atoms directly, confirm the existence of both Cd-O bonds and Se-Na bonds, consistent with previous experimental findings. Furthermore, it seems that there are very few possibilities of the formation of the Se-O bonds, Se-Se bonds, and Cd-Cd bonds.

In terms of the CdSe QD, the glass matrix has a greater influence on the reconstruction of the QD compared to QD in solutions. It is hard to maintain the stable 3-coordinated and 4-coordinated CdSe basic units when it is introduced into the glass matrix, with the 3-membered and 4- membered ring disappearing. Additionally, a few examples of

disassociated Cd atoms and Se-Cd-Se clusters were observed to migrate in the glass matrix. The complex structure of the glass matrix and the difference of the bond nature between the inorganic ions and QD might be linked to the instability of QD in the glass matrix compared with the QD in organic solutions.

The work in this chapter gives an intuitive visual illustration of the local atomic interfacial structure of the CdSe QD-doped glass, promoting the understanding of the structural reconstructions of the glass matrix as well as the CdSe QD. These results shed light on the impact of the glass matrix on the CdSe QD, exploring the possible defect structure of the QD, thus can give guidance to the adjustment of the component of the glass matrix and to the fabrication of highly luminescent CdSe QD-doped glasses. However, my current investigations only cover the geometry structure, which is not enough in order to further improve the mutual understanding of defect emission of CdSe QDs doped glasses. It is necessary to calculate their electronic structures. Based on this calculation, I can probe the impact of these structure reconstructions found in this chapter on the luminescence properties of CdSe QD-doped glasses, which I will explore in the next chapter.

Chapter 6

6 Atomic and electronic structures of CdSe quantum dot-doped xNa$_2$O-(1-x)SiO$_2$ glasses

6.1 Introduction

In last chapter, a combination of classical MD and AIMD has been employed to investigate the interfacial structure between the glass matrix and QD, the reconstruction occurring in this composite system. Interfacial Se-Na and Cd-O bonds were observed to be formed and the breakage of some stable Cd-Se rings were found, demonstrating the local atomic structure is far more complex than the simplified model I had previously built in chapter 3. However, the exploration of the local atomic structure of CdSe quantum dot-doped glass may provide the possible structural origins of defects, but did not shed light on the relationships between these structures and defect emission. In order to answer the question why the quantum efficiency of quantum dots-dopped glasses is so low compared with their colloidal counterparts, the electronic structures are of predominant importance to the understanding of their luminescence mechanisms. Thus, in this chapter, I have studied the electronic structures of CdSe quantum dot-doped glasses to probe the possible origins at the microscopic scale of the poor performance of QD embedded in glasses.

Furthermore, in chapter 3, sodium ions were found to sharply decrease the HOMO-LUMO gap by static DFT calculations.[156] Moreover, in their role of glass modifiers, sodium ions can also alter the structure of silicate glasses, and it was experimentally observed that there is a disappearance of the visible absorption of Se-Se color centers upon increasing concentration of Na$_2$O in a silicate glass doped with ZnSe.[58] The Se-Se contacts are considered to be the nucleation sites of the CdSe QD. Therefore in this chapter, I varied the amount of Na$_2$O in the glass $(Na_2O)_x(SiO_2)_{1-x}$ (x = 0, 0.25, 0.33, 0.5 in molar fraction) to explore the compositional dependence of the atomic and electronic structure of CdSe quantum dot in glass matrices.

The results demonstrate that an increase in the amount of Na$_2$O contributes to the

formation of Cd-O and Se-Na bonds, with breaking of Si-O, O-Na and Cd-Se bonds. The density of states (DOS) and projected density of states (PDOS) were also calculated. From this systematic study I conclude that, with the same chemical composition, the dominant luminescence mechanisms in different configurations can be very different. The top of the valence band and the bottom of the conduction band are decided by the hybrid QD in most compositions. However, in the majority of configurations of CdSe quantum-dot-doped glass with composition of $0.33Na_2O$-$0.67SiO_2$ (in molar fraction) exhibit totally different luminescence mechanisms, that the top of the valence band is determined by the hybrid glasses. These results provide a better understanding of the electronic structure and luminescence mechanisms of these complex systems, giving guidance for future compositional design of highly luminescent glass containing quantum dots.

6.2 Computational details

First of all, I want to outline some definitions here to better illustrate the complex hybrid systems I modelled. Actually, the CdSe quantum dot-doped glasses can be divided into three parts or regions of space: (a) the hybrid QD, (b) the hybrid glasses, and (c) the pristine glasses whose structure is not affected by the QD, as **Figure 6.1** illustrates.

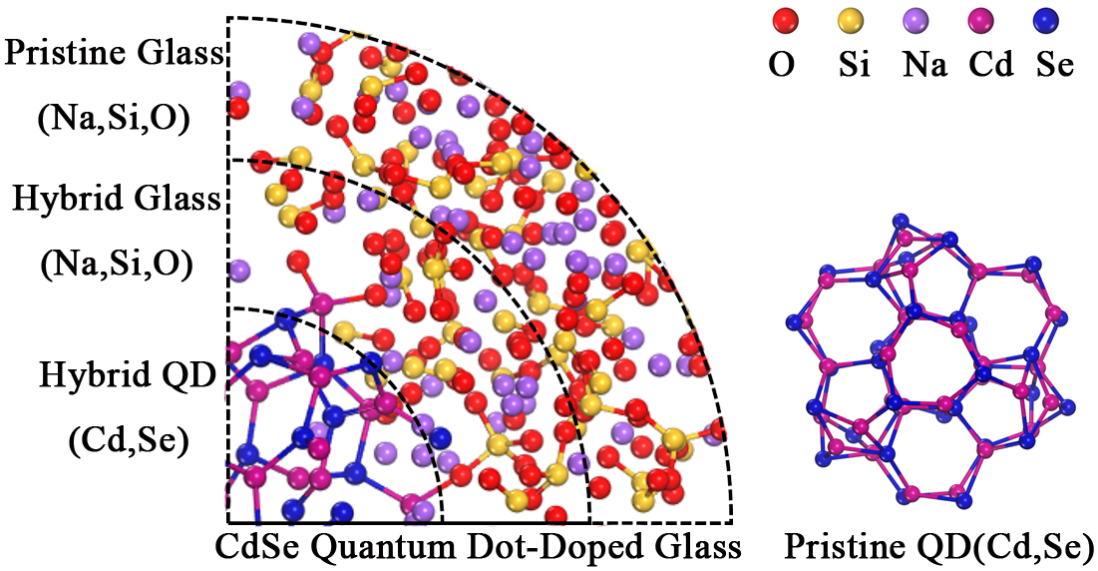

Figure 6.1 Illustration of structural composition of CdSe quantum dot-doped glasses.

When the pristine CdSe QD is introduced into the glass matrices, enormous structural reconstruction is observed, resulting in the formation of hybrid QD (including Cd and Se atoms) whose structure is very different from the pristine QD. At the same time, the structural reconstruction also happens in the glass matrices due to interactions with QD, forming a hybrid glass (including O, Na and Si atoms). The hybrid QD and hybrid glass are connected by forming interfacial bonds such as Na-Se and Cd-O bonds. However, the density of the QDs in the glass matrix is small, thus the incorporation of CdSe QD can only influence the glass structure in the short range, without further impact on the glass structure in the long range. Therefore, the structure of the pristine glass which is far from the CdSe QD remains unchanged. These micro regions are separated by dense and amorphous pristine glass.

6.2.1 Generation of *x* Na_2O-*(1-x)* SiO_2 glasses matrix

The pristine glass configurations were generated using the classical MD method developed in chapter 4 (4.2.4). The randomly distributed atoms in a simulation cell, giving the same glass composition and density, were melted from 300 K to 6000 K in steps of 1000 K with a 60 ps MD run at each temperature in NVT ensemble. After equilibration of the liquid at 6000 K during 400 ps, the system was cooled gradually in steps of 500 K with a 60 ps run at each temperature from 6000 K to 300 K. Another 200 ps NVT simulation was carried out at 300 K, together a 200 ps NVE simulation in order to equilibrate the structure. It should be noted here the CdSe QD will be introduced into the glass structure obtained only by classical MD.

Besides, I wanted to investigate the impact of CdSe QD on the electronic structures of pristine glass, thus, for each chemical composition, a further AIMD simulation was conducted using the final configuration of classical MD as initial configuration. It was quenched from 1000 K to 300 K in steps of 50 K, with a total 10 ps AIMD run at a time step of 2 fs. The production run was conducted in the NVT ensemble at 300 K for 10 ps. 500 configurations were selected at equal interval from a 10 ps production run of *ab initio* molecular dynamics simulation. Among those, 50 configurations were picked

to perform the full calculation and analysis of the electronic structure of pristine glass.

6.2.2 Generation of CdSe quantum dot-doped glasses structure

The pristine CdSe QD was directly introduced to the glass matrix by removing the glass atoms so interatomic distances between the QD and the glass matrix were longer than 2.5 Å. The whole structure was equilibrated at 1000 K, first using 200 ps of NVT dynamics and then 200 ps of NVE dynamics, initially with atoms from the CdSe QD frozen. The structure was then cooled gradually in steps of 50 K with a 60 ps MD run at each temperature from 1000 K to 500 K, while keeping CdSe QD frozen. Subsequent cooling from 500 K to 300 K took place in steps of 10 K, with all atoms allowed to move. Finally, the structure were further equilibrated at 300 K with a 200 ps NVT dynamics, and a final 200 ps NVE dynamics (as described in detail in 5.2.3).

6.2.3 *AIMD* of CdSe quantum dot in glass matrix

Then, after equilibration of systems using the classical MD simulations described above, I used the resulting configurations as starting point for AIMD runs. The structure was quenched from 500 K to 300 K in steps of 50 K, with a total 10 ps AIMD run at a time step of 2 fs. The production run was conducted in the NVT ensemble at 300 K for 10 ps (as described in detail in 5.2.3). 500 configurations were selected at equal interval from a 10 ps production run of *ab initio* molecular dynamics simulations. Among those, 50 configurations were picked to perform the calculation and analysis of the electronic structure of CdSe quantum dot-doped glasses.

6.2.4 Electronic structures calculation

Before performing the electronic structures calculations of all the configurations obtained from AIMD runs, the density of states of $Cd_{33}Se_{33}$ QD (**Figure 6.2**) was calculated to test the accuracy of several exchange-correlation functionals. The PBE, PBE0, B3LYP, and HSE06 exchange-correlation functionals incorporated in the CP2K code were chosen. The top of the valence band and Fermi level was set at 0 eV. The HOMO-LUMO gap was measured 1.23 eV, 2.07 eV, 2.24 eV and 3.43 eV, obtained from calculations based on PBE,[157] PBE0,[193] B3LYP,[159] and HSE06[194] exchange-

correlation functionals respectively.

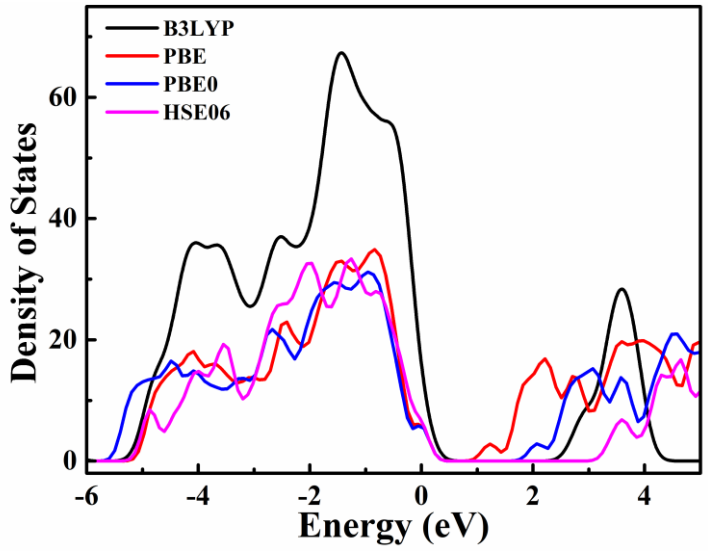

Figure 6.2 Density of states of $Cd_{33}Se_{33}$ quantum dot calculated based on B3LYP (black line), PBE (red line), PBE0 (blue line), and HSE06 (magenta line) exchange-correlation functionals. The top of the valence band and the Fermi level was set at 0 eV.

Comparing with the experimental value (~ 2.86 eV) of $Cd_{33}Se_{33}$ QD, we can see that hybrid functionals have better performance in estimating the HOMO-LUMO gap. However, the computational cost of calculations based on B3LYP and HSE06 functionals are demanding especially considering the large system of CdSe quantum dot-doped glasses. Therefore, the hybrid functional PBE0-TC-LRC was chosen for the further electronic structures calculation of pristine glasses and CdSe quantum dot-doped glasses with a cutoff radius of 2 Å. It underestimates the bandgap but we will be intended in relative trends, not absolute values.

The 50 configurations of pristine glasses and CdSe quantum dots-doped glasses of each composition together the pristine QD performed the calculations and analysis of the electronic structures. **Table 6.1** shows the compositions of pristine glasses and CdSe quantum dot-doped glasses with various sodium oxygen content.

Table 6.1 Composition of the different x Na_2O $(1–x)$ SiO_2 (in molar fraction) glasses investigated in this study and their respective densities. For each system, I list the number of O, Si, Na, Cd and Se atoms in the simulation cell of the CdSe quantum dot-

doped glass.

Pristine Glass		CdSe quantum dot-doped glasses				
$(Na_2O)_x(SiO_2)_{1-x}$	Density (g/cm^3)	O	Si	Na	Cd	Se
$x = 0$	2.20	224	112	--	33	33
$x = 0.25$	2.43	210	90	60	33	33
$x = 0.33$	2.49	195	78	78	33	33
$x = 0.5$	2.56	186	62	124	33	33

From previous work, the electronic structure calculations based on the generalized gradient approximation (GGA) or local density approximation(LDA) exchange-correlation functionals severely underestimated the HOMO-LUMO gap and long range Coulombic interactions. The inclusion of the Hartree-Fock exchanges was found in literature, to provide a more accurate description of the band gap,[105, 133] moreover, the computational cost of nonlocal functional calculations can be reduced using the auxiliary density matrix method (ADMM).[195]

6.3 Results of calculations & Discussions

6.3.1 Atomic structure

The final structures of the CdSe quantum dot-doped glasses with different sodium ratios were shown in **Figure 6.3**. The chemical environment of the final structure was analyzed as shown in **Table 6.2**. As glass modifiers, sodium ions can break the bond between Si atoms and O atoms, contributing to the appearance of non-bridging oxygen atoms. The percentage of O atoms bonded with Si atoms decreased from 96.79% to 31.97% with the increasing Na_2O amount. Meanwhile, the non-bridging oxygen preferred to be bonded with Cd atoms rather than Na atoms, as demonstrated by an increase of percentages of O atoms bonded with Cd atoms from 2.91% to 5.87%. Se atoms also tend to be bonded preferentially with sodium ions as the concentration of the Na_2O ascended in the glass matrices, with 37.09% of Se atoms bonded with Na

atoms when $x = 0.5$. In some configurations, even 33 Se atoms were found to be bonded with sodium ions. It was expected to observe the increased breakage of the bond between Cd atoms and Se atoms when adding Na_2O into the glass matrices. These results showed that the CdSe QD is sensitive to the composition of the glass matrices. This has been experimentally validated by the Raman spectra that the Raman shift of CdSe QDs with the same size in different hosting mediums were different. The lattice contraction effect, depended on the thermodynamic conditions decided by the interactions between QDs and glass matrix, were proposed to explain this phenomenon.[63] In the colloidal method, the CdSe QD core was observed to maintain its bulk structure when capped by organic ligands.[113, 120, 129] However, the interfacial structure and the structure of the CdSe QD is reconstructed in a large scale when the ratio of sodium oxygen is changed.

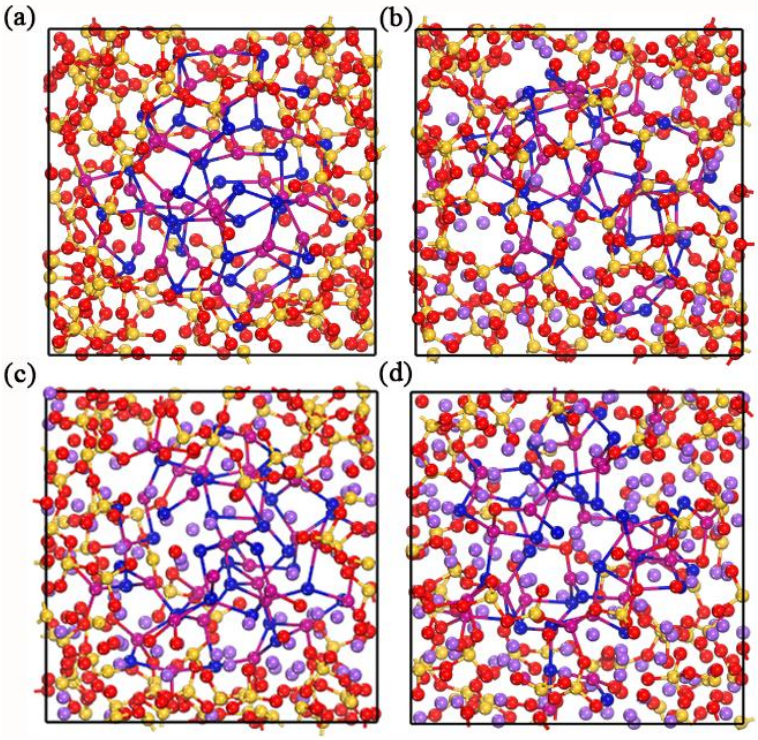

Figure 6.3 Final configuration from the AIMD simulations of the CdSe quantum dot-doped glasses. Glass composition: (a)112 SiO_2-33 CdSe, (b) 30 Na_2O-90 SiO_2-33 CdSe, (c) 39 Na_2O-78 SiO_2-33 CdSe, (d) 62 Na_2O-62 SiO_2-33 CdSe.

Table 6.2 Average percentage of O, Na, Si Se, and Cd bonded with different atoms averaged over the AIMD simulations of CdSe QD in x Na_2O - (1-x) SiO_2 glass matrix.

	Bonds	$x = 0$	$x = 0.25$	x = 0.33	$x = 0.5$
O	O-Si	96.79	59.44	50.29	31.97
	O-Na		36.82	44.54	62.16
	O-Cd	2.91	3.72	5.17	5.87
Si	Si-O	97.99	96.25	94.54	83.07
Na	Na-O		87.45	86.21	83.57
	Na-Se		7.4	8.05	7.73
Se	Se-Na		17.06	23.72	37.09
	Se-Cd	89.61	81.9	76.26	62.88
Cd	Cd-O	12.88	19.87	27.7	35.95
	Cd-Se	87.1	79.89	71.72	59.73

6.3.2 HOMO-LUMO gap distribution

The HOMO-LUMO gap for the pristine QD was found to be 2.08 eV with the methodology chosen, which is smaller than the experimental value (~ 2.84 eV).[156] The goal of the calculation is not to reproduce the exact value of the experimentally observed absorption peak, but rather to predict the impact of the glass matrices on a relative energy scale, which can be corrected "a posteriori" by a constant energy shift to a first approximation. 10 configurations were selected from the AIMD production run of pristine glasses, and the average HOMO-LUMO gaps were 7.19 eV, 4.44 eV, 4.33 eV and 4.41 eV when x changed from 0, 0.25, 0.33, 0.5, respectively. The reported experimental value for amorphous SiO_2 lies in the range of 8.7-9.4eV.[196-197] The calculated HOMO-LUMO gap of SiO_2 glass in our work was comparable to other researchers' work, which were 5.3 eV,[98] 5.35 eV,[94] 5.657 eV,[101] and 8.47 eV[99], depending on the computational methodology. It was found in previous research that when Na_2O is introduced into pure SiO_2, first the band gap decreases sharply but the decreasing rate slows down after $x = 0.2$.[101] The gap of pristine glass with $x = 0.5$ was

higher than that with x = 0.33, which may be due to strained regions after structure relaxation in x = 0.5 model.[99]

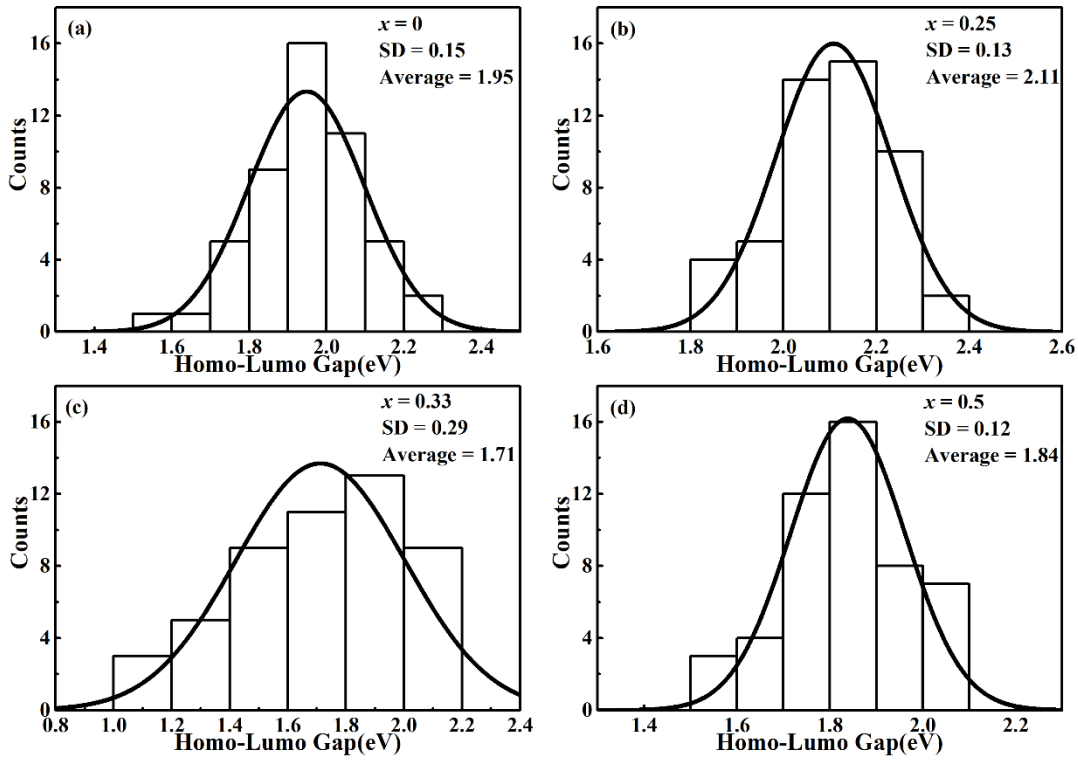

Figure 6.4 Histograms of HOMO-LUMO gap for 50 configurations of CdSe quantum dot-doped silicate glasses. The composition of the x Na_2O- (1-x) SiO_2 glass matrices: (a) x = 0; (b) x= 0.25; (c) x = 0.33; (d) x =0.5. A simple Gaussian function was used to fit the data and SD represent the standard deviation. This is not a physical model but a guide for the eye and a way of comparing distributions.

50 configurations were chosen from the AIMD production runs of the CdSe quantum dot-doped glasses to conduct the DFT calculations. The HOMO-LUMO gap distribution of each composition is shown in **Figure 6.4**. The average values of the gap are 1.95 eV, 2.11 eV, 1.71 eV and 1.84 eV, when x changed from 0 (**Figure 6.4 (a)**), 0.25 (**Figure 6.4 (b)**), 0.33 (**Figure 6.4 (c)**) to 0.5 (**Figure 6.4 (d)**), respectively. The relationship between the HOMO-LUMO gap and the ratio of the Na_2O was nonlinear, different from the relationship between the HOMO-LUMO gap of the pristine glass and sodium oxygen contents.

Due to the fluctuation in the composition and thermal condition, the experimentally fabricated glasses are regarded as inhomogeneous in microscopic regions. Thus, each configuration in our calculation can represent a small part of the real glass sample, meaning that each CdSe QD can have different interfacial environment in the glass matrices. Our systems therefore represent spatial fluctuations of the real physical system. The optical properties of the glass sample are a collective representation of these micro regions. Even though the composition for each simulated configuration was the same with equal amount of the Na_2O in glass matrices, the HOMO-LUMO gap still fluctuated, with standard deviation ranging from 0.15, 0.13, 0.29 and 0.12 eV, respectively. These results reflect that the interfacial environment of each QD in glass matrices is rather complicated in terms of the electronic structures.

It should be noted that the standard deviation of $x = 0.33$ was much higher than other glasses composition. Therefore, it indicates broad distribution in absorption and photoluminescence of CdSe QD formed in the glasses, resulting in low photoluminescence quantum yield of QDs in glasses, which is unfavorable for their potential application. Thus, it gives guidance to the compositional design of glass matrix that $x = 0.33$ is not a desirable ratio if we want to fabricate highly luminescent glasses.

6.3.3 Luminescence Mechanisms

In order to have a better understanding of the impact of glass matrices on the electronic structures of the CdSe QD, I calculated the density of states and projected density of states of the pristine glass, pristine QD, and CdSe quantum dot-doped glass (**Figure 6.5**). For the final structure of $x = 0$ (**Figure 6.5 (a)**), $x = 0.25$ (**Figure 6.5 (b)**) and $x = 0.5$ (**Figure 6.5 (d)**), the HOMO orbitals and LUMO orbitals were determined by the hybrid QD. Interestingly, the HOMO orbitals in $x = 0.33$ (**Figure 6.5 (c)**) were special compared to other composition, because it was determined by hybrid glass instead of the hybrid QD. Meanwhile, the LUMO orbitals were still decided by hybrid QD. These results demonstrated two different luminescence mechanisms of CdSe quantum dot-doped glasses (**Figure 6.6**). For what I will call type I (**Figure 6.6 (a)**), when the electrons are excited from the hybrid glass, they will leave holes on the valence band.

These photogenerated electrons will relax to the LUMO orbitals formed by the hybrid QD. The holes and electrons are in different spatial locations, resulting in indirect recombination (red straight dash line) and enhanced nonradiative recombination (red curve dash line). For what I will call Type II (**Figure 6.6 (b)**), both electrons and holes are generated in hybrid QD upon excitation, leading to the direct recombination (red straight line) and subsequent intrinsic emission from the hybrid QD.

Besides, the impact of the interfacial bonds was also investigated. As we can clearly see from **Figure 6.5**, the projected density of states of Se-Na (magenta solid line) and Cd-O (blue line) contribute to the peak at the bottom of conduction band. However, the peak formed by the hybrid QD (red solid line), Se-Na, and Cd-O are at the same position. Therefore, we can conclude that both Se-Na and Cd-O bonds contribute to the frontier orbitals but not shift the energy level of the frontier orbitals.

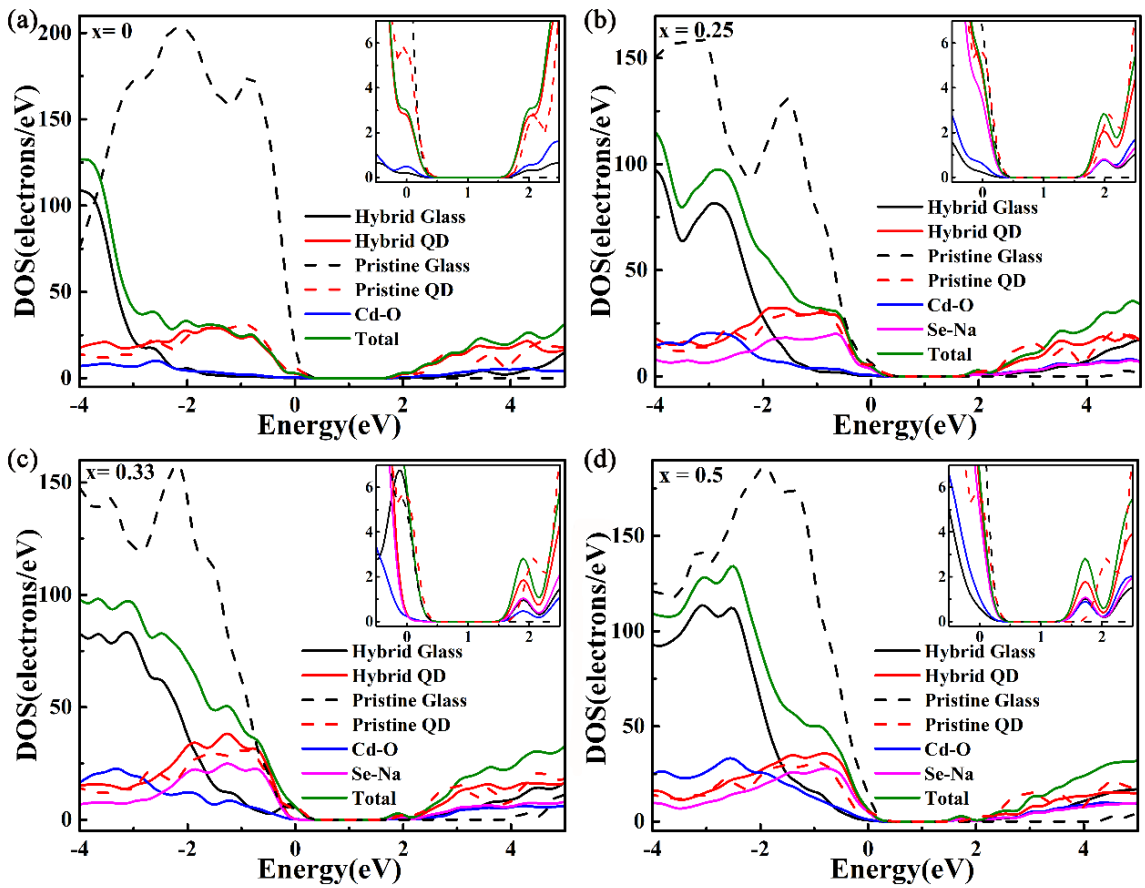

Figure 6.5 Density of states and projected density of states of final structure of the

AIMD calculation of CdSe quantum dot-doped glasses. The hybrid glass included O atoms, Na atoms and Si atoms, while hybrid QD was composed of Cd atoms and Se atoms. Cd-O (Se- Na) represent the projected density of states of the Cd(Se) atoms bonded with O(Na) atoms and O(Na) atoms bonded with Cd(Se) atoms. The HOMO and the Fermi level are set at 0 eV. Panel (a) to (d) correspond to compositions of x = 0, 0.25, 0.33, and 0.5, respectively.

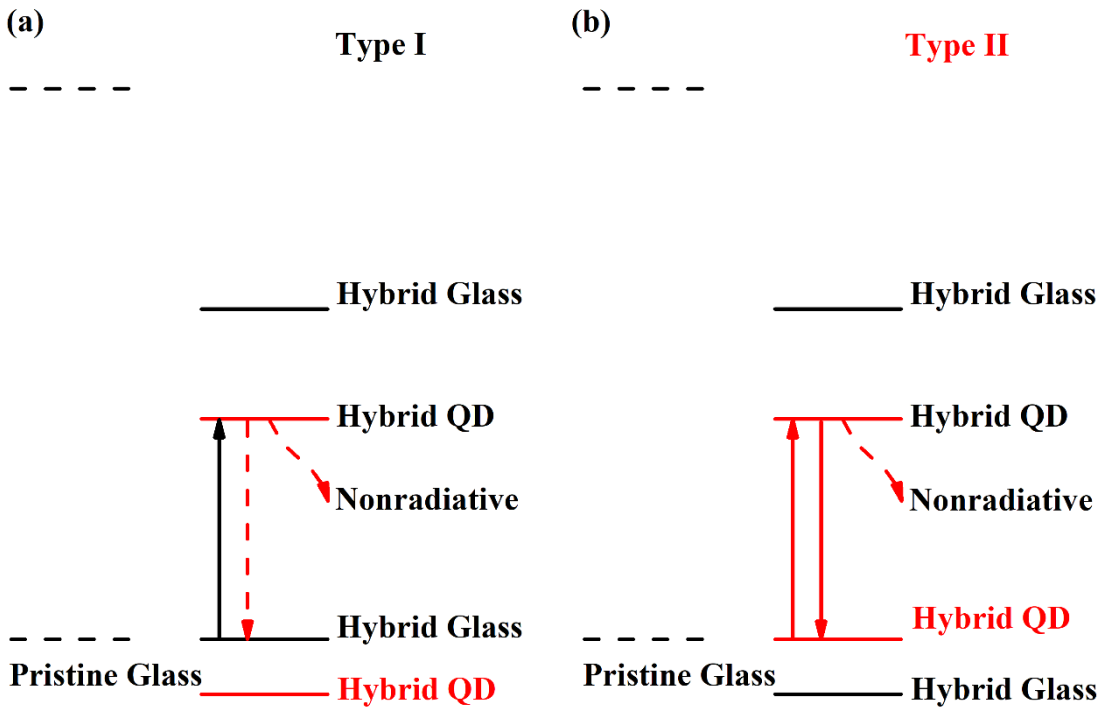

Figure 6.6 Energy diagrams of CdSe quantum dot-doped glasses.

I further analyzed the density of states of 50 configurations of each composition. Based on the DOS, each configuration was assigned to one type of luminescence mechanism (**Figure 6.7**). Importantly, the luminescence mechanisms of CdSe quantum dot-doped glasses were found to be strongly dependent on the composition of the glass matrices. When x = 0, 0.25, and 0.5, luminescence was mainly determined by the direct transition between HOMO and LUMO of hybrid QD (Type II mechanism). On the other hand, when x=0.33 (**Figure 6.7 (c)**), the luminescence was mainly determined by the indirect transition between the LUMO of hybrid QD and HOMO of hybrid glass (Type I mechanism), and only 7 out of 50 configurations were classified to Type II. Thus, the composition of the glass with x= 0.33 is less favorable for practical application. For

one thing, the standard deviation of x = 0.33 (**Figure 6.4**) is much higher than other compositions, contributing to the broad distribution of photoluminescence. For another thing, the electrons and holes are generated in different spatial regions, tending to induce indirect recombination. Both are likely to reduce the quantum efficiency.

Traditionally, the luminescence of the CdSe quantum dot-doped glass can be divided into two competitive parts, which are defect emission and intrinsic emission.[29, 72] The defect emission is attributed to trap states formed by surface defects such as dangling bond, vacancies and so on. Meanwhile, the intrinsic emission of CdSe QD is related to the direct recombination of the excitons formed within the QD.

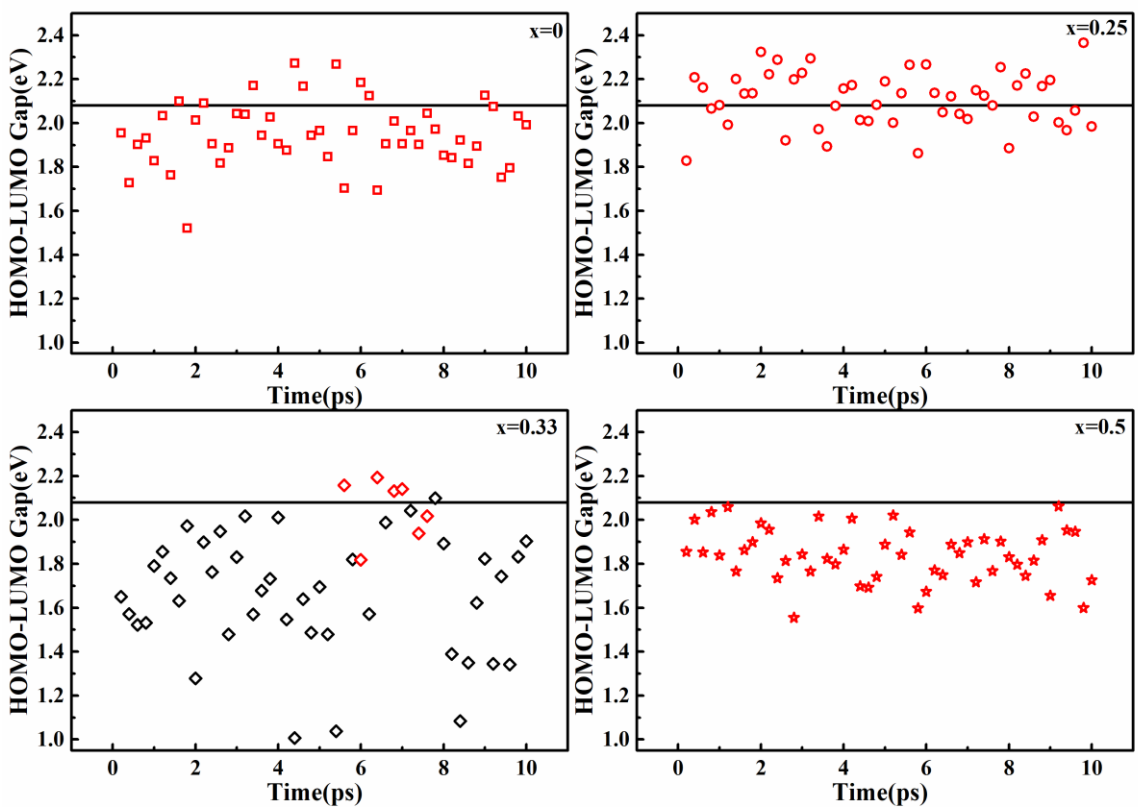

Figure 6.7 HOMO-LUMO gap of the 50 configurations of the AIMD production run of CdSe quantum dot-doped glass. The solid black line represent the HOMO-LUMO gap of the pristine QD which is for reference here. The black symbols represent the luminescence mechanism of this configuration belonging to type I and red symbols represent type II (see **Figure 6.6**).

However, according to the atomic structure and the HOMO-LUMO gap as well as the density of states of each configuration, a new luminescence mechanism quite different from previously published researchers' models was proposed. We hypothesize that the luminescence of CdSe quantum dots embedded in silicate glass matrices observed in experiments, was not defect emission induced by the surface defects, nor intrinsic emission from pristine QD as the common model proposed by experimentalists, but the intrinsic emission of the hybrid QD and hybrid glasses.

It is a highly hybrid system, in which the surface defects and core cannot be separately discussed because their coupling is too important. Firstly, I analyzed the 200 configurations of all the compositions, the large-scale structure reconstruction can be observed in each configuration and it is hard for the core to maintain its bulk crystalline structure (**Figure 6.3**). Na atoms were found to be bonded with the Se atoms even near the core of the QD. Therefore, there is little possibility of CdSe QD to avoid the interaction with glass matrices, and keep the pristine state. Secondly, only a small ratio of configurations were found to have the same value of HOMO-LUMO gap as the pristine QD (**Figure 6.7**) with a broad distributions of values instead, further proving the little possibility of the existence of pristine QD in glass matrices. Thirdly, no midgap state was found to be formed inside the HOMO-LUMO gap, as observed in some colloidal quantum dots where the orbital of pristine QD still exists.[113-114, 116, 118, 126] Based on the density of states (**Figure 6.5**), it is therefore clear that the peak of the pristine peak disappeared and the frontier orbitals were shifted in hybrid QD. Therefore, pristine QD is less likely to exist in the sodium silicate glass. The emission of the CdSe quantum dot-doped glasses originates from the exciton recombination of the hybrid system formed by the hybrid QD and hybrid glass, and cannot be described by simplistic models .

6.3.4 Impact of glass matrices on the electronic structure of CdSe QD

I investigated the impact of the glass matrices on the electronic structure of CdSe quantum dot investigated by comparing the density of states of hybrid QD and pristine QD (**Figure 6.8**). The top of the valence band of pristine QD was decided by Se atoms and the bottom of conduction band was determined by Cd atoms (**Figure 6.8 (e)**). When

the quantum dot was introduced to the glass matrices, the top of the valence band was still decided by Se atoms but the Se atoms bonded with Na atoms contributed mostly to the frontier orbitals. It should be noted that all Se atoms were bonded with Na atoms in the final structure of x = 0.5 (**Figure 6.8 (d)**). The bottom of the conduction band was determined by Cd atoms and the Cd atoms not bonded with O atoms contributed mostly to the LUMO. However, the energy separation between Cd atoms bonded with O atoms and Cd atoms not bonded with O atoms has not been observed.

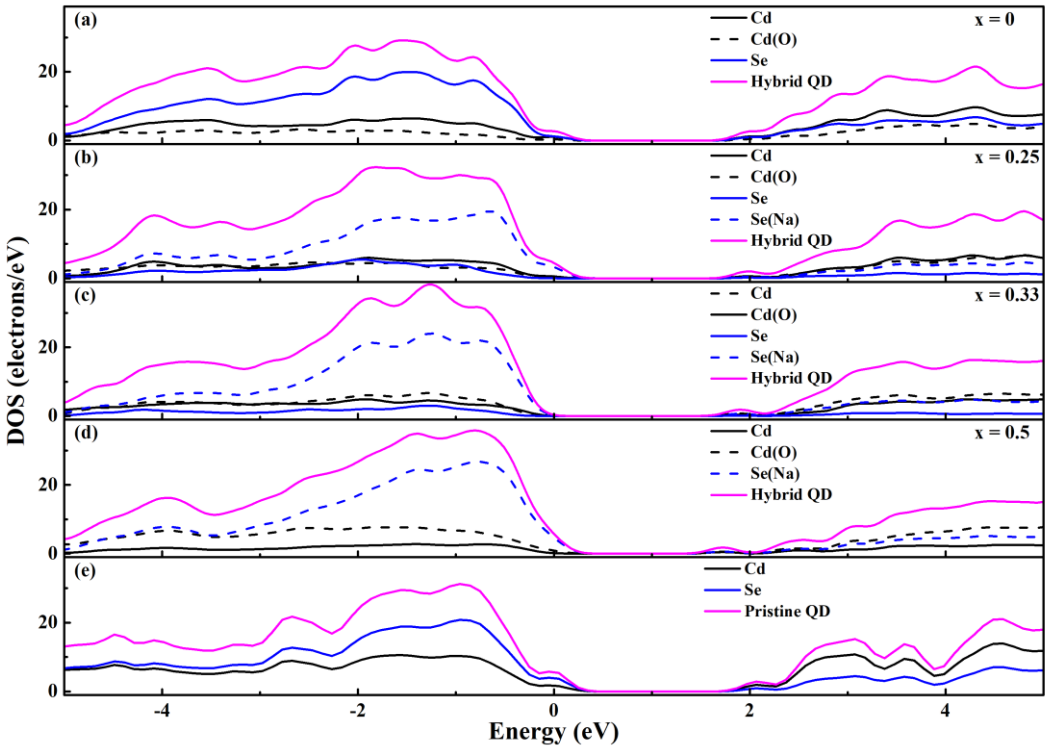

Figure 6.8 The density of states of the hybrid QD of AIMD simulation of CdSe quantum dot-doped glasses and pristine QD. Cd(O) represents the Cd atoms bonded with O atoms and Se(Na) represents the Se atoms bonded with Na atoms. Cd represents the Cd atoms not bonded with O atoms. Se represent the Se atoms not bonded with Na atoms.

6.3.5 Impact of CdSe QD on the electronic structures of glass matrices

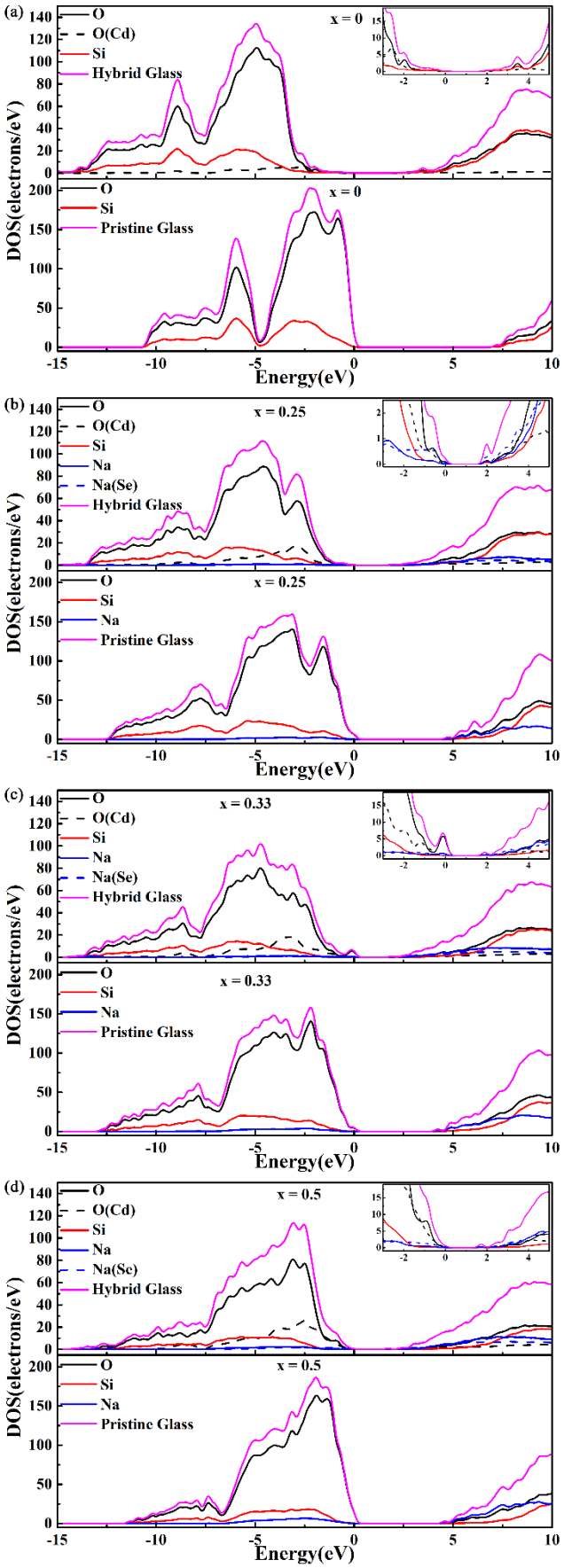
(a)
x = 0
O
O(Cd)
Si
Hybrid Glass
Pristine Glass
(b)
x = 0.25
Na
Na(Se)
(c)
x = 0.33
(d)
x = 0.5
DOS(electrons/eV)
Energy(eV)

Figure 6.9 The density of states of the hybrid of the AIMD simulation of CdSe quantum dot-doped glasses and pristine glasses. O(Cd) represents the O atom bonded with Cd atom and Na(Se) represent the Na atom bonded with Se atom.

I also investigated the effect of the presence of CdSe QD on the electronic structure of the pristine glass. There were two typical segments in the upper valence band of pristine glasses as well as the hybrid glasses (**Figure 6.9**). They mainly consist in oxygen *2p* lone pair orbitals of for the highest orbitals and in bonding states between silicon sp^3 hybrids and oxygen *2p* orbitals from -10 eV to -5 eV.[198-199] It is apparent that the introduction of CdSe QD sharply decreases the gap of pristine glass with the bottom of the conduction band shifting to the lower energy part. Besides, an additional peak appears at the shoulder of the upper segments formed by the oxygen lone pair orbitals in CdSe quantum dot-doped glasses, which can be attributed to non-bonding oxygen atoms.

Although there were 7 configurations (red symbols in **Figure 6.7 (c)**) which luminescence mechanism belonged to type II when x =0.33, the impact of the CdSe QD on the pristine glass and the effect of the pristine glass on CdSe was the same as in other configurations. For example, the configuration obtained from the AIMD production run at 7 ps with x =0.33, it is apparent that the top of the valence band is determined the hybrid QD, so the luminescence mechanism of this configuration is assigned to type II (**Figure 6.10 (a)),** different from the majority of the configurations of x = 0.33. However, the impact of glass or CdSe QD demonstrates similar tendency. A much smaller HOMO-LUMO gap of hybrid glasses compared with pristine glasses (**Figure 6.10 (b)**) can be observed, indicating the presence of CdSe QD can greatly decrease the bandgap of pristine glass. The hybrid orbitals formed by Se atoms and Na atoms played a dominate role in the HOMO orbitals. Meanwhile, similarly, the HOMO orbital is found to be decided by Se atoms which are bonded with Na atoms in hybrid QD (**Figure 6.10 (c)**).

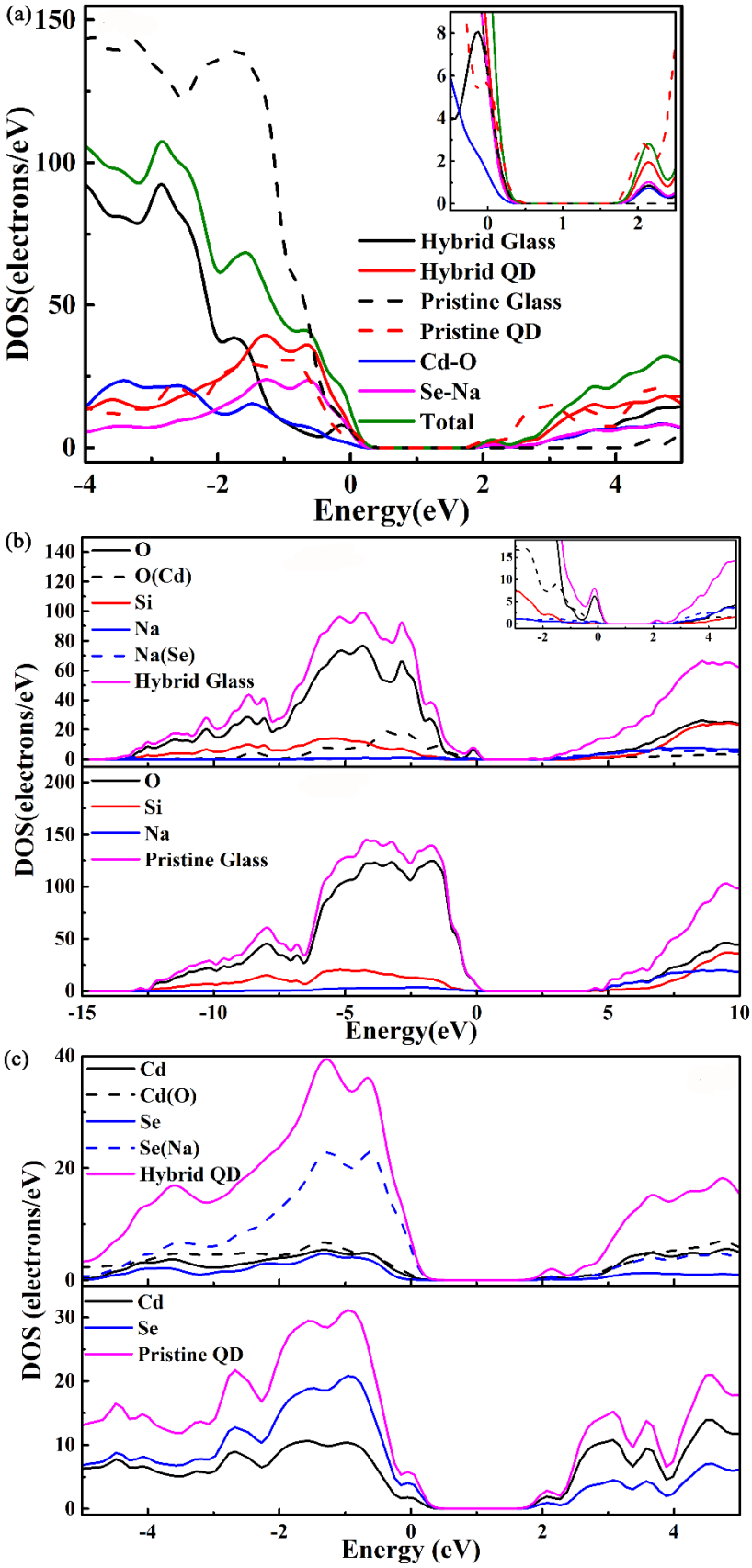
(a)
DOS(electrons/eV)
Energy(eV)
Hybrid Glass
Hybrid QD
Pristine Glass
Pristine QD
Cd-O
Se-Na
Total
(b)
DOS(electrons/eV)
Energy(eV)
O
O(Cd)
Si
Na
Na(Se)
Hybrid Glass
O
Si
Na
Pristine Glass
(c)
DOS (electrons/eV)
Energy (eV)
Cd
Cd(O)
Se
Se(Na)
Hybrid QD
Cd
Se
Pristine QD

Figure 6.10 This configuration was obtained from the AIMD production run with x = 0.33 at 7 ps. (a) The density of states of hybrid glass, hybrid QD, pristine QD, pristine glass (x= 0.33), Cd-O bonds and Se-Na bonds. (b) The density of states of the hybrid glasses and pristine glasses (x =0.33). (c) The density of states of the hybrid QD and the pristine QD.

6.4 Summary & conclusions

To the best of my knowledge, my calculations are the first realistic electronic structure calculations of CdSe quantum dot-doped glasses, which is of prominent importance of exploring their optical properties. By varying the amount of the sodium oxygen in xNa$_2$O-(1-x)SiO$_2$ glass matrices, the compositional dependency of structural reconstruction and luminescence mechanisms was illustrated.

The additional introduction of Na$_2$O promotes the formation of Cd-O bonds and Se-Na bonds, breaking some Cd-Se bonds. We extend here the results of the previous chapter by studying this impact of glass composition. Meanwhile, the luminescence mechanisms show an important dependency on the composition of the glass matrices. When x = 0, 0.25, 0.5, the HOMO is decided by the hybrid QD, while the HOMO is determined by the hybrid glasses in most configurations of x = 0.33.

The existence of the CdSe QD sharply decreases the bandgap of the glass in the interface between CdSe QD and glass matrices compared with pristine glasses. The interfacial bonds contribute greatly to the frontier orbitals, without forming midgap states within the HOMO-LUMO gap. Besides, the HOMO-LUMO gap show a broader distribution in x = 0.33 compared with other compositions. The spatial separation of the holes and electrons in most configurations of x = 0.33 and its wide HOMO-LUMO distribution, predicting the low quantum efficiency of this composition.

In particular, given the atomic structure, HOMO-LUMO gap distribution and density of states of the CdSe quantum dot-doped glasses, it is apparent that there is little possibility of the existence of the pristine QD, demonstrating no intrinsic emission from the pristine QD. Thus, a totally new energy diagram model is proposed, much different from the colloidal QD and the model generally proposed in the literature by the experimentalists fabricating CdSe quantum dot-doped glasses. The CdSe QD is

surrounded by the glass matrices, where the structural reconstruction happens, forming the structure of hybrid QD and hybrid glasses. Due to the low concentration of the QDs in glass matrices, these hybrid system only exist in micro regions, surrounded by the dense amorphous pristine glass matrix, acting as a shell towards the hybrid systems composed of hybrid QD and hybrid glasses. Therefore, the emission of the CdSe quantum dot-doped glasses originate from the intrinsic emission of the hybrid systems, rather than the intrinsic and defect emission from the pristine QD and its trap states in traditional model.

Our results answered why the quantum efficiency of CdSe quantum dot-doped glass is much lower than their colloidal part. On the one hand, there is no intrinsic emission from the pristine QD due to the strong impact of the glass matrices on CdSe QD. On the other hand, from the experimental part, the glass is inhomogeneous in microscopic regions due to the fluctuation of the thermal condition and composition. Even with the same composition of these hybrid systems, the electronic structures of each configuration was variable, exhibiting different optical properties, resulting in the broad emission.

My results demonstrate that the composition of glass matrix is of significant importance on the optical properties of CdSe QD. Therefore, the compositional design of glass matrix is supposed to be taken into consideration if we want to obtain highly luminescent glasses. The ratio of sodium should be adjusted cautiously from experimental part, but the role of Na ions as glass modifiers also should be taken into consideration. It is suggested that x = 0.33 may not be a desirable ratio for the glass matrix, and x=0.25 would be a good choice. For one thing, the melting point of fabricating the CdSe quantum dots doped glasses will not be too high for glass with composition of x= 0.25. For another thing, the standard deviation is 0.13 eV, which is smaller compared with other compositions, indicating sharper emission peaks. Moreover, the HOMO and LUMO orbitals are determined by hybrid QD, resulting in the higher possibility of intrinsic luminescence.

Chapter 7

7 Conclusions and perspectives

7.1 Conclusions

CdSe quantum dots doped glasses combines the excellent mechanical, thermal, and chemical stability of glasses matrix with the remarkable optical properties of CdSe quantum dots. However, the development of these materials is restricted by its poor quantum efficiency, which reason is challenging to be investigated from experimental parts. In this thesis, multiscale methodologies have been developed in this thesis to probe the structural and electronic origins of defect emission of CdSe quantum dots doped glasses.

In the first stage of the studies, a simplified model was built by capping the Cd_nSe_n (n = 3, 10, 13, and 33) clusters with non-bridging oxygen atoms and glass modifiers (Na, Ca, Zn), apart from which the intrinsic defects were also explored by capping with Se atoms and Cd atoms. Based on the geometry optimization results and electronic structures calculation under the DFT framework, the adatoms were found to contribute to enormous structural reconstruction and paired defect states at the edge of the valence and conduction band, resulting the redistribution of HOMO and LUMO orbitals. Most importantly, Na ions were found sharply decrease the HOMO-LUMO gap from 2.84 eV to 1.2 eV, leading to the near-infrared photoluminescence, which has been proved by experiments.

However, these simplified model was far from the real interfacial structure between the CdSe QD and glass matrix, and the passivation of the surface atoms was intended, which cannot really reflect the impact of the glass matrix on CdSe QD. Thus, CdSe QD was supposed to be directly introduced to the glass matrix to give a straightforward illustration of the local atomic structures of CdSe quantum dot-doped glasses.

In the second stage, the structures of glass matrix have been obtained from melt-quenching method using classical molecular dynamics simulation. The parameters of pairwise potential and thermal process have been adjusted by reproducing the radial

distribution functions with high accuracy and quality compared with experimental findings.

Then, the CdSe QD was incorporated into the glass matrix by a combination of classical molecular dynamics and *ab initio* molecular dynamics. Based on the analysis of radial distribution functions, coordination environment and ring structures, an important structural reconstruction occurs at the interface between the CdSe QD and glass matrix, with the formation of Cd-O and Se-Na bonds and breakages of some Na-O and Cd-Se bonds. The structural properties and bond length were in excellent agreement with experimental observations, enhancing better understanding of interactions between CdSe QD and glass matrix.

Finally, the electronic structures of CdSe quantum dots doped glasses have been studied with emphasis on the impact of glass compositions on the optical properties of the whole system. The types of luminescence mechanisms depended on the compositions of glass. In all the configurations with sodium content equal to 0, 0.25 and 0.5, both the top of valence band and bottom of conduction band was decided by hybrid QD. But in most configurations with sodium content equal to 0.33, the top of the valence band was determined by hybrid glass, indicating the indirect recombination of holes and electrons. Importantly, based on the analysis of structures, HOMO-LUMO gap distributions and density of states, my results provided a new explanation to the photoluminescence, which was originated from the intrinsic emission of these hybrid systems rather than the combination of defect emission and intrinsic emission of pristine CdSe QDs.

The results of this thesis explained why the quantum efficiency of the glass matrix was so low. First of all, the sufficient supply of non-bridging oxygen and glass modifiers provided abundant source of defects of CdSe QDs by forming the interfacial bonds such as Se-Na and Cd-O bands. These strong interactions between glass matrix and CdSe QD resulted in the enormous structural reconstruction of CdSe QD, thus the disappearance of pristine QD. Secondly, even with the same composition, the inhomogeneous nature in glass microstructures contributed to various interfacial structures, leading to the different energy the diagram, further resulting in the broad emission of CdSe quantum dots doped glasses.

To the best of my knowledge, the methodology I developed in this thesis was the first computational study of the local atomic structure and electronic structure of CdSe

quantum dot-doped glasses. These results significantly extend our understanding of the interfacial structure of CdSe QD-doped glasses, and provide physical and chemical insight into the possible defect structure origin of CdSe QD, of interest to the fabrication of the highly luminescent CdSe QD-doped glasses.

7.2 Perspectives

In future work, various glass systems will be studied since I only focused on the sodium silicate glass matrix while the glass components are much more complex in experimental fabrication. Glass structure with multiple components (such as CaO, Al_2O_3, and ZnO) will be built to study the effect of the glass matrix.

Sodium ions were found to be detrimental to the optical properties of CdSe QDs in my study by altering the networks of glass matrix and further the structure of CdSe QD and forming defect states with high possibility of defect emission. These results can give guidance for the adjustment of the component of the glass matrix and the fabrication of highly luminescent CdSe QD-doped glasses. For example, my work suggest that it is worth adjusting the amount of sodium in the glass composition to neglect the unfavorable defect emission. At the same time, I recommend reaching a compromise between the low sodium contents and melting temperature because sodium can alter the melting point of glass. The sodium content equal to 0.33 would not be a good trial composition.

Besides, my results demonstrated that the surface Cd atoms are more likely to be passivated by the oxygen in the glass matrix, which may provide possibilities of fabricating core-shell CdSe QDs by adjusting the thermal treatment. The fabrication of a core-shell structure of CdSe QDs is more difficult and less explored compared with colloidal quantum dots.

I also aim at studying more in depth the influence of the QD size on the nature of the QD/glass interface and the properties of the hybrid system. While the influence of QD size on its emission properties is well known for QDs in solution, the nature of the interface reconstruction for QDs embedded in glass matrices is not currently known. I expect, from the results obtained in this thesis, that the interfacial reconstruction remains similar: it is, after all, linked in large part not to the system size but to the

nature of the competition between Cd-Se, Cd-O, and Na-O interactions. However, because the surface/bulk ratio is directly linked to the size of the QD, the properties of the composite systems would be affected. While it is not currently possible to explore larger QD sizes at the level of theory chosen here (*ab initio* molecular dynamics), studies using QM/MM strategies could be of use in order to directly address the question of larger quantum dot sizes.

All of my calculations about the electronic structures of CdSe quantum dot-doped glasses were based on time-independent density functional theory. With the development of the computational power and algorithm, time-dependent functional theory (TD-DFT) can reasonably simulate the excited process in QDs, allowing for inclusions of electron-hole interactions at moderate computational time. The excellent description of qualitative trend in optical response to stoichiometry and ligand modifications of CdSe QDs has been reported in other researcher's work.

In my future work, I want to probe the optical active or inactive nature of these hybridized states obtained in this thesis under the TD-DFT framework, which can predicts the qualitative trends in lower-energy optical transitions. There are a lot of questions remaining to be answered in the realm of CdSe QDs. With the help of computational simulation, one can expect its suggestion to the adjustment of the fabrication method of quantum dots doped glasses to achieve its potential application.

Bibliography

1. Pietryga, J. M.; Park, Y. S.; Lim, J.; Fidler, A. F.; Bae, W. K.; Brovelli, S.; Klimov, V. I., Spectroscopic and Device Aspects of Nanocrystal Quantum Dots. *Chem Rev* **2016,** *116* (18), 10513-622.
2. Brus, L. E., A Simple Model for the Ionization Potential, Electron Affinity, and Aqueous Redox Potentials of Small Semiconductor Crystallites. *J Chem Phys* **1983,** *79* (11), 5566-5571.
3. Pu, Y.; Cai, F.; Wang, D.; Wang, J.-X.; Chen, J.-F., Colloidal Synthesis of Semiconductor Quantum Dots toward Large-Scale Production: A Review. *Ind Eng Chem Res* **2018,** *57* (6), 1790-1802.
4. Reda, S. M., Synthesis and Optical Properties of CdS Quantum Dots Embedded in Silica Matrix Thin Films and Their Applications as Luminescent Solar Concentrators. *Acta Mater* **2008,** *56* (2), 259-264.
5. Huang, F.; Hou, J.; Wang, H.; Tang, H.; Liu, Z.; Zhang, L.; Zhang, Q.; Peng, S.; Liu, J.; Cao, G., Impacts of Surface or Interface Chemistry of ZnSe Passivation Layer on the Performance of CdS/CdSe Quantum Dot Sensitized Solar Cells. *Nano Energy* **2017,** *32*, 433-440.
6. Colvin, V. L.; Schlamp, M. C.; Allvlsatos, A. P., Light-emitting Diodes made from Cadmium Selenide Nanocrystals and a Semiconducting Polymer. *Nature* **1994,** *370* (354-356).
7. VanWie, T.; Wysocki, E.; McBride, J. R.; Rosenthal, S. J., Bright Cool White Emission from Ultrasmall CdSe Quantum Dots. *Chem Mater* **2019,** *31* (20), 8558-8562.
8. Yang, Y.; Zheng, Y.; Cao, W.; Titov, A.; Hyvonen, J.; Manders, J. R.; Xue, J.; Holloway, P. H.; Qian, L., High-efficiency Light-Emitting Devices based on Quantum Dots with Tailored Nanostructures. *Nat Photonics* **2015,** *9* (4), 259-266.
9. Snee, P. T., The Role of Colloidal Stability and Charge in Functionalization of Aqueous Quantum Dots. *Acc Chem Res* **2018,** *51* (11), 2949-2956.
10. Wichner, S. M.; Mann, V. R.; Powers, A. S.; Segal, M. A.; Mir, M.; Bandaria, J. N.; DeWitt, M. A.; Darzacq, X.; Yildiz, A.; Cohen, B. E., Covalent Protein Labeling and Improved Single-Molecule Optical Properties of Aqueous CdSe/CdS Quantum Dots. *ACS Nano* **2017,** *11* (7), 6773-6781.
11. Voznyy, O.; Sargent, E. H., Atomistic Model of Fluorescence Intermittency of Colloidal Quantum Dots. *Phys Rev Lett* **2014,** *112* (15), 157401.
12. Li, W.; Zhang, W.; Xia, M.; Liu, C.; Wang, J., Optical Properties and Charge Carrier Dynamics of CdTe Quantum Dots in Silicate Glasses. *J Appl Phys* **2017,** *121* (18), 183104.
13. Heuer-Jungemann, A.; Feliu, N.; Bakaimi, I.; Hamaly, M.; Alkilany, A.; Chakraborty, I.; Masood, A.; Casula, M. F.; Kostopoulou, A.; Oh, E.; Susumu, K.; Stewart, M. H.; Medintz, I. L.; Stratakis, E.; Parak, W. J.; Kanaras, A. G., The Role of Ligands in the Chemical Synthesis and Applications of Inorganic Nanoparticles. *Chem Rev* **2019,** *119* (8), 4819-4880.
14. Kilina, S.; Kilin, D.; Tretiak, S., Light-Driven and Phonon-Assisted Dynamics in Organic and Semiconductor Nanostructures. *Chem Rev* **2015,** *115* (12), 5929-78.
15. Xu, L.; Liang, H. W.; Yang, Y.; Yu, S. H., Stability and Reactivity: Positive and Negative Aspects for Nanoparticle Processing. *Chem Rev* **2018,** *118* (7), 3209-3250.
16. Ghosh Chaudhuri, R.; Paria, S., Core/shell Nanoparticles: Classes, Properties, Synthesis Mechanisms, Characterization, and Applications. *Chem Rev* **2012,** *112* (4), 2373-433.
17. Ekimov, A. I.; Onushchenko, A. A., Quantum Size Effect in Three-Dimensional Microscopic Semiconductor Crystals. *JETP Lett* **1981,** *34*, 345-348.
18. Li, Y.; Cui, R.; Zhang, P.; Chen, B. B.; Tian, Z. Q.; Li, L.; Hu, B.; Pang, D. W.; Xie, Z. X., Mechanism-oriented Controllability of Intracellular Quantum Dots Formation: the Role of Glutathione Metabolic Pathway. *ACS Nano* **2013,** *7* (3), 2240-8.
19. Zhu, Y. J.; Chen, F., Microwave-assisted Preparation of Inorganic Nanostructures in Liquid Phase. *Chem Rev* **2014,** *114* (12), 6462-555.
20. Arachchige, I. U.; Brock, S. L., Sol-gel methods for the assembly of metal chalcogenide quantum dots. *Acc Chem Res* **2007,** *40* (9), 801-9.
21. Rossetti, R.; Ellison, J. L.; Gibson, J. M.; Brus, L. E., Size Effects in the Excited Electronic States of Small Colloidal CdS Crystallites. *J Chem Phys* **1984,** *80* (9), 4464-4469.

22. Rogach, A. L.; Kornowski, A.; Gao, M.; Eychmüller, A.; Weller, H., Synthesis and Characterization of a Size Series of Extremely Small Thiol-Stabilized CdSe Nanocrystals. *J Phys Chem B* **1999,** *103* (16), 3065-3069.
23. Murray, C. B.; Norris, D. J.; Bawendi, M. G., Synthesis and Characterization of Nearly Monodisperse CdE（E = S,Se, Te）Semiconductor Nanocrystallites. *J Am Chem Soc* **1993,** *115*, 8705-8715.
24. Peng, Z. A.; Peng, X., Formation of High-Quality CdTe, CdSe, and CdS Nanocrystals Using CdO as Precursor. *J Am Chem Soc* **2001,** *123* (1), 183-184.
25. Qu, L.; Peng, Z. A.; Peng, X., Alternative Routes toward High Quality CdSe Nanocrystals. *Nano Lett* **2001,** *1* (6), 333-337.
26. Deng, Z.; Cao, L.; Tang, F.; Zou, B., A New Route to Zinc-Blende CdSe Nanocrystals: Mechanism and Synthesis. *J. Phys. Chem. B* **2005,** *109*, 16671-16675.
27. Ouyang, J.; Zaman, M. B.; Yan, F.; Johnston, D.; Li, G.; Wu, X.; Leek, D.; Ratcliffe, C. I.; Ripmeester, J. A.; Yu, K., Multiple Families of Magic-Sized CdSe Nanocrystals with Strong Bandgap Photoluminescence via Noninjection One-Pot Syntheses. *J Phys Chem C* **2008,** *112* (36), 13805-13811.
28. Guerreiro, P. T.; Ten, S.; Borrelli, N. F.; Butty, J.; Jabbour, G. E.; Peyghambarian, N., PbS Quantum-Dot Doped Glasses as Saturable Absorbers for Mode Locking of a Cr:forsterite laser. *Appl Phys Lett* **1997,** *71* (12), 1596-1597.
29. Han, K.; Yoon, S.; Chung, W. J., CdS and CdSe Quantum Dot-Embedded Silicate Glasses for LED Color Converter. *Int J Appl Glass Sci* **2015,** *6* (2), 103-108.
30. Han, K.; Im, W. B.; Heo, J.; Chung, W. J., A Complete Inorganic Colour Converter Based on Quantum-Dot-Embedded Silicate Glasses for White Light-Emitting-Diodes. *Chem Commun (Camb)* **2016,** *52* (17), 3564-7.
31. Wang, Y.; Yao, X.; Wang, M.; Kong, F.; He, J., Optical Responses of ZnSe Quantum Dots in Silica Gel Glasses. *J Cryst Growth* **2004,** *268* (3-4), 580-584.
32. Mashford, B.; Baldauf, J.; Nguyen, T.-L.; Funston, A. M.; Mulvaney, P., Synthesis of Quantum Dot Doped Chalcogenide Glasses via Sol-Gel Processing. *J Appl Phys* **2011,** *109* (9), 094305.
33. Jiang, H.; Yao, X.; Che, J.; Wang, M.; Kong, F., Preparation of ZnSe Quantum Dots Embedded in SiO_2 Thin Films by Sol–Gel Process. *Ceram Int* **2004,** *30* (7), 1685-1689.
34. El Boukhari, T.; Kaygusuz, H.; Bilir, G.; Erim, F. B.; Özen, G., Microstructural and Optical Properties of SiO_2 Glasses Doped with ZnSe Quantum dots and Nd^{3+} Ions. *Physica B: Condensed Matter* **2017,** *509*, 41-45.
35. Mazzoldi, P.; Arnold, G. W.; Battaglin, G.; Gonella, F.; R. F. Haglund, J., Metal Nanoclusters Formation by Ion Implantation in Silicate Glasses: Nonlinear Optical Applications. *J Nonlinear Opt Phys* **1996,** *5* (2), 285-330.
36. J. K. Lee; C. R. Tewell; R. K. Schulze; M. Nastasi; D. W. Hamby; D. A. Lucca; H. S. Jung; Hong, K. S., Synthesis of ZnO Nanocrystals by Subsequent Implantation of Zn and O Species. *Appl Phys Lett* **2005,** *86*, 183111.
37. Bell, G.; Filin, A. I.; Romanov, D. A.; Levis, R. J., Direct Growth of CdSe Semiconductor Quantum Dots in Glass Matrix by Femtosecond Laser Beam. *Appl Phys Lett* **2016,** *108* (6), 063112.
38. Manikandan, D.; Mohan, S.; Nair, K. G. M., Photoluminescence of Embedded Copper Nanoclusters in Soda-Lime Glass. *Mater Lett* **2003,** *57* (8), 1391-1394.
39. Xia, M.; Luo, J.; Chen, C.; Liu, H.; Tang, J., Semiconductor Quantum Dots - Embedded Inorganic Glasses: Fabrication, Luminescent Properties, and Potential Applications. *Adv Opt Mater* **2019,** *7* (21), 1900851.
40. Liu, L.-C.; Kim, M. J.; Risbudand, S. H.; Carpenter, R. W., High-resolution Electron Microscopy and Microanalysis of CdS and CdTe Quantum Dots in Glass Matrices.Philos Mag B **2006,** *63* (3), 769-776.
41. Nagpal, S., CdS Quantum Dots in a Novel Glass with a Very Low Activation Energy and its Variation of Diffusivity with Temperature. *J Nanopart Res* **2011,** *13* (7), 2733-2741.
42. Sonawane, R. S.; Naik, S. D.; Apte, S. K.; Kulkarni, M. V.; Kale, B. B., CdS/CdSSe Quantum Dots in Glass Matrix. *Bull. Mater. Sci.* **2008,** *31* (3), 495–499.
43. Fuyu, Y.; Parker, J. M., Quantum Size Effects in Heat Treated Cd(S, Se) Doped Glasses. *Mater Lett*

1988, *6*, 233-237.
44. Y¨ukselici, M. H., Two Different Mechanisms of Formation of Quantum Dots in Borosilicate Glass. *J Phys: Condensed Matter* **2001,** (13), 6123–6131.
45. Demourgues, A.; Greaves, G. N.; Bilsborrow, R.; Baker, G.; Sery, A.; Dent, A. J.; Speit, B., Evolution of Cadmium Chalcogen Quantum Dots in Silicate Glasses. *Physica B* **1995,** *208&209*, 354-356.
46. Lee, Y. K.; Choi, Y. G.; Heo, J.; Chung, W. J.; Ballato, J., Compositional Dependence of CdSe Quantum Dot Formation on Silicate Host Glass Composition. *J Amer Ceram Soc* **2013,** *96* (12), 3868-3871.
47. Liu, L. C.; Risbud, S. H., Quantum - dot size - Distribution Analysis and Precipitation Stages in Semiconductor Doped Glasses. *J Appl Phys* **1990,** *68* (1), 28-32.
48. Xia, M.; Liu, C.; Xu, Y.; Zhao, X., Effect of Al_2O_3 on the Formation of Color Centers and CdSe/Cd $_{1-x}$ Zn_x Se Quantum Dots in SiO_2-Na_2O-ZnO Glasses. *J Amer Ceram Soc* **2019,** *102* (4), 1726-1733.
49. Miiller, M.; Woggon, U., Direct Spectroscopic Investigation of Phase Formation in Glasses Containing Semiconductor Microcrystals in Correlation to their Luminescence Properties. *Ber. Bunsenges. Phys. Chem.* **1996,** *100* (9), 1446-1449.
50. Lipatova, Z. O.; Kolobkova, E. V.; Babkina, A. N., Luminescent Properties of Cadmium Selenide Quantum Dots in Fluorophosphate Glasses.Opt Spectrosc**2016,** *121* (5), 713-721.
51. Chang, J.; Liu, C.; Heo, J., Optical Properties of PbSe Quantum Dots Doped in Borosilicate Glass. *J Non-Cryst Solids* **2009,** *355* (37-42), 1897-1899.
52. Ju, S.; Watekar, P. R.; Kim, C. J.; Han, W.-T., Particle Size Control of PbTe Quantum Dots Incorporated in the Germano-Silicate Glass Optical Fiber by Heat Treatment. *J Non-Cryst Solids* **2010,** *356* (43), 2273-2276.
53. Liu, C.; Heo, J.; Zhang, X.; Adam, J.-L., Photoluminescence of PbS Quantum Dots Embedded in glasses. *J Non-Cryst Solids* **2008,** *354* (2-9), 618-623.
54. Ai, B.; Liu, C.; Wang, J.; Xie, J.; Han, J.; Zhao, X., Precipitation and Optical Properties of $CsPbBr_3$ Quantum Dots in Phosphate Glasses. *J Amer Ceram Soc* **2016,** *99* (9), 2875-2877.
55. Ye, Y.; Zhang, W.; Zhao, Z.; Wang, J.; Liu, C.; Deng, Z.; Zhao, X.; Han, J., Highly Luminescent Cesium Lead Halide Perovskite Nanocrystals Stabilized in Glasses for Light - Emitting Applications. *Adv Opt Mater* **2019,** *7* (9), 1801633.
56. Ekimov, A. I.; Onushchenko, A. A., Size Quantization of the Electron Energy Spectrum in Microscopic Semiconductor Crystal. *JETP Lett* **1984,** *40*, 1136-1139.
57. Demourgues, A.; Greaves, G. N.; Bilsborrow, R.; Baker, G.; Sery, A.; Speit, B., XAFS study of CdSe Quantum Dots in a Silicate Glass. *Nucl Instrum Meth B* **1995,** *97*, 166-168.
58. Choi, J.; Park, B. J.; Choi, Y. G.; Heo, J.; Chung, W. J., Compositional Dependence of Se^{2-} Color Center Formation in Silicate Glasses. *J Non-Cryst Solids* **2013,** *377*, 70-73.
59. Munishwar, S. R.; Pawar, P. P.; Gedam, R. S., Influence of Electron-Hole Recombination on Optical Properties of Boro-Silicate Glasses Containing CdS Quantum Dots. *J Lumin* **2017,** *181*, 367-373.
60. Xu, K.; Heo, J., New Functional Glasses Containing Semiconductor Quantum Dots. *Phys Scripta* **2010,** *T139*, 014062.
61. Xu, K.; Liu, C.; Chung, W. J.; Heo, J., Optical Properties of CdSe Quantum Dots in Silicate Glasses. *J Non-Cryst Solids* **2010,** *356* (44-49), 2299-2301.
62. Morcos, R. M.; Mitterbauer, C.; Browning, N.; Risbud, S.; Navrotsky, A., Energetics of CdS_xSe_{1-x} Quantum Dots in Borosilicate Glasses. *J Non-Cryst Solids* **2007,** *353* (29), 2785-2795.
63. Hwang, Y.-N.; Shin, S.; Park, H. L.; Park, S.-H.; Kim, U., Effect of Lattice Contraction on the Raman shifts of CdSe Quantum Dots in Glass Matrices. *Phys Rev B* **1996,** *54* (21), 15120-15124.
64. Padilha, L. A.; Neves, A. A. R.; Cesar, C. L.; Barbosa, L. C.; Cruz, C. H. B., Recombination Processes in CdTe Quantum-Dot-Doped Glasses. *Appl Phys Lett* **2004,** *85* (15), 3256-3258.
65. Gaponenko, S. V.; Woggon, U.; M. Saleh; Langbein, W.; Uhrig, A.; Muller, M.; Klingshirn, C., Nonlinear-optical Properties of Semiconductor Quantum Dots and their Correlation with the Precipitation Stages. *J. Opt. Soc. Am. B* **1993,** *10*, 1947-1954.
66. Woggon, U.; Wind; Gindele, F.; Tsitsishvilib, E.; Miller, M., Optical Transitions in CdSe quantum dot-From Discrete Levels to Broad Gain Spectra. *J Lumin* **1996** *70*, 269-280.

67. Esch, V.; Kang, K.; Fulegel, B.; Hu, Y. Z.; Khitrova, G.; Gibbs, H. M.; Koch, S. W.; Peygambarain, N.; Liu, L. C.; Risbud, S. H., Optical Properties of CdTe and CdS Quantum Dots in Glass. *Int J Nonliear Opt Phys* **1992**, *1*, 25-50.
68. T. Tokizaki; Akiyama, H.; Takaya, M.; Nakamura, A., Linear and Nonlinear Optical Properties of CdSe Microcrystallites in glasses. *J Cryst Growth* **1992,** *117*, 603-607.
69. Tanaka, A.; Onari, S.; Arai, T., Raman Scattering from CdSe Microcrystals Embedded in a Germanate Glass Matrix. *Phys Rev B* **1992,** *45* (12), 6587-6592.
70. Hwang, Y.-N.; Park, S.-H., Size-dependent Surface Phonon Mode of CdSe quantum dots. *Phys Rev B* **1999,** *59* (11), 7285-7288.
71. Scamarcio, G.; Lugara, M.; Manno, D., Size-dependent Lattice Contraction in $CdS_{1-x}Se_x$ Nanocrystals Embedded in Glass Observed by Raman Scattering. *Phys Rev B* **1992,** *45* (23), 13792-13795.
72. Xia, M.; Liu, C.; Zhao, Z.; Wang, J.; Lin, C.; Xu, Y.; Heo, J.; Dai, S.; Han, J.; Zhao, X., Surface Passivation of CdSe Quantum Dots in All Inorganic Amorphous Solid by Forming $Cd_{1-x}Zn_xSe$ Shell. *Sci Rep* **2017,** *7*, 42359.
73. A.N.CORMACKA; Cao, Y., Molecular Dynamics Simulation of Silicate Glasses. *Mol Eng* **1996,** *6*, 183-227.
74. Horbach, J.; Kob, W.; Binder, K., Structural and Dynamical Properties of Sodium Silicate Melts: an Investigation by Molecular Dynamics Computer Simulation. *Chem Geol* **2001,** *174*, 87–101.
75. MORGAN, N. A.; SPERA, F. J., Glass Transition, Structural Relaxation, and Theories of Viscosity: A Molecular Dynamics Study of Amorphous $CaAl_2Si_2O_8$. *Geochim Cosochim Ac* **2001,** *65*, 4019-4041.
76. Cormack, A. N.; Du, J.; Zeitler, T. R., Alkali Ion Migration Mechanisms in Silicate Glasses Probed by Molecular Dynamics Simulations. *Phys Chem Chem Phys* **2002,** *4* (14), 3193-3197.
77. Lusvardi, G.; Malavasi, G.; Menabue, L.; Menziani, M. C., Synthesis, Characterization, and Molecular Dynamics Simulation Of Na_2O-CaO-SiO_2-ZnO Glasses. *J Phys Chem B* **2002,** *106*, 9753-9760.
78. Cormack, A. N.; Du, J.; Zeitler, T. R., Sodium Ion Migration Mechanisms in Silicate Glasses Probed by Molecular Dynamics Simulations. *J Non-Cryst Solids* **2003,** *323* (1-3), 147-154.
79. Du, J.; Cormack, A. N., The Medium Range Structure of Sodium Silicate Glasses: a Molecular Dynamics Simulation. *J Non-Cryst Solids* **2004,** *349*, 66-79.
80. Du, J.; Corrales, L. R., Compositional Dependence of the First Sharp Diffraction Peaks in Alkali Silicate Glasses: A Molecular Dynamics Study. *J Non-Cryst Solids* **2006,** *352* (30-31), 3255-3269.
81. Tilocca, A.; Cormack, A. N.; Leeuw, N. H. d., The Structure of Bioactive Silicate Glasses: New Insight from Molecular Dynamics Simulations. *Chem. Mater.* **2007,** *19*, 95-103.
82. Du, J., Molecular Dynamics Simulations of the Structure and Properties of Low Silica Yttrium Aluminosilicate Glasses. *J Amer Ceram Soc* **2009,** *92* (1), 87-95.
83. Bouhadja, M.; Jakse, N.; Pasturel, A., Structural and Dynamic Properties of Calcium Aluminosilicate Melts: a Molecular Dynamics Study. *J Chem Phys* **2013,** *138* (22), 224510.
84. Xiang, Y.; Du, J.; Smedskjaer, M. M.; Mauro, J. C., Structure and Properties of Sodium Aluminosilicate Glasses from Molecular Dynamics Simulations. *J Chem Phys* **2013,** *139* (4), 044507.
85. Zhang, C.-H.; Wang, Y.; Sun, D.-B., The Molecular Dynamics Simulation on the mechanical Properties of Ni Glass with External Pressure. *Int J Mod Phys B* **2017,** *31* (20).
86. Pedone, A.; Tavanti, F.; Malavasi, G.; Menziani, M. C., An Atomic-Level Look at the Structure-Property Relationship of Cerium-Doped Glasses Using Classical Molecular Dynamics. *J Non-Cryst Solids* **2018,** *498*, 331-337.
87. Shih, Y.-T.; Jean, J.-H., Composition-structure-properties Relationship of Lithium-Calcium Borosilicate Glasses Studied by Molecular Dynamics Simulation. *Ceram Int* **2018,** *44* (10), 11554-11561.
88. Soules, T. F., A Molecular Dynamic Calculation of the Structure of Sodium Silicate Glasses. *J Chem Phys* **1979,** *71* (11), 4570-4578.
89. Soules, T. F.; Busbey, R. F., Sodium Diffusion in Alkali Silicate Glass by Molecular Dynamics. *J Chem Phys* **1981,** *75* (2), 969-975.
90. Van Beest, B. W.; Kramer, G. J.; Van Santen, R. A., Force fields for Silicas and Aluminophosphates Based on *Ab Initio* Calculations. *Phys Rev Lett* **1990,** *64* (16), 1955-1958.

91. Pedone, A.; Malavasi, G.; Menziani, M. C.; Cormack, A. N.; Segre, U., A New Self-Consistent Empirical Interatomic Potential Model for Oxides,Silicates and Silica-Based Glasses. *J Phys Chem B* **2006,** *110*, 11780-11795.
92. Tilocca, A.; de Leeuw, N. H.; Cormack, A. N., Shell-model molecular dynamics calculations of modified silicate glasses. *Phys Rev B* **2006,** *73* (10), 104209.
93. Lei, X.; Jee, Y.; Huang, K., Amorphous Na2Si2O5 as a fast Na+ conductor: an ab initio molecular dynamics simulation. *J Mater Chem A* **2015,** *3* (39), 19920-19927.
94. Tilocca, A.; de Leeuw, N. H., Structural and electronic properties of modified sodium and soda-lime silicate glasses by Car–Parrinello molecular dynamics. *J. Mater. Chem.* **2006,** *16* (20), 1950-1955.
95. Baral, K.; Li, A.; Ching, W. Y., Ab Initio Modeling of Structure and Properties of Single and Mixed Alkali Silicate Glasses. *J Phys Chem A* **2017,** *121* (40), 7697-7708.
96. Konstantinou, K.; Sushko, P. V.; Duffy, D. M., Modelling the local atomic structure of molybdenum in nuclear waste glasses with ab initio molecular dynamics simulations. *Phys Chem Chem Phys* **2016,** *18* (37), 26125-26132.
97. Ishii, Y.; Salanne, M.; Charpentier, T.; Shiraki, K.; Kasahara, K.; Ohtori, N., A DFT-Based Aspherical Ion Model for Sodium Aluminosilicate Glasses and Melts. *J Phys Chem C* **2016,** *120* (42), 24370-24381.
98. Konstantinou, K.; Duffy, D. M.; Shluger, A. L., Structure and Luminescence of Intrinsic Localized States in Sodium Silicate Glasses. *Phys Rev B* **2016,** *94* (17).
99. Murray, R. A., Electronic Structure of Sodium Silicate Glasses. *J Non-Cryst Solids* **1987,** *95*, 144-159.
100. Baral, K.; Adhikari, P.; Ching, W. Y.; Sinnott, S., *Ab initio* Modeling of the Electronic Structures and Physical Properties of a - Si_{1-x} Ge_xO_2 Glass (x = 0 to 1). *J Amer Ceram Soc* **2016,** *99* (11), 3677-3684.
101. Baral, K.; Ching, W.-Y., Electronic Structures and Physical Properties of Na_2O Doped Silicate Glass. *J Appl Phys* **2017,** *121* (24).
102. Yu, M.; Fernando, G. W.; Li, R.; Papadimitrakopoulos, F.; Shi, N.; Ramprasad, R., First principles study of CdSe quantum dots: Stability, Surface Unsaturations, and Experimental Validation. *Appl Phys Lett* **2006,** *88* (23).
103. Puzder, A.; Williamson, A. J.; Zaitseva, N.; Galli, G.; Manna, L.; Alivisatos, A. P., The Effect of Organic Ligand Binding on the Growth of CdSe Nanoparticles Probed by *Ab Ini*tio Calculations. *Nano Letters* **2004,** *4* (12), 2361-2365.
104. Jose, R.; Zhanpeisov, N. U.; Fukumura, H.; Baba, Y.; Ishikawa, M., Structure-Property Correlation of CdSe Clusters Using Experimental Results and First-Principles DFT Calculations. *J Am Chem Soc* **2006,** *128*, 629-626.
105. Nguyen, K. A.; Pachter, R.; Day, P. N., Computational Prediction of Structures and Optical Excitations for Nanoscale Ultrasmall ZnS and CdSe Clusters. *J Chem Theory Comput* **2013,** *9* (8), 3581-96.
106. Voznyy, O.; Mokkath, J. H.; Jain, A.; Sargent, E. H.; Schwingenschlögl, U., Computational Study of Magic-Size CdSe Clusters with Complementary Passivation by Carboxylic and Amine Ligands. *J Phys Chem C* **2016,** *120* (18), 10015-10019.
107. Wang, X.; Zeng, Q.; Shi, J.; Jiang, G.; Yang, M.; Liu, X.; Enright, G.; Yu, K., The Structure and Optical Absorption of Single Source Precursors for II-VI Quantum Dots. *Chem Phys Lett* **2013,** *568-569*, 125-129.
108. Yu, S.; Huang, D.; Withanage, K., Computational Insights into Structural and Optical Properties of P-containing and N-containing Ligands capped CdSe Clusters. *Mol Simulat* **2019,** *45* (17), 1426-1431.
109. Houtepen, A. J.; Hens, Z.; Owen, J. S.; Infante, I., On the Origin of Surface Traps in Colloidal II–VI Semiconductor Nanocrystals. *Chem Mater* **2017,** *29* (2), 752-761.
110. Kamisaka, H.; Kilina, S. V.; Yamashita, K.; Prezhdo, O. V., *Ab Initio* Study of Temperature and Pressure Dependence of Energy and Phonon-Induced Dephasing of Electronic Excitations in CdSe and PbSe Quantum Dots. *J Phys Chem C* **2008,** *112* (21), 7800-7808.
111. Yang, P.; Tretiak, S.; Ivanov, S., Influence of Surfactants and Charges on CdSe Quantum Dots. *J Clust Sci* **2011,** *22* (3), 405-431.

112. Ingole, P. P.; Markad, G. B.; Saraf, D.; Tatikondewar, L.; Nene, O.; Kshirsagar, A.; Haram, S. K., Band Gap Bowing at Nanoscale: Investigation of CdS_xSe_{1-x} Alloy Quantum Dots through Cyclic Voltammetry and Density Functional Theory. *J Phys Chem C* **2013,** *117* (14), 7376-7383.
113. Tamukong, P. K.; Peiris, W. D.; Kilina, S., Computational Insights into CdSe Quantum Dots' Interactions with Acetate Ligands. *Phys Chem Chem Phys* **2016,** *18* (30), 20499-510.
114. Kuznetsov, A. E.; Beratan, D. N., Structural and Electronic Properties of Bare and Capped $Cd_{33}Se_{33}$ and $Cd_{33}Te_{33}$ Quantum Dots. *J Phys Chem C* **2014,** *118* (13), 7094-7109.
115. Kilina, S.; Cui, P.; Fischer, S. A.; Tretiak, S., Conditions for Directional Charge Transfer in CdSe Quantum Dots Functionalized by Ru(II) Polypyridine Complexes. *J Phys Chem Lett* **2014,** *5* (20), 3565-76.
116. Ganesan, P.; Lakshmipathi, S., Impact of Heterogeneous Passivation of Trimethylphosphine Oxide and Di-Methylphosphine Oxide Surface Ligands on the Electronic Structure of Cd_nSe_n (n =6, 15) Quantum Dots: A DFT Study. *Physica E: Low-dimensional Systems and Nanostructures* **2016,** *83*, 284-296.
117. Bloom, B. P.; Zhao, L.-B.; Wang, Y.; Waldeck, D. H.; Liu, R.; Zhang, P.; Beratan, D. N., Ligand-Induced Changes in the Characteristic Size-Dependent Electronic Energies of CdSe Nanocrystals. *J Phys Chem C* **2013,** *117* (43), 22401-22411.
118. Puzder, A.; Williamson, A. J.; Gygi, F.; Galli, G., Self-healing of CdSe Nanocrystals: First-Principles Calculations. *Phys Rev Lett* **2004,** *92* (21), 217401.
119. Troparevsky, M. C.; Kronik, L.; Chelikowsky, J. R., *Ab Initio* Absorption Spectra of CdSe Clusters. *Phys Rev B* **2001,** *65* (3), 033311.
120. Troparevsky, M. C.; Kronik, L.; Chelikowsky, J. R., Optical Properties of CdSe Quantum Dots. *J Chem Phys* **2003,** *119* (4), 2284-2287.
121. Abuelela, A. M.; Mohamed, T. A.; Prezhdo, O. V., DFT Simulation and Vibrational Analysis of the IR and Raman Spectra of a CdSe Quantum Dot Capped by Methylamine and Trimethylphosphine Oxide Ligands. *J Phys Chem C* **2012,** *116* (27), 14674-14681.
122. Sun, J.; Zheng, X.; He, H.; Chen, X.; Dong, B.; Fei, R., Theoretical Study of Ligand and Solvent Effects on Optical Properties and Stabilities of CdSe Nanoclusters. *J Mol Struct* **2016,** *1114*, 123-131.
123. Kilina, S.; Velizhanin, K. A.; Ivanov, S.; Prezhdo, O. V.; Tretiak, S., Surface Ligands Increase Photoexcitation Relaxation Rates in CdSe Quantum Dots. *ACS Nano* **2012,** *6* (7), 6515-24.
124. Kilina, S. V.; Tamukong, P. K.; Kilin, D. S., Surface Chemistry of Semiconducting Quantum Dots: Theoretical Perspectives. *Acc Chem Res* **2016,** *49* (10), 2127-2135.
125. Trivedi, D. J.; Wang, L.; Prezhdo, O. V., Auger-mediated Electron Relaxation is Robust to Deep Hole Traps: Time-Domain *Ab Initio* Study of CdSe Quantum Dots. *Nano Lett* **2015,** *15* (3), 2086-91.
126. Giansante, C.; Infante, I., Surface Traps in Colloidal Quantum Dots: A Combined Experimental and Theoretical Perspective. *J Phys Chem Lett* **2017,** *8* (20), 5209-5215.
127. Prezhdo, O. V., Photoinduced Dynamics in Semiconductor Quantum Dots: Insights from Time-Domain *Ab Initio* Studies. *Acc Chem Res* **2009,** *42* (12), 2005-16.
128. Nadler, R.; Sanz, J. F., Effect of Capping Ligands and TiO_2 Supporting on the Optical Properties of a $(CdSe)_{13}$ cluster. *J Phys Chem A* **2015,** *119* (7), 1218-27.
129. Del Ben, M.; Havenith, R. W. A.; Broer, R.; Stener, M., Density Functional Study on the Morphology and Photoabsorption of CdSe Nanoclusters. *J Phys Chem C* **2011,** *115* (34), 16782-16796.
130. Isborn, C. M.; Kilina, S. V.; Li, X.; Prezhdo, O. V., Generation of Multiple Excitons in PbSe and CdSe Quantum Dots by Direct Photoexcitation: First-Principles Calculations on Small PbSe and CdSe Clusters. *J Phys Chem C* **2008,** *112* (47), 18291-18294.
131. Chung, S. Y.; Lee, S.; Liu, C.; Neuhauser, D., Structures and Electronic Spectra of CdSe-Cys Complexes: Density Functional Theory Study of a Simple Peptide-Coated Nanocluster. *J Phys Chem B* **2009,** *113* (1), 292-301.
132. Kilina, S.; Ivanov, S.; Tretiak, S., Effect of Surface Ligands on Optical and Electronic Spectra of Semiconductor Nanoclusters. *J Am Chem Soc* **2009,** *131*, 7717-7726.
133. Nadler, R.; Sanz, J. F., Simulating the Optical Properties of CdSe Clusters Using the RT-TDDFT Approach. *Theor Chem Acc* **2013,** *132* (4), 204-211.
134. Smith, W.; Yong, C. W.; Rodger, P. M., DL_POLY: Application to Molecular Simulation. *Mol*

Simulat **2010,** *28* (5), 385-471.
135. VandeVondele, J.; Krack, M.; Mohamed, F.; Parrinello, M.; Chassaing, T.; Hutter, J., Quickstep: Fast and Accurate Density Functional Calculations Using A Mixed Gaussian and Plane Waves Approach. *Comput Phys Commun* **2005,** *167* (2), 103-128.
136. Delley, B., From Molecules to Solids with the DMol^3 Approach. *J Chem Phys* **2000,** *113* (18), 7756-7764.
137. Delley, B., An All-Electron Numerical Method for Solving the Local Density Functional for Polyatomic Molecules. *J Chem Phys* **1990,** *92* (1), 508-517.
138. Stoddard, S. D.; Ford, J., Numerical Experiments on the Stochastic Behavior of a Lennard-Jones Gas System. *Phys Rev A* **1973,** *8*, 1504.
139. Verlet, L., Computer "Experiments" on Classical Fluids. I. Thermodynamical Properties of Lennard-Jones Molecules. *Phys Rev* **1967,** *159*, 98-103.
140. VERLET, L., Computer "Experiments" on Classical Fluids. II. Equilibrium Correlation Functions. *Phys Rev* **1968,** *165*, 201-214.
141. Swope, W. C.; Andresen, H. C.; Berens, P. H.; Wilson, K. R., A Computer Simulation Method for the Calculation of Equilibrium Constants for the Formation of Physical Clusters of Molecules: Application to Small Water Clusters. *J Chem Phys* **1982,** *76* (1), 637-649.
142. Hoover, W. G., Canonical Dynamics: Equilibrium Phase-Space Distributions. *Phys Rev A Gen Phys* **1985,** *31* (3), 1695-1697.
143. Rabani, E., An Interatomic Pair Potential for Cadmium Selenide. *J Chem Phys* **2002,** *116* (1), 258.
144. Rabani, E., Structure and Electrostatic Properties of Passivated CdSe Nanocrystals. *J Chem Phys* **2001,** *115* (3), 1493-1497.
145. Ewald, P. P., Die Berechnung Optischer und Elektrostatischer Gitterpotentiale. *Annalen der physik* **1921,** (369), 253-287.
146. Hohenberg, P.; Kohn, W., Inhomogeneous Electron Gas. *Phys Rev* **1964,** *136*, B864-B871.
147. Kohn, W.; Sham, L. J., Self-Consistent Equations Including Exchange and Correlation Effects. *Phys Rev* **1965,** *140* (4A), A1133-A1138.
148. Tuckerman, M. E., *Ab Initio* Molecular Dynmacis：Basic Concepts, Current Trends and Novel Applications. *J. Phys.: Condens. Matter* **2002,** *14*, R1297-R1355.
149. Tse, J. S., *Ab Initio* Molecular Dynamics with Density Functional Theory. *Annu Rev Phys Chem* **2002,** *53*, 249-90.
150. Paquet, E.; Viktor, H. L., Computational Methods for *Ab Initio* Molecular Dynamics. *Adv Chem Ser* **2018,** *2018*, 1-14.
151. Kühne, T. D.; Iannuzzi, M.; Ben, M. D.; Rybkin, V. V.; Seewald, P.; Stein, F.; Laino, T.; Khaliullin, R. Z.; Schütt, O.; Schiffmann, F.; Golze, D.; Wilhelm, J.; Chulkov, S.; Bani-Hashemian, M. H.; Weber, V.; Borštnik, U.; Taillefumier, M.; Jakobovits, A. S.; Lazzaro, A.; Pabst, H.; Müller, T.; Schade, R.; Guidon, M.; Andermatt, S.; Holmberg, N.; Schenter, G. K.; Hehn, A.; Bussy, A.; Belleflamme, F.; Tabacchi, G.; Glöß, A.; Lass, M.; Bethune, I.; Mundy, C. J.; Plessl, C.; Watkins, M.; VandeVondele, J.; Krack, M.; Hutter, J., CP2K: An Electronic Structure and Molecular Dynamics Software Package-Quickstep:Efficient and Accurate Electronic Structure Calculations. *J Chem Phys* **2020,** *152*, 194103.
152. Le Roux, S.; Jund, P., Ring Statistics Analysis of Topological Networks: New Approach and Application to Amorphous GeS_2 and SiO_2 Systems. *Comput Mater Sci* **2010,** *49* (1), 70-83.
153. Kadono, K.; Itakura, N.; Akai, T.; Yamashita, M.; Yazawa, T., Formation of Color Centers in a Soda-Lime Silicate Glass by Excimer Laser Irradiation. *J Phys Condens Matter* **2010,** *22* (4), 045901.
154. Fu, X.; Song, L.; Li, J., Radiation Induced Color Centers in Cerium-Doped and Cerium-Free Multicomponent Silicate Glasses. *J Rare Earth* **2014,** *32* (11), 1037-1042.
155. DF, U.; T, K.; SJ, R., Ultrafast Carrier Dynamics in CdSe Nanocrystals Determined by Femtosecond Fluorescence Upconversion Spectroscopy *J Phys Chem B* **2001,** *105*, 436-443.
156. Li, W.; Li, N.; Liu, C.; Greaves, G. N.; Ong, W. J.; Zhao, X., Understanding the Atomic and Electronic Structures Origin of Defect Luminescence of CdSe Quantum Dots in Glass Matrix. *J Amer Ceram Soc* **2019,** *102* (9), 5375-5385.
157. Perdew, J. P.; Burke, K.; Ernzerhof, M., Generalized Gradient Approximation Made Simple. *Phys Rev Lett* **1996,** *78* (18), 3865-3868.

158. JP, P., Self-Interaction Correction to Density-Functional Approximations for Many-Electron Systems. *Phys Rev B* **1981,** *23*, 5048-5079.
159. Becke, A. D., Density-functional Thermochemistry. III. The Role of Exact Exchange. *J Chem Phys* **1993,** *98* (7), 5648-5652.
160. J, C.; J, H.; YG, C.; WJ, C., Visible Light Emission from Selenium Color Centers Formed in Silicate Glasses. *Opt Mater.* **2012,** *34*, 1231-1234.
161. XB, C.; A, S.; YB, L.; C, B., Investigation of the Crystallization Process in 2 nm CdSe Quantum Dots. *J Am Chem Soc* **2005,** *127*, 4372-4375.
162. A, B.; PK, C.; S, G., Origin of Stokes Shift in InAs and CdSe Quantum Dots: Exchange Splitting of Exciton States. *Phys Rev B* **2006,** *74*, 35341.
163. Y, Xiong; C, Liu.; J, Wang.; J, Han; X, Zhao, Near-infrared Anti-Stokes Photoluminescence of PbS QDs Embedded in Glasses. *Opt Express* **2017,** *25*, 6874-6882.
164. G, S.; C, L.; Z, D.; X, Z.; X, Z., Size-dependent Photoluminescence of PbS QDs Embedded in Silicate Glasses. *Opt Mater Express* **2017,** *7*, 2194-2207.
165. Ayele, D. W.; Su, W.-N.; Chou, H.-L.; Pan, C.-J.; Hwang, B.-J., Composition-controlled Optical Properties of Colloidal CdSe Quantum Dots. *Appl Surf Sci* **2014,** *322*, 177-184.
166. H, Z.; N, S.; T, L., Controlling Charge Separation and Recombination Rates in CdSe/ZnS Type I Core-Shell Quantum Dots by Shell Thicknesses. *J Am Chem Soc* **2010,** *132*, 15038 – 15045.
167. S, K.; B, F.; HJ, E.; M, B., Type-II Quantum Dots: CdTe/CdSeCore/Shell and CdSe/ZnTeCore/Shell. *J Am Chem Soc* **2003,** *125*, 11466-11467.
168. VV, M.; L, D.; VV, B.; T, B.; J, W., Ultrafast Charge Separation in Multiexcited CdSe Quantum Dots Mediated by Absorbed Electron Acceptors. *J Am Chem Soc* **2009,** *131*, 2424-2425.
169. Carmona, E.; Galindo, A., Direct bonds between Metal Atoms: Zn, Cd, and Hg Compounds with Metal-Metal Bonds. *Angew Chem Int Ed Engl* **2008,** *47* (35), 6526-36.
170. Gualdron-Reyes, A. F.; Melendez, A. M.; Tirado, J.; Mejia-Escobar, M. A.; Jaramillo, F.; Nino-Gomez, M. E., Hidden Energy Levels? Carrier Transportability of $CdS/CdS_{1-x}Se_x$ Quantum Dot Solar Cells Impacted by Cd-Cd Level Formation. *Nanoscale* **2019,** *11* (2), 762-774.
171. B., V.; Greaves, G. N.; T., M. P.; V., C. A.; R., M.; S., H.-W., Cation Microsegregation and Ionic Mobility in Mixed Alkali Glasses. *Nature* **1992,** *356*, 504-506.
172. Greaves, G. N.; Ngai, K. L., Reconciling Ionic-Transport Properties with Atomic Structure in Oxide Glasses. *Phys Rev B Condens Matter* **1995,** *52* (9), 6358-6380.
173. WW, Y.; L, Q.; W, G.; X, P., Experimental Determination of the Extinction Coefficient of CdTe, CdSe, and CdS nanocrystals. *Chem Mater.* **2003,** *15*, 2854-2860.
174. Harrell, S. M.; McBride, J. R.; Rosenthal, S. J., Synthesis of Ultrasmall and Magic-Sized CdSe Nanocrystals. *Chem Mater* **2013,** *25* (8), 1199-1210.
175. Proshchenko, V.; Dahnovsky, Y., Spectroscopic and Electronic Structure Properties of CdSe Nanocrystals: Spheres and Cubes. *Phys Chem Chem Phys* **2014,** *16* (16), 7555-61.
176. Kudera, S.; Zanella, M.; Giannini, C.; Rizzo, A.; Li, Y.; Gigli, G.; Cingolani, R.; Ciccarella, G.; Spahl, W.; Parak, W. J.; Manna, L., Sequential Growth of Magic-Size CdSe Nanocrystals. *Adv Mater* **2007,** *19* (4), 548-552.
177. Kasuya, A.; Sivamohan, R.; Barnakov, Y. A.; Dmitruk, I. M.; Nirasawa, T.; Romanyuk, V. R.; Kumar, V.; Mamykin, S. V.; Tohji, K.; Jeyadevan, B.; Shinoda, K.; Kudo, T.; Terasaki, O.; Liu, Z.; Belosludov, R. V.; Sundararajan, V.; Kawazoe, Y., Ultra-Stable Nanoparticles of CdSe Revealed from Mass Spectrometry. *Nat Mater* **2004,** *3* (2), 99-102.
178. Zachariasen, W. H., The Atomic Arrangement in Glass. *J Am Chem Soc* **1932,** *54* (10), 3841-3851.
179. Martinez, J. M.; Martinez, L., Packing Optimization for Automated Generation of Complex System's Initial Configurations for Molecular Dynamics and Docking. *J Comput Chem* **2003,** *24*, 819-825.
180. Martinez, L.; Andrade, R.; Birgin, E. G.; Martinez, J. M., PACKMOL: A Package for Building Initial Configurations for Molecular Dynamics Simulations. *J Comput Chem* **2009,** *30* (13), 2157-64.
181. Bussi, G.; Donadio, D.; Parrinello, M., Canonical Sampling through Velocity Rescaling. *J Chem Phys* **2007,** *126* (1), 014101.
182. Konstantinou, K. Computational Modelling of Structural, Dynamical and Electronic Properties of

Multicomponent Silicate Glasses. PhD Thesis, University College London, London, 2017.
183. Rushton, M. J. D. Simulation of Glass and Ceramic Systems for Nuclear Waste Applications. PhD Thesis, Imperial College London, London, 2007.
184. Henderson, G. S.; Neuville, D. R.; Cochain, B.; Cormier, L., The Structure of GeO_2-SiO_2 Glasses and Melts: A Raman Spectroscopy Study. *J Non-Cryst Solids* **2009,** *355* (8), 468-474.
185. Drijvers, E.; De Roo, J.; Martins, J. C.; Infante, I.; Hens, Z., Ligand Displacement Exposes Binding Site Heterogeneity on CdSe Nanocrystal Surfaces. *Chem Mater* **2018,** *30* (3), 1178-1186.
186. Xu, S.; Wang, C.; Cui, Y., Theoretical Investigation of CdSe Clusters: Influence of Solvent and Ligand on Nanocrystals. *J Mol Model* **2010,** *16* (3), 469-73.
187. Meulenberg, R. W.; Jennings, T.; Strouse, G. F., Compressive and Tensile Stress in Colloidal CdSe Semiconductor Quantum Dots. *Phys Rev B* **2004,** *70*, 235311.
188. Ballauff, M.; Brader, J. M.; Egelhaaf, S. U.; Fuchs, M.; Horbach, J.; Koumakis, N.; Kruger, M.; Laurati, M.; Mutch, K. J.; Petekidis, G.; Siebenburger, M.; Voigtmann, T.; Zausch, J., Residual Stresses in Glasses. *Phys Rev Lett* **2013,** *110* (21), 215701.
189. Kurkjian, C. R.; Gupta, P. K.; Brow, R. K., The Strength of Silicate Glasses: What Do We Know, What Do We Need to Know? *Int J Appl Glass Sci* **2010,** *1* (1), 27-37.
190. Mastelaro, V. R.; Zanotto, E. D., Residual Stresses in a Soda-Lime-Silica Glass-Ceramic. *J Non-Cryst Solids* **1996,** *194*, 297-304.
191. Mu, L.; Feng, C., Topological Research on Lattice Energies for Inorganic Compounds. *MATCH Commun Math Comput Chem* **2006,** *56*, 97-111.
192. Giberti, F.; Voros, M.; Galli, G., Design of Heterogeneous Chalcogenide Nanostructures with Pressure-Tunable Gaps and without Electronic Trap States. *Nano Lett. 17* (4), 2547-2553.
193. Adamo, C.; Barone, V., Toward Reliable Density Functional Methods without Adjustable Parameters: The PBE0 model. *J Chem Phys* **1999,** *110* (13), 6158-6170.
194. Krukau, A. V.; Vydrov, O. A.; Izmaylov, A. F.; Scuseria, G. E., Influence of the Exchange Screening Parameter on the Performance of Screened Hybrid Functionals. *J Chem Phys* **2006,** *125* (22), 224106.
195. Guidon, M.; Hutter, J.; VandeVondele, J., Auxiliary Density Matrix Methods for Hartree-Fock Exchange Calculations. *J Chem Theory Comput* **2010,** *6* (8), 2348-64.
196. D.L.Griscom, The electronic structure of SiO_2: A Review of Recent Spectroscopic and Theoretical Advances. *J Non-Cryst Solids* **1977,** *24* (2), 155-234.
197. G.HSiegelJr., Ultraviolet Spectra of Silicate Glasses: A Review of Some Experimental Evidence. *J Non-Cryst Solids* **1974,** *13* (3), 372-398.
198. Ispas, S.; Benoit, M.; Jund, P.; Jullien, R., Structural and Electronic Properties of the Sodium Tetrasilicate Glass $Na_2Si_4O_9$ from Classical and *Ab Initio* Molecular Dynamics Simulations. *Phys Rev B* **2001,** *64* (21).
199. Du, J.; Corrales, L. R., Structure, Dynamics, and Electronic Properties of Lithium Disilicate Melt and Glass. *J Chem Phys* **2006,** *125* (11), 114702.

Résumé en Français

Contexte de mon travail

(1) Point Quantique ou *Quantum Dot*

Un exciton (un état lié composé d'un trou et d'un électron) dans un semi-conducteur massique a une longueur de délocalisation caractéristique, qui est appelée son «rayon de Bohr». L'exciton devient quantique lorsqu'une ou plusieurs dimensions spatiales du cristal semi-conducteur sont de l'ordre du rayon de Bohr, ou plus petites que celui-ci. Un point quantique, ou boîte quantique (plus souvent appelé par son nom anglais de *quantum dot*, ou QD) est un semi-conducteur dont la fonction d'onde électronique est confinée dans toutes les dimensions. Une caractéristique spécifique du semi-conducteur dans le régime QD est la structure discrète des états électroniques, très différente des bandes d'énergie continues du matériau massique (ou *bulk*) (**Figure S1**). Les états quantifiés sont ordonnés en énergie et sont désignés par un couple de nombres quantiques principaux (n) et de nombres quantiques azimutaux (L), dans lequel n est généralement représenté par un nombre et L par une lettre (S, P, D, ... pour L = 0, 1, 2, ..., respectivement) et les états correspondants sont 1S, 1P, 1D, 2S, etc.

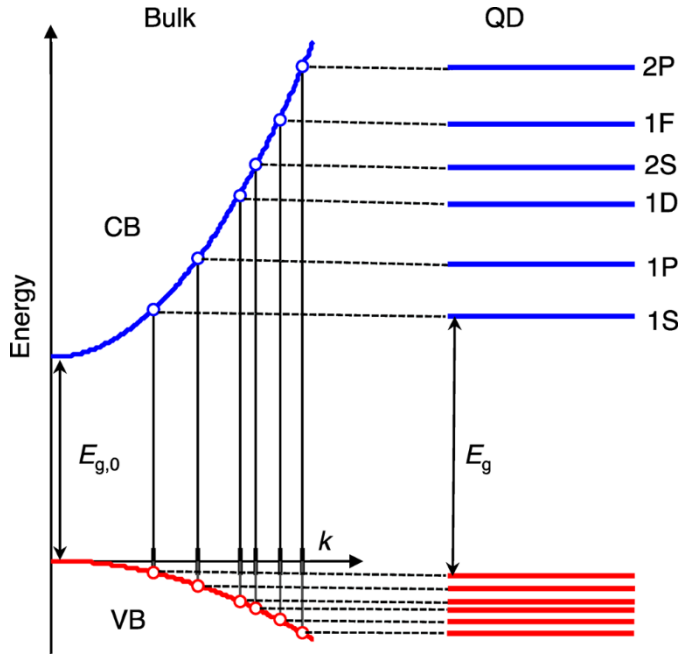

Figure S1 Modèle idéalisé des états électroniques dans un semi-conducteur massique (à gauche) et un QD sphérique fait du même matériau (à droite). Tiré de la référence 1.

(2) Confinement quantique et effet de taille

Les excitons quantiques peuvent être approximativement illustrés par un simple potentiel de particules dans une boîte en trois dimensions. La fonction d'onde des états du niveau fondamental a pour partie radiale l'expression suivante:

$$\Phi_{1,0,0}(\mathbf{r},\boldsymbol{\theta},\boldsymbol{\varphi}) = \frac{1}{\sqrt{2\pi R}}\frac{\sin(\pi r/R)}{r} \qquad \textbf{Eq. 1-1}$$

L'énergie correspondante est:

$$\boldsymbol{E}_{1,0} = \frac{\hbar^2\pi^2}{2mR^2} \qquad \textbf{Eq. 1-2}$$

où $\hbar$ est la constante réduite de Planck et m est la masse de la particule, qui est remplacée par la masse effective de l'électron (m_e) ou la masse du trou (m_h) dans le cas de la conduction ou de la bande de valence, respectivement. R est le rayon du point quantique (QD). L'énergie de la bande interdite (E_g) est définie par l'espacement entre les niveaux de l'électron de bord de bande ($1S_e$) et du trou ($1S_h$), et elle peut être calculée comme la somme des énergies de la bande interdite globale ($E_{g,0}$) et $E_{1,0}$ de l'électron et du trou:[2]

$$\boldsymbol{E_g} = \boldsymbol{E}_{g,0} + \frac{\hbar^2\pi^2}{2m_eR^2} + \frac{\hbar^2\pi^2}{2m_hR^2} = \boldsymbol{E}_{g,0} + \frac{\hbar^2\pi^2}{2m_{eh}R^2} \qquad \textbf{Eq. 1-3}$$

où $m_{eh} = m_e m_h/(m_e+m_h)$ est la masse réduite des trous électroniques. Les effets de Coulomb doivent également être pris en considération :

$$\boldsymbol{E_g} = \boldsymbol{E}_{g,0} + \frac{\hbar^2\pi^2}{2m_{eh}R^2} - \frac{1.765e^2}{\varepsilon_\infty R} \qquad \textbf{Eq. 1-4}$$

où ε_∞ est la constante diélectrique à haute fréquence. En calculant l'énergie de l'interaction electron–trou (e–h) de Coulomb dans le cadre de la théorie des perturbations du premier ordre, on obtient le troisième terme à droite.

Par conséquent, la bande interdite des points quantiques (QDs) peut être ajustée en fonction de leur taille. Un décalage vers le bleu du premier pic d'absorption peut être observé par rapport aux matériaux homologues massiques. Cette caractéristique unique

à l'échelle nanométrique a suscité un développement rapide de la recherche et de la commercialisation des QDs. En choisissant des matériaux appropriés avec une bande interdite dimensionnée « sur mesure » et en modifiant la taille des QDs, leurs spectres d'émission peuvent ainsi couvrir les régions du spectre électromagnétique situées dans l'ultraviolet (UV), le visible et le proche infrarouge (NIR) (**Figure S2**).[3]

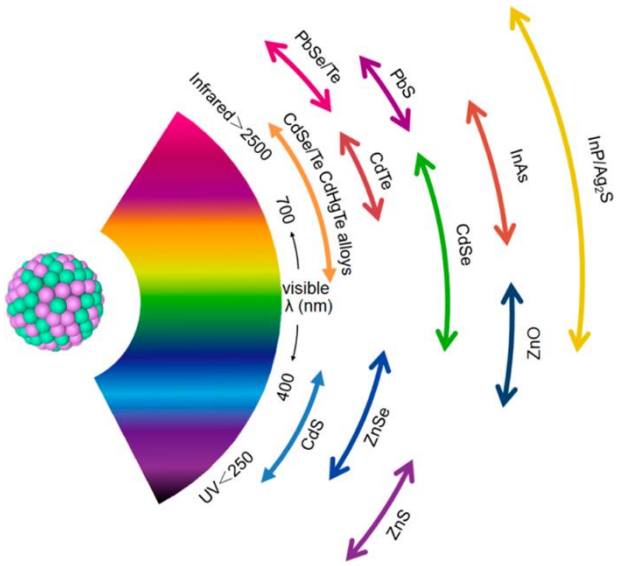

Figure S2 Matériaux QDs représentatifs mis à l'échelle en fonction de leur longueur d'onde d'émission superposée sur le spectre électromagnétique. Tiré de la réf. 3.

Les points quantiques peuvent être divisés en plusieurs catégories en fonction de leur composition：

(1) Les points quantiques II-VI (CdS, CdSe, CdTe, ZnSe) sont les matériaux les plus couramment étudiés car leurs spectres d'émission peuvent couvrir tout la région visible du spectre.

(2) Les points quantiques IV-VI (PbS, PbSe, PbTe) font également l'objet d'une grande attention en raison de leurs avantages pour l'émission dans le proche infrarouge.

(3) Les points quantiques III-V (GaAs, InAs) trouvent une application principalement dans les amplificateurs laser, avec émission dans l'infrarouge moyen.

(4) Récemment, les points quantiques basés sur des matériaux pérovskites ($CsPbBr_3$, $CH_3NH_3PbCl_3$) ont suscité un intérêt grandissant en raison de leur grande efficacité quantique dans les régions visibles. En outre, les points quantiques de carbone, de

silicium et d'argent attirent également l'attention des chercheurs. Leur rendement quantique élevé, leur largeur de raie d'émission étroite et leurs propriétés optiques ajustables en taille rendent les points quantiques fascinants dans les applications dans les cellules solaires[4-5], les LED[6-8], le bio-étiquetage[9-10], etc.

(3) Le mécanisme de luminescence

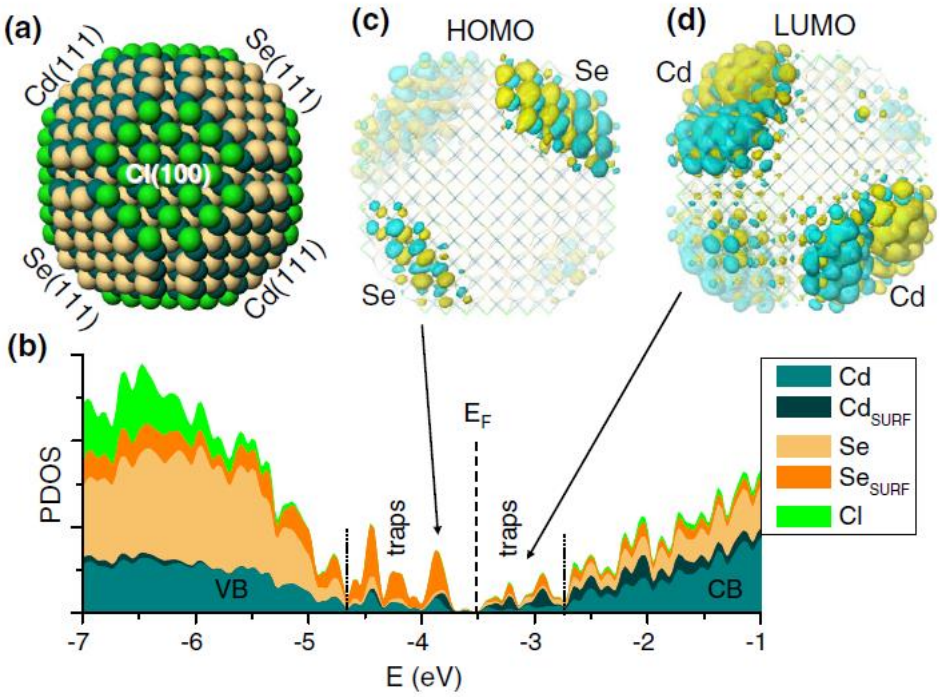

Figure S3 États de surface dans un point quantique colloïdal CdSe sphérique avec des facettes non passivées (111). (a) Modèle, (b) Densité projetée des états, (c) État de surface lié au Se^{-} du côté de la bande de valence, (d) État lié au Cd du côté de la bande de conduction. Tiré de la réf. 11.

En raison de leur rapport surface/volume très important, il peut y avoir beaucoup de défauts de surface présents sur les points quantiques, tels que des liaisons pendantes ou des lacunes, formant des états dits «pièges» dans la bande interdite (**Figure S3**),[11]peu profonds ou profonds selon les cas. [11] Par exemple, on a observé que les états pièges étaient localisés du côté de la bande de valence en fonction de la densité partielle d'états (PDOS, *partial density of state*) (**Figure S3(b)**), et on a constaté que la densité

électronique des orbitales moléculaires occupées les plus élevées (HOMO, *highest occupied molecular orbital*) était distribuée dans les facettes non passivées terminées par Se- (111) (**Figure S3(c)**). Parallèlement, les facettes terminées par Cd (111) ont également introduit des états pièges près du bord de la bande de conduction, la densité électronique des orbitales moléculaires les plus basses vacantes (LUMO, *lowest unoccupied molecular orbital*) étant localisée sur ces facettes (**Figure S3(d)**).

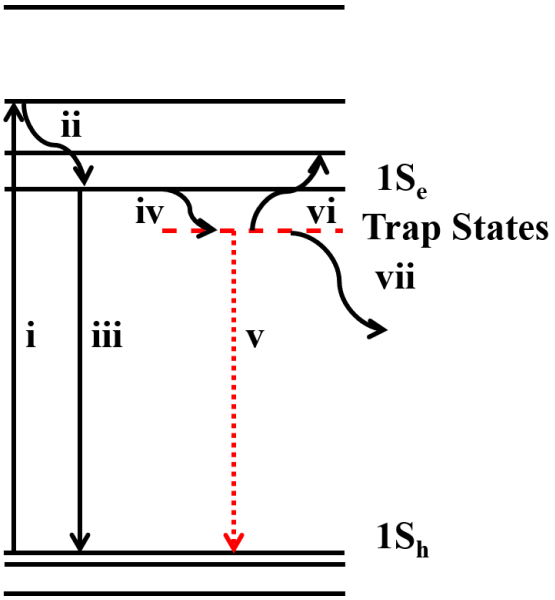

Figure S4 Schématisation du mécanisme de luminescence des points quantiques

Le mécanisme de luminescence des points quantiques est illustré à la **Figure S4**.[12] Lors de l'excitation, l'électron peut être excité à un niveau d'énergie élevé dans la bande de conduction (processus i), et un trou est créé dans la bande de valence, qui se refroidit rapidement au niveau de valence le plus élevé ($1S_h$). L'électron dans les niveaux d'énergie élevés relaxe jusqu'au niveau de conduction le plus bas ($1S_e$) en quelques centaines de femtosecondes, en dissipant l'énergie excédentaire en énergie thermique (processus ii). Par la suite, l'électron au niveau de conduction le plus bas peut se recombiner directement avec le trou au niveau de valence le plus élevé par voie radiative, processus désiré qui entraîne l'émission intrinsèque des points quantiques (processus iii). Cependant, les électrons peuvent également être piégés par les états pièges (processus iv), puis se désexciter dans la bande de valence (processus v),

contribuant ainsi à l'émission dite « de défaut », qui est décalée vers le rouge par rapport à l'émission intrinsèque. La Auger recombinaison est également observée dans les points quantiques lors d'une excitation intense (processus vi). Enfin, l'énergie peut être totalpoement dissipée par un processus non radiatif (processus vii) sans émission.

L'émission de défauts est en compétition par rapport à l'émission intrinsèque, ce qui peut se traduire par une large largeur de raie d'émission et une faible efficacité quantique. En pratique, les défauts peuvent être passivés par des ligands organiques pour en réduire le rôle, mais dans la réalité, la couverture insuffisante des couches organiques peut ne pas permettre de supprimer suffisament les états de défaut (**Figure S5(a)**). Cependant, les défauts de surface peuvent être éliminés en formant une couche de ligands organiques pour mettre fin aux liaisons pendantes (**Figure S5(b)**).[13-14] La présence d'une structure cœur/couronne (*core/shell*) est également une méthode courante et efficace pour éliminer les défauts de surface et améliorer l'efficacité quantique.[15-16]

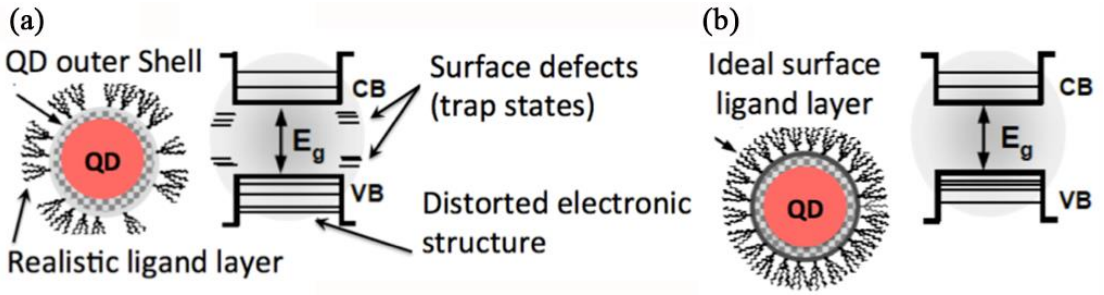

Figure S5 La structure électronique du point quantique en présence de ligands illustrant l'apparition d'états de piège dus à une passivation imparfaite (a) et l'élimination de ces états de défaut par une passivation parfaite (b). Adapté de la réf.14.

(4) Méthode de fabrication

Il existe pour ce qui est des procédés de fabrication deux grandes catégories de points quantiques à considérer: les points quantiques colloïdaux, et les verres dopés aux points quantiques. Bien que les points quantiques aient d'abord été fabriqués dans des matrices de verres,[17] la plupart des efforts de recherche dans le domaine des nanocristaux se sont orientés vers les échantillons colloïdaux car ceux-ci permettent un contrôle plus facile de la taille, des distributions de taille plus étroites, une facilité de passivation de la surface, et un rendement quantique plus élevé. Il existe plusieurs méthodes pour

fabriquer ces QDs colloïdaux: (1) méthodes aqueuses, (2) méthodes organométalliques par injection à chaud, (3) méthodes organométalliques sans injection. En dehors de ces méthodes, les QDs peuvent être synthétisés par biosynthèse,[18] micro-ondes,[19] sol-gel,[20] etc.

Comme je l'ai mentionné plus haut, le rapport surface/volume élevé des points quantiques contribue à leur double nature (faible stabilité et réactivité élevée), de sorte qu'ils peuvent être extrêmement instables et se modifient facilement ou réagissent avec des substances actives, pour atteindre un état relativement stable dans certains cas de passivation. D'une part, leur réactivité élevée leur permet d'être facilement transformés en nanomatériaux fonctionnels par des transformations chimiques ciblées. D'autre part, leur réactivité élevée les rend également instables et difficiles à contrôler et manipuler, alors que pour les application des QDs, il est nécessaire de maintenir un état stable pendant le stockage, le traitement et l'utilisation. Même passivés par des couches de ligands, l'utilisation de solutions organiques ne peut pas protéger les QDs de l'oxygène, de l'eau et des effets thermiques, de sorte que les QDs colloïdaux peuvent être facilement oxydés ou dégradés pendant leur utilisation.[15] C'est le principal obstacle des points quantiques colloïdaux en termes d'applications pratiques.

La recherche sur les points quantiques a été lancée en 1980 par Ekimov et al.[17] qui ont fabriqué des nanocristaux de CuCl. Les points quantiques intégrés dans une matrice de verre peuvent tirer parti de la stabilité mécanique, thermique et chimique des verres. Ainsi, le verre dopé aux points quantiques peut avoir des applications potentielles dans les lasers,[28] les LED,[29-30] etc.

Les verres dopés aux points quantiques peuvent être fabriqués par la méthode sol-gel,[4,31-34] la méthode d'implantation ionique,[35-37] et la méthode d'échange d'ions.[38] Les défauts des verres préparés par sol-gel sont la contrainte résiduelle et la difficulté d'élimination des ligands organiques alors que la profondeur des ions qui peuvent être implantés ou échangés est limitée dans les deux dernières méthodes.

En-dehors des méthodes ci-dessus, la voie la plus courante de préparation des QDs dans une matrice de verre est la méthode de trempe à l'état fondu (**Figure S6**).[39] Tout d'abord, les matières premières, y compris les composants du verre et les composants des QDs, sont mélangées soigneusement. Ensuite, les poudres mélangées sont fondues à haute température dans des creusets. Les masses fondues sont versées sur un moule en laiton

et trempées par pressage avec d'autres plaques. Les verres obtenus sont ensuite recuits à une température plus basse pour éliminer la contrainte thermique. Après le recuit, d'autres traitements thermiques à différentes températures (en fonction de la température de transition et de cristallisation des verres) et d'une durée variable (de plusieurs minutes à quelques heures) sont effectués sur les verres tels qu'ils sont préparés afin de fabriquer les verres dopés aux points quantiques.

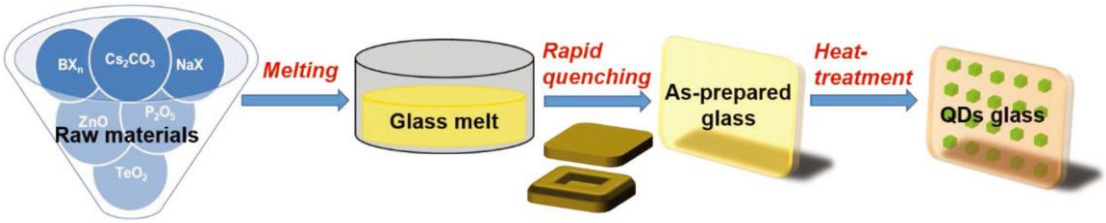

Figure S6 Schéma du processus de préparation des verres intégrant des points quantiques. Tiré de la réf. 39.

Questions scientifiques ouvertes

Comparés à leurs homologues colloïdaux, les points quantiques incorporés dans une matrice de verre présentent un faible rendement quantique de photoluminescence (PLQY, *photoluminescence quantum yield*). L'énorme différence de PLQY entre les points quantiques dans les solutions colloïdales et dans les matrices de verre conduit naturellement à la question suivante : pourquoi le rendement quantique dans la matrice de verre est-il si faible ? Comment peut-on améliorer cette situation, afin d'améliorer l'application pratique, par des modifications des points quantiques ou des verres ?

Des expérimentateurs ont travaillé pendant des décennies pour faire la lumière sur ces questions, et certains mécanismes ont été proposés pour expliquer ce phénomène. Il a été supposé que la présence de défauts à l'interface entre la QD et la matrice de verre peut réduire l'émission excitonique et produire une émission liée aux défauts (*defect emission*) préjudiciable pour les applications. Cependant, il est difficile, sur le plan expérimental, de sonder finement l'origine microscopique des défauts interfaciaux et de caractériser la structure et l'environnement chimique du verre dopé de points

quantiques, en raison de la résolution limitée des techniques existantes, de l'instabilité de la matrice de verre sous faisceau électronique et de la concentration relativement faible des QDs dans le verre.

Les méthodes de modélisation théorique ont été appliquées comme alternatives pour apporter un éclairage sur ces questions, et une exploration complète de la structure atomique locale peut donner des indications pour la conception de verres hybrides hautement luminescents. L'étude numérique des matériaux permet d'étudier un système au niveau atomique, ce qui n'est pas directement possible dans le cadre d'expériences, et de mieux comprendre les propriétés physiques et chimiques des matériaux. Les deux principales méthodes de modélisation numérique des matériaux sont les approches classiques (basées sur les champs de force) et les simulations *ab initio*, qui ont toutes deux été utilisées avec succès dans la modélisation de nombreuses propriétés des matériaux en verre multicomposants et des nanocristaux de CdSe.

Toutefois, aucun calcul atomique n'a encore abordé directement la question de la nature des systèmes composites QD/verre et de leurs propriétés interfaciales. Il existe dans la littérature des exemples de recherches sur la structure électronique des états de défaut, l'effet de ligand, la dynamique des porteurs de charge sur les CdSe QDs, mais aucun effort de recherche ne s'est concentrée jusqu'à présent sur la structure électronique des points quantiques dans une matrice de verre et la nature de l'interface par une modélisation atomiquement réaliste de leur interface.

Apports de mes travaux

Mon étude de la structure atomique et électronique locale du verre dopé aux CdSe QDs peut être divisée en quatre étapes principales:

(1) Construction du modèle des clusters Cd_nSe_n (n=3,10,13,33) et Cd_nSe_n-X clusters (X = O, Na, Cd, Se, etc.)

Les états de surface des QDs dans les matrices de verre sont complexes, comme les centres de couleur (par exemple, S_2^-, Se_2^- incorporés dans les matériaux hôtes inorganiques, ce qui entraîne l'émission visible et donne de la couleur aux verres),[153-154] et les défauts intrinsèques[155] des QDs, y compris la présence de liaisons pendantes.

En outre, les défauts interfaciaux entre le verre et la surface des QDs (par exemple, les oxygènes non pontants et les modificateurs de réseau, tels que les ions sodium et d'autres ions de métaux alcalino-terreux) peuvent avoir un impact important sur la structure électronique des QDs.[57] En ce qui concerne les points quantiques de composition CdSe incorporés dans les matrices de verre, des atomes de Cd et Se peuvent être présents dans les environnements des verres tels qu'ils sont préparés, avec des contracts «premiers voisins» de type Cd-O, Cd-Se, mais aussi Cd-Cd et Se-Se. Lors du recuit thermique, les contacts de Se-Se sont considérés comme les sites de nucléation, et la diffusion thermique du Cd vers les zones riches en Se-Se favorise la croissance des points quantiques CdSe. Au cours de ces processus, le Cd-O s'est progressivement transformé en Cd-Se, comme le montre l'analyse par spectroscopie EXAFS (*Extended X-ray Absorption Fine Structure*).[57] À l'interface entre les CdSe QDs et la matrice vitreuse, la présence de liaisons Cd-O, Cd-Cd et Se-Se est encore possible en raison de la distribution aléatoire de ces éléments dans les matrices vitreuses, ce qui conduit à un grand nombre de combinaisons d'états de surface. Pour l'équilibre des charges, les liaisons pendantes des CdSe QDs dans les verres peuvent être compensés par de l'oxygène non pontant, et des modificateurs de structure (comme Na, etc.) dans les verres. Cependant, les effets de ces états d'interface sur les propriétés optoélectroniques des CdSe QDs restent encore largement inconnus. C'est pourquoi j'ai voulu étudier les structures contenant les états de surface et d'interface mentionnés ci-dessus, tels que Cd-Cd_nSe_n, Cd_nSe_n-Se, Cd_nSe_n-Cd, Cd_nSe_n-O, Cd_nSe_n-Na, Cd_nSe_n-Ca, Cd_nSe_n-O-Na, Cd_nSe_n-O-Ca, etc. (**Figure S7**).

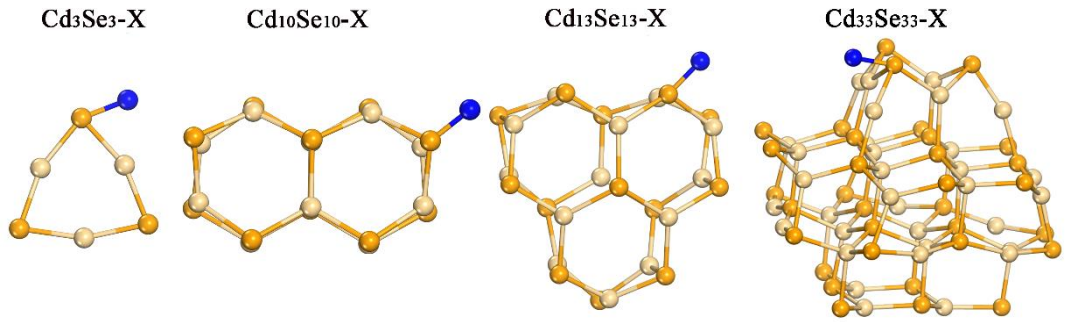

Figure S7 Structure initiale du Cd_nSe_n-X (X=Se, Cd, O, Na et Ca). Les billes blanches, jaunes et bleues représentent respectivement les atomes de Cd, de Se et de X.

Au cours de cette étape, les liaisons pendantes des CdSe QDs et leurs interactions avec les matrices de verre ont été systématiquement explorées en combinant les calculs de DFT non périodique et les approches expérimentales. En raison des contraintes de taille de la méthode DFT pour aborder une collection complète de nombreuses configurations de clusters différentes, j'ai limité mon étude aux simulations atomiques de la morphologie et de la structure électronique des nanoclusters Cd_3Se_3, $Cd_{10}Se_{10}$, $Cd_{13}Se_{13}$ et $Cd_{33}Se_{33}$ comme étant les modèles les plus représentatifs. Les effets des adatomes tels que Cd, Se, O, Na et Ca sur les énergies HOMO/LUMO et la densité des états des CdSe QDs dans les verres ont été étudiés.

(2) Construire des modèles des verres Na_2O-$2SiO_2$ en utilisant la dynamique moléculaire classique

Dans la partie précédente, j'ai utilisé un modèle très simplifié pour simuler les clusters de CdSe dans une matrice de verre, loin de la description réaliste de leur environnement chimique en termes de compositions et de désordre. D'une part, il est peu probable que les amas de CdSe ne soient entourés que de quelques atomes dans la matrice de verre, compte tenu de l'apport suffisant de modificateurs du réseau de verre, des atomes d'oxygène ne formant pas de pont dans la matrice de verre et du rapport élevé d'atomes de Cd ou de Se de surface active à deux coordinateurs. Par ailleurs, la neutralité électrique des amas de CdSe peut être détruite lorsqu'ils sont recouverts par un atome de modificateur du réseau de verre ou un atome d'oxygène ne formant pas de pont, ce qui tend à interagir avec d'autres atomes de la matrice de verre afin de maintenir la neutralité électrique. Par conséquent, la structure atomique locale réelle du verre dopé par des points quantiques de CdSe est censée être plus complexe que le modèle que j'ai construit et étudié lors de la dernière étape.

La meilleure approche pour imiter l'environnement interfacial du point quantique CdSe dans la matrice de verre est d'introduire le QD directement dans un modèle de matrice de verre, en décrivant explicitement l'interface QD/verre. Bien qu'il existe diverses études sur la modélisation atomistique du verre et du point quantique séparément, à ma connaissance, aucune étude de la littérature n’a sondé ce système hybride modélisé explicitement. Il est techniquement difficile de générer ces structures hybrides par des simulations classiques de MD, surtout si l'on considère la faible disponibilité des

potentiels d'interaction de paires adéquats pour un système contenant simultanément tous les éléments (O, Si, Na, Cd et Se). De plus, la méthodologie permettant d'incorporer le CdSe QD dans une matrice de verre est difficile à développer. La grande différence entre la géométrie du cluster de CdSe et la matrice de verre rend difficile la relaxation de l'interface entre eux. Comme je l'ai présenté dans l'introduction, les CdSe QDs sont préparés dans la matrice de verre par une étape de nucléation et de croissance cristalline ultérieure, dont l'échelle de temps dépasse de loin les capacités actuelles de la simulation. Par conséquent, je n'avais pas l'intention de simuler complètement le processus thermique dans la procédure de trempe et de traitement thermique de la préparation des verres dopés au CdSe par points quantiques, mais je cherchais néanmoins à m'en approcher.

Dans cette étape, j'ai fait l'approximation qu'une bonne configuration de départ pour les simulations MD classiques et *ab initio* MD serait produite en introduisant directement les CdSe QDs dans la matrice de verre préformée et équilibrée. En conséquence, les configurations de la matrice de verre seront générées avant l'incorporation du CdSe QD. Expérimentalement, les verres peuvent être préparés en faisant fondre les composants du verre à haute température et en les trempant rapidement. Par conséquent, la dynamique moléculaire peut imiter le processus thermique qui s'est produit sur le verre, pour générer la structure atomique locale des verres.

La structure initiale (**Figure S8**) a été chauffée progressivement par étapes de 1000 K avec une simulation MD de 60 ps à chaque température de 300 K à 6000 K. Après équilibrage du liquide à 6000 K pendant 400 ps, le système a été refroidi progressivement par étapes de 500 K avec une simulation MD de 60 ps à chaque température de 6000 K à 300 K. Une autre simulation NVT de 200 ps a été réalisée à 300 K, ainsi qu'une simulation NVE de 200 ps afin de finir d'équilibrer la structure.

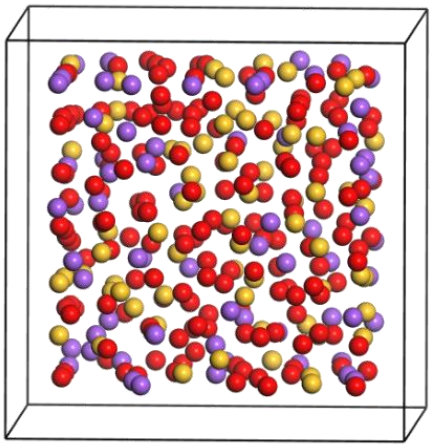

Figure S8 Structure initiale de la simulation classique de la dynamique moléculaire. Les sphères rouges, jaunes et violettes représentent respectivement les atomes de O, Si et Na.

(3) Construire le modèle des verres dopés au CdSe QD

Génération de la structure des verres quantiques $Cd_{33}Se_{33}$ dopés par points à l'aide de la méthode classique MD. Le point quantique $Cd_{33}Se_{33}$ (obtenu à l'étape 1) a alors été incorporé dans la matrice de verre (obtenue à l'étape 2), en éliminant les atomes de verre de sorte que les distances interatomiques entre le QD et la matrice de verre soient supérieures à 2.5 Å. La composition finale était de 39 Na_2O-78 SiO_2-33 CdSe(**Figure S9(a)**). Toute la structure a été équilibrée à 1000 K, en utilisant d'abord 200 ps de dynamique NVT, puis 200 ps de dynamique NVE, initialement avec des atomes du CdSe QD gelés. La structure a ensuite été refroidie progressivement par étapes de 50 K avec un MD de 60 ps à chaque température de 1000 K à 500 K, tout en maintenant le CdSe QD congelé. Le refroidissement ultérieur de 500 K à 300 K s'est fait par étapes de 10 K, en laissant tous les atomes se déplacer. Enfin, la structure a été rééquilibrée à 300 K avec une dynamique NVT de 200 ps, et une dynamique NVE finale de 200 ps (**Figure S9(b)**).

Dynamique moléculaire *ab initio* du point quantique CdSe dans la matrice de verre. Après équilibrage de ces systèmes à l'aide de simulations MD classiques comme décrit ci-dessus, nous avons utilisé les configurations résultantes comme point de départ pour la modélisation *ab initio* au niveau de la théorie fonctionnelle de la densité (DFT), en utilisant la formulation de Kohn-Sham telle qu'elle est implémentée dans le

code CP2K. Les simulations ont été effectuées au niveau de l'approximation du gradient généralisé (méthode GGA), en utilisant la fonctionnelle d'échange-corrélation PBE. Après une première optimisation de la géométrie avec la DFT, la structure relaxée ainsi obtenue (**Figure S9(c)**) a été utilisée comme structure initiale pour les simulations AIMD. La structure a été trempée de 500 K à 300 K par pas de 50 K, avec un total de 10 ps AIMD à un pas de temps de 2 fs. La simulation de production a été réalisée dans l'ensemble NVT à 300 K pour 10 ps (**Figure S9(d)**).

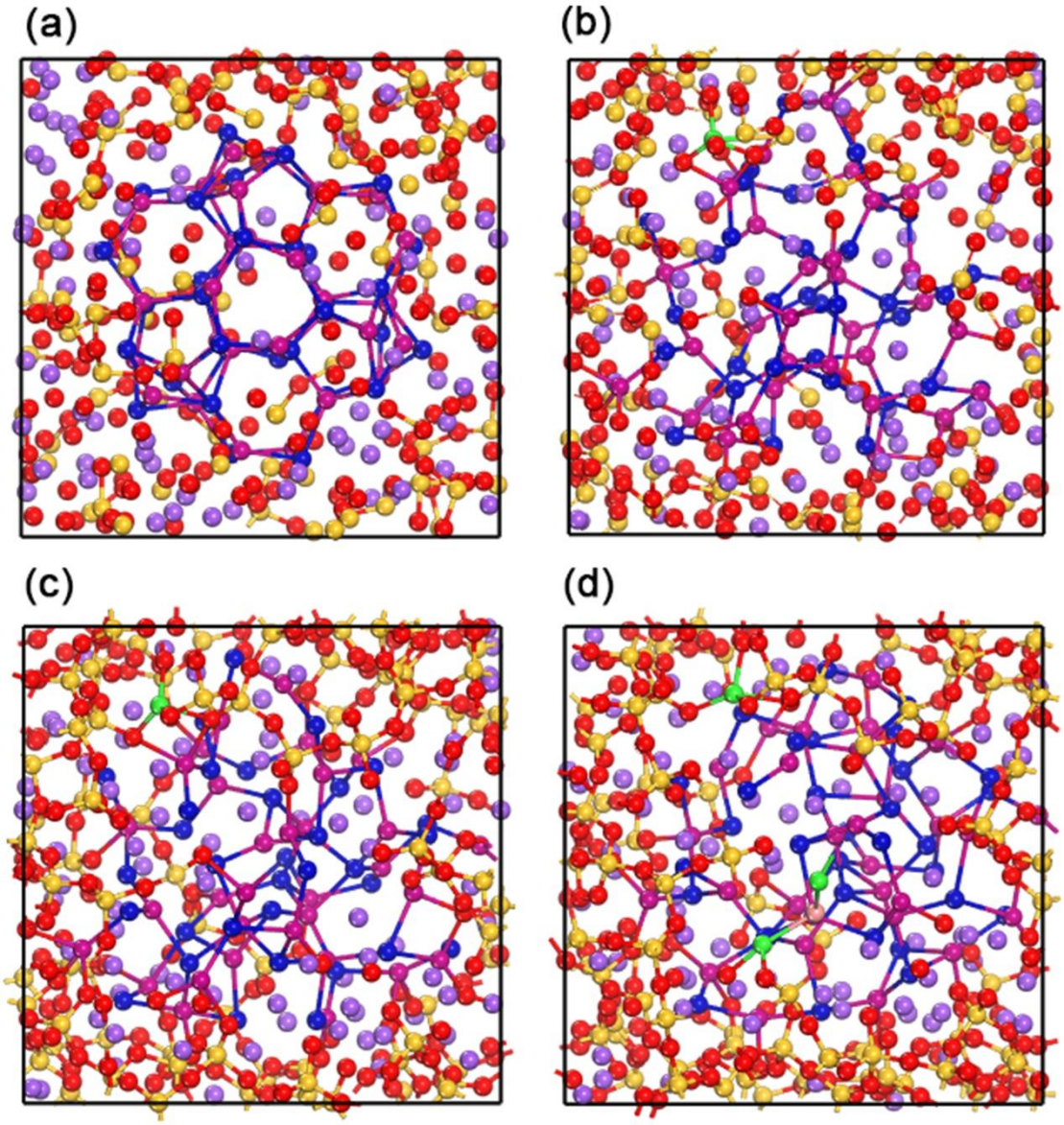

Figure S9 (a) La configuration initiale pour les calculs classiques de MD. (b) La configuration finale pour les simulations MD classiques, utilisée comme configuration

initiale pour l'optimisation de la géométrie par la méthode DFT. (c) La structure à géométrie optimisée au niveau de la DFT, utilisée comme configuration initiale pour la dynamique moléculaire *ab initio*. (d) La configuration finale des simulations AIMD. Les atomes de Se et de Cd dissociés du point quantique sont mis en évidence en rose et en vert, respectivement.

(4) Structure électronique des verres CdSe QD dopés x Na_2O-(1-x) SiO_2 (x = 0, 0,25, 0,33, 0,5 en fraction molaire)

Dans la dernière étape, j'ai utilisé une combinaison de la méthode MD classique et de la méthode AIMD pour étudier la structure interfaciale entre la matrice de verre et le point quantique, ainsi que la reconstruction qui s'est produite à ce niveau. Cependant, l'exploration de la structure atomique locale du verre dopé au CdSe QD peut fournir des informations sur les origines structurales possibles des défauts, ce qui ne peut pas nécessairement éclairer les relations entre ces structures et les propriétés d'émission. Afin de répondre à la question de savoir pourquoi l'efficacité quantique des verres dopés par points quantiques était si faible par rapport à leurs homologues colloïdaux, les structures électroniques sont d'une importance majeure pour la compréhension mutuelle de ses mécanismes de luminescence. Ainsi, dans cette partie de mes travaux, les structures électroniques des verres dopés aux points quantiques CdSe ont été étudiées pour sonder les origines possibles des faibles performances des QDs intégrés dans les verres.

En outre, dans leur rôle de modificateurs du verre, les ions sodium peuvent modifier la structure des verres de silicate, et il a été observé expérimentalement qu'il y a une disparition de l'absorption visible des centres de couleur du Se-Se lorsque la concentration de Na_2O augmente dans un verre de silicate dopé au ZnSe.[58] Par conséquent, dans cette étape, j'ai modifié la quantité de Na_2O dans le verre $(Na_2O)_x(SiO_2)_{1-x}$ (x = 0, 0,25, 0,33, 0,5 en fraction molaire) pour explorer la dépendance de la composition de la structure atomique et électronique du CdSe QD dans les matrices de verre.

Les structures des verres de silicate de sodium dopés au CdSe QD ont été générées par les trois premiers procédés que j'ai décrits. Pour calculer leurs structures électroniques, j'ai utilisé la fonctionnelle d'échange-corrélation non locale PBE0-TC-LRC, car d'après

des travaux antérieurs de la littérature, les calculs de structure électronique basés sur les fonctions d'échange-corrélation d'approximation de gradient généralisé (GGA) ou d'approximation de densité locale (LDA) sous-estiment fortement l'écart HOMO-LUMO et les interactions coulombiennes à longue distance. L'inclusion d'une partie de l'échange Hartree–Fock est attestée dans la littérature afin de fournir une description plus précise de la bande interdite. De plus, le coût des calculs avec des fonctionnelles non locales peut être réduit en utilisant la méthode de la matrice de densité auxiliaire (ADMM). Avec cette méthode, j'ai ainsi analysé l'écart HOMO-LUMO et la densité des états pour étudier les propriétés optiques de ces systèmes hybrides.

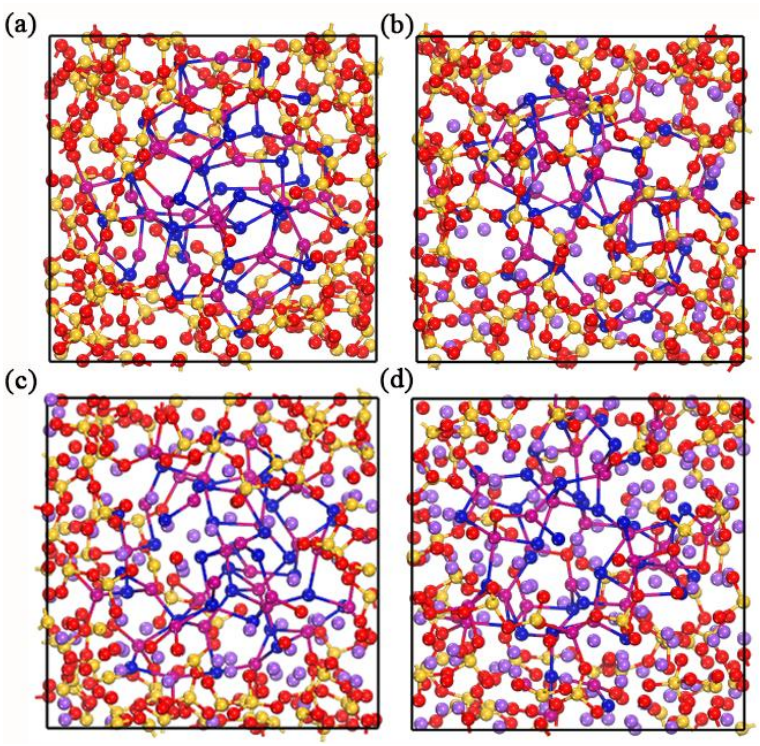

Figure S10 Configuration finale issue des simulations AIMD des verres dopés au point quantique CdSe. Composition du verre: (a)112 SiO_2-33 CdSe, (b) 30 Na_2O-90 SiO_2-33 CdSe, (c) 39 Na_2O-78 SiO_2-33 CdSe, (d) 62 Na_2O-62 SiO_2-33 CdSe.

Conclusions et perspectives

Les verres dopés aux points quantiques CdSe combinent l'excellente stabilité mécanique, thermique et chimique de la matrice des verres avec les remarquables propriétés optiques des points quantiques CdSe. Toutefois, le développement de ces matériaux est limité par leur faible efficacité quantique pour la luminescence. Dans le cadre de cette thèse, une méthodologie d'étude théorique multi-méthodes a été développée pour sonder les origines structurales et électroniques de l'émission de défauts des verres dopés aux QDs de type CdSe.

Dans la première étape des études, un modèle simplifié a été construit en coiffant les amas de Cd_nSe_n (n = 3, 10, 13 et 33) avec des atomes d'oxygène non pontants et des modificateurs de verre (Na, Ca, Zn). Les défauts intrinsèques ont également été explorés par coiffage avec des atomes de Se et des atomes de Cd. Sur la base des résultats de l'optimisation de la géométrie et du calcul des structures électroniques dans le cadre de la DFT, j'ai constaté que les adatomes contribuaient à une reconstruction structurelle très importante et à des états de défauts appariés au bord de la bande de valence et de conduction, ce qui entraîne la redistribution des orbitales HOMO et LUMO. Plus important encore, j'ai constaté que les ions Na diminuent fortement l'écart HOMO-LUMO de 2.84 eV à 1.2 eV, ce qui conduit à la photoluminescence dans le proche infrarouge, ce qui est en accord avec les observations issues des expériences.

Cependant, ce modèle simplifié était loin de la structure interfaciale réelle entre le point quantique CdSe et la matrice de verre, et une passivation importante des atomes de surface était prévisible, ce qui ne peut pas vraiment refléter l'impact de la matrice de verre sur le QD. Ainsi, le point quantique CdSe était censé être directement introduit dans la matrice de verre pour donner une illustration simple des structures atomiques locales des verres dopés au CdSe par points quantiques.

Dans un deuxième temps, les structures de la matrice de verre ont été obtenues par la méthode de trempe à l'état fondu en utilisant la simulation classique de la dynamique moléculaire. Les paramètres du potentiel d'interaction de paires et du processus thermique ont été ajustés en reproduisant correctement les fonctions de distribution radiale par rapport aux résultats expérimentaux.

Ensuite, le point quantique CdSe a été incorporé dans la matrice de verre préformée par une combinaison de la dynamique moléculaire classique et de la dynamique moléculaire *ab initio*. Sur la base de l'analyse des fonctions de distribution radiale, de

l'environnement de coordination et des structures annulaires, une reconstruction structurelle importante se produit à l'interface entre le QD de CdSe et la matrice de verre, avec la formation de liaisons Cd-O et Se-Na et la rupture des liaisons Na-O et Cd-Se. Les propriétés structurelles et la longueur des liaisons étaient en excellent accord avec les observations expérimentales, ce qui a permis d'améliorer la compréhension mutuelle des interactions entre le point quantique CdSe et la matrice de verre.

Enfin, les structures électroniques des verres dopés aux QDs de CdSe ont été étudiées en mettant l'accent sur l'impact des compositions de verre sur les propriétés optiques de l'ensemble du système. Les types de mécanismes de luminescence dépendaient des compositions du verre. Dans toutes les configurations où la teneur en sodium était égale à 0, 0.25 et 0.5, le haut de la bande de valence et le bas de la bande de conduction étaient décidés par le point quantique dit «hybride». Mais dans la plupart des configurations où la teneur en sodium était de 0.33, le haut de la bande de valence était déterminé par le verre hybride, ce qui indique la recombinaison indirecte des trous et des électrons. Il est important de noter que, sur la base de l'analyse des structures, des distributions de trous HOMO-LUMO et de la densité des états, mes résultats ont fourni une nouvelle explication à la photoluminescence, qui provenait de l'émission intrinsèque de ces systèmes hybrides plutôt que de la combinaison de l'émission de défauts et de l'émission intrinsèque de QD de CdSe « parfaits », ou isolés.

Les résultats de cette thèse ont expliqué pourquoi l'efficacité quantique de la matrice de verre était si faible. Tout d'abord, l'apport suffisant d'oxygène non pontant et de modificateurs de verre a fourni une source abondante de défauts des points quantiques CdSe en formant les liaisons interfaciales telles que les bandes de Se-Na et de Cd-O. Ces fortes interactions entre la matrice de verre et les QDs ont entraîné une énorme reconstruction structurelle de ces derniers, ce qui a entraîné la disparition des QDs «isolés» ou «parfaits». Deuxièmement, même avec la même composition, la nature inhomogène des microstructures de verre a contribué à la création de diverses structures interfaciales, ce qui a conduit à des différences d'énergie dans le diagramme, et a entraîné une large émission de verres dopés par points quantiques de CdSe.

À ma connaissance, la méthodologie que j'ai développée dans cette thèse est la première étude par modélisation explicite à ce niveau de la structure atomique locale et de la

structure électronique des verres dopés par points quantiques CdSe. Ces résultats élargissent considérablement notre compréhension de la structure interfaciale des verres dopés au QDs de type CdSe, et fournissent un aperçu physique et chimique de l'origine possible de la structure des défauts du point quantique CdSe, intéressant pour la fabrication des verres hautement luminescents.

RÉSUMÉ

Les verres dopés aux points quantiques (ou quantum dots, QDs) CdSe ont attiré une attention considérable en raison de leurs propriétés optiques et électroniques ajustables, permettant leur application dans les dispositifs optoélectroniques. Cependant, le principal obstacle de ces verres dopés est leur faible efficacité quantique par rapport aux QDs colloïdaux. Mon travail de doctorat s'est concentré sur l'étude de l'origine structurale et électronique des états défectueux d'émission des verres dopés aux QDs CdSe en utilisant des simulations moléculaires multi-échelles.

J'ai utilisé la combinaison de la dynamique moléculaire classique et de la méthode de dynamique moléculaire ab initio pour générer la structure atomique des verres dopés aux CdSe QDs. En particulier, je me suis intéressée à la caractérisation de la structure de l'interface QD/verre et une très grande reconstruction structurelle a été observée. En outre, j'ai calculé leurs structures électroniques pour sonder leurs propriétés optiques. L'impact de la matrice de verre sur les structures électroniques des verres dopés par des QDs CdSe a été exploré sur la base de calculs de densité d'états.

MOTS CLÉS

Points quantiques, Verres, Simulation moléculaire, Structure interfaciale, Structure électronique

ABSTRACT

CdSe Quantum dots (QDs) doped glasses attracted enormous attention due to tunable optical and electronic properties, enabling their application in optoelectronic devices. However, the main roadblock of quantum dots doped glasses is the poor quantum efficiency compared with colloidal QDs. My Ph.D work was focused on investigating the structural and electronic structural origins of defect states of CdSe QDs doped glasses using multiscale computational simulations.

I employed the combination of classical molecular dynamics and *ab initio* molecular dynamics method to generate the atomic structure of CdSe QDs doped glasses. Particularly, I am interested in characterizing the QD/glass interfacial structure and enormous structural reconstruction were observed, based on the analysis of radial distribution function, coordination and ring structures. Furthermore, I calculated their electronic structures to probe their optical properties. The impact of glass matrix on the electronic structures of CdSe QDs doped glasses was explored based on the calculation of density of states.

KEYWORDS

Quantum dots, Glass, Molecular simulation, Interfacial structure, Electronic structure